SPHERES IN POWER-LAW LIQUIDS WITH VELOCITY SLIP AT SOLID-LIQUID INTERFACE: MOMENTUM AND HEAT TRANSFER PHENOMENA

Submitted in partial fulfillment of the
requirements for the degree of

DOCTOR OF PHILOSOPHY

by

Rahul Ramdas Ramteke

DEPARTMENT OF CHEMICAL ENGINEERING

INDIAN INSTITUTE OF TECHNOLOGY GUWAHATI

GUWAHATI, ASSAM – 781039, INDIA

NOVEMBER 2016

CERTIFICATE

It is certified that the work contained in the thesis entitled "**Spheres in Power-law Liquids with Velocity Slip at Solid-Liquid Interface: Momentum and Heat Transfer Phenomena**", by Rahul Ramdas Ramteke (Roll No. 126107007)**,** has been carried out under my supervision and that this work has not been submitted elsewhere for a degree.

Date: 4-11-2016

Dr. Nanda Kishore
Associate Professor
Department of Chemical Engineering
Indian Institute of Technology Guwahati
Guwahti-781 039
Assam

Acknowledgements

This space of the thesis is as essential as any other. It is imperative, at this point, that I express my heart-felt thanks and gratitude to all the people that have direct or indirect connect in lending their warmth and support during the course of my PhD studies and also being so quintessentially related to me in my ups and downs of life. May I also state that the names of those that are not been mentioned here, for space limitation, should not feel they are unimportant to me. They mean to me as much as others and I have immense respect for them too.

Foremost, I would like to thank my supervisor Dr. Nanda Kishore for providing me with the opportunity to complete my PhD thesis at IIT Guwahati, India. I especially want to thank my supervisor, Dr. Nanda Kishore, whose support and guidance made my thesis work possible. He has been actively interested in my work and has always been available to advise me. I express sincere thanks to my doctoral committee chairman Prof. V. S. Ramgopal Uppaluri and other committee members Dr. V. R. Prasanna and Dr. S. Bag for their periodic assessment of the findings of my research and their constructive suggestions that had helped a great deal in shaping the thesis in the present form. Thanks to other faculty members of the department for their concern and motivation towards my endeavor.

I express thanks to all the staff members of the Department of Chemical engineering for their help in every which way. I express sincere thanks to my labmates Harsaraj, Ravi Kiran Anjani, Anand, Abhipsit, Harinath, Dilleswararao, Subramanyam and Vasu Kiran for their support throughout my research. Thank are also to my friends of IITG for their love and wishes throughout my studies.

Last, but not the least, thanks to my family members who have always been by me through thick and thin and for their help in ways not known to them. I owe sincere thanks for the selfless continued support and encouragement of my mother and father toward my academic pursuit.

Rahul Ramdas Ramteke

Contents

List of Tables

List of Figures

Abbreviations

AFM = atomic force microscopy

BGK = Bhatnagar Gross Krook

FEP = fluoropolymer

HAM = homotopy analysis method

HDPE = high-density polyethylene

LDPE = low-density polyethylene

LLDPE = linear low-density polyethylene

MPIV = microscopic particle imaging velocimetry

PBD = polybutadiene

PC = polycarbonate

PDMS = polydimethylsiloxane

PEPDM = poly-ethylene-propylene-diene-monomer

PEVA = poly(ethylene-vinyl) acetate

PI = polyisoprene

PIB = polyisobutylene

PP = polypropylene

PR-DNS = particle-resolved direct numerical simulation

PS = polystyrene

PTFE = polytetrafluoroethylene

PVC = polyvinylchloride

SFA = surface force apparatus

TMAC = tangential momentum accommodation coefficient

Nomenclature

b, C_1, C_2 = slip coefficient, dimensionless

C_d = total drag coefficient, dimensionless

C_{df} = friction drag coefficient, dimensionless

C_{dp} = pressure drag coefficient, dimensionless

C_p = specific heat, $JKg^{-1}K^{-1}$

d = diameter of sphere, m

F_D = drag force, N

h = convective heat transfer coefficient, $Wm^{-2}K^{-1}$

I_2 = second invariant of the rate of deformation tensor, s^{-2}

k = thermal conductivity, $Wm^{-1}K^{-1}$

Kn = Knudsen number, dimensionless

l = mean free path of gas molecules

L_r = wake length, m

l_s = slip length, m

L_s = slip length, dimensionless

L_{slam} = slip length for laminar layer, m

L_{sturb} = slip length for turbulent layer, m

$\mathcal{L}_T$ = temperature jump length, dimensionless

m = power-law consistency index, $Pa.s^n$

n = power-law behavior index, dimensionless

Nu = Nusselt number, dimensionless

Nu_{avg} = average Nusselt number, dimensionless

p = pressure, dimensionless

Pe = Peclet number, dimensionless

Pr = Prandtl number, dimensionless

R = sphere radius, m

Re = mean slip Reynolds number, dimensionless

Re = Reynolds number, dimensionless

R_∞ = domain radius, dimensionless

T = temperature, K

T_o = temperature of power-law liquid, K

T_s = temperature of sphere surface, K

U_o = free stream velocity, ms^{-1}

u_s = slip velocity, ms^{-1}

V = velocity vector, ms^{-1}

v_r = r-component of velocity, dimensionless

v_θ = θ-component of velocity, dimensionless

v_ϕ = ϕ-component of velocity, dimensionless

We = Weissenberg number, dimensionless

Greek symbols

β = slip coefficient, m $(Pas)^{-1}$

ε_{ij} = rate of strain tensor, s^{-1}

Υ = heat capacity ratio, dimensionless

θ_S = separation point, degree

Π_ε = second invariant of the rate of strain tensor, s^{-2}

Φ = Volume fraction of spheres, dimensionless

η = dynamic viscosity of fluid, Pa s

ρ = density of fluid, kg m^{-3}

Ω = angular velocity, rad s^{-1}

σ_v = tangential momentum accommodation coefficient (TMAC), dimensionless

σ_T = thermal accommodation coefficient, dimensionless

τ = extra stress, Pa

λ = slip parameter, dimensionless

γ = shear rate, s^{-1}

γ_c = critical shear rate, s^{-1}

ABSTRACT

Fluid Flow in contact with solid particles occur in numerous applications such as fixed and fluidized bed reactors, pneumatic conveying, nuclear reactors, sedimentation, sewage sludge, coal combustion, airborne dynamics and suspension flows. On the other hand, velocity slip along the solid surface can arise in the case of aerosols, flow through porous materials, suspension, capillary flows, polymer flow through extruders and flow along smooth solid surfaces. Thus, the momentum and heat transfer from spheres can be affected by velocity slip at the fluid-solid interface as well as rheology of surrounding continuous liquid and adjacent spheres. Thus, in the present work, the momentum and heat transfer phenomena of a single spherical particle and those of assemblages of spheres in Newtonian and power-law liquids with linear velocity slip boundary condition at the fluid-solid interface are numerically analyzed. The effect of the velocity slip at fluid-solid interface is studied by the use of linear velocity slip model. While the effect of volume fraction of spheres in assemblages is deliberated by the use of free surface cell model. The flow behavior and heat transfer phenomena of single solid spheres and assemblages of spheres in Newtonian and power-law fluids are studied using a finite difference method based simplified marker and cell (SMAC) semi implicit algorithm. For computational simplicity sphere-in-sphere type computational domain has been chosen. Thus the governing continuity, momentum and energy equations are considered in spherical coordinates. The convective terms being discretized using the quadratic upstream interpolation for convective kinematics (QUICK) scheme; while the diffusive and non-Newtonian terms discretized using central differencing scheme. Further, the velocity slip effects on the streamline patterns, iso-vorticity contours, drag coefficients, surface vorticity, surface pressure, surface viscosity, isotherm contours, surface Nusselt number and average Nusselt number of single sphere and of assemblages of spheres in

Newtonian and power-law fluids are extensively deliberated as functions of the Reynolds number, slip parameter, power-law index, Prandtl number and volume fraction of spheres. In summary, in the case of single sphere at $Re \leq 20$, there is no flow separation for all slip parameters and power-law indices in the present range of investigation. Regardless of value of the Reynolds number, there is no flow separation for all values of power-law index provided the slip parameter is ≤ 1. For $\lambda \geq 5$ and $Re > 20$, the recirculation wake length increases with increasing Reynolds number and slip parameter. Further, a crossover Reynolds number (at $Re \approx 5$) is found on C_d versus Re curve for all values of the power-law indices; however, this crossover Reynolds number is found to be weak function of the slip parameter. Regardless of the values of the slip parameter, below this crossover Reynolds number, the drag coefficients increased with the decreasing power-law indices, while the opposite trend is observed above this crossover Reynolds number. Furthermore, the drag coefficient of spheres in an assemblage increased with increasing slip parameter and/or volume fraction of spheres. The thermal boundary layer becomes thinner with increasing Reynolds number and/or Prandtl number and/or decreasing power-law indices. The average Nusselt number increases with increasing Reynolds number and/or Prandtl number and/or volume fraction of spheres and/or decreasing slip parameter and/or power-law index. Finally, on the basis of present numerical results, several correlations for C_d and Nu_{avg} of single and multiple spherical particles in Newtonian and power-law fluids with velocity slip at the interface are proposed.

Chapter 1

INTRODUCTION

1.1. Background

The fluid flow in contact with solid surface is most common phenomena in environment such as desertification and air pollution, and also in industries like in fluidization, sedimentation, pneumatic conveying, polymer processing, etc. The choice of appropriate boundary conditions at the fluid-solid interface to analyze the flow phenomena may satisfy the most of these practical applications. The boundary conditions at the fluid-solid interface vary from ideal to non-ideal, i.e., no-slip to slip and in case of temperature constant wall temperature/wall flux to temperature jump. The most commonly used boundary condition at the solid surface is 'no-slip'. The no-slip boundary condition at a fluid-solid interface states that the fluid molecules adjacent to the surface of the solid acquire the same velocity as that of the solid surface velocity. The tangential and normal components of the fluid velocity at the fluid-solid interface are zero if the non-porous solid is not moving, i.e., the no-slip means that the relative velocity between the fluid and the solid is zero at the point of contact. The fluid flow may then acquire various types of non-zero velocity field away from the solid surface depending on the nature of flow. The natural basis for the no-slip boundary condition is that the interaction potential between the fluid and solid keeps the fluid molecules bound to the solid interface. This obstructs fluid movement along the interface and prevents the fluid molecules from adopting a velocity that is different from the solid surface [1–4]. Perhaps Bernoulli [4] first suggested that for a fluid flowing along a solid surface the fluid velocity at the solid surface must be the same as that of the surface and gradually vary when moving away from the surface into the fluid. Afterward, the no-slip

boundary condition was enunciated by Coulomb [5] though no convincing explanation was presented. Stokes [6] while reviewing various fluid-solid interactions referred to Coulomb's experiments and clarify that this experiment only partially justify the no-slip condition. The reliability of the no-slip boundary condition is often subjected to following factors [6–7].

1. Comparisons between experiments and theoretical solution of fluid flow problems with the use of the no-slip boundary condition.
2. The nature of the physical surface.
3. The rheological behavior of the fluid flowing along solid surface.
4. The interactions between fluid and solid surfaces.

All these factors are given by Stoke [6–7] but overall justification for the use of the no-slip condition is mainly based on the comparison between theoretical and experimental results. After abundant controversy in the 19^{th} century, the no-slip boundary condition became accepted because it fitted most physically observed behavior depending on availability of sophisticated equipment available till then [8–9]. This fact holds true in most of the macroscopic experiments, i.e., the use of the no-slip boundary condition is reliable. In fact, the no-slip boundary condition cannot be derived from the principles of fundamental physics. This is an assumption based on the experimental observations of fluid flows over solid surfaces.

Although this might be a good assumption for many macroscopic systems, there have been tenacious doubts for a century about the validity of the no-slip boundary condition. In the traditional flow analysis, at the point of fluid-solid contact the velocity continuity is enforced along the fluid-solid interface but in case of some macroscopic and many microscopic systems the discontinuity of the velocity at the fluid-solid interface arises due to the breakdown of the

local thermodynamic equilibrium between the solid surface and adjacent fluid. Therefore, use of no-slip boundary condition is questionable for the cases of polymer solutions and melts, complex fluids, gas flows, flows over lyophobic surfaces and flows in micro and nano channels [10–15]. **Figure 1.1** represents the no-slip and velocity slip boundary conditions at the fluid-solid interface. It is well-known that many highly non-Newtonian liquids and/or complex fluids such as polymer melts/solutions show effective slip at the surface of solid due to reduction in the viscosity of the fluid layer close to the solid surface resulting from compositional variation or shear thinning [16].

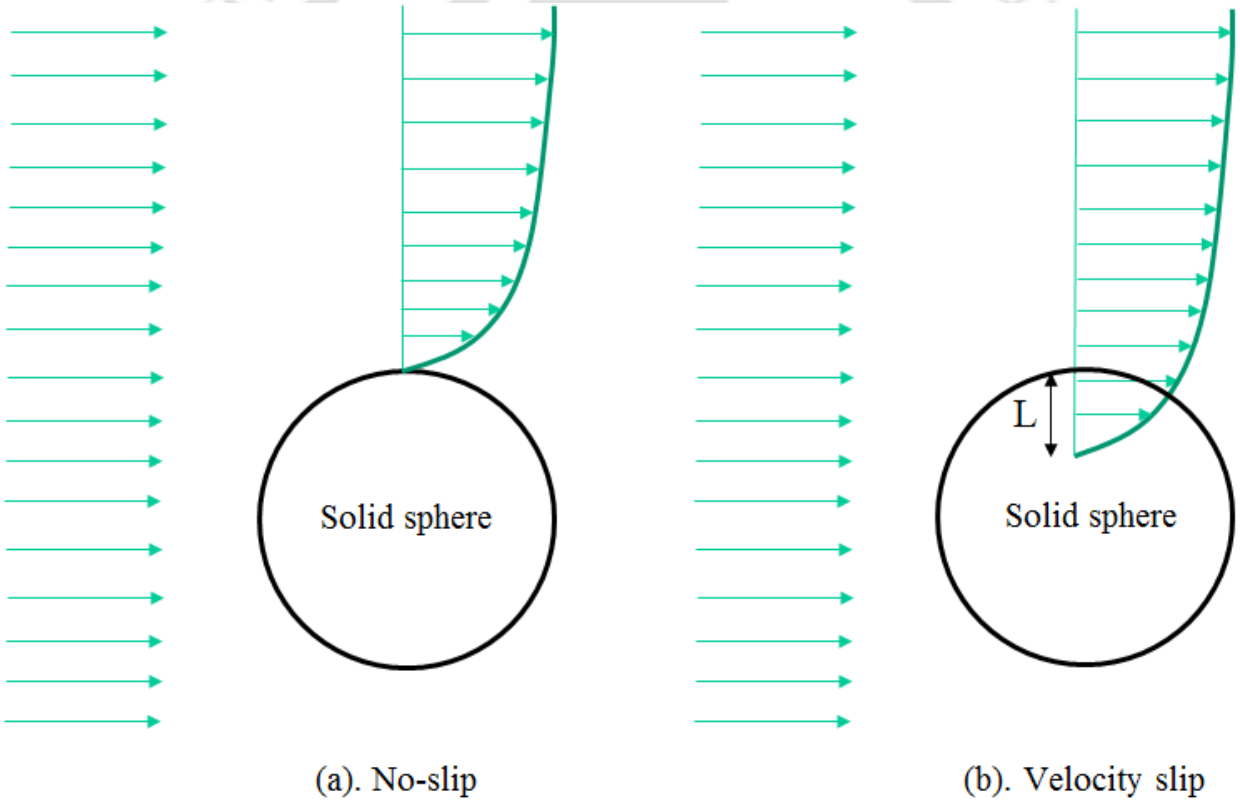

Figure 1.1 Schematic representations of (a) no-slip and (b) velocity slip boundary conditions at te fluid-solid interface.

Several complex/non-Newtonian fluids, do not obey no-slip boundary condition such as polymer melts and solution [17–22, 23–27], suspensions [28–33], dispersions [34–36], gels [37–41], colloidal dispersions [42–43], pastes [44–45], and foams [46–48]. In case of polymer melts/solutions, several polymer melts/solutions obey slip boundary condition for example high-density polyethylene (HDPE) [16, 19–20, 49], linear low-density polyethylene (LLDPE) [50], fluoropolymer (FEP) [51], polyisoprene (PI) [52], polybutadiene (PBD) [18, 53–54], polydimethylsiloxane (PDMS) [22 55], polystyrene (PS) [56–57], polycarbonate (PC) [58], polyisobutylene (PIB) [59–60], polypropylene (PP) [61–63], poly(ethylene-vinyl) acetate (PEVA) [64], polyvinylchloride (PVC) [65–67], polyethylene–propylene–diene-monomer (PEPDM) and other rubbers/elastomers [23–25, 68]. The slip mechanism on account of polymer melts is due to the first layer of adsorbed macromolecules on the solid surface offering discontinuity of velocity at the interface. The slip condition is also found in the cases of gels such as hydroxypropyl guar gel [37], microgels of deformable particles [38–40], skin/hair care gels [69], viscoplastic hydrogel [41], and gels of colloidal particles [33]. Further in the case of pastes as well, significant level of slip has been observed, for examples potato pastes [44], starches [45], mayonnaise [70], polytetrafluoroethylene (PTFE) pastes [71–72], bread dough [73], and ice cream [74]. Numerous researchers by various experimental approaches showed persuasively that variety of Newtonian liquids can also slip over the surfaces of solids [75–85].

Furthermore, recent simulations [86–87] and experiments [88–89] presented that if smooth surfaces are partially wetted then low-viscosity fluids can slip over those surfaces. In case of rough surfaces as well fluid particles can be trapped into the pocket of the rough solid surface causing fluid slip [92]. Earlier, it was assumed that the slip over smooth surfaces is constrained to situations where the solid surface was incompletely wetted by the fluids, but

recent experimental studies demonstrate that this is not so. The fluid slip can also occur in cases where smooth solid surfaces are wetted completely by the fluid [91–92]. The shear-dependent slip was reported in many experiments [93–102]. A few possible reasons for the fluid slip over solid surface are surface roughness [103–104], roughness-induced dewetting on hydrophobic surfaces [105–106], dissolved gases [107–109], and wetting properties of solid [110]. It is possible to make fluid to slip over solid surface by modifying surface properties so that to reduce the drag. Schnell [111] treated a glass surface with vapors of dimethyldichlorosilsne to measure slip; and thus made glass surface becomes water repellant causing water slippage over the glass surface. Several such successful modifications of solid surface have been performed experimentally by many researchers [94, 102, 112].

The amount of slip in a given system can be quantified by a number of parameters, but the most commonly quoted parameter across the literature is slip length which is based on Navier's slip model [113] who first relate a linear slip velocity to the wall shear stress in the form of $u_s = L_s \left(\frac{\partial u}{\partial n}\right)$, where L_s is the slip length that can be interpreted as the fictitious distance into the surface to the point where the no-slip boundary condition is satisfied. This slip length is believed to be dependent on temperature, pressure, normal stress, molecular parameter, types of fluids, surface properties and the characteristic of the fluid-solid interface. Several non-linear slip models have also been proposed especially for non-Newtonian fluid flows, for instance, the slip velocity is approximated by power law equation i.e. $u_s = L_s \left(\frac{\partial u}{\partial n}\right)^m$, where m is the power law exponent [20]. There are number of experimental methods, indirect and direct, available to measure the velocity slip at the solid surface such as fluorescence recovery [75, 77], surface force apparatus (SFA) [78, 80], atomic force microscopy (AFM) [93, 95–97], sedimentation

[76], streaming current [114], particle image velocimetry [81], pressure drop versus flow rate [102, 112], fluorescence cross-correlations [115]. However the traditional method to measure the wall slip is by the use of Mooney plots [116–118] rather than by direct observation and measurement. In the recent past molecular dynamics simulations have also been widely used [86–87, 119–126] to investigate the fluid slip over solid surfaces especially for the cases where experimental measurements are very difficult [127]. The molecular dynamics are also applied for the sake of validating experimental results or vice-versa [121]. The advantage of molecular dynamics is that it can be used to deal with extreme conditions such as high shear rates [125]. Other simulation and numerical methods have also been employed to investigate slip such as Lattice Boltzmann method [110], direct numerical simulation [117] and large eddy simulation [120]. Some of these approaches have been used to overcome the limitations of molecular dynamic simulations such as dealing with low shear rates and large system sizes [110] because molecular dynamic simulations are usually limited to molecular level.

1.2. Slip Mechanism

Slip is a varied phenomenon with different fluid and solid properties and it diverges depending on the surrounding conditions and flow system. The fluid-solid interaction can be influenced by a number of dynamic and static factors that stimulate the slip. There is no single general concept to describe slip phenomena in all situations though, there are numerous phenomena suggested to elucidate slip mechanism in certain conditions and flow systems. Some of them are discussed here. In the case of flow of polymers, slip is due to the first monolayer of macromolecules which adsorbed on the solid surface. Molecular chains form loops and adsorbed on the solid surface at abundant locations. The adsorbed chains are also warped with chains in the bulk. Under the impact of flow, the following circumstances can happen: (i) desorption/detachment of the chains

from the solid induces to weak slip. This is stated as adhesive/true slip. This occurs when the solid surface is covered with low surface energy polymer-based coatings or other low surface energy coating such as fluoropolymers [58, 84–85, 128–129] (ii) partial chain unraveling from the bulk of chains, which are strongly adhere on the solid surface that also causes weak slip. This is defined as cohesive slip. This is the more typical phenomena of slip in polymer melts flow past the metallic surfaces and is of concern to polymer processing [16-17, 20, 53–54, 130–133]. For this situation, interfacial rheological slip laws are required to pretend the respected processes [134–139]; (iii) under heavy fluid flow and because of orientation of chain loops adhered on the solid in the directions of flow abrupt unraveling arises that indicates the transition of weak slip to strong slip [140]. For the instance of polymer solutions, the slip velocity has been accounted to rely upon polymer adsorption [25], polymer concentration and wetting properties of the surface and the type of polymer molecules [26–27]. Polymer solutions and suspensions exhibit behaviors that co-exist with the no-slip boundary condition [23–27]. This is because of a formation of very thin low-viscosity layer on the surface due to the movement of the solid particles (suspensions) or solute (polymer solutions) away from the surface that is of entropic origin which is defined as apparent slip. The slip layer may vary between 0.1 and 2 μm or higher, depending on the particle size and concentration. Also in the case of suspensions, the apparent slip depends on concentration [31, 141], temperature [30, 142], particle size [30–31] and wetting properties of the wall [143]. In case of gel, microgel, colloidal gel/glasses and paste i.e. concentrated dispersion of soft particles exhibits a generic slip phenomena in which slip resulted from balance between osmatic forces and non-contact elastohydrodynamic interaction between the squeezed particle and solid surface. In the case of gels, slip velocity depends on the surface energy of the wall (hydrophilic versus hydrophobic surfaces) [144], surface roughness [37–40], and shear

history because many of these fluids reveal thixotropic behavior [69]. Similar slip mechanisms have been discussed for the colloidal gels/glasses elsewhere [42–43].

In the case of gases, the mean free path is commonly longer than the molecule size, so there will be interaction of gas molecules with the surface without involving another gas molecule. Therefore, this interaction can be treated as a simple reflection. If gas molecules have some momentum along the solid surface and an incident gas molecule simply sticks to the wall, then all of its tangential momentum is transferred to the wall. This is defining as 'stick' or the no-slip condition. At the other extreme, assumed that an incident molecule undergoes specular reflection and bouncing off from solid surface with no change in its tangential momentum, then the gas molecules experience true slip. While specular reflection is characterized as the balance of well-defined angles of incidence and reflection, the key part of the interaction is that the surface particle force is always perpendicular to the surface, so the wall cannot change the tangential momentum of the colliding molecules. This situation will be always if the surface is perfectly flat and rigid, though this is an ideal case [120, 140]. In real systems revealing Knudsen slip, there only some fraction of gas molecules will undergo specular reflection [150].

It is valuable to recognize three distinct circumstances for a boundary slip since the dynamics of fluids at the interface present at different length scales.

1.2.1. Molecular slip

True slip at the molecular level occurs, when the fluid molecules are effectively sliding on the solid surface if the viscous force between fluid molecules at the interface is stronger than that of molecules of the fluid and solid. Molecular slip refers to the prospect of utilizing hydrodynamics to force liquid molecules to slip against solid surface. Such concept necessarily involves large

forces. In case of gases, the gas-wall interactions were divided into two processes: incidence and reflection. In kinetic theory, Maxwell established two classical reflection models, i.e., the diffusive and specular models. In the diffusive model, gas molecules are adsorbed near the wall for a long time and totally forget the incident information. After that, these molecules are desorbed and re-emitted to the half space above the wall. The tangential momentum is completely lost and the normal momentum changes to fixed values related to the wall temperature in diffusive reflections. In the specular model, where gas molecules experience direct elastic collisions with the wall without adsorption which results in molecular slip at the fluid-solid interface. In case of liquid, at the ground state the configuration of the atoms in the first liquid layer at the wall has a lower energy than any other configuration. Therefore, the diffusion of the atoms from the bulk into and out of the first liquid layer will be biased. On the other hand, in the absence of a ground state, the arrival and departure of liquid atoms at the solid surface are unbiased. The dynamics of the number of atoms can be made equivalent to a random walk by determining the change in number of atoms in the bulk and first layer of liquid. This random walk of atoms at solid surface results in to true slip at fluid-solid interface.

Most recent studies have stated that molecular slip (true slip) decreases with increasing fluid-solid interactions [87, 123], density of liquid and wall [145–146], whereas increases with increasing pressure [87]. The roughness is also found to strongly influence the molecular slip [119, 146–149]. Lichter et al. [150] studied the facts of the molecular slip mechanism and showed that slip at low shear rates arises by localized defect propagation and changes to slipping of entire molecular layers for larger rates. This is true for liquid repellant surfaces [11], but might also hold, under particular situations, for lyophilic surfaces [75]. If the sizes of the liquid molecules are of equivalent size to the cavities or pockets on the solid surface, then the

molecules can trapped in the cavity/pocket on the surface. If molecules size is much larger or much smaller cavities on surface then fluids can slide on the surface. This is true for two solids sliding along each other [151], but simulations show that it might also hold for liquids on solid surfaces [149, 152].

1.2.2. Apparent slip

Apparent slip occurs in a thin layer of low viscosity liquid which forms on the smooth surface of solid or in regions of higher shear stress beside of the ridges and peaks of rough solid surfaces [153]. However, experiments [154–155] and simulations [150] have revealed that the viscosity of simple fluids is in close agreement with the bulk value down to very small separations. This occurs when a thin layer of fluid molecules is strongly bound to the surface of solid and the velocity gradient adjacent to the surface is so high then the fluid molecules beyond this layer seem to slide on the solid surface. The thickness of this layer can be large or as small as a single monolayer which is known as a stagnant layer. At room temperature and pressure, there are always residual dissolved gases in the liquid. Also at the critical levels of shear stress may be cavitation induces in the liquid and produces gas bubbles which may adhere to the surface and form a layer at the surface onto which the liquid can slip [78, 80, 98–109]. At a critical value of shear rate, a microscopic surface roughness can favor the formation of a layer of turbulent flow at the interface, even if the overall flow is laminar and therefore viscosity of this layer is different with respect to the bulk liquid [156]. The nature example is the shark-skin effect [157]. Arrangement of liquid molecules at surface of solid decreases the friction between adjacent layers of liquid and consequently enables the sliding of one layer over other. The arrangement of molecules is robust so closer the molecules are on to the solid surface only [119, 158].

1.2.3. Effective slip

Effective slip is for the cases where molecular or apparent slip at a complex heterogeneous surface is estimated by averaging an appropriate measurement over the length scale of the experimental apparatus [111, 159–160]. In other words, instead of attempting to solve equations of motion at the size of the individual pattern or corrugation, it is suitable to assume the macro-scale fluid motion on the size larger than the characteristic length of corrugation or the thickness of the channel by utilizing effective boundary conditions that can be implemented at the imaginary smooth surface. Such an effective condition replicates the actual one along the heterogeneous surface. It completely describes that the flow at a real surface and can be utilized to solve intricate hydrodynamic problems without complicated calculations. Such an approach is supported by a statistical diffusion arguments theory of heterogeneous porous materials, and has been acceptable for the situation of Stokes flow over a broad class of surfaces [159–161]. For anisotropic surfaces effective slip depends on the direction of flow and is generally a tensor. Effective slip also depends on the typical length scales of the system. The example of such a heterogeneous system is composite super-hydrophobic surfaces, where a gas layer is steady with a rough solid surface texture. For these cases effective slip lengths are frequently very large compared to the value of effective slip length on smooth solid surfaces, similarly that observed for wetting surface, when the surface is rough and heterogeneous then the contact angle can be dramatically enhanced [159].

1.3. Development of Slip Models

The concept of the slip boundary condition at the fluid-solid interface was first suggested by Navier [113] based on the knowledge of the dissipative kinetic energy of the external friction and external friction force between fluid (A) and solid surface (B) which is delineate as $F_{AB} = vu$,

where v = external viscosity, u = tangential fluid velocity component over solid surface. From Navier's various formulations of fluid dynamics he was able to formulate slip boundary condition, i.e., $v\text{v} = 2\mu dn$ and simplified in the form of $u_s = \mu \Big/ v\left(\frac{\partial u}{\partial n}\right)$. Next, trying to compare the model of external and internal viscous flow with Girard's experiments, Navier has arranged three analytical solutions for different flows in open channels and in pipes [11]. In these solutions, he considered both viscous coefficients μ and v and defined the slip length l_s as a ratio of fluid viscosity (μ) to external viscosity (v). Navier has also proposed the first closure for the slip length for flow of water over glass as equal $l_s = \mu/(0.0023\rho)$ where ρ and μ are density and viscosity of water respectively. This was verified by Hemholtz and Von Piotrowski [162]. The first closure on external friction of a rarefied air over a glass was determined by Kundt and Warburg [163] in the form of $l_s = \mu/\upsilon = 0.7122l$ where l, is the mean free path of gas molecules at actual pressure. The first systematic experimental study reporting the external viscosity for liquids and gases has been made by Wiedemann [164], who also invented technical devices allowing for measurement of v and l_s. Whetham [165] made several other systematic and critical experimental studies. Later on dimensionless slip length ($L_s = l_s/\text{L}$) propoed by Navier, Maxwell [166] interpreted slip length in terms of dimensionless mean free path of molecules, $L_s = \left(\frac{2-\sigma_v}{\sigma_v}\right) Kn$ where σ_v is the tangential momentum accommodation coefficient (TMAC). It depends on the type of fluid and solid surface. The coefficient σ has been calculated for various materials by fitting the experimental data to the simulation results [167]. TMAC is defined as the fraction of gas molecules reflected diffusively from a solid surface in rarefied gas microflows. Beskok and Karniadakis [168] proposed a model of a two-parametrical dimensionless slip

length, which strongly depends on rarefaction and pressure, $L_s = \left(\frac{2-\sigma_v}{\sigma_v}\right)\frac{Kn}{1-bKn}$ where b is the slip coefficient, which is an empirical parameter to be determined either experimentally or from linearized Boltzmann or DSMC data. To et al. [169] extended Beskok and Karniadakis's model for different range of Knudsen number and a constant acceleration gradient in the boundary layer in the form of $L_s = \left(\frac{2-\sigma_v}{\sigma_v}\right)Kn\left[\lambda\frac{Kn}{Re}+1\right]$. Here, λ is slip parameter which accounts for the differences between the idealized conditions used to derive the slip model and the realistic ones. Thompson and Trojan [146] proposed the dimensionless slip length for shear flow of liquid as function of shear rate i.e. $L_s = L_s^o\left[1-\frac{\gamma}{\gamma_c}\right]^{-0.5}$. Where L_s^o is classical rate-independent slip length, γ and γ_c are the shear rate and critical shear rate respectively. Thompson and Trojan [172] suggested that close to a critical shear rate the boundary condition can significantly affect flow behavior at macroscopic distances from the wall. They also proposed the slip length for turbulence layer, $L_{sturb} = L_{slam}(1+\mathrm{t}^2\Pi_d)^{-0.5}$ where Π_d is the second invariant of the surface deformation rate, t is an intermittency time. After the transition from laminar to layer turbulence, enhancement of the external friction may be observed. Numerous values of the slip length and the methods of their determination have been reported [3, 37]. Fitting the experimental results, with the theoretical results based on slip models, it is often necessary to hypothesize various dependency of the slip coefficient on the Knudsen number, and the geometry of a channel [59, 61]. Loyalka [170] based on Bhatnagar Gross Krook (BGK) kinetic theory proposed a slip length $\frac{2-\sigma_v}{\sigma_v}\left(1-0.1871\sigma_v\right)$, and results are exact for $\sigma_v \to 0$. Loyalka et al. [171] also presented one

more slip length model $\frac{2-\sigma_v}{\sigma_v}(1-0.1621\sigma_v)$, and results are accurate for σ_v value varies from 0 to 1. Maurer et al. [172] performed helium and nitrogen flow experiments in shallow micro-channel at Knudsen number, *Kn* = 0.8 and 0.6 respectively and developed slip length model that is $\left(1+6\frac{2-\sigma_v}{\sigma_v}Kn\right)$ and $\left(1+6\frac{2-\sigma_v}{\sigma_v}Kn+12C_2Kn\right)$. Myong [173] proposed a gaseous slip model $\left(\frac{P}{4w\,\mathrm{Pr}\,Kn+P}\lambda\right)$, based on the langmuir adsorption isotherm. Fichman and Hetsroni [174] presented the correction factor for Maxwell equation for 1-D plane and tubular isothermal and incompressible flow as function of Knudsen number, $\left(1+6Kn+18Kn^2-4Kn^3\right)$. Lilley and sader [175] presented slip length, $\frac{1}{2Kn}\left(\frac{1}{\gamma_L}-1\right)$ in Knudsen layer. Whereas, Xue and Fan [176] put a step forward and presented a high-order slip expression replacing *Kn* by *tanh(Kn)* of Maxwell slip length i.e. $L_s=\left(\frac{2-\sigma_v}{\sigma_v}\right)\tanh Kn$. Bahukudumbi et al. [177] developed new higher order slip length model, $1.2977+0.71851\tan^{-1}\left(-1.17488Kn^{0.58642}\right)$ which accurately predicts the velocity distribution and shear stress in a wide range of Knudsen number ($Kn \leq 12$), and it is valid for low subsonic flows with Mach number ≤ 0.3.

Also various second order velocity slip models have been proposed which are applicable at high value of Knudsen number. Generalized form of second order velocity slip model can be written as follows and **Table 1.1** represents the expression of the second order slip coefficients that have been discovered by various researchers.

$$u_s - u_w = C_1 Kn\left(\frac{\partial u}{\partial n}\right)_s + C_2 Kn^2\left(\frac{\partial^2 u}{\partial n^2}\right)_s \quad (1.1)$$

Table 1.1 Expressions for second order slip coefficients reported in the literature

Authors	Slip coefficient 1, C_1	Slip coefficient 2, C_2
Beskok and Karniadakis [168]	$\frac{1-\sigma_v}{\sigma_v}$	0.5
Aubert and Colin [172]	$\frac{1-\sigma_v}{\sigma_v}$	9/8
Karniadakis and Beskok [178]	$\frac{1-\sigma_v}{\sigma_v}$	$-\frac{1-\sigma_v}{\sigma_v}$
Jie et al. [179]	$\frac{1-\sigma_v}{\sigma_v}$	$-\frac{1-\sigma_v}{\sigma_v}\frac{\mathrm{Re}}{Kn}$
Lockerby et al. [180]	$\frac{1-\sigma_v}{\sigma_v}$	$\frac{9}{4\pi}\frac{\mathrm{Pr}(\gamma-1)}{\gamma}$
Ng and Liu [181]	$1.15\,Kn$	$0.25Kn^{1.35}$
Wu [183]	$\frac{2}{3}\left[\frac{3-\sigma_v f_w^3}{\sigma_v};-\frac{3}{2}\frac{3(1-f_w^2)}{Kn}\right.$	$\frac{1}{4}\left[f_w^4+\frac{2}{Kn^2}\left(1-f_w^2\right)\right];$ $f_w=\min\left[1/Kn,1\right]$

1.4. Effect of Parameters on Velocity Slip

Direct experimental evidence supported by analytical and computational solutions indicate that several factors affect the magnitude of slip. Although the primary mechanism of slip is not completely resolved but factors that revealing apparent effect on measured slip has been acknowledged. Among the most scrutinized factors are lyophobic surfaces along with that surface coating and roughness. Shear stress is one of the controversial parameter which is open

up more paths to potential applications. Several other factors that affect the slip are temperature, pressure, viscosity, dissolved gases, molecular weight and molecular structure. Some of them are discussed here.

1.4.1. Surface wettability

Slip is an interfacial phenomenon and so interfacial parameters are imperative. The interfacial parameter most comprehensively concerted in the literature is the surface wettability. The preliminary assumption that the slippage is only occur on the low wettability solid surface due to the weaker fluid-solid molecular attraction. Tentatively, slip has been broadly stated on surfaces that have a low surface wettability [11]. Substantial slip expected over the hydrophobic/lyophobic surface [11, 14, 79, 88]. After some experimental studies demonstrated that slip is likewise present on entirely wetted surfaces at very high shear stress [146]. The surface wettability contacting with a liquid droplet can be measured by the contact angle and high contact angle indicate the weaker fluid-solid interaction. Thus the friction reduces and liquid can slip over the solid surface. Slip has been computed for systems in complete wetting [61, 93, 83] and partial wetting [94–98, 100–102]. The amount of slip has usually been found to be increasing with contact angle due to the weaker fluid-solid intermolecular attraction. Voronov et al. [184] studied a dimensional analysis based on data from molecular dynamic simulations and concluded that distinctive fluid-solid combination did not get same slip lengths even with having comparable contact angles, as evident in their earlier work (Voronov et al. [124]). From their results demonstrated that slip lengths may not always increase with contact angle but the relative molecular weight of the fluid and solid should also be considered. Based on experiments and simulation studies, one can conclude that the wetting and non-wetting surface slippage is

widely accepted but also it depends on the other factors and slip phenomena may be a molecular or apparent slip.

1.4.2. Surface roughness

The effect of surface roughness on the slip length is debatable in the literatures because it has been accounted for that the surface roughness reduces or enhances the slip of fluid over solid. In fluid mechanics, the argument is that surface roughness increases viscous dissipation as the fluid flows over surface irregularities, which turns to increase the resistance to flow and reduce slip [122, 185–189]. Other researchers have claimed that surface roughness limit the fluid-solid contact and prevent the fluid from penetrating into the valleys, which can enhance the magnitude of slip [93, 149, 190]. Hocking [190] discussed the solution of the Navier-Stokes equation for grooves of finite and infinite depth. He concluded that the effect of surface irregularities introduces an effective slip coefficient that is proportional to their depth. Wantanabe et al. [191] used the Cassie model of surface roughness to argue that the surface tension of the fluid prevents penetration into fine grooves on the surface of a wall, reducing the contact area. The lower contact area raised the free surface energy at the interface, causing the onset of slip at lower shear rates. Thompson et al. [146] studied molecular dynamic simulations of a Newtonian fluid over a corrugated surface. They declared that slip is precise by the extent to which the fluid fills the solid surface due to corrugations in the surface energy of the solid. In experiments [119, 147] and molecular dynamic simulations [125, 148–149,], it is observed that surface roughness suppressed slip. An inevitable effect of the surface roughness is the changing of wettability of surface. If there are trapped gases in the gaps between the rough surfaces, then the interaction between the liquid and solid surface reduces and slip can enhance.

1.4.3. Shear rate

A few experiments [78, 80, 134, 93, 96–97, 99, 101] and molecular dynamic simulations [125, 192–195] discovered shear-dependent slip. The slip length is a nonlinear function of the shear rate. It will be easy to understand how shear stress influences the fluid-solid interface boundary condition when analogy of solid material considered. When the shear force applied to solid at low shear rates the molecular bonding within the solid material is capable to endure the strain force and the bulk material holds together. As the shear force increases, the molecular bonding is ultimately overcome and results in a shear failure of the solid. The same analogy has been considered for a solid-liquid interface in case of slip. If the shear rate continues to increase finally something within the system must fail. This could be a failure of the no slip boundary condition assumption. Slip has also been experimentally reported to increase with shear rate, rather than remain as a constant. A variety of SFA and AFM lubrication experiments have reported shear dependent slip lengths [78, 80, 96, 99]. Thompson et al. [86] provided molecular dynamics simulations to quantify shear rate dependent slip boundary condition. They found that the slip length is independent to the shear stress at low value shear stress, but increases rapidly with the shear stress above critical value of shear stress. The experimental results of Ulmanella and Ho [196] from nano-channel flow measurements to hint at a limiting value of slip velocity at high shear rates.

1.4.4 Absorption of surfactant on solid surface

Adsorption of surfactants will diminish the solid−liquid surface vitality by adsorbing on the surface. The surfactant can likewise have a high two dimensional diffusivity along an interface thus they are a sensible decision when endeavoring to persuade slip. Zhu and Granick [85] used surfactant in slip experiments of organic solution and observed the enhancement of the slip

length. Henry et al. [96] observed that if surface covered with surfactant then the slip is independent of surface wettability and also observed the similar magnitude of slip on hydrophobic and hydrophilic surfaces. Various researchers have contended that slip might be brought on by a gas crevice or nano-bubbles nucleating on the surface of solid [12, 14, 107]. However, recollect that surfactant at a solid−liquid interface can avert velocity transfer from the liquid phase to the gas phase. The surfactant particles can deliver a Marangoni diffusive back pressure that balances the shear stress at the interface and immobilizes the liquid−gas interface. In the vicinity of surfactant, nanobubbles at the solid-fluid interface might be relied upon to carry on more such as deformable solids or inflatables, with zero fluid velocity at the gas-liquid interface. Under these conditions, the accumulation of surfactant can be expected to eliminate any apparent slip on the solid-fluid interface [197].

1.4.5 Dissolved gases

The magnitude of slip depends on the quantity and type of dissolved gas. The group of E. Charlaix at the University of Lyon reports that slip experiments on hydrophobic surfaces performed in a clean room environment lead to much smaller slip lengths than similar experiments performed in contact with air, with results that are reproducible and agree with molecular dynamic simulations. A similar result is observed in the sedimentation study of Boehnke et al. [76] there is no-slip in vacuum conditions but slip observed only when the liquid is in contact with air. It is also revealed that the type of dissolved gas matters. Granick et al. [198] performed experiment on tetradecane saturated with CO_2 which is consistent with no-slip but significant slip observed when saturated with argon whereas the opposite behavior is observed for water.

1.4.6 Temperature and pressure

Temperature and pressure [14, 110, 155, 199–202] also have an influence on the degree of slip either through a change in the properties of solid surface and/or fluid, or by changing the nature of fluid-solid interaction. Temperature and pressure can also affect another phase which contributes in the slip of fluids such as a thin film of gas or a dissolved species or nanobubbles accumulated on the surface [200, 203]. The surface wettability is usually depend on temperature, and the temperature may also have an effect on the molecular collision frequency, and therefore on the momentum exchange between the solid surface and the fluid. The molecular dynamics simulations based work due to Guo et al. [201] stated that the slip length usually decreased with increasing temperature. Based on Lauga et al.'s model for the slip length, the slip may be inversely proportion to temperature [204]. However, Choi et al. [205] verified that high shear rates generated viscous heating and increases the slip length. Tretheway et al. [199] observed that the slip decreases with the increasing pressure. This is due to that an increasing pressure might decrease the sizes of the surface trapped bubbles. The pressure gradient dependence slip length proposed by Ruckenstein et al. [14] based on equilibrium thermodynamics.

1.4.7 Viscosity

Apparent slips are supposed to arise in a thin layer of liquids with low viscosity adjacent to smooth solid surface or in regions of higher shear beside to the crests and edges of a rough solid surface [205]. From the Navier-Stokes equations it is known that the velocity gradient in the flow field is a function of the solution viscosity. By reducing the viscosity in regions of high shear stress, the hydrodynamic drag may be reduced because of the greater velocity gradient. This may be thought of as providing an apparent slip. In many flow profiles, the shear stresses are greatest near the solid-liquid interface. If a fluid is shear-thinning non-Newtonian, it can show a reduction

in viscosity in these high shear regions. This can also result in the apparent slip. Craig et al. [82] reported that the slip length increases with increasing liquid viscosity. Based on molecular dynamics simulations Lichter et al. [122] presented linear dependence of the slip length on the viscosity of liquid, which is in agreement with the experimental results.

1.5. Velocity Slip along the Surface of Spherical Particles

Most of the aforementioned details are often restricted to cylindrical solid walls or/and flat plates; however, a few researchers have also investigated the effect of slip velocity on the surface of solid particles in the limit of zero Reynolds number [206–209]. It is not exaggeratory to mention that the flow past solid particles occur in numerous applications such as fixed and fluidized bed reactors, pneumatic conveying, nuclear reactors, sedimentation, sewage sludge, coal combustion, airborne dynamics and suspension flows. Furthermore examples includes particulate matters in a smog, coal liquification, polymer processing, catalytic cracking, paint, paper pulp, aluminium powders in combustion chambers, mixing processes in chemical engineering, and heavy materials separation in nuclear engineering. Thus Basset [210] derived an analytical solution for the slip flow past a solid spherical particle translating in infinite fluid at low Reynolds numbers and generalized stokes law for the drag force. Keh and Chen [211] generalized Faxen's law to calculate slip velocity on a surface of spherical particle. Faltas and Saad [214] studied the Stokes flow past assemblages of slip spherical particles-in-cell with a linear slip boundary condition at the interface in conjunction with Happel [215] and Kuwabara [216] boundary conditions at the cell fictitious surface. Atefi et. al. [217] numerically studied 3-D steady viscous fluid flow past stationary suspended spherical particle with slip condition at low to moderate Reynolds numbers and discussed the effect of slip on wake length, flow separation and drag coefficient at Reynolds number in the range of $0.1 \leq Re \leq 200$.

Along with the momentum transfer phenomena, heat transfer phenomena is also important because in most of the aforementioned processes, fluid dynamics combined with heat transfer plays an important role in the effectiveness of their performance. Temperature distributions play important roles in the fluid-solid interaction. Temperature distribution and flux between particle and fluid are known to affect many chemical reactions, for example fluidization in pharmaceutical process. Also in the petroleum, mineral and chemical industries, the heat transfer between catalyst particle and reactants is decisive for the stable chemical reaction. Therefore, an adequate knowledge of the rate of heat transfer from particles to fluids is a prerequisite for the understanding characteristics of system. In fluidized and packed bed, the rate of heat transfer between the particles and fluid is influenced by a large number of variables like efficiency of fluid slip, solid and fluid properties, distribution of particles, temperature, fluid flow rate as well as boundary conditions. The most common boundary condition for energy equation is constant wall temperature or constant wall flux. Experimental observations show that the temperature of a fluid at a surface may not equal to the surface temperature. The difference is known as temperature jump and is determined by the heat flux normal to the surface. Based on the analogy of slip flow, Poisson suggested that the temperature jump can be described by $T_s - T_w = \mathcal{L}_T \left(\frac{\partial T}{\partial n}\right)$, where $\mathcal{L}_T$ is temperature jump length. Smoluchowski [218] experimentally confirmed this hypothesis and proposed an equation for $\mathcal{L}_T = \left(\frac{2-\sigma_T}{\sigma_T}\right)\left(\frac{2\Upsilon}{\Upsilon+1}\right)\frac{Kn}{\mathrm{Pr}}$. A general temperature jump condition for rarefied multicomponent gas flows is also described by Zade et al. [219]. Gokcen and MacCormack [220] proposed a temperature jump condition both to simplify the smoluchowski jump condition, and to yield the correct heat transfer in free molecular flow in the limiting case of very large Knudsen numbers. Some researchers

investigated the effect of slip velocity and temperature jump on the heat transfer from a sphere in a low Reynolds number flow [221–223]. Vasudeviah and Balamurugan [224] obtained an analytical expression for the mean Nusselt number, where $Re < 1$ and Pr of O(1). They considered slip velocity boundary condition in their calculations and neglected the temperature jump. Most of the literatures of heat transfer in slip flow past solid are available for the flow over single spherical particle where $Re < 1$, rotating sphere, particle motion under rarefied condition, microfluidic and nanofluidic systems [225–231]. There is very less number of literature on momentum and heat transfer study for slip flow of Newtonian and non-Newtonian fluid past single particle as well as assemblages of particles. Therefore, the main aim of this work is to numerically study the momentum and heat transfer phenomena of the Newtonian and non-Newtonian power law fluids flow past single and assemblage of solid spherical particles with a linear slip boundary condition at the solid-fluid interface.

1.6. Outline of Thesis

This dissertation work dealing with the numerical investigation of momentum and heat transfer phenomena of single and assemblages of spherical particles in Newtonian and power-law fluids with linear velocity slip boundary condition at the fluids-solid interface is organized into seven chapters as follows:

- Chapter 1 gives the background of the research highlighting the importance of the fluid-particle flow as well as velocity slip boundary condition. Some specific applications which involve particle-fluid flow are revised. The mechanism of slip flow, various slip models, and parameters that affect the slip boundary condition are also discussed in this chapter.

- Chapter 2 deals with literature available for single and assemblage of spherical particles in Newtonian and non-Newtonian fluids. Reviews relevant theories and previous work closely related to the scope of this study. The objectives are also given in this chapter.

- Chapter 3 deals with problem statement and mathematical formulation for the momentum and heat transfer phenomena of single and assemblages of spherical particles in Newtonian and non-Newtonian fluids. This chapter also presents the underlying assumptions, field equations, appropriate boundary conditions and the dimensionless parameters associated with the present study. Further this chapter also presents the post processing of results to infer the values of the derived parameters like drag coefficients, Nusselt numbers, streamlines, concentration contours, etc. as functions of pertinent kinematic and rheological parameters.

- Chapter 4 deals with the numerical methodology for studying momentum and heat transfer phenomena of single and assemblages of spherical particles in Newtonian and non-Newtonian fluids. This chapter also presents discretization of governing equations and boundary conditions.

- Chapter 5 presents choice of numerical parameters by means of domain and grid independence studies. Further this chapter also presents the reliability and accuracy of present numerical solver by comparing present results with literature counterparts.

- Chapter 6 deals with results and discussion of different cases considered in this study. To be specific, the momentum transfer behavior of single particle in unconfined Newtonian and power-law fluids is investigated; whereas the associated heat transfer phenomenon also has been investigated. Finally the drag and heat transfer phenomenon of assemblages

of spherical particles in Newtonian and power-law fluids are studied. The streamline patterns, vorticity contours, surface pressure distribution, surface vorticity distribution, drag coefficient, drag ratio, isotherm contours, surface Nusselt number and average Nusselt number for wide range of Reynolds number, Prandtl number, volume fraction, power-law indices and slip parameter are delineated and discussed in details.

- Chapter 7 summarizes the major findings of this dissertation work along with the possible scope for future work.

Chapter 2

LITERATURE REVIEW

The literatures on the momentum and heat transfer phenomena of spherical particles in Newtonian and non-Newtonian fluids with no-slip boundary condition at the solid-fluid interface have been thoroughly reviewed in several books [232−234]. Neto *et al.* [235] reviewed experimental investigations of hydrodynamic boundary conditions for the Newtonian fluid flow in contact with solid surface and found evidence for slip of Newtonian liquid at solid-fluid interface by number of techniques which are suitable for the study of flow phenomena near interfaces. Sochi [236] reviewed the experimental as well as theoretical studies of non-Newtonian liquids slip at the fluid-solid interface, its mechanism and parameter affecting the slip flow. Lauga *et al.* [237] presented the view of the usage of slip boundary condition to explain the motion at a solid-liquid interface. They gave emphasize on to distinguish between continuum slip at a liquid-solid interface, microscopic slip at the individual molecules level and apparent slip at the complex and heterogeneous boundaries. Colin [238] and Kandlikar *et al*. [239] presented a review on heat transfer in microchannels, concentrating on rarefaction effects in the slip flow regime. Colin [238] compared numerical and analytical models available in literatures for various heat transfer conditions and microchannel geometries. Thus this chapter presents brief recount of analogous literature for the case of slip flow of Newtonian and non-Newtonian fluids past spherical particle as well as flow through micro-channel. However, the literature on the momentum and heat transfer phenomena of assemblages of spherical particles in non-Newtonian fluids is virtually non-existent even in the creeping flow regime, let alone for intermediate to large Reynolds numbers.

2.1 Flow Phenomena

2.1.1 Newtonian fluids

The concept of velocity slip boundary condition at solid-fluid interface was first advised by Navier [113]. Thereafter several models have been suggested to improve the prediction of the non-equilibrium regions near the solid boundaries with continuum methods. Basset [210] first obtained an analytical result for the slip flow past a spherical particle in infinite fluid medium with linear velocity slip boundary condition at solid-fluid interface at low Reynolds numbers (*Re* ≤ 1) and obtained following correlation for drag coefficient on sphere in the creeping flow limit:

$$C_d = \frac{12}{\mathrm{Re}}\left(\frac{\lambda+2}{\lambda+3}\right) \tag{2.1}$$

Allen [240] studied the freely falling sphere in the viscous fluids and obtained following expression for limiting velocity of sphere freely falling in the viscous fluid in the limit of infinite slip ($\lambda\to 0$) to no-slip ($\lambda\to\infty$). He used this expression to calculate velocity of solid sphere and fluid sphere in viscous fluid

$$V = \frac{2}{9} gR^2 \left(\frac{\rho_s - \rho_l}{\mu}\right)\left(\frac{\lambda R + 3\mu}{\lambda R + 2\mu}\right) \tag{2.2}$$

Padmavathi *et al*. [207] obtained the solution to Stokes equation for an incompressible flow of viscous fluid past a spherical particle with mixed no-slip ($\lambda\to 0$) and infinite slip ($\lambda\to\infty$) boundary conditions. They presented the Faxen's law for the torque and drag on the surface of sphere for all value of λ. Takata *et al*. [241] investigated the flow of the rarefied gas over a solid sphere on the basis of the linearized Boltzmann (LBM) equation for the hard-sphere molecules with the diffuse reflection condition. Keh and Chang [31] analytically studied the Faxen relation for a solid sphere in an unbounded Stokesian flow for the case where the surrounding fluids slip

at the surface of the solid particle. They obtained analytical equations for the hydrodynamic torque, force and stress-let on the particle. Keh and Shaiu [242] theoretically examined the motion of spherical particles and circular cylindrical particles in unbounded fluid with linear velocity slip at solid-fluid interface at small Reynolds number ($0 \le Re \le 1$). They also suggested following correlation for drag exerted on sphere for slip parameter in the range of $0 \le \beta \le \infty$.

$$C_d = \frac{12}{\mathrm{Re}}\left(\frac{1+2\beta}{1+3\beta}\right)\left[1+\frac{3}{8}\left(\frac{1+2\beta}{1+3\beta}\right)\mathrm{Re}+\frac{9}{40}\left(\frac{1+2\beta}{1+3\beta}\right)^2 \mathrm{Re}^2 \log \mathrm{Re}+0\left(\mathrm{Re}^2\right)\right] \tag{2.3}$$

Barber and Emerson [243] derived an analytical solution for rarefied gas flow past an unconfined sphere in creeping flow range with linear velocity slip boundary condition at solid-fluid interface and obtained the following total drag formulae for $Kn \le 1$. It contains pressure drag, skin-friction drag and normal stress drag.

$$\text{Total drag} = 6\pi\mu R U_\infty \left(\frac{1+4\dfrac{2-\sigma_v}{\sigma_v}Kn}{1+6\dfrac{2-\sigma_v}{\sigma_v}Kn}\right) \tag{2.4}$$

Where σ_v thermal momentum accommodation coefficient. Keh and Huang [244] investigated a combined analytical-numerical solution for the Stokes flow caused by a rotating spheroidal rigid particle in viscous fluid with slip at fluid-solid interface. Wen and Lai [245] theoretically investigated the flow passing a solid sphere moving in micro-tube with linear velocity slip boundary condition at solid-fluid solid in the slip flow regime ($0.01 \le Kn \le 0.1$). In this, two cases have been studied. Case I is for a sphere moving along the centerline, though case II for a sphere moving parallel to the centerline of a micro-tube. Meigounpoory *et al*. [246] numerically studied the lift and drag forces acting on a rotating spherical particle suspended in uniform flow of Newtonian liquid. They assumed that the velocity slip is directly proportional to the tangential

shear stress at surface of sphere and analyzed the effect of slip in range of Reynolds number, $0.1 \leq Re \leq 100$, angular velocity, $0 \leq \Omega \leq 1$, slip number, $10^{-5} \leq \lambda \leq 10^{5}$. Using similar slip boundary condition, Atefi *et al*. [217] analyzed 3-D steady Newtonian fluid flow past a stationary solid spherical particle at low and moderate Reynolds numbers ($0.1 \leq Re \leq 200$) for infinite slip ($\lambda \rightarrow 0$) to no-slip ($\lambda \rightarrow \infty$) at the interface. Swan and Khair [247] investigated the hydrodynamic of a slip-stick boundary condition on a sphere whose surface was partitioned into no-slip regions and finite slip regions. They first analyzed the translational velocity of a sphere because of the force density on particle surface and then the rotational velocity and the response to an ambient straining field of a stick-slip sphere. Willmott [248] stated the dynamic resistances of a solid sphere in an infinite medium of Newtonian fluid at $Re \rightarrow 0$ with inhomogeneous velocity slip boundary condition by treating boundary condition as perturbation for a homogeneous sphere and assumed the slip length is much smaller than radius of sphere. Luo and Pozrikidis [249] studied the motion of a sphere in unbound linear flow and near the plane of a wall with velocity slip boundary condition on both the surfaces particle as well as the wall at $Re \rightarrow 0$. An exact solution is derived using the singularity method, and provided analytical expressions for the torque, force, and stress-let in the form of the slip coefficients by simplifying the Stokes–Basset–Einstein law. Moshfegh *et al*. [250] studied the 3-D incompressible slip flow over a aerosol particle by solving Navier-Stokes equation. They used the first order linear slip boundary condition at gas-particle interface and obtained expression for slip correction factor in slip flow regime as a function of Reynolds number ($0 \leq Re \leq 1$) and Knudsen number ($0.01 \leq Kn \leq 0.1$). Further they extended their study in the range of Reynolds number, $0.125 \leq Re \leq 20$ and proposed the following correlation for drag, but it is accurate only for Reynolds number close to zero [251].

$$\ln\left(C_d\right)=a+b\ln\left(\mathrm{Re}\right)+\frac{c}{\sqrt{\mathrm{Re}}}+\frac{d}{\mathrm{Re}}+e\left(\exp\left(-Kn\right)\right) \tag{2.5}$$

Feng [252] numerically investigated the hydrodynamics of flow around a sphere in presence of interface slip and in the range of Reynolds number, $0 \le Re \le 75$. He developed a following correlation for drag coefficient based on numerical results in range of infinite slip ($\lambda \to 0$) to no-slip ($\lambda \to \infty$).

$$C_d=\frac{(\lambda+2)}{(\lambda+3)}\frac{12}{\mathrm{Re}}\left[1+0.2415\sqrt{\frac{\lambda+2}{\lambda+3}}\,\mathrm{Re}^{0.678}-0.0546\frac{1}{\lambda+3}\mathrm{Re}^{1.104}\right] \tag{2.6}$$

Datta and Singhal [253] deliberated the uniform velocity slip flow of viscous fluid over a solid sphere with a source at its centre under Stokes approximation at range of low Reynolds number. The matched asymptotic expansions method is used to generate the inner and outer solutions pertaining to the problem. The effects of slip boundary condition on streamlines pattern and drag force are discussed thoroughly. Ashmawy [254] analyzed the rotational motion of an axisymmetric body in the Newtonian fluid using analytical and numerical techniques. He employed a linear approximation for the density functions and also applied the collocation technique to satisfy the linear velocity slip boundary condition at the solid-fluid interface. He obtains the numerical results for the special cases of prolate, prolate spheroid, and oblate Cassini oval and oblate spheroid by using singularity method. Later on Ashmawy [255−257] extended his work to the unsteady rotational motion of a slip sphere, unsteady stoke flow of incompressible couple stress fluid around rotating sphere and drag on a slip sphere moving in a couple stress fluid. Chang and Keh [258] examined the problem of slow slip flow of Newtonian fluid past a slightly deform rigid spherical particle. Further they also studied the rotation of a solid spheroidal particle in viscous fluid with velocity slip boundary condition at the solid-fluid interface in the limit of zero Reynolds number [259]. Niazmand and Anbarsooz [260] a

numerical analysis performed to recognize the effect of rarefaction on the flow phenomena of a micron-sized spherical particle in the slip flow regime at the range of intermediate Reynolds numbers ($1 \leq Re \leq 50$). They applied Maxwell's velocity slip boundary condition at the interface to analysis the effect of slip and proposed the following correlation based on numerical results.

$$C_d = \frac{27.979 - 63.722Kn + 207.029Kn^2 - 2.893\ln(\mathrm{Re})}{1 - 0.097Kn + 0.656\ln(\mathrm{Re}) + 0.456\ln^2(\mathrm{Re})} \tag{2.7}$$

Varet et al. [261] analyzed the free falling sphere in the viscous fluid and investigate the effect of the velocity slip boundary conditions at the solid-fluid interface. Lee and Keh [262] analytically and numerically investigated creeping flow caused by the translation and rotational motion of a sphere in the viscous fluid within a spherical cavity and established a general solution to Stokes equations from fundamental solutions in two spherical coordinate system based on both the cavity and particle.

In case of multiple particles, Hocking [263] analyzed the effect of velocity slip on the motion of a spherical particle closed to wall and on the two adjacent spheres using lubrication theory. He considered Maxwell slip flow approximation to prove that when gap is small between surfaces then the resisting forces are logarithmically dependent on gap between the approaching surfaces and contact can be attained in a finite time. Reed and Morrison [206] presented an analysis of continuum-slip flow of the motion of two solid spheres and motion of a solid sphere normal to a wall and examined the effect of the spherical particle interaction with other particle and with plane wall in continuum-slip flow regime in the limit of infinite slip and no-slip at $Re \rightarrow 0$. Datta and Deo [264] obtained the solution to the Stokes flow past randomly and homogeneously distributed cylinders/spheres with slip velocity boundary condition at solid-fluid interface. They used particle-in-cell model to handle multi-particle system and implement

Kuwabara boundary condition at cell surface. Faltas and Saad [214] investigated the axisymmetric Stoke flow of an incompressible Newtonian fluid past an assemblage of slip spheres using combined analytical-numerical method. They also applied particle-in-cell models to study the multi-particle system. Happel and Kuwabara boundary condition was applied at the cell surface whereas linear velocity slip of Basset-type boundary condition was applied at the fluid-solid interface. Using similar slip boundary condition, they extended their work to the steady axisymmetric flow of Newtonian fluid confined in two eccentric spheres which rotate about an axis joining their centers with different angular velocities [265]. Ghosh *et al*. [266] experimentally examined the effect of the particle concentration on the apparent slip length for the flow of suspensions of the colloidal hard spheres through micro-channels. They measured apparent slip length by extrapolating the velocity profiles to zero and this analysis made by systematic variations of particle volume fraction ($0.03 \leq \Phi \leq 0.42$) and Peclet number ($2 \leq Pe \leq 50$). Sahu *et al*. [267] and Ghosh *et al*. [268-270] studied the velocity slip flow in the plane and slippery channel.

In case of fixed and fluidized bed, Subramanian [271] carried out experiments in a circulating fluidized bed to measure the total pressure drop and axial pressure profile in the extensive range of the operating conditions. He developed a slip velocity model by considering the effect of all hindrance such as particle-wall, particle-particle and particle agglomeration. Palani *et al*. [272] experimentally investigated the slip between the phases in liquid-solid circulating fluidized bed and discussed the variation of slip velocity with solids velocity, superficial liquid velocity, bed voidage and particle size and density. They proposed following empirical correlation of slip velocity.

$$u_s = 1.3u_t \left(\frac{(\rho_s - \rho_l)}{\rho_l} \right)^{-0.0167} \varepsilon^{3.5} \tag{2.8}$$

Tenneti *et al*. [273] used well-resolved particle-resolved direct numerical simulation (PR-DNS) based on the particle-resolved Reconcilable Immersed Boundary Method continuum solver to simulate the Navier-Stokes equations and obtained the drag force in gas-solid flows in the wide range of flow parameters ($0.1 \leq \Phi \leq 0.5$; $0.01 \leq Re_m \leq 300$). They also suggested a drag law as a function of Φ and Re_m. Mehrabadi *et al*. [274] also used particle-resolved direct numerical simulation (PR-DNS) to compute the drag force on fixed particle assemblies as well as freely evolving suspension over the intermediate range of particle volume fraction, $0.1 \leq \Phi \leq 0.35$ and the mean slip Reynolds number, $0.01 \leq Re_m \leq 50$.

2.1.2 Non-Newtonian fluids

Moosaie and Atefi [275] analyzed the Stokes flow of micropolar fluids past a rigid sphere based on the theory of Cosserat continua. A linear velocity slip boundary condition was applied on the solid-fluid interface and obtained following expression for drag coefficient in range of infinite slip ($\lambda \to 0$) to no-slip ($\lambda \to \infty$).

$$C_d = \frac{24}{\mathrm{Re}} \left(\frac{(1+\chi)(1+\zeta)(2+\zeta)(\lambda+\zeta+2)}{(4+3\chi)\zeta^2 + 2(1+\chi)(\lambda+3) + \zeta\left[\lambda(3+2\chi)+(11+9\chi)\right]} \right) \tag{2.9}$$

Sherif *et al*. [276] performed a combined analytical-numerical solution for the axisymmetric Stokes flow caused by the translating motion of a solid sphere in micropolar fluid perpendicular to a plane wall at the random position from the wall. A linear, Basset type velocity slip boundary condition has been used at the fluid-solid interface. Kalyon and Malik [277] provided an analytical solution for the axial annular incompressible flows of Hershel−Bulkley, Bingham

plastic, power-law, and Newtonian fluids with non-linear slip and no-slip boundary condition at one or both the surface of annulus in creeping flow regime. Ansari *et al*. [278] experimentally and numerically studied the capillary flow of the HDPE melt and examined the effect of temperature and pressure on viscosity, and effect of slip velocity on capillary flow. They concluded the effects of wall slip are significant for HDPE flow compared to viscous heating. Ferras *et al*. [279] presented analytical solutions for both Newtonian and non-Newtonian fluids with velocity slip boundary conditions in Poiseuille and Couette flows using the Navier's linear and non-linear slip condition. Further Ferras *et al*. [280] numerically and analytically studied the flow of viscoelastic fluid flows through axial and helical annular with linear and non-linear Navier's slip condition. Mallik [281] developed a mathematical model to study the blood flow through an atherosclerotic artery with slip velocity at wall and power-law fluid model used to account blood phenomena. Tang and Kalyon [137] experimentally and numerically studied the time-dependent compressible flow of poly (dimethyl siloxane) in circular tube with pressure dependent slip at the wall. They determined parameters of pressure-dependent wall slip and shear viscosity of the PDMS using combinations of steady torsion, small-amplitude oscillatory shear, and squeeze flows which employed to predict the time-dependent flow behavior of the PDMS in circular tube. Housiadas [282] analytically investigated the effect of slip at the wall for viscoelastic fluids flow in channel/slits and circular tubes with non-linear velocity slip boundary condition at solid-fluid interface. Khan and Mahmood [283] investigated the effect of the slip boundary condition on the flow of third order fluid over inclined plane by using perturbation method and developed expressions for average film velocity and volume flux. Allende and Kalyon [284] revealed the influence of the slip at the wall slip for the migration of spherical particles in the transverse flow direction in Poiseuille flow. Although numerous studies have

been made on the rheological behavior of polymer solutions, relatively little work has been done on concentrated suspensions. Such concentrated suspensions are usually non-Newtonian and exhibit various degrees of plasticity, dilatancy and/or thixotropy. Several researchers proposed that wall slip of suspensions is due to the formation of a slip layer between the bulk flow and the wall. Green [285] identified a thin slip layer of a pure polymeric fluid in the flow of suspensions under a microscope whereas Bingham [286] suggested that slip arises from a lack of adhesion between the shearing surface and the material. Yilmazer and Kalyon [287] obtained the ratio of the thickness of slip layer thickness to the particle diameter to be 0.06 for the 60% volume of ammonium sulfate particles in suspension. Whereas Soltani and Yilmazer [289] determined the ratio of the thickness of slip layer to the particle diameter for glass beads and Aluminium particles suspended in polybutadiene as 0.04 and 0.07, respectively. Kalyon [30] measured slip layer thickness in the range of 2- 30 μm for KCI particles suspension (61.9% by volume) in the capillary flow. The ratio 0.09 of the mean slip layer thickness over the harmonic mean particle diameter (≈121 μm) was obtained. For shear thickening solutions, a slip layer thickness about 100 μm at low shear rates, and 50-60 μm at high shear rates, was determined using Microscopic Particle Imaging Velocimetry (MPIV) [285]. Ellahi [290] examine the significances of the slip at the surface of the plates for the flows of an Oldroyd 8-constant fluid. The governing non-linear problems are solved by using homotopy analysis method (HAM). Sunarso *et al*. [291] implemented numerical simulation to investigate the influence of slip at the wall for flow of Newtonian and non-Newtonian fluids in micro and macro channels with power-law velocity slip boundary condition at the interface. They observed that the slip introduces different vortex growth for the flow in micro channel as compared to that in macro channel.

2.2 Heat Transfer

2.2.1 Newtonian fluids

Taylor [292] analytically investigated the influence of velocity slip and temperature jump on the heat transfer from a sphere to fluid at low Reynolds number slip flow and for small and large Peclet number. Mikami *et al*. [293] obtained the experimental results on the conductive heat transfer from a solid spherical particle to pure gases and their mixtures and also obtained its analytical solution. They obtained the following correlation for Nusselt number based on their analytical results which is in good agreement with experimental data that in range of Knudsen number $0.016 \leq Kn \leq 0.8$ for various mixtures of hydrogen, helium and nitrogen gases.

$$Nu = \frac{2}{1+\frac{15}{2}\alpha_{mix}^{-1} Kn} \tag{2.10}$$

Finally, the rate of heat transfer predicted by Eq. (2.10) also agrees well with the predictions obtained using the expression recently derived by Feng and Michaelides in the limit $Pe \rightarrow 0$. Kavanau and Drake [294] experimentally and analytically studied the overall heat transfer from sphere to rarefied gas in subsonic flow in the presence of temperature jump boundary condition at intermediate Reynolds number ($1.7 \leq Re \leq 124$). Using the method of matched asymptotic expansions, Vasudeviah and Balamurugan [224] acquired an analytical solution for convective heat transfer from a sphere to viscous incompressible fluid with mixed slip-stick boundary conditions at Reynolds number $Re < 1$ and Pr of O(1). Here, they neglected the temperature jump but considered velocity slip boundary condition in their calculations. Strom and Sasic [223] investigated the effects slip flow on heat transfer for the motion of small particles in rarefied flow and obtained the suitable framework as a generic multiphase DNS method for rarefied flows. Mohajer et al. [221] carried out a 3D numerical simulation of slip flow past an unconfined

stationary spherical particle with variable properties of gas and Knudsen number ($0.01 \le Kn \le 0.1$). They explored the effects of three variables Reynolds number, Knudsen number and temperature difference between the ambient and particle on heat transfer from a sphere to fluid in slip flow regime. It was observed that the velocity slip and temperature jump affect the heat transfer in reverse ways. Anbarsooz and Niazmand [295] numerically investigated the heat transfer characteristics of slip flow over an isolated solid sphere at intermediate Reynolds numbers ($0 \le Re \le 50$) for Prandtl numbers in the range of $0.7 \le Pr \le 7.0$. They solved Navier–Stokes and energy equations by a control volume technique in conjunction with the linear velocity slip and temperature jump boundary conditions. Also for the limiting case of Re→0, derived an analytical solution for the average Nusselt number in slip regime and proposed following expression.

$$Nu_{avg} = \frac{1}{0.5 + \frac{2\gamma}{\gamma+1}\frac{2-\sigma_T}{\sigma_T}\frac{Kn}{\mathrm{Pr}}} \tag{2.11}$$

Hashizume and Kimura [296] experimentally studied the heat transfer characteristics in solid-liquid fluidized bed. They observed that the heat transfer coefficient is function of the slip velocity between liquid and the particles and proposed a correlation for Nusselt number based on their experimental data.

Colin [238] and Kandlikar *et al*. [239] presented a review on convective heat transfer in microchannels, concentrating on rarefaction effects in the slip flow regime. Numerical and analytical models are compared for various heat transfer conditions and microchannel geometries. Convection heat transfer in circular and non-circular microchannels has been studied by several researchers over the years [297−302]. In these studies, the influence of velocity slip and temperature jump at the solid surface is considered. The main finding was that velocity slip

and temperature jump has reverse effects on the rate of heat transfer. The velocity slip tends to increase the heat transfer rate whereas the temperature jump tends to decrease it. Ozturk [303] analytically investigated the steady laminar flow and heat transfer of an electrically conducting viscous fluid between two parallel plates with a velocity slip and temperature jump boundary condition is in the presence of a transverse magnetic field. Ozturk [303] discussed the influence of Hartmann number, Brinkman number and Knudsen number on the temperature and velocity distribution and on the heat transfer characteristics. Sircar [304] derived an analytical solution for fully developed, immiscible two-phase (gas and liquid) flow between parallel plates with velocity slip and temperature jump boundary condition and obtained the velocity field, temperature distribution and Nusselt number in flow regime. The influence of the thermal accommodation coefficients and Knudsen number on the velocity and temperature profiles, and overall temperature rise at the lower plate and the reduction of the shear stress due to the gas layer were also examined. Niazmand [305] studied the rarefaction effects in simultaneously hydrodynamically and thermally developing 3-D micro flows in rectangular channels for Kn $\leq$ 0.1 based on a control-volume numerical approach. The effects of velocity slip, thermal creep and temperature jump on the momentum and heat transfer phenomena are examined in detail. EI-Nahhas [306] studied the nonlinear flow of Newtonian fluid in a microchannel between two parallel plates and analyzed the effects of velocity slip, viscous dissipation, and temperature jump at the surface of solid. The homotopy analysis technique is used to obtain analytic approximations for this problem. Yazdi *et al*. [307] studied the convective heat transfer of the slip flow past horizontal solid surface within the porous media with constant heat flux boundary conditions. They assumed the fluid is a continuum, but employs a slip boundary condition on the wall. Ambethkar and Srivastava [308] numerically investigated 2-D incompressible viscous fluid

flow and heat transfer at moderate Reynolds number with velocity slip boundary conditions at the interface. Rana *et al*. [309] numerically investigated the flow phenomena and heat transfer characteristics of a rarefied gas confined in a bottom heated square cavity with velocity slip and jump boundary condition by solving NSF equations. Boutebba and Kaabar [310] studied heat transfer between heated tungsten wire and surrounding rarefied gas (N_2) with low pressure boundary slip at the interface.

2.2.1 Non-Newtonian fluids

Ahmad *et al*. [311] designed the stationary and moving thermocouple experiment to analyze the heat transfer between the fluid and a particle in tube flow using water and carboxymethylcelluse (CMC) solution. Analyzed the effect of fluid temperature, viscosity and fluid-to-particle slip velocity on heat transfer rate and obtained following correlation for Nusselt number for particle in CMC solution.

$$Nu_G = 2 + 361\mathrm{Re}_G^{0.132}\,\mathrm{Pr}_G^{0.230}\left(d_p/D_t\right)^{0.94} \tag{2.12}$$

Barkhordari and Etemad [312] performed numerical investigation to study flow behavior and temperature profile of non-Newtonian liquids in circular micro-channels. The flow is considered to be steady, axisymmetric, incompressible, laminar, slip and power law model is used to characterize the behavior of the non-Newtonian fluid. Mahmoud [313] analyzed the effects of slip and heat generation on the flow of a power-law fluid over a continuously moving surface. Power-law slip model is used to account the influence of slip at moving surface. Prasad et al. [314] numerically analyzed the flow behavior and heat transfer characteristics of Casson fluid from a permeable isothermal solid sphere in the presence of velocity slip and temperature jump boundary condition. Gaffar et al. [315] studied the nonlinear steady boundary layer flow and heat

transfer from an isothermal sphere to incompressible non-Newtonian liquid in the presence of hydrodynamic and thermal slip condition. The dimensionless conservation equations are solved numerically with appropriate boundary conditions using a second-order accurate implicit finite difference Keller-box method. The influence of dimensionless parameters, namely power law index (n), Velocity slip (S_f), Prandtl number (Pr), Weissenberg number (We), thermal jump (S_T), and dimensionless tangential coordinate (ξ) on velocity and temperature field in the boundary layer regime are investigated in detail.

Therefore, based on literature review, it can be concluded that very less information is available on the momentum and heat transfer studies for the cases of the power-law fluid flow past a spherical particle with linear velocity slip boundary condition at fluid-solid interface. Whereas no literature available on momentum and heat transfer studies for power-law fluid flow past assemblages of spherical particle with linear velocity slip boundary condition at fluid-solid interface. These literature gaps are set as objectives of present work.

2.3 Objective of Thesis

The objectives of work are decided based on literature review and the application of slip flow and fluid-solid particles contact in various industries like chemical, polymer, pharmaceutical industries as well as in micro and nano scales. The objective is to study the effect of linear velocity slip boundary condition on momentum and heat transfer of Newtonian and power-law fluid flow past solid particles. Here, power law model is selected because most of polymer solutions and melts, agro- and food related products, and crude oil i.e. heavy as well as blended crude oil exhibits the power-law behavior. Therefore, the present dissertation is targeted to numerically explore the following objectives over the wide range of dimensionless parameters:

- Effect of linear velocity slip boundary condition on momentum transfer phenomena of a solid spherical particle in Newtonian and power-law fluids.

- Effect of linear velocity slip boundary condition on heat transfer phenomena of a solid spherical particle in Newtonian and power-law fluids.

- Effect of linear velocity slip boundary and volume fraction of particles on momentum transfer phenomena of an assemblage of spherical particles in Newtonian and power-law fluids.

- Effect of linear velocity slip boundary and volume fraction of particles on heat transfer phenomena of an assemblage of spherical particles in Newtonian and power-law fluids.

PROBLEM STATEMENT AND DESCRIPTION

The present dissertation includes numerical study on momentum and heat transfer phenomena of single and multiple spheres in Newtonian and power-law fluids with velocity slip at the interface. This chapter presents the physical description and mathematical representation of the present problems. Further it should be noted that the momentum and heat transport phenomena are obtained using suggested approach.

3.1. Momentum and Heat Transfer of Single Spherical Particles

Consider a rigid spherical particle of radius, R, in an infinite medium of power law fluids flowing with a uniform velocity U_o and temperature T_o. The flow is assumed to be steady and axisymmetric along the surface of spherical particles. Because of the axisymmetry along the azimuthal direction (ϕ), the velocity component in the azimuthal direction (v_ϕ) and derivatives with respect to ϕ are zero. Assume that this non-Newtonian power-law fluid experiences slippage while flowing along the surface of the sphere. This slippage is considered to be linear, i.e., slip velocity at the surface of solid is proportional to the shear stress as: $\tau_{r\theta} = \lambda V_\theta$. This can be represented in terms of a dimensionless form as slip parameter λ ($\lambda = \beta R/\eta_{app}$), where β is slip coefficient, η_{app}-apparent viscosity. The infinite slip sphere (i.e., spherical bubble) and no-slip sphere (i.e., solid sphere) can be achieved from the present study by setting $\lambda \rightarrow 0$ and $\lambda \rightarrow \infty$, respectively.

In the case of the heat transfer, consider the transfer of energy between heated spheres (at T_s) to surrounding infinite expanse of non-Newtonian power-law fluids at temperature of T_o (<

T_s) with velocity slip at the interface. The temperature gradient is assumed to be moderate so that the physical properties and rheological constants of fluids are remaining unaltered. The viscous dissipation, reaction and dissolution of spheres in the fluid are absent in this work. It is also assumed that the temperature gradients exist between the surface of the spheres and the surrounding fluids only or in other words the Biot number is very small to neglect the temperature gradients inside the spheres. In this numerical study, for computational simplicity a sphere-in-sphere domain is considered as shown in **Figure 3.1**.

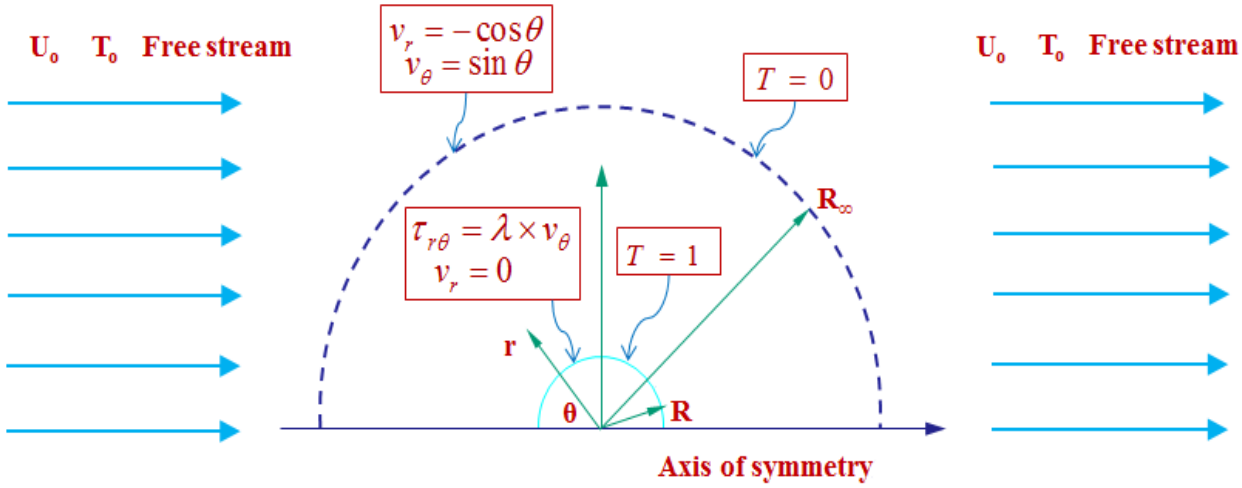

Figure-3.1: Schematic representation of the flow domain of a single spherical particle in power-law fluids

3.2. Momentum and Heat Transfer of Assemblages of Spherical Particles

Consider steady flow of an unbounded non-Newtonian power-law fluid with a uniform velocity U_o and temperature T_o past assemblages of spherical particles (of radius R) with velocity slip conditions at the fluid-solid sphere interface as shown in **Figure 3.2 (a)**. This multi-particle

system is converted in to a simple single particle system as shown in **Figure 3.2 (b)**, yet considering the effects of volume fraction of spherical particles using free surface cell model. According to cell model, all the spheres of equal size and equidistant from each other so that the effect of neighboring particles on the motion of the surrounding fluid can be nullified along the dotted line indicating the size of the computational domain, i.e., R_∞. The value of R_∞ is indicative of the relation between the size of the spheres and the volume fraction of the spheres, i.e., from volume fraction considerations one can obtain that $\frac{R_\infty}{R} = (\Phi)^{-1/3}$ where Φ is the volume fraction of the spherical particles in the assemblage containing both fluid and spheres. Thus a complex multi-particle system is converted into a simple single particle system including the effects of the volume fraction of the spherical particles. For instance, the system in the limit of $\Phi \rightarrow 0$ indicate the single particle system with $R_\infty \rightarrow \infty$ wherein the particles are infinitely away from each other and do not exert any influence on each other. Further, here also a linear velocity slip boundary condition is applied on fluid-solid interface. The results obtained with limits of zero and infinity slip numbers would correspond to those of fully slip spherical bubbles and no-slip solid spherical particles, respectively. The power-law type non-Newtonian fluid considered in this study is assumed to be incompressible and the size of the spheres is constant because of no dissolution and/or reaction between the spheres and the surrounding fluid. For heat transfer analysis, consider the energy transfer from heated sphere to surrounding infinite media of power-law fluid and thermo-physical properties of power-law fluids are assumed to be independent of the temperature difference $T_s - T_o$, i.e., the temperature gradient between the solid sphere and the outer fluid is in the moderate range. Also assumed that the spheres are maintained at constant temperature T_S and there is no temperature gradient within the sphere, i.e., the Biot number is

negligible. The flow is assumed to be axisymmetric and particle-in-cell flow domain is chosen as shown in **Figure 3.3**.

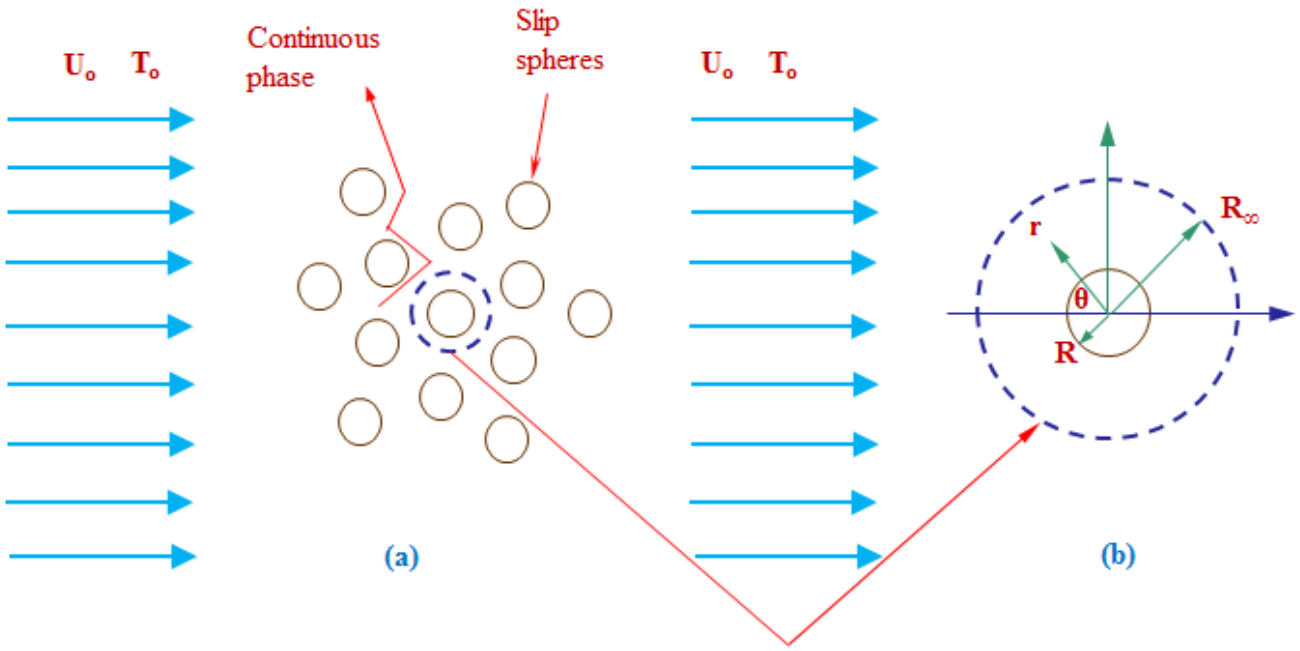

Figure 3.2 Schematic representation of the flow past an assemblage of spherical particles

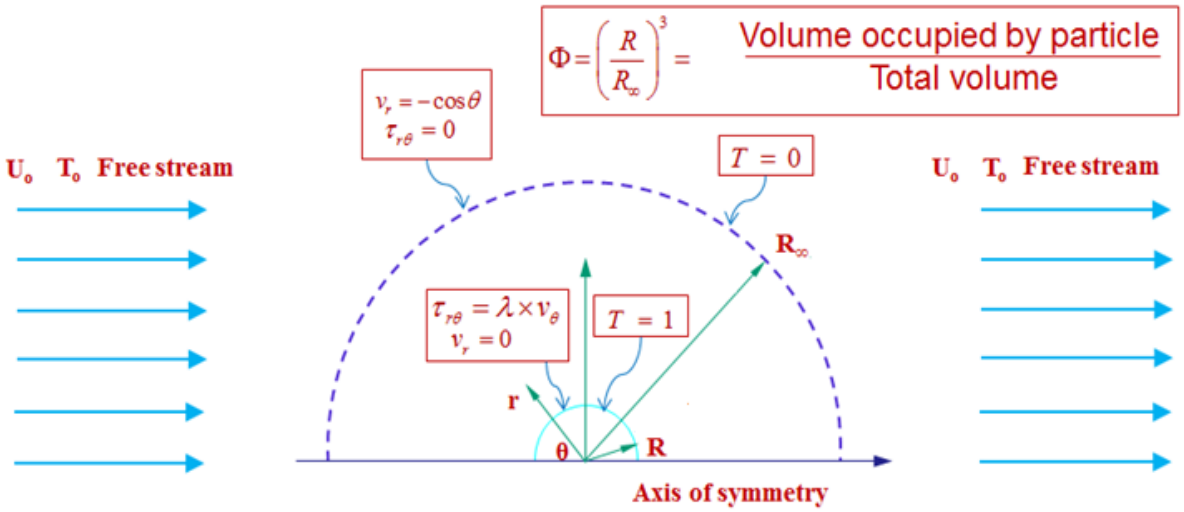

Figure 3.3 Schematic representation of the flow domain of assemblages of spherical particles in power-law fluids

Finally, in the view of cell model, the two problems of single and multiple spheres are dissimilar only in terms of the boundary condition at R_∞. Thus the governing equation and boundary conditions for these problems are presented together in the following section.

3.3. Governing Equations

The continuity, momentum and energy equations describe the transfer characteristics of these problems; and are considered in spherical coordinates. Over the range of conditions spanned in this work, the flow is assumed to be axisymmetric and a sphere-in-sphere computational domain is chosen. Thus a spherical coordinate system (r, θ, ϕ) with its origin located at the center of the sphere is employed and the polar axis (θ = 0^o) is directed along the direction of flow. Due to axisymmetry the velocity component in the ϕ- direction (v_ϕ) and derivatives with respect to ϕ are zero. In order to obtain fully converged velocity, pressure and temperature profiles, segregated approach has been used, i.e., first momentum equations are solved for fully converged velocity and pressure profiles, and then the so-obtained velocity profile is used as input to solve the energy equation. Assuming the flow to be incompressible, the final non-dimensionalized governing equations of continuity, momentum and energy equations in their conservative forms as:

- Continuity equation

$$\frac{1}{r^2}\frac{\partial}{\partial r}\left[r^2 v_r\right]+\frac{1}{r\sin\theta}\frac{\partial}{\partial\theta}\left[v_\theta \sin\theta\right]=0 \tag{3.1}$$

- r – component of momentum equation

$$\frac{\partial v_r}{\partial t}+\frac{1}{r^2}\frac{\partial}{\partial r}\left[r^2 v_r^2\right]+\frac{1}{r\sin\theta}\frac{\partial}{\partial\theta}\left[v_r v_\theta \sin\theta\right]-\frac{v_\theta^2}{r}=-\frac{\partial p}{\partial r}+\frac{2^{n+1}}{\mathrm{Re}}\left[\varepsilon_{rr}\frac{\partial\eta}{\partial r}+\frac{\varepsilon_{r\theta}}{r}\frac{\partial\eta}{\partial\theta}\right]$$
$$+\frac{2^n\eta}{\mathrm{Re}}\left[\frac{1}{r^2}\frac{\partial^2}{\partial r^2}\left(r^2 v_r\right)+\frac{1}{r^2\sin\theta}\frac{\partial}{\partial\theta}\left(\sin\theta\frac{\partial v_r}{\partial\theta}\right)\right] \quad (3.2)$$

- θ - component of momentum equation

$$\frac{\partial v_\theta}{\partial t}+\frac{1}{r^2}\frac{\partial}{\partial r}\left[r^2 v_r v_\theta\right]+\frac{1}{r\sin\theta}\frac{\partial}{\partial\theta}\left[v_\theta^2\sin\theta\right]+\frac{v_r v_\theta}{r}=-\frac{1}{r}\frac{\partial p}{\partial\theta}+\frac{2^{n+1}}{\mathrm{Re}}\left[\varepsilon_{r\theta}\frac{\partial\eta}{\partial r}+\frac{\varepsilon_{\theta\theta}}{r}\frac{\partial\eta}{\partial\theta}\right]$$
$$+\frac{2^n\eta}{\mathrm{Re}}\left[\frac{1}{r^2}\frac{\partial}{\partial r}\left(r^2\frac{\partial v_\theta}{\partial r}\right)+\frac{1}{r^2}\frac{\partial}{\partial\theta}\left(\frac{1}{\sin\theta}\frac{\partial}{\partial\theta}\left[v_\theta\sin\theta\right]\right)+\frac{2}{r^2}\frac{\partial v_r}{\partial\theta}\right] \quad (3.3)$$

- Energy equation

$$\frac{\partial T}{\partial t}+\frac{1}{r^2}\frac{\partial}{\partial r}\left[r^2 v_r T\right]+\frac{1}{r\sin\theta}\frac{\partial}{\partial\theta}\left[v_\theta T\sin\theta\right]=\frac{2}{Pe}\left\{\left[\frac{1}{r^2}\frac{\partial}{\partial r}\left(r^2\frac{\partial T}{\partial r}\right)\right]\right.$$
$$\left.+\left[\frac{1}{r^2\sin\theta}\frac{\partial}{\partial\theta}\left(\sin\theta\frac{\partial T}{\partial\theta}\right)\right]\right\} \quad (3.4)$$

In equations (3.1) - (3.4), velocity terms are scaled using free stream velocity U_o, radial coordinate r using spherical particle radius R, pressure using ρU_o^2, components of rate of deformation tensor by $\left(U_o/R\right)$, viscosity by a reference viscosity $\eta_{ref}\left(=m\left(U_o/R\right)^{(n-1)}\right)$, stress components by $\eta_{ref}\left(U_o/R\right)$, temperature difference (T-T_o) by (T_s-T_o) and time by $\left(R/U_o\right)$. Further, although the main interest is to obtain the steady state solution, the transient terms are retained in equations (3.2) – (3.4) because the false-transient scheme is used here to obtain the steady state solution.

For an incompressible liquid, the components of the extra stress tensor are related to the rate of deformation tensor as follows:

$$\tau_{ij} = 2\eta\varepsilon_{ij}; \quad \text{where i, j = r, } \theta, \phi \tag{3.5}$$

The non-dimensional power-law viscosity is given by:

$$\eta = \left(\frac{\Pi_{\varepsilon}}{2} \right)^{(n-1)/2} \tag{3.6}$$

Where, Π_{ε} is second invariant of rate of deformation tensor which can be expressed in terms of velocity components and their derivatives e.g., see Bird *et al*. [307].

The dimensionless numbers appearing in above equations are defined as follows:

- Reynolds number: $\mathrm{Re} = \dfrac{\rho U_o^{(2-n)} (2R)^n}{m}$ (3.7)
- Prandlt number: $\mathrm{Pr} = \dfrac{C_p}{k} m \left[\dfrac{U_0}{2R} \right]^{n-1}$ (3.8)
- Peclet number: $Pe = \mathrm{Re} \times \mathrm{Pr} = \dfrac{U_0 (2R)}{k}$ (3.9)

where, ρ is the density of the fluid, m is the power-law fluid consistency index, n is the power-law behavior index and k is the thermal conductivity. (here n = 1 for Newtonian; n > 1 for shear thinning fluid; n < 1 for shear thickening fluids).

3.4. Boundary Conditions

The boundary conditions for single and assemblages of spherical particles differ from each other only pertaining to one of the boundary conditions at the cell boundary and all other boundary conditions are identical in both cases as given below:

- At the outer cell boundary ($r = R_{\infty}$):

  $v_r = -\cos\theta$; $\quad v_{\theta} = \sin\theta$; $\quad T = 0 \quad \leftarrow$ For single sphere (3.10)

$$v_r = -\cos\theta\,; \qquad \tau_{r\theta} = 0\,; \qquad T = 0 \qquad \leftarrow \text{For assemblages of spheres} \tag{3.11}$$

- Along the axis of symmetry ($\theta = 0, \pi$):

$$v_\theta = 0\,; \qquad \frac{\partial v_r}{\partial \theta} = 0\,; \qquad \frac{\partial T}{\partial \theta} = 0 \tag{3.12}$$

- Along the surface of slip sphere ($r = 1$, $\theta = 0, \pi$):

$$v_r = 0\,; \qquad \tau_{r\theta} = \lambda \times v_\theta \tag{3.13}$$

Suffice it to add here that for the case of single sphere, the outer cell boundary condition should obey the uniform velocity field due to the imposed unbounded nature of the flow (Eq. 3.10). On the other hand for the case of assemblages of spheres the normal velocity component along the cell boundary is same as that of the free stream velocity (Eq. 3.11); however, the zero shear stress condition (Eq. 3.11) indicates the non-interacting nature of the cells within the frame work of the free surface cell model [137]. Equation (3.12) is simply a statement of the axisymmetric flow condition; while equations (3.13) refer to linear slip velocity along the surface of spheres.

Finally equations (3.1) – (3.4), subject to the boundary conditions outlined in equations (3.10) – (3.13) provide the theoretical framework to map the entire computational domain ($1 \leq r \leq R_\infty$) in terms of the primitive variables, i.e., v_r, v_θ, p and T.

3.5. Streamlines and Vorticity Profiles

Further insights about the detailed flow kinematics can be gained from the streamlines, vorticity and isotherm contours around the sphere. The vorticity in spherical coordinates can be calculated as follows:

$$\omega_{r\theta} = \frac{\partial v_\theta}{\partial r} + \frac{v_\theta}{r} - \frac{1}{r}\frac{\partial v_r}{\partial \theta} \tag{3.14}$$

The stream function in spherical coordinates can be calculated using the following expression:

$$E^2(\psi) = \frac{\partial^2 \psi}{\partial r^2} + \frac{\sin\theta}{r^2}\frac{\partial}{\partial \theta}\left(\frac{1}{\sin\theta}\frac{\partial \psi}{\partial \theta}\right) = \omega_{r\theta} r \sin\theta \tag{3.15}$$

where the stream function is related to velocity components as follows:

$$v_r = \frac{-1}{r^2 \sin\theta}\frac{\partial \psi}{\partial \theta} \quad ; \quad v_\theta = \frac{1}{r \sin\theta}\frac{\partial \psi}{\partial r} \tag{3.16}$$

Suffice it to add here that the vorticity and streamline profiles are computed from the fully converged velocity profiles as a post-processing procedure to display results, and not as primary means of solution (through stream function – vorticity formulation). The "primitive variable" approach for solving velocity components directly is used. Finally, the isotherm contours are plotted from the temperature field obtained by solving the energy equation.

3.6. Individual and Total Drag Coefficients

Once the fully converged velocity and pressure profiles are known, individual and total drag coefficients can be evaluated as follows:

Total drag coefficient is defined as:

$$C_d = \frac{2F_d}{\rho_o U_o^2 A_p} = C_{dp} + C_{df} \tag{3.17}$$

The pressure component (C_{dp}) is evaluated as:

$$C_{dp} = 2\int_0^\pi \left[p \sin 2\theta\right]_{r=1} d\theta \tag{3.18}$$

and the frictional component (C_{df}) is evaluated as:

$$C_{df} = \frac{2^{n+2}}{\mathrm{Re}} \int_0^\pi \left\{\eta\left[\left(\frac{\partial v_\theta}{\partial r} - \frac{v_\theta}{r}\right)\sin^2\theta - \left(\frac{\partial v_r}{\partial r}\right)\sin 2\theta\right]\right\}_{r=1} d\theta \tag{3.19}$$

3.7. Local and Average Nusselt Numbers of Spheres

Once the fully converged temperature profile is known, by equating the rates of heat transfer by conduction and by convection at the surface of the particle, the local Nusselt number (Nu_θ) can be seen as follows

$$Nu_\theta = \frac{h(2R)}{k} = -2\left[\frac{\partial T}{\partial r}\right]_{r=1} \tag{3.20}$$

where h is the convective heat transfer coefficient and k is the thermal conductivity, respectively. Therefore, by using the fully converged temperature profile, the temperature gradient can be evaluated at the surface of the sphere and substituted in equation (3.17) to obtain the local (surface) Nusselt number along the surface of the sphere as function of θ-coordinate.

The average Nusselt number, which is useful in real engineering applications, is evaluated by integrating the local Nusselt number along the surface of the sphere; and is given as

$$Nu_{avg} = \frac{1}{2}\int_0^\pi Nu_\theta \sin\theta d\theta \tag{3.21}$$

It should be noted that the numerical integration of the local Nusselt number is carried out along the curved spherical surface of particles, thus the local (surface) Nusselt number is multiplied by "sinθ" to account for spherical coordinates over which the temperature profile is obtained.

Finally the dimensional considerations of governing momentum and energy equations and the boundary conditions discussed above suggest that the isotherm contours and the local and average Nusselt numbers of the spheres in power-law fluids with velocity slip at the fluid-solid interface are functions of the Reynolds number (*Re*), Prandtl number (*Pr*), Peclet number (*Pe*), dimensionless slip number (λ) and the dimensionless flow behavior index (n) of the power-law fluids.

Chapter 4

NUMERICAL METHODOLOGY

4.1. SMAC Solver

Concisely, the non-dimensional momentum equations segregated from continuity equation, subject to the boundary conditions (as described in previous chapter) have been numerically solved on a sphere-in-sphere type concentric spherical computational domain. The momentum and energy transfer equations are solved using a segregated approach. A finite difference method based implicit simplified marker and cell (SMAC) method has been implemented on a staggered grid arrangement in spherical coordinates. This algorithm is a modified version of explicit solver, namely, marker and cell (MAC) method developed by Harlow and Welch [312] for free surface flows. The modifications in MAC method are to bring in the non-Newtonian power-law fluid viscosity and the semi-implicit formulation. Before implementing the SMAC method using a finite difference method based approach, the governing partial differential equations are converted in to a set of difference equations by using following differencing schemes. The forward time stepping differencing scheme for temporal and pressure force terms; quadratic upstream interpolation for convective kinematics (QUICK) scheme due to Leonard [313] for convective terms and a second order central differencing scheme for the viscous and non-Newtonian terms are adopted. The final steady-state solution is obtained by using a false-transient time stepping method and this is why the time-dependent terms are retained in the momentum equations. This procedure involves three steps: in the first step, the non-Newtonian viscosity equation is used to evaluate the dimensionless non-Newtonian viscosity field over the entire flow domain using the previous time-step values of the velocity field. In the next step, the

unknown velocity field is predicted using the previous time-step pressure field. Finally, the pressure field is corrected using the predicted velocity field which is further used to correct the velocity field. For the next time-step calculations, the sums of the predicted and corrected velocity fields are used as new values of the velocity field. This sequence is continued until the final steady state velocity and pressure fields satisfy the continuity equation. The stopping criterion for simulations is fixed as the maximum difference of any quantity between the two consecutive time-steps divided by the time step (Δt) should be below 10^{-3}. The fully converged steady velocity and pressure profiles are used to evaluate individual and total drag coefficients as functions of pertinent dimensionless parameters. Further fully converged velocity field is used as input to the energy equation and similar iterative approach as used to obtain velocity and pressure fields is adopted to obtain fully converged final steady temperature profile in the entire computational domain. The convergence criterion used for the steady temperature field is defined as the maximum difference between temperatures of two successive iterations divided by the time step (Δt) is $\leq 10^{-6}$. Finally this dimensionless temperature field is used to evaluate the local (along the surface of the sphere) and average (integrated over the entire surface of the sphere) Nusselt numbers as detailed below.

4.2. Staggered Grid Arrangement

The convergence of predictor-corrector kind of solvers is poor on normal collocated grids. The collocated grid may also cause checkerboard velocity-pressure distribution. To overcome this problem the staggered grid system is used in this work. Another important advantage of a staggered grid is that the transport rates across the faces of control volume can be computed without interpolation of velocity components. The computational domain is divided into a number of cells, which are shown in **Figure 4.1** as a two-dimensional section of a sphere. This

figure shows a spherical staggered grid arrangement for a 2-D axisymmetric spherical computational flow domain, where the dependent variables (v_r(i,j), v_θ(i,j) and p(i,j)) with same indices staggered to one another. In this arrangement, the scalars are located at the center of the cell, whereas, velocity vectors will be located at the center of the cell faces to which they are normal. Thus, the location of the velocity components are at the center of the cell faces to which they are normal and the grid points for the pressure and temperature are at the center of the cell. In such an arrangement, the pressure difference between the two adjacent cells is the driving force for the velocity component located at the interface of these cells during the numerical iterations. Thus the pressure-velocity corrections are directly related to each other, and the pressure-velocity iterative loops converge quickly. As shown in **Figure 4.1** cells are labeled as (i,j), where i and j denote the cell number as counted in θ- and r - directions respectively. The pressure is defined at the center of the cell and is denoted by p(i,j). The r-component velocity of cell (i,j) is defined at the cell face in r-direction i.e., at the center of the cells (i,j) and (i,j+1), and is denoted by v_r(i,j+1/2). The θ-component velocity of cell (i,j) is defined at the cell face in θ-direction i.e., at the center of the cells (i,j) and (i+1,j), and is denoted by v_θ(i+1/2,j). In a staggered grid arrangement, velocities are not defined at the cell centers, so whenever needed these are calculated by interpolation.

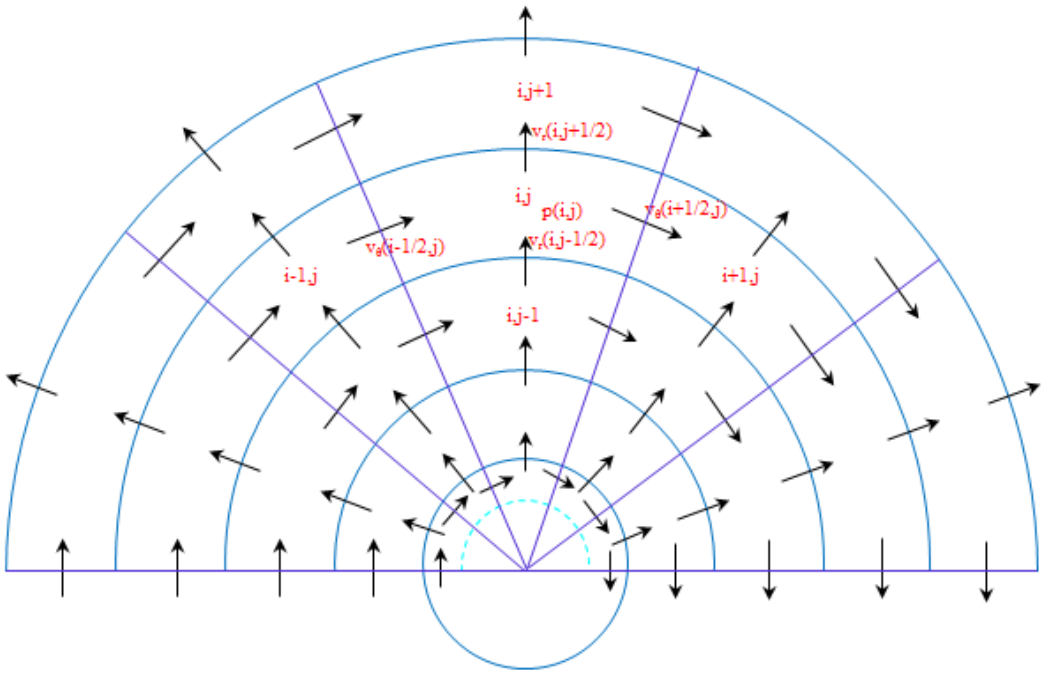

Figure 4.1 Two dimensional staggered grid arrangement in spherical coordinate system.

All computations are performed in half-domain assuming the axisymmetry in ϕ-direction, i.e., $v_\phi = 0$ and no variables depend on ϕ-coordinate. **Figure 4.2** shows the physical and computational domains appropriately divided into many small cells (or grids). The domain with solid lines represent the physical domain, whereas, the domain enclosed by dashed lines represents the computational domain. The cells with dashed lines also serve as boundary cells or fictitious cells. A solid line denoted by "s" represents the interface between spherical particle and outside continuous fluid flow field. Two dashed lines along θ-direction on the either side of $\theta = 0$ and $\theta = \pi$ serves as fictitious cells for computations. When we solve for the continuous flow field, the dashed line denoted by (s-1) serves as the boundary for the continuous fluid flow field.

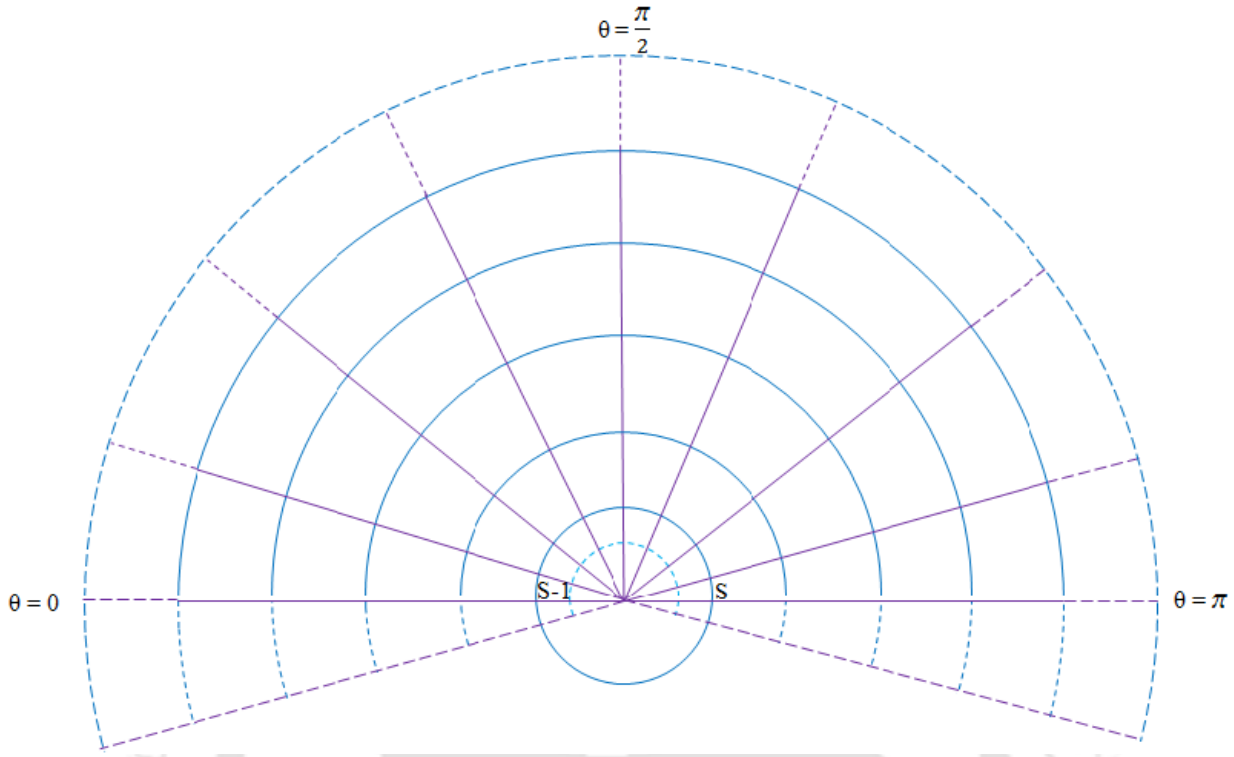

Figure 4.2 Grid arrangement in computational domain.

4.3. Discretization of Governing Equations

The diffusive and non-Newtonian terms of *r*- and *θ*- momentum equations have been discretized by second order central difference scheme. But convective terms have been discretized using the QUICK scheme for better accuracy and to avoid numerical instabilities. In convective schemes, each convective term is divided as two parts; a variable and a coefficient depending on which component of momentum equation is considered. Then, the coefficient will be averaged and the convective scheme will be employed on the variable term depending on whether the coefficient is positive or negative. For example, in the *r*-momentum equation the variable is v_r and coefficient can be v_θ or v_r depending on the term being discretized. Similarly, in *θ*-momentum equation the variable is v_θ and coefficient can be v_θ or v_r.

The r- and θ-components of momentum equations, respectively, can be written as follows:

$$\frac{\partial v_r}{\partial t}+[CONVR]=-\frac{\partial p}{\partial r}+[DIFF-R]+[NON-R] \tag{4.1}$$

$$\frac{\partial v_\theta}{\partial t}+[CONV\theta]=-\frac{1}{r}\frac{\partial p}{\partial \theta}+[DIFF-\theta]+[NON-\theta] \tag{4.2}$$

4.3.1. Discretization of r-component of momentum equation

Since for r-component of momentum equation (i, j+1/2) is the centre of the v_r-control volume, the convective term of equation (4.1) can be discretized as follows:

$$CONVR=\left[\frac{1}{r^2}\frac{\partial(v_r{}^2 r^2)}{\partial r}+\frac{1}{r\sin\theta}\frac{\partial(v_r v_\theta \sin\theta)}{\partial\theta}-\frac{v_\theta{}^2}{r}\right]$$

$$\left[\frac{1}{r^2}\frac{\partial\left(v_r{}^2 r^2\right)}{\partial r}\right]_{(i,j+1/2)}=\frac{\left(v_{ravg}v_{rup}r^2\right)_{i,j+1}-\left(v_{ravg}v_{rup}r^2\right)_{i,j}}{r_{j+1/2}{}^2\Delta r_{j+1/2}}$$

where

$$v_{ravg}(i,j+1)=\frac{v_r(i,j+1/2)+v_r(i,j+3/2)}{2}$$

$$v_{ravg}(i,j)=\frac{v_r(i,j-1/2)+v_r(i,j+1/2)}{2}$$

if $v_{ravg}(i,j+1)\geq 0$ then

$$v_{rup}=\frac{3}{8}v_r(i,j+1)+\frac{3}{4}v_r(i,j)-\frac{1}{8}v_r(i,j-1)$$

else

$$v_{rup}=\frac{3}{8}v_r(i,j)+\frac{3}{4}v_r(i,j+1)-\frac{1}{8}v_r(i,j+2)$$

if $v_{ravg}(i,j)\geq 0$ then

$$v_{rup}=\frac{3}{8}v_r(i,j)+\frac{3}{4}v_r(i,j-1)-\frac{1}{8}v_r(i,j-2)$$

else

$$v_{rup}(i,j)=\frac{3}{8}v_r(i,j-1)+\frac{3}{4}v_r(i,j)-\frac{1}{8}v_r(i,j+1)$$

$$\left[\frac{1}{r\sin\theta}\frac{\partial(v_r v_\theta \sin\theta)}{\partial\theta}\right]_{(i,j+1/2)}=\frac{\left(v_{rup}v_{\theta avg}\sin\theta\right)_{i+1/2,j+1/2}-\left(v_{rup}v_{\theta avg}\sin\theta\right)_{i-1/2,j+1/2}}{r_{j+1/2}\sin\theta_i d\theta}$$

$$v_{\theta avg}(i+1/2,j+1/2)=\frac{v_\theta(i+1/2,j)+v_\theta(i+1/2,j+1)}{2}$$

$$v_{\theta avg}(i-1/2,j+1/2)=\frac{v_\theta(i-1/2,j)+v_\theta(i-1/2,j+1)}{2}$$

If $v_{\theta avg}$ (i+1/2,j+1/2) ≥ 0 then

$$v_{rup}=\frac{3}{8}v_r(i+1,j)+\frac{3}{4}v_r(i,j)-\frac{1}{8}v_r(i-1,j)$$

else

$$v_{rup}=\frac{3}{8}v_r(i,j)+\frac{3}{4}v_r(i+1,j)-\frac{1}{8}v_r(i+2,j)$$

if $v_{\theta avg}$ (i-1/2,j+1/2) ≥ 0 then

$$v_{rup}=\frac{3}{8}v_r(i,j)+\frac{3}{4}v_r(i-1,j)-\frac{1}{8}v_r(i-2,j)$$

else

$$v_{rup}=\frac{3}{8}v_r(i-1,j)+\frac{3}{4}v_r(i,j)-\frac{1}{8}v_r(i+1,j)$$

$$\left[\frac{v_\theta^{\,2}}{r}\right]_{i,j+1/2}=\frac{\left[v_\theta(i-1/2,j+1)+v_\theta(i+1/2,j+1)+v_\theta(i-1/2,j)+v_\theta(i+1/2,j)\right]^2}{16r_{j+1/2}}$$

$$-\left[\frac{\partial p}{\partial r}\right]_{i,j+1/2}=-\left(\frac{p(i,j+1)-p(i,j)}{\Delta r}\right)$$

The non-Newtonian term of equation (4.1) can be discretized as follows:

$$NONR=\frac{2^{(n+1)}}{Re}\left[\varepsilon_{rr}\frac{\partial\eta}{\partial r}+\frac{\varepsilon_{r\theta}}{r}\frac{\partial\eta}{\partial\theta}\right]$$

where

$$\varepsilon_{rr} = \left(\frac{\partial v_r}{\partial r}\right)_{i,j+1/2} = \frac{v_r(i, j+3/2) - v_r(i, j-1/2)}{2\Delta r}$$

$$\varepsilon_{r\theta} = \frac{1}{2}\left(\frac{1}{r}\frac{\partial v_r}{\partial \theta} + \frac{\partial v_\theta}{\partial r} - \frac{v_\theta}{r}\right)_{i,j+1/2}$$

$$\left(\frac{1}{r}\frac{\partial v_r}{\partial \theta}\right)_{i,j+1/2} = \left(\frac{1}{r_{j+1/2}}\right)\left[\frac{v_r(i+1, j+1/2) - v_r(i-1, j+1/2)}{2\Delta\theta}\right]$$

$$\left(\frac{\partial v_\theta}{\partial r}\right)_{i,j+1/2} = \left[\frac{v_\theta(i, j+1) - v_\theta(i, j)}{\Delta r}\right]$$

$$= \left[\frac{v_\theta(i+1/2, j+1) + v_\theta(i-1/2, j+1) - \left(v_\theta(i+1/2, j) + v_\theta(i-1/2, j)\right)}{2\Delta r}\right]$$

$$\left(\frac{v_\theta}{r}\right)_{i,j+1/2} = \left[\frac{v_\theta(i+1/2, j+1) + v_\theta(i-1/2, j+1) - \left(v_\theta(i+1/2, j) + v_\theta(i-1/2, j)\right)}{4r_{j+1/2}}\right]$$

$$\left(\frac{\partial \eta}{\partial \theta}\right)_{i,j+1/2} = \left[\frac{\eta(i+1, j+1/2) - \eta(i-1, j+1/2)}{2\Delta\theta}\right]$$

$$= \left[\frac{\eta(i+1, j) + \eta(i+1, j+1) - \left(\eta(i-1, j) + \eta(i-1, j+1)\right)}{4\Delta\theta}\right]$$

$$\left(\frac{\partial \eta}{\partial r}\right)_{i,j+1/2} = \left[\frac{\eta(i, j+1) - \eta(i, j)}{\Delta r}\right]$$

4.3.2. Discretization of θ-component of momentum equation

Since for θ-component of momentum equation (i+1/2,j) is the centre of the v_θ-control volume, diffusive term of equation (4.2) can be discretized as follows:

$$DIFF\theta = \frac{2^n \eta}{Re}\left[\frac{1}{r^2}\frac{\partial}{\partial r}\left(r^2\frac{\partial v\theta}{\partial r}\right) + \frac{1}{r^2}\frac{\partial}{\partial \theta}\left(\frac{1}{\sin\theta}\frac{\partial}{\partial \theta}(v_\theta \sin\theta\right) + \frac{2}{r^2}\frac{\partial v_r}{\partial \theta}\right]$$

$$\left[\frac{1}{r^2}\frac{\partial}{\partial r}\left(r^2\frac{\partial v_\theta}{\partial r}\right)\right]_{i+1/2,j}=\left(\frac{1}{r_j^{\,2}}\right)\left[\frac{\left(r^2\frac{\partial v_\theta}{\partial r}\right)_{i+1/2,j+1/2}-\left(r^2\frac{\partial v_\theta}{\partial r}\right)_{i+1/2,j-1/2}}{\Delta r}\right]$$

where

$$\left(r^2\frac{\partial v_\theta}{\partial r}\right)_{i+1/2,j+1/2}=\left(r^2{}_{j+1/2}\right)\left[\frac{v_\theta(i+1/2,j+1)-v_\theta(i+1/2,j)}{\Delta r}\right]$$

$$\left(r^2\frac{\partial v_\theta}{\partial r}\right)_{i+1/2,j-1/2}=\left(r^2{}_{j-1/2}\right)\left[\frac{v_\theta(i+1/2,j)-v_\theta(i+1/2,j-1)}{\Delta r}\right]$$

$$\left[\frac{1}{r^2}\frac{\partial}{\partial\theta}\left(\frac{1}{\sin\theta}\frac{\partial}{\partial\theta}(v_\theta\sin\theta)\right)\right]_{i+1/2,j}=\left(\frac{1}{r_j^{\,2}}\right)\left[\frac{\left(\frac{1}{\sin\theta}\frac{\partial}{\partial\theta}(v_\theta\sin\theta)\right)_{i+1,j}-\left(\frac{1}{\sin\theta}\frac{\partial}{\partial\theta}(v_\theta\sin\theta)\right)_{i,j}}{\Delta\theta}\right]$$

where

$$\left[\frac{1}{\sin\theta}\frac{\partial}{\partial\theta}(v_\theta\sin\theta)\right]_{i+1,j}=\left(\frac{1}{\sin\theta_{i+1}}\right)\left[\frac{v_\theta(i+3/2,j)\sin\theta_{i+3/2}-v_\theta(i+1/2,j)\sin\theta_{i+1/2}}{\Delta\theta}\right]$$

$$\left[\frac{1}{\sin\theta}\frac{\partial}{\partial\theta}(v_\theta\sin\theta)\right]_{i,j}=\left(\frac{1}{\sin\theta_i}\right)\left[\frac{v_\theta(i+1/2,j)\sin\theta_{i+1/2}-v_\theta(i-1/2,j)\sin\theta_{i-1/2}}{\Delta\theta}\right]$$

$$\left[\frac{2}{r^2}\frac{\partial v_r}{\partial\theta}\right]_{i+1/2,j}=\left(\frac{2}{r_j^{\,2}}\right)\left[\frac{v_r(i+1,j)-v_r(i,j)}{\Delta\theta}\right]$$

$$=\left(\frac{2}{r_j^{\,2}}\right)\left[\frac{\left(v_r(i+1,j+1/2)+v_r(i+1,j-1/2)\right)-\left(v_r(i,j+1/2)+v_r(i,j-1/2)\right)}{2\Delta\theta}\right]$$

$$\eta(i+1/2,j)=\left[\frac{\eta(i+1,j)+\eta(i,j)}{2}\right]$$

Similarly, other terms of *r*-momentum and θ-momentum equations as well as continuity equation, energy equations, Poisson's equation for pressure correction, vorticity equation, and vorticity transport equation are being discretized.

4.4. SMAC-Implicit Algorithm

The major difficulty encountered in obtaining the solution of incompressible fluid flow using primitive variables based momentum equation is the non-availability of any obvious equation for calculating the pressure field. SMAC-semi implicit scheme is implicit for diffusion and non-Newtonian terms while explicit in convective term (pressure terms are explicit in predictor step but in combined predictor-corrector scheme pressure terms are implicit). An advantage of the SMAC-semi implicit scheme over SMAC-explicit (which is explicit in convective and diffusion terms) scheme is that one can use larger values of time-step. This numerical scheme mainly consists of three steps, velocity prediction, pressure correction and finally velocity correction. All these steps are solved by the Gauss-Seidel iteration procedure. In the first step, we assume the pressure field at the $(t_s)^{th}$ time-step and "predict"' the velocity field at the $(t_s+1)^{th}$ time-step by using the Gauss-Seidel iterations. In the second step, this predicted velocity field is used to solve the Poisson's equation which yields pressure correction. This pressure correction is then used to calculate the velocity corrections. Finally, all the predictor and corrector quantities are added to estimate the modified velocity and pressure field for the next time-step. These steps are repeated until a fully converged steady-state solution is obtained. The predictor and corrector equations used in this work are derived below.

4.4.1. Velocity prediction

Consider r- and θ- components of momentum equation in the following form:

$$\left[\frac{\partial v_r}{\partial t}\right]_{i,j+1/2} + [CONVR]_{i,j+1/2} = -\left[\frac{\partial p}{\partial r}\right]_{i,j+1/2} + [DIFFR]_{i,j+1/2} + [NONR]_{i,j+1/2} \quad (4.3)$$

$$\left[\frac{\partial v_\theta}{\partial t}\right]_{i+1/2,j} + [CONV\theta]_{i+1/2,j} = -\left[\frac{1}{r}\frac{\partial p}{\partial \theta}\right]_{i+1/2,j} + [DIFF\theta]_{i+1/2,j} + [NON\theta]_{i+1/2,j} \quad (4.4)$$

Discretizing the above equations we get

$$\frac{v_r^{t_s+1}(i,j+1/2) - v_r^{t_s}(i,j+1/2)}{\Delta t} + [CONVR]_{i,j+1/2}^{t_s} = -\left[\frac{\partial p}{\partial r}\right]_{i,j+1/2}^{t_s+1} + [DIFFR]_{i,j+1/2}^{t_s+1} + [NONR]_{i,j+1/2}^{t_s+1} \quad (4.5)$$

$$\frac{v_\theta^{t_s+1}(i+1/2,j) - v_\theta^{t_s}(i+1/2,j)}{\Delta t} + [CONV\theta]_{i+1/2,j}^{t_s} = -\left[\frac{1}{r}\frac{\partial p}{\partial \theta}\right]_{i+1/2,j}^{t_s+1} + [DIFF\theta]_{i+1/2,j}^{t_s+1} + [NON\theta]_{i+1/2,j}^{t_s+1} \quad (4.6)$$

where the superscript (t_s) represents the current time-step at which the variable values are known and (t_s+1) indicates the next time-step at which the variables are unknown. Here the convective term is explicit while the diffusion, non-Newtonian and pressure terms are implicit. The pressure at the (t_s+1)th step is unknown and there is no equation for pressure which can be used to obtain it. So we assume an approximate pressure field at the (t_s+1)th time-step by its previous time-step value. Therefore here we predict velocity field v_r* and v_θ* at the (t_s+1)th time-step by using an assumed pressure field (and obviously will not satisfy continuity). Hence equations (4.5) and (4.6) lead to give prediction equations which can be written as follows:

$$\frac{v_r^*(i,j+1/2) - v_r^{t_s}(i,j+1/2)}{\Delta t} + [CONVR]_{i,j+1/2}^{t_s} = -\left[\frac{\partial p}{\partial r}\right]_{i,j+1/2}^{t_s+1} + [DIFFR]_{i,j+1/2}^{*} + [NONR]_{i,j+1/2}^{*} \quad (4.7)$$

$$\frac{v_\theta^*(i+1/2,j) - v_\theta^{t_s}(i+1/2,j)}{\Delta t} + [CONV\theta]_{i+1/2,j}^{t_s} = -\left[\frac{1}{r}\frac{\partial p}{\partial \theta}\right]_{i+1/2,j}^{t_s} + [DIFF\theta]_{i+1/2,j}^{*} + [NON\theta]_{i+1/2,j}^{*} \quad (4.8)$$

where v_r* and v_θ* are predicted velocities. In Eq. 4.7 and Eq. 4.8, all variables are at (t_s)th time-step are known, while variables with an asterisk (*) are unknown. Thus Eq. 4.7 and Eq. 4.8 are solved to get v_r* and v_θ* by using Gauss-Seidel iterations. In Eq. 4.7, [DIFFR]* is a function of v_r* only, but [NONR]* is function of v_r* and v_θ*. So to predict v_r*, the value of v_θ*, which is unknown is required. So for computations, v_θ* is lagged to v_θ^{ts}. But in Eq. 4.8, where too

[DIFFθ]* and [NONθ]* are functions of both v_r* and v_θ*, however, there is no need of lagging here, since v_r* is computed before predicting v_θ*, since in the prediction-step usually first v_r* will be predicted before predicting v_θ*. (It may be noted that, this kind of lagging is not required in case of Newtonian calculations, since [NONR]* and [NONθ]* drops to zero for the case of Newtonian fluids).

4.4.2. Velocity correction

In order to estimate the velocity corrections at $(t_s+1)^{th}$ time-step, the velocity correction should be added to the velocity prediction to count as final values for the next time-step calculations. In this section, the formulation of the velocity correction equations is presented. Subtracting Eq. 4.7 and Eq. 4.8 from Eq. 4.5 and Eq. 4.6 respectively we get expressions for the velocity correction which can be written as:

$$\frac{v_r'(i,j+1/2)}{\Delta t} = -\left[\frac{\partial p}{\partial r}\right]'_{i,j+1/2} + [DIFFR]'_{i,j+1/2} + [NONR]'_{i,j+1/2} \tag{4.9}$$

$$\frac{v_\theta'(i+1/2,j)}{\Delta t} = -\left[\frac{1}{r}\frac{\partial p}{\partial \theta}\right]'_{i+1/2,j} + [DIFF\theta]'_{i+1/2,j} + [NON\theta]'_{i+1/2,j} \tag{4.10}$$

where

$$\frac{v_r'(i,j+1/2)}{\Delta t} = \frac{v_r^{t_s+1}(i,j+1/2) - v_r^*(i,j+1/2)}{\Delta t}$$

$$\frac{v_\theta'(i+1/2,j)}{\Delta t} = \frac{v_\theta^{t_s+1}(i+1/2,j) - v_\theta^*(i+1/2,j)}{\Delta t}$$

$$\left[\frac{\partial p}{\partial r}\right]'_{i,j+1/2} = \left[\frac{\partial p}{\partial r}\right]^{t_s+1}_{i,j+1/2} - \left[\frac{\partial p}{\partial r}\right]^{t_s}_{i,j+1/2}$$

$$\left[\frac{1}{r}\frac{\partial p}{\partial \theta}\right]'_{i+1/2,j} = \left[\frac{1}{r}\frac{\partial p}{\partial \theta}\right]^{t_s+1}_{i+1/2,j} - \left[\frac{1}{r}\frac{\partial p}{\partial \theta}\right]^{t_s}_{i+1/2,j}$$

$$\left[DIFFR\right]^{/}_{i,j+1/2} = \left[DIFFR\right]^{t_s+1}_{i,j+1/2} - \left[DIFFR\right]^{*}_{i,j+1/2}$$

$$\left[DIFF\theta\right]^{/}_{i+1/2,j} = \left[DIFF\theta\right]^{t_s+1}_{i+1/2,j} - \left[DIFF\theta\right]^{*}_{i+1/2,j}$$

$$\left[NONR\right]^{/}_{i,j+1/2} = \left[NONR\right]^{t_s+1}_{i,j+1/2} - \left[NONR\right]^{*}_{i,j+1/2}$$

$$\left[NON\theta\right]^{/}_{i+1/2,j} = \left[NON\theta\right]^{t_s+1}_{i+1/2,j} - \left[NON\theta\right]^{*}_{i+1/2,j}$$

In all above expressions, primed variables indicate correction quantities. Eq. 4.9 and Eq. 4.10 can be solved using Gauss-Seidel iterations but the difficulty is the non-availability of $p_{ij}^{/}$; the pressure corrector. Therefore, before calculating the velocity correction, pressure correction should be known which can be obtained as explained below.

4.4.3. Pressure correction

The quantities v_r^{ts+1} and v_θ^{ts+1}, the velocity components at $(t_s+1)^{th}$ time-step, must satisfy the continuity equation i.e.,

$$\frac{1}{r^2}\frac{\partial\left(r^2 v_r^{t_s+1}\right)}{\partial r} + \frac{1}{r\sin\theta}\frac{\partial\left(v_\theta^{t_s+1}\sin\theta\right)}{\partial\theta} = 0 \tag{4.11}$$

where v_r^{ts+1} and v_θ^{ts+1} are given as:

$$v_r^{t_s+1} = v_r^{*} + v_r^{/}, \qquad v_\theta^{t_s+1} = v_\theta^{*} + v_\theta^{/} \tag{4.12}$$

From the continuity equation

$$\Rightarrow \nabla.V^{t_s+1} = \nabla.V^{*} + \nabla.V^{/} = 0 \Rightarrow \nabla.V^{*} = -\nabla.V^{/}$$

Now by expanding the term $\nabla.V^{/}$, we get

$$\nabla.V^{/} = \frac{1}{r^2}\frac{\partial\left(r^2 v_r^{/}\right)}{\partial r} + \frac{1}{r\sin\theta}\frac{\partial\left(v_\theta^{/}\sin\theta\right)}{\partial\theta}$$

Here v_r' and v_θ' given by Eq. 4.9 and Eq. 4.10 respectively. Thus by using Eqs. 4.9 and Eq. 4.10; and considering these two equations only for Newtonian case we get:

$$\nabla.V' = \frac{1}{r^2}\frac{\partial}{\partial r}\left[r^2\left(-\left[\frac{\partial p}{\partial r}\right]'_{i,j+1/2} + \left[DIFFR\right]'_{i,j+1/2}\right)\Delta t\right] + \frac{1}{r\sin\theta}\frac{\partial}{\partial\theta}\left[\sin\theta\left(-\left[\frac{1}{r}\frac{\partial p}{\partial\theta}\right]'_{i+1/2,j} + \left[DIFF\theta\right]'_{i+1/2,j}\right)\Delta t\right]$$

$$\Rightarrow \frac{\nabla.V'}{\Delta t} = \frac{1}{r^2}\frac{\partial}{\partial r}\left[r^2\left(-\left[\frac{\partial p}{\partial r}\right]'_{i,j+1/2} + \left[DIFFR\right]'_{i,j+1/2}\right)\right] + \frac{1}{r\sin\theta}\frac{\partial}{\partial\theta}\left[\sin\theta\left(-\left[\frac{1}{r}\frac{\partial p}{\partial\theta}\right]'_{i+1/2,j} + \left[DIFF\theta\right]'_{i+1/2,j}\right)\right]$$

$$\Rightarrow \frac{\nabla.V'}{\Delta t} = \frac{1}{r^2}\frac{\partial}{\partial r}\left(-\left[r^2\left[\frac{\partial p}{\partial r}\right]'_{i,j+1/2}\right]\right) + \frac{1}{r\sin\theta}\frac{\partial}{\partial\theta}\left[\left(-\sin\theta\left[\frac{1}{r}\frac{\partial p}{\partial\theta}\right]'_{i+1/2,j}\right)\right] + \frac{1}{r^2}\frac{\partial}{\partial r}\left(r^2\left[DIFFR\right]\right)'_{i,j+1/2} + \frac{1}{r\sin\theta}\frac{\partial}{\partial\theta}\left(\sin\theta\left[DIFF\theta\right]\right)'_{i+1/2,j}$$

By simplifying the right hand side term of the above expression and writing in conservative from, the resulting expression can be represented as:

$$\frac{\nabla.V'}{\Delta t} = -\nabla^2 p' + \frac{2^n\eta}{\mathrm{Re}}\nabla^2\left(\nabla.V'\right) \tag{4.13}$$

where the operator ∇^2 is given by

$$\nabla^2 = \frac{1}{r^2}\frac{\partial}{\partial r}\left(r^2\frac{\partial}{\partial r}\right) + \frac{1}{r\sin\theta}\frac{\partial}{\partial\theta}\left(\frac{\sin\theta}{r}\frac{\partial}{\partial\theta}\right)$$

Since we know that $\nabla.V^* = -\nabla.V'$ and by making use of this expression in Eq. 4.13, we get

$$\nabla^2 p' = \frac{\nabla.V^*}{\Delta t} - \frac{2^n\eta}{\mathrm{Re}}\nabla^2\left(\nabla.V^*\right) \tag{4.14}$$

Eq. 4.14 is solved for $p'_{i,j}$ with appropriate boundary conditions and using the predicted velocity V^*. Then with the resultant pressure correction, Eq. 4.9 and 4.10 are solved for v_r' and v_θ' respectively. (In the Eq. 4.14, the viscosity and power-law index terms appear because the radial distances have been normalized using the radius of the drop, however, this term would have not appeared in the pressure corrector equation if the radial distances were normalized using the

diameter of the fluid sphere). Finally we get the corrected velocity and pressure fields by $v_r^{t_s+1} = v_r^* + v_r^1$, $v_\theta^{t_s+1} = v_\theta^* + v_\theta^1$ and $p_{ij}^{t_s+1} = p_{ij}^* + p_{ij}^/$. The Eq. 4.10 is for Newtonian case only, however, in the present study, the similar equation has been used for non-Newtonian systems to avoid further complications. However, this is justified since the Eq. 4.14 ensures that the velocity field satisfies the continuity equation, which is the same for both Newtonian and non-Newtonian flows. The momentum equations ensure that the correct non-Newtonian solution is obtained.

Finally, the fully converged velocity and pressure fields can be used to evaluate the derived quantities such as the individual and total drag coefficients, streamlines and vorticity contours, distributions of viscosity, pressure, vorticity and tangential velocity on the surface of the drop, etc., as discussed in the previous chapter as functions of the pertinent dimensionless parameters.

4.5. Segregated Algorithm for Heat Transfer

In the numerical study of heat transfer problems, sometimes scalars like temperature are solved along with the momentum equations. However, how the solutions of the flow equations and the energy equations are sequenced is determined by the kind of flow and heat transfer problem being solved. In this work, it is assumed that the flow field is steady and independent of the temperature being solved. Such situations would arise in steady forced convective problems, say, when the temperature field is not strong enough to cause substantial changes in the density so as to affect the flow by buoyancy. In such cases, the momentum equations can be solved independent of temperature equations. Thus, in this study, the steady velocity field in the entire flow domain is obtained by numerically solving the momentum equations segregated from the energy equation. Therefore the fully converged velocity field was used as the input for the

energy equation to obtain the temperature field by using a time-stepping procedure applied to the continuity equation. Because an implicit scheme is used each time-step solution is obtained by Gauss-Seidel iterations. The temperature profile in the continuous phase is obtained with a similar implicit algorithm which uses the QUICK and second order central differencing schemes, respectively, for the convective and diffusive terms of the energy equation. After obtaining the steady temperature field for the continuous phase, one can readily calculate the values of the local and average Nusselt numbers, as explained in the previous chapter as functions of pertinent dimensionless parameters.

Chapter 5

CHOICE OF NUMERICAL PARAMETERS

The optimum domain size and grid of sufficient resolution are most important in momentum and heat transfer phenomena of unbounded flow past solid objects. Thus in this chapter, numerical details such as optimum domain, and optimum grid have been carried out. Also validity and reliability of solution methodology are established for momentum and heat transfer phenomena of unconfined spherical particle and assemblages of spherical particles in Newtonian and power-law liquids. The effect of domain size on flow behavior is more significant at small values of the Reynolds number because of domination of viscous forces in comparison with convection forces. Thus, the effect of domain size has been carried out at small Reynolds number for two extreme values of slip parameter. Whereas the effect of grid is predominant at large values of Reynolds numbers because of domination of convection forces. Thus, the effect of grid size has been carried out at large value of Reynolds number for two extreme values of slip parameter. In case of heat transfer study, the heat transfer problem is solved using a segregated approach. In other words, the momentum equations are solved first to obtain the fully converged velocity and pressure fields and then the energy equation is solved to obtain the fully converged temperature field in the entire computational domain using the already fully converged velocity field as input. However, the detailed domain (at small Reynolds number) and grid (at large Reynolds number) independence studies have also been carried out at extreme value of slip parameter and Prandlt number.

5.1. Drag Behavior of Unconfined Single Sphere in Power-law Fluids with Velocity Slip at the Interface

5.1.1. Domain and grid independence study

Table 5.1 presents the effect of domain size on the total drag coefficient of a single sphere in shear thinning (n = 0.5), Newtonian (n = 1) and shear thickening (n = 1.6) fluids at Re = 0.1. To check the effect domain, three values for dimensionless R_∞ has been chosen viz. R_∞ = 100, 150, 200 for two extreme values of the slip parameter. It can be seen from this table that the domains of size 150 and 200 produce C_d values very close to each other, thus the domain of size R_∞ = 150 has been chosen as optimum domain in this work. Because the size of the domain is 150 times the radius of the sphere, having uniform fine grid in the entire unbounded computational domain would be computationally very expensive. Thus in the radial direction a logarithmic stretching, i.e., $y = \ln r$ is considered where "r" is the dimensionless radial coordinate. Because of this logarithmic stretching or transformation of radial direction is to ensure clustering of the grids near the surface of the sphere where the gradients are strong. Further due to this logarithmic transformation, the size of grid gradually becomes coarser as fine grid is not required far away from the sphere surface where the gradients are not fine. Thus by the use of this logarithmic transformation of radial direction ensure the accuracy of the near surface kinetics such as the local and average Nusselt numbers with sufficient accuracy but with limited CPU time and processor memory.

For this optimum domain (i.e., for R_∞ = 150), a detailed grid independence study has been carried out for the case of shear thinning (n = 0.5), Newtonian (n = 1) and Shear thickening (n = 1.6) fluids flow past a single sphere at Re = 200 for two extreme values of slip parameter

and presented in **Table 5.2**. In order to check the effect of grid, three grids viz. 90×200, 90×240, 120×200 are used and it can be seen from this table that all grids produce almost identical results. However, because of large computational time required by grids 90×240 and 120×200, a moderately fine grid i.e., 90×200 has been chosen for $Re > 1$. Since the effect of convection force is very small for the case of $Re \leq 1$, a slightly coarse grid, i.e., 60×150 has been used.

Table 5.1 Effect of domain size on C_d of single smooth sphere at $Re = 0.1$

Domain (R_∞)	$n = 0.5$		$n = 1$		$n = 1.6$	
	$\lambda = 0.01$	$\lambda = 100$	$\lambda = 0.01$	$\lambda = 100$	$\lambda = 0.01$	$\lambda = 100$
100	213.368	342.157	159.193	245.712	90.585	170.842
150	212.853	340.418	160.998	259.680	88.822	162.229
200	212.521	341.363	159.043	252.455	86.268	160.082

Table 5.2 Effect of grid size on C_d of single smooth sphere at $Re = 200$.

Grid (θ- × r-)	$n = 0.5$		$n = 1$		$n = 1.6$	
	$\lambda = 0.01$	$\lambda = 100$	$\lambda = 0.01$	$\lambda = 100$	$\lambda = 0.01$	$\lambda = 100$
90 × 200	0.153	0.461	0.207	0.794	0.343	1.191
90 × 240	0.150	0.425	0.204	0.798	0.343	1.190
120 × 200	0.152	0.435	0.205	0.810	0.341	1.182

5.1.2. Validation

Tables 5.3 and **Table 5.4** presents the comparison of present values of total drag coefficients on solid spheres ($\lambda \to \infty$) with no-slip condition and on spherical bubbles ($\lambda \to 0$) with fully slip

condition in Newtonian fluids at different Reynolds numbers and the present results are found to be in good agreement with literature results [314, 315, 316−321]. **Table 5.5** shows a comparison of present C_d values of an unconfined single slip sphere in Newtonian fluids at Re = 0.1 for different values of the slip parameter (λ) with analytical solution of Basset [210]; and the two values are in good agreement with each other with a maximum relative difference being within ±4.5%. Similarly **Table 5.6** shows a comparison of present C_d values of unconfined single slip spheres in Newtonian fluids with λ = 1 at Re = 10 – 200 with the numerical results of Atefi et al. [217]. Here too the agreement between two values is satisfactory. However, in such numerical studies, discrepancies of such order of magnitude are not at all uncommon and are often because of the differences in the solution method, domain and grid, etc. Therefore, on the basis of our previous experience and the present comparisons, the present solver is believed to be reliable and accurate to within ±4-5%.

Table 5.3 Comparison of C_d of no-slip solid spheres ($\lambda\rightarrow\infty$) in Newtonian fluids.

Re	Present	Song et al. [315]	Dhole et al. [314]	Tripathi et al. [316]	LeClair et al. [317]
1	27.708	26.673	26.13	27.15	27.37
10	4.344	4.313	4.281	4.26	4.337
20	2.739	2.748	2.692	-	2.736
100	1.094	1.083	1.062	1.08	1.096
200	0.779	-	0.744	-	0.772

Further in this work, **Table 5.7** presents the comparisons of the present drag coefficients of spheres in Newtonian fluids with varying degree of slip (λ = 0, 0.1, 1, 5, 10, 50, ∞) at the interface with those of Feng [252] and Murthy and Kumar [322]. Here too the reliability of this solver is found to be satisfactory as the maximum absolute relative error is within 5% compared to those of Feng [252].

Table 5.4 Comparison of C_d of fully slip spherical bubble ($\lambda = 0$) in Newtonian fluids.

Re	Present	Brabston and Keller [318]	Ryskin and Leal [319]	Feng and Michaelides [320]	Dhole et al. [321]
1	17.174	17.59	17.5	17.57	-
10	2.392	2.350	2.43	2.441	2.464
20	1.397	1.362	1.41	1.404	1.434
100	0.374	-	0.38	0.379	0.383
200	0.206	0.197	0.22	0.206	0.212

Table 5.5: Comparison of C_d of unconfined single slip spheres in Newtonian fluids at *Re* = 0.1.

λ	Basset [210]	Present
0.1	162.58	163.620
1	180	183.366
5	210	217.532
10	221.54	230.726

Table 5.6: Comparison of C_d of unconfined single slip spheres in Newtonian fluids at $\lambda = 1$.

Re	Atefi *et al*. [217]	Present
	$\lambda = 1$	
10	2.86	2.921
50	0.87	0.864
100	0.51	0.500
200	0.28	0.285

Table 5.7: Comparisons of present total drag coefficients of spheres in Newtonian fluids for different values of Reynolds and slip numbers.

Slip parameter (λ)	Murthy and Kumar [322]	Feng [252]	Present	Feng [252]	Present	Feng [252]	Present	Feng [252]	Present
		Re = 1		*Re* = 10		*Re* = 50		*Re* = 100	
0	-	17.6	17.174	2.37	2.392	0.676	0.666	0.391	0.374
0.1	-	18.1	17.513	2.42	2.498	0.698	0.692	0.406	0.387
1	19.28	20.0	19.757	2.88	2.921	0.860	0.864	0.515	0.500
10	23.08	25.1	25.026	3.86	4.027	1.360	1.387	0.904	0.911
∞	-	27.4	27.708	4.30	4.344	1.560	1.584	1.075	1.094

5.2. Average Nusselt Number of Unconfined Single Sphere in Power-law Fluids with Velocity Slip at the Interface

5.2.1. Domain and grid independence study

Table 5.8 and **Table 5.9** presents the effect of domain size on the average values of Nusselt number of a single sphere in Newtonian (**Table 5.8**), shear thinning (**Table 5.9**) and shear thickening (**Table 5.8**) fluids at Re = 0.1 for extreme value of slip parameter and Prandlt number. From tables it can be seen that for either extreme values of the Prandtl number and dimensionless slip parameter, the average Nusselt number at Re = 0.1 is unaffected (maximum absolute relative error within 1%) by varying the size of the domain from R_∞ = 100 to R_∞ = 200 via R_∞ = 150. Thus the domain of size R_∞ = 150 has been chosen in the present study.

Table 5.8: Effect of domain size on Nu_{avg} of spheres in Newtonian fluids with slip velocity at the interface at Re = 0.1.

Domain size (R_∞)	λ = 0.01		λ = 100	
	Pr = 1	Pr = 100	Pr = 1	Pr = 100
100	2.1196	3.6431	2.1173	3.2366
150	2.1196	3.6541	2.1191	3.2707
200	2.1194	3.6433	2.1172	3.2894

Whereas **Table 5.10** and **Table 5.11** presents the effect of grid size on the average values of Nusselt number of a single sphere in Newtonian (**Table 5.10**), shear thinning (**Table 5.11**) and shear thickening (**Table 5.11**) fluids at Re = 200. Similarly from these tables, it can be observed that for the optimum domain size of R_∞ = 150, the average Nusselt number is almost identical

(maximum absolute relative error within 1%) by all three grids tested for either extreme values of the Prandtl number and the dimensionless slip number at *Re* = 200. Therefore grid size 90 × 200 (in θ- × r-) is found to be optimum and is used in the present study.

Table 5.9: Effect of domain size on Nu_{avg} of spheres in power-law fluids with slip velocity at the interface at *Re* = 0.1.

Domain	*n* = 0.5				*n* = 1.6			
(R_∞)	λ = 0.01		λ = 100		λ = 0.01		λ = 100	
	Pr = 1	*Pr* = 100	*Pr* = 1	*Pr* = 100	*Pr* = 1	*Pr* = 100	*Pr* = 1	*Pr* = 100
100	2.121	4.105	2.120	3.681	2.119	3.203	2.117	3.100
150	2.076	4.104	2.075	3.665	2.118	3.183	2.118	3.071
200	2.071	4.104	2.068	3.671	2.118	3.165	2.117	3.064

Table 5.10: Effect of grid size on Nu_{avg} of spheres in Newtonian fluids with fluid slip velocity at the solid-fluid interface at *Re* = 200.

Grid	λ = 0.01		λ = 100	
	Pr = 1	*Pr* = 100	*Pr* = 1	*Pr* = 100
90 × 200	15.4601	152.9411	11.7861	75.0432
90 × 240	15.4252	151.7997	11.6227	74.3022
120 × 200	15.3576	152.050	11.5880	74.2264

Table 5.11: Effect of grid size on Nu_{avg} of spheres in power-law fluids with slip velocity at the interface at Re = 200.

Grid	n = 0.5				n = 1.6			
(θ- × r-)	λ = 0.01		λ = 100		λ = 0.01		λ = 100	
	Pr = 1	Pr = 100	Pr = 1	Pr = 100	Pr = 1	Pr = 100	Pr = 1	Pr = 100
90 × 200	16.080	157.904	13.845	98.804	15.212	150.964	10.409	60.359
90 × 240	15.744	156.045	13.553	98.708	15.088	148.208	10.225	58.386
120 × 200	15.676	156.001	13.459	96.310	15.049	149.345	10.259	59.791

5.2.2. Validation

Table 5.12 shows a comparison of the present values of Nu_{avg} of the spherical particle in Newtonian fluids with the literature results for the cases of the slip numbers of λ = 0.01 (fully slip spherical bubbles) and λ = 100 (no-slip spherical particles) over a wide range of the Reynolds and Peclet numbers. From this table it can be seen that the results obtained by the present solver for two extreme limits of the slip numbers are in good agreement with their literature counterparts; and thus the results obtained for other intermediate values of slip numbers between these two limits would be reliable and accurate to within ±4-5%. Finally, the reliability and accuracy of the present numerical solver is established and can be safely used to produce new results of the forced convective heat transfer phenomena of spheres in Newtonian fluids with interface slip over wide range of the Reynolds, Prandtl and slip numbers.

Table 5.12 Comparison of present values of Nu_{avg} of infinite slip and no-slip sphere in Newtonian fluids.

		Feng and Michaelides [323]		Present	
Re	*Pe*	$\lambda = 0$	$\lambda = \infty$	$\lambda = 0.01$	$\lambda = 100$
1	1	2.354	2.315	2.374	2.341
	10	3.778	3.33	3.781	3.312
	50	6.482	4.869	6.352	4.879
	100	8.482	5.865	8.432	5.852
100	100	11.223	7.695	11.189	7.948
	1000	32.441	15.946	31.896	17.042
200	200	15.851	9.951	15.893	10.527

Table 5.13 presents analogous comparison of present Nu_{avg} values with literature values but in power-law (both shear-thinning and shear-thickening) fluids at Pe = 1000 (i.e., Re = 100 and Pr = 10). It can be seen from this table that the results obtained by the present solver for two extreme limits of slip number are in good agreement with literature values; and thus the results obtained for other intermediate values of the slip number between these two limits are believed to be reliable and accurate to within ±2-3%.

Table 5.13 Comparison of present values of Nu_{avg} of infinite slip and no-slip spherical particles in Newtonian and power-law fluids at Pe = 1000.

n = 0.8		n = 1		n = 1.6	
Dhole et al. [324] (λ = 0)	Present (λ = 0.01)	Dhole et al. [324] (λ = 0)	Present (λ = 0.01)	Dhole et al. [324] (λ = 0)	Present (λ = 0.01)
27.247	27.393	32.717	31.205	25.055	23.841
Song et al. [325] (λ = ∞)	Present (λ = 100)	Song et al. [325] (λ = ∞)	Present (λ = 100)	Song et al. [325] (λ = ∞)	Present (λ = 100)
14.437	14.28	15.983	16.825	12.051	12.075

5.3. Drag Behavior of Assemblages of Spherical Particles in Power-law Fluids with Velocity Slip at the Interface

5.3.1. Grid independence study

According to the cell model, the size of the computational domain in the case of assemblages of spheres or cylinders is fixed for a given value of the volume fraction of the dispersed phase as per the expression $R_\infty = \Phi^{-1/3}$, hence the domain independence study is not applicable in the case of assemblages of spheres. However a detailed grid independence study has been carried out by checking the effect of grid size on the drag coefficients of assemblages of spheres of volume fraction 0.1 in power-law fluids of fluid behavior index n = 0.6, n = 1 and n = 1.6 for either extremes of the slip parameter and presented in **Table 5.14**. From this table it can be realized that

grids 60 × 30 and 90 × 60 produce the values of drag coefficients almost identical to each other; and hence grid 60 × 30 has been chosen for all other calculations involved in this study.

Table 5.14 Effect of grid size on C_d of assemblages of spheres at Re = 200 in power-law fluids.

Grid size	λ = 0.01			λ = 100		
(θ- × r-)	n = 0.6	n = 1	n = 1.6	n = 0.6	n = 1	n = 1.6
30 × 30	0.211	0.298	0.504	0.871	1.468	2.377
60 × 30	0.210	0.300	0.511	0.892	1.505	2.439
60 × 60	0.211	0.302	0.497	0.981	1.438	2.370
90 × 60	0.211	0.301	0.506	0.989	1.494	2.374

5.3.2. Validation

The comparison of motion of single spheres in Newtonian and non-Newtonian fluids is presented; hence the validations of assemblages of spheres in Newtonian and power-law fluids are only presented herein. **Table 5.15** presents a comparison of present values of drag coefficients of assemblages of spheres in Newtonian fluids at Re = 0.1 for $\lambda \to 0$ and $\lambda \to \infty$ with the analytical C_d values of Gal-Or and Waslo [326] for swarms of bubbles and assemblages of solid spheres, respectively; and the comparison between two results is excellent. **Table 5.16** presents a comparison of present values of $C_d/C_{d,0}$ (where $C_{d,0}$ is total drag coefficient of an unconfined sphere in Newtonian fluids) with the analytical results of Faltas and Saad [214] at Re = 0.1 for different values of the volume fraction and the agreement between two results is satisfactory. However, the discrepancies of this order of magnitude are not at all uncommon in numerical studies of this kind; and are often ascribed to numerical artifacts such as the grid,

solution algorithm, etc. Thus, based on the validation shown in **Table 5.15** and **Table 5.16** the present solver is believed to be reliable and accurate to within ± 4 – 5%.

Table 5.15 Comparison of C_d of assemblages of spheres of no-slip and infinite slip at fluid-solid interface at Re = 0.1 with analytical results due to Gal-Or and Waslo [326].

Φ	Present ($\lambda \to 0$)	Fully slip bubbles	Present ($\lambda \to \infty$)	No-slip solid spheres
0.1	288.343	298.60	752.327	746.59
0.2	378.111	385.36	1356.310	1353.58
0.3	478.981	484.02	2425.921	2432.35
0.4	605.288	607.92	4507.936	4539.68
0.5	776.271	775.57	8991.742	9097.76

Table 5.16 Comparison of C_d/C_{d0} of assemblages of spheres at Re = 0.1.

Φ	Present	Faltas and Saad [214]	Present	Faltas and Saad [214]
	λ = 1		λ = 10	
0.1	2.005	2.086	2.612	2.712
0.3	3.792	3.893	6.802	7.075
0.5	7.382	7.546	18.850	19.636

Here comparison between power-law fluids, n = 0.6 and n = 1.6 for infinite slip ($\lambda \rightarrow 0$) and no-slip ($\lambda \rightarrow \infty$) are presented. **Table 5.17** shows a comparison of present values of drag coefficients of assemblages of spheres in shear thinning fluid for $\lambda \rightarrow 0$ with Gummalam and Chhabra [327] and Chhabra [328] for swarms of bubble in shear thinning fluid and the present results are accurate within ± 2%. Whereas **Table 5.18** and **Table 5.19** represents a comparison of present values of drag coefficients of assemblages of spheres in shear thickening fluid for $\lambda \rightarrow 0$ and $\lambda \rightarrow \infty$ with Kishore et al. [329, 330] for swarms of full slip bubbles and assemblage of no-slip solid spheres in shear thinning fluids and shear thickening fluids and the present results are accurate within ± 1–4%. **Table 5.20** represents a comparison of present values of drag coefficients of assemblages of spheres in shear thinning fluid for $\lambda \rightarrow \infty$ with Dhole et al. [331] assemblage of no-slip solid sphere in shear thinning fluids and present results are satisfactory.

Table 5.17 Comparison of C_d of assemblages of spheres infinite slip at fluid-solid interface ($\lambda \rightarrow 0$) for n =0.6 and Φ = 0.1

Re	Gummalam and Chhabra [327] Bubble	Chhabra [328] Bubble	Present ($\lambda \rightarrow 0$)
1	21.264	–	21.611
50	–	0.686	0.685

Table 5.18 Comparison of C_d of assemblages of spheres infinite slip at fluid-solid interface ($\lambda \rightarrow 0$) for n =1.6 and Φ = 0.1.

Re	Kishore et al. [329] Solid sphere	Present ($\lambda \rightarrow \infty$)
1	48.225	49.137
100	0.916	0.874
200	0.535	0.511

Table 5.19 Comparison of C_d of assemblages of spheres no-slip at fluid-solid interface **($\lambda \rightarrow \infty$)** for n =1.6 and Φ = 0.1.

Re	Kishore et al. [330] Solid sphere	Present ($\lambda \rightarrow \infty$)
1	145.68	146.382
100	3.383	3.318
200	2.430	2.439

Table 5.20 Comparison of C_d of assemblages of spheres no-slip at fluid-solid interface **($\lambda \rightarrow \infty$)** for n = 0.6.

Re	Dhole et al. [331] Solid sphere		Present ($\lambda \rightarrow \infty$)	
	Φ = 0.4	Φ = 0.5	Φ = 0.4	Φ = 0.5
1	131.113	208.606	134.218	214.613
100	3.363	–	3.533	–

5.4. Average Nusselt Number of Assemblages of Spheres in Power-law Fluids with Velocity Slip at the Interface

5.4.1. Grid independence study

The effect of the grid on the average Nusselt number of the assemblages of spheres in Newtonian and power-law fluids for volume fraction of dispersed phase Φ = 0.1 at Re = 200 for extreme values of slip parameter has been presented in **Table 5.21** and **Table 5.22**. It can be seen from this tables that grids of 60 × 30 and 90 × 60 produce almost same values of average Nusselt number except for the case of λ = 100 and Pr = 50. The reason may be ascribed to convergence difficulty of present solver for extremely finer grids for large values of Peclet numbers and slip parameters. Furthermore the CPU time for convergence with the grid 90 × 60 is several folds larger than that with the grid 60 × 30. Thus the moderately fine grid 60 × 30 has been chosen for all other computations.

Table 5.21 Effect of grid size on Nu_{avg} of assemblages of spheres of Φ = 0.1 at Re = 200

Grid size (θ-× r-)	λ = 0.01		λ = 100	
	Pr = 1	Pr = 50	Pr = 1	Pr = 50
30 × 30	18.6477	227.0813	13.9693	67.4344
60 × 30	18.4539	209.0477	13.8302	68.5843
90 × 60	18.4891	209.1867	13.7711	60.2986

Table 5.22 Effect of grid size on Nu_{avg} of assemblages of spheres of Φ = 0.1 at Re = 200

Grid	n = 0.5				n = 1.6			
(θ- × r-)	λ = 0.01		λ = 100		λ = 0.01		λ = 100	
	Pr = 1	Pr = 50	Pr = 1	Pr = 50	Pr = 1	Pr = 50	Pr = 1	Pr = 50
30 × 30	19.306	122.681	15.358	70.946	18.225	118.712	12.818	69.673
60 × 30	18.657	120.319	15.006	70.241	18.065	116.519	12.695	67.358
90 × 60	18.349	119.845	15.103	69.747	18.014	116.035	12.648	67.059

5.4.2. Validation

Table 5.23 Comparison of present values of Nu_{avg} with literature values for different volume fractions at $\lambda \to \infty$ (no-slip solid spheres)

Re	Pe	Φ = 0.1		Φ = 0.5	
		Pfeffer and Happel [332]	Present	Pfeffer and Happel [332]	Present
1	10	4.103	4.294	9.634	9.734
	50	6.251	6.535	11.143	11.165
100	100	-	-	13.657	13.235

Table 5.23 represents a comparison of the present values of average Nusselt numbers of the assemblages of no-slip spheres ($\lambda \to \infty$) of volume fractions Φ = 0.1 and Φ = 0.5 at Re = 1 and Re = 100 with the analytical results of Pfeffer and Happel [332]; and here too the agreement between two values is excellent. Therefore, on the basis of present comparisons, it can be concluded that the present solver is reliable and accurate within ±4-5% of deviations.

RESULTS AND DISCUSSIONS

6.1. Momentum Transfer Study of a Single Spherical Particle in Newtonian Fluids

The range of the pertinent dimensionless parameters considered C_d for delineating their effects on the flow and drag behavior of a spherical particle in Newtonian fluids with velocity slip at the interface are: Re = 0.1, 1, 10, 20, 50, 100, 200 and λ = 0.01, 0.1, 1, 2, 5, 10, 50, 100.

6.1.1. Flow pattern

Figure 6.1 shows the effect of slip parameter on streamline (upper half) and iso-vorticity (lower half) contours around a single spherical particle in Newtonian fluids at Re = 1. In this figure maximum and minimum values of stream function and iso-vorticity are depicted. The difference between values of any two consecutive streamlines and iso-vorticity contours is 0.1. It can be observed from this figure, the streamline are remain symmetric around a single spherical particle without any flow separation at all values of slip parameters. Indeed the difference in streamline patterns are indistinguishable by changing the slip parameter from one value to other indicating the effect of slip number on streamlines is insignificant at Re = 1. The iso-vorticity is also uniformly distributed around the sphere in the radial direction for all values of the slip parameter; but as the value of the slip parameter gradually increases, more amount of vorticity contours are created around the sphere because the surface of the sphere gradually turns into finite slip surface from infinite slip surface. **Figure 6.2** shows the effect of slip parameter on streamlines (upper half) and vorticity (lower half) contours around a single spherical particle at Re = 200. The

maximum and minimum values of stream function and iso-vorticity are displayed in the figure. The difference between values of any two consecutive streamlines and iso-vorticity contours is 0.1. It can be observed from this figure that there is no flow separation and the streamlines are attached to the surface of the sphere for the value of slip parameter $\lambda \leq 1$.

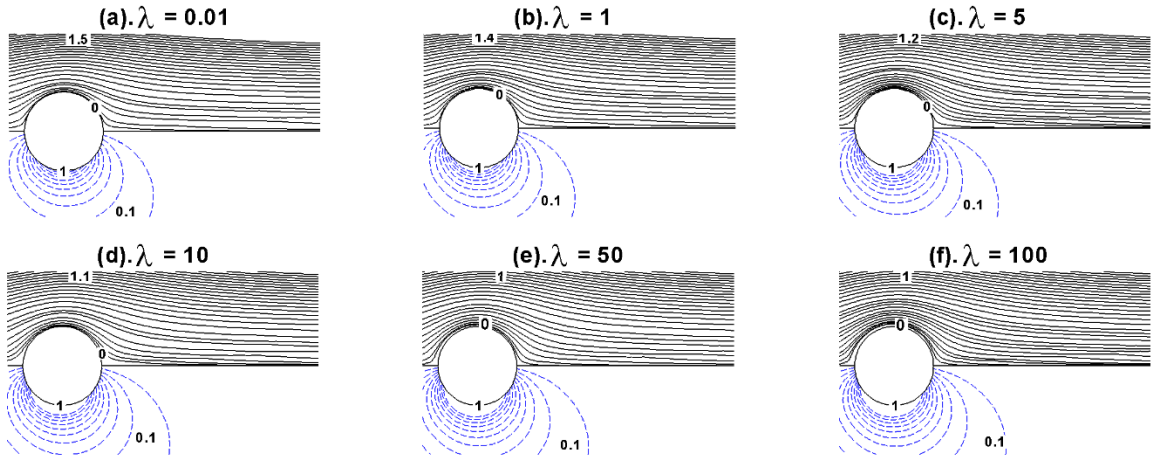

Figure 6.1 Streamlines (upper half) and vorticity contours (lower half) around a sphere in a Newtonian fluid at *Re* = 1 for different values of λ.

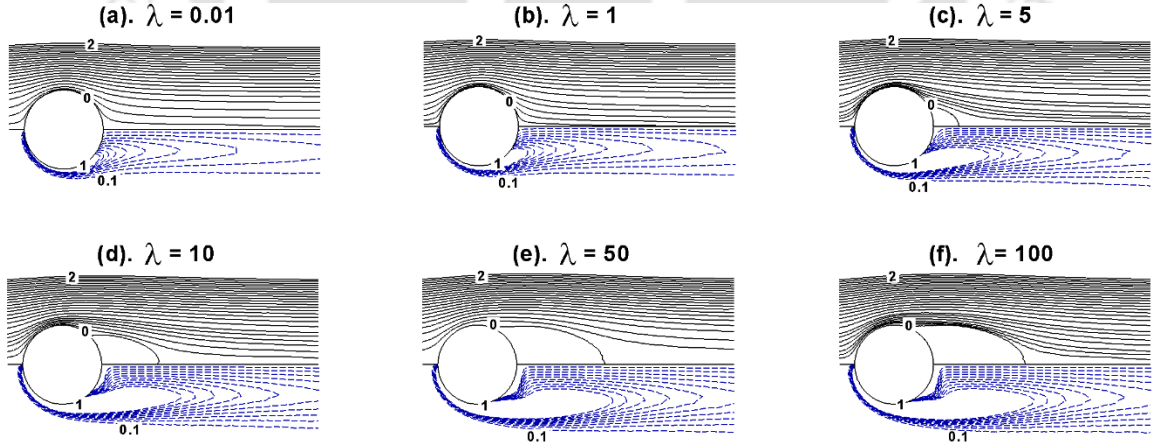

Figure 6.2 Streamlines (upper half) and vorticity contours (lower half) around a sphere in Newtonian fluid at *Re* = 200 for different values of λ.

Hence for small values of slip parameter, the flow pattern is similar to the case of infinite slip flow past spherical bubble. A recirculation wake appears at the rear end of the sphere and the flow is separated as the value of the slip parameter increases to $\lambda = 5$. Because of increasing slip parameter, immobility of fluid on the surface of sphere increases which lead to increase in vorticity which ultimately lead to flow separation at the rear end of the sphere. The size of the recirculation wake increases with increasing the value of slip parameter. From the iso-vorticity contours, for all values of slip parameter the vorticity is being carried away in the flow direction; however a small void is appeared at the rear end of the sphere at $Re = 100$ for $\lambda \geq 5$ which is because of the formation of recirculation wake. Further increasing the value of slip parameter the size of this void increases because the amount of vorticity being generated increases with slip parameter.

6.1.2. Surface pressure distribution

Figure 6.3 presents the effects of Reynolds number and slip parameter on the distribution of pressure coefficient (C_p) along the surface of a spherical particle in Newtonian fluids. At $Re = 0.1$, regardless the values of slip parameter, the pressure coefficient is maximum at the front stagnation point, as one traverses from front stagnation point it gradually decreases to a minimum value at rear stagnation point. Whereas for Reynolds number, $Re \geq 10$, irrespective values of slip parameter, as one traverses from front stagnation point to rear stagnation point, the value of the pressure coefficient is maximum at the front stagnation point and it gradually decreases to a minimum value at around equator of the spherical particle and again gradually increases at the rear stagnation point of the sphere because of pressure recovery. For all values of Reynolds number, at the front stagnation point of the sphere the value of pressure coefficient decreases with decreasing slip parameter whereas the reverse trends observed at rear stagnation

point of the sphere. Further for $Re \geq 20$, the minimum value of pressure coefficient at around equator decreases with the decreasing slip parameter. Further the difference between pressure coefficient values at front and rear stagnation point increases with the increasing slip parameter.

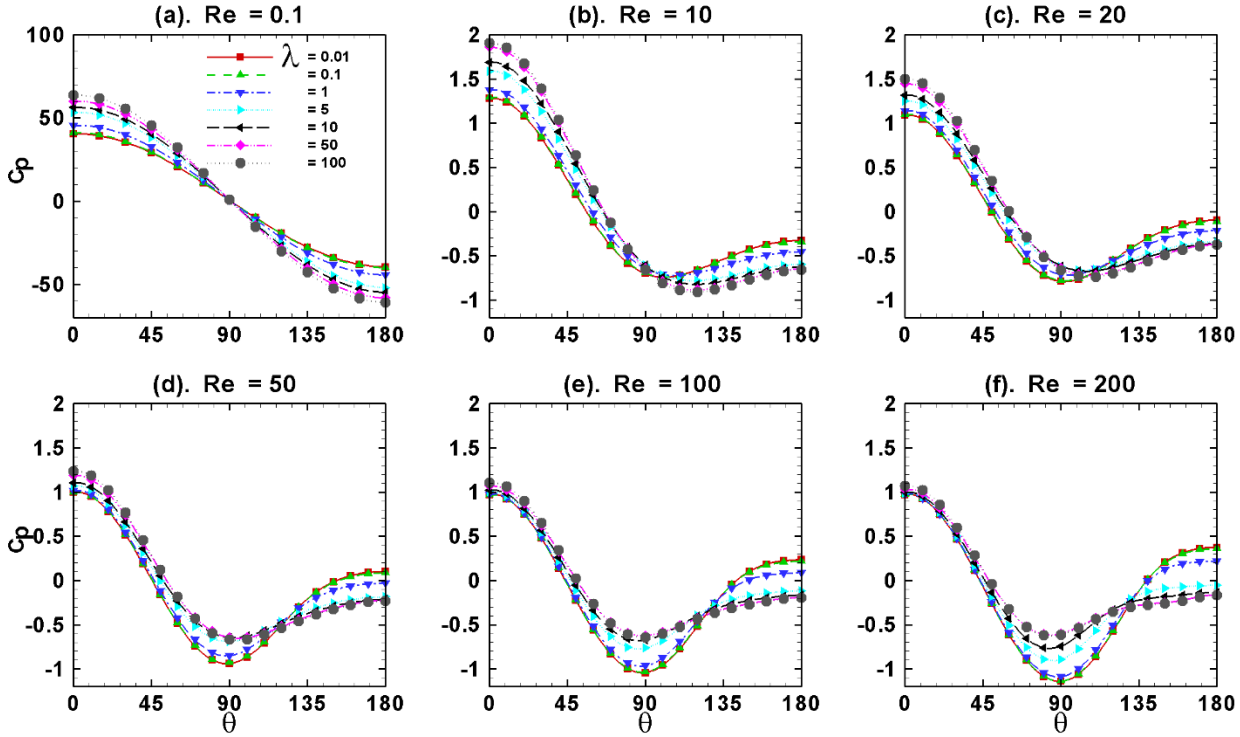

Figure 6.3 Surface pressure coefficient distributions along the surface of a sphere in Newtonian fluids at different Reynolds number and slip parameter.

6.1.3. Surface velocity distribution

Figure 6.4 shows the influence of Reynolds number and slip parameter on the distribution of tangential velocity (v_θ) along the surface of the slip sphere in Newtonian fluids. There is no flow separation at $Re \leq 20$ for any value of slip parameter. Thus at all values of the slip parameter as one traverses along the surface of sphere the tangential velocity is zero at front stagnation point and the tangential velocity gradually increases to some maximum value at around equator of the sphere and again gradually decreases to zero value at the rear stagnation point.

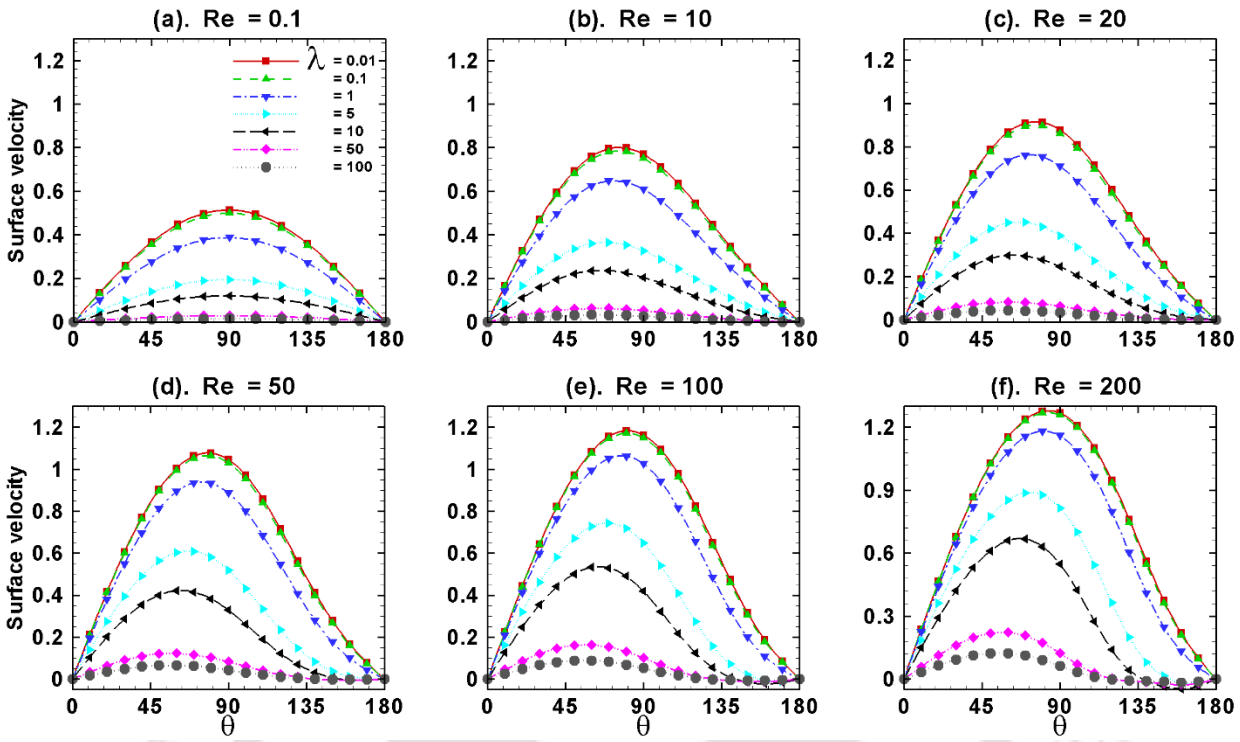

Figure 6.4 Surface velocity distributions along the surface of a sphere in Newtonian fluids at different Reynolds number and slip parameter.

However, the maximum value of tangential velocity at around equator is large for $\lambda = 0.01$ and because of decrease in slip (or increasing immobility) the tangential velocity decreases as the value of slip parameter increases. Further similar effects on tangential velocity are observed at $Re \geq 20$ for $\lambda \leq 5$ because of no flow separation in this range of Reynolds number and slip parameter. Because of presence of recirculation wakes (for $\lambda \geq 5$), in the rear end of the slip sphere, the tangential velocity exhibits a secondary curve. The size of the secondary curve increases with the increasing slip parameter.

6.1.4. Surface vorticity distribution

Figure 6.5 shows the variation of the surface vorticity at different value of Reynolds number and slip parameter for Newtonian fluid. For the range of Reynolds number $0.1 \leq Re \leq 20$ and slip

parameter $0.01 \leq \lambda \leq 1$, the surface vorticity around sphere increases from zero value at front stagnant point to a certain large value at around equator and then gradually decreases to its zero value at the rear stagnation point.

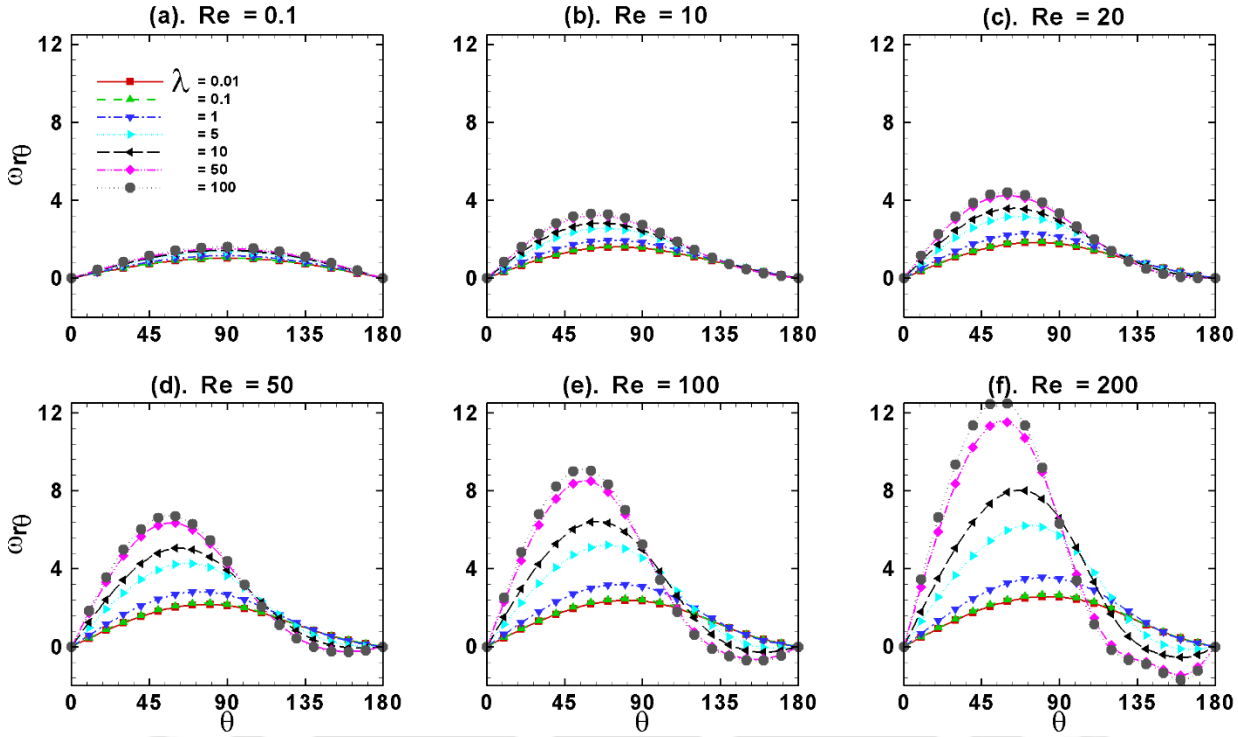

Figure 6.5 Surface vorticity coefficient distributions along the surface of a sphere in Newtonian fluids at different Reynolds number.

Whereas for range Reynolds number $50 \leq Re \leq 200$ and slip parameter $5 \leq \lambda \leq 100$, the surface vorticity around slip sphere increases from zero value at front stagnant point to a certain large value at around equator, then gradually decreases until the point of flow separation. At the rear end because of flow detachment a secondary wake form and negative value at the point of flow separation and finally recovers to its zero value at the rear stagnation point. The surface vorticity exhibits complete fore and aft symmetry for all values of slip parameter λ. For all values of the Reynolds number, the surface vorticity value is maximum for $\lambda = 100$ because of less degree of

fluid slip at solid surface and it is minimum for λ = 0.01 due to the maximum degree of fluid slip at solid surface. For intermediate values of λ, the vorticity distribution is in the interim of the two vorticity curves for the case of λ = 0.01 and λ = 100.

6.1.5. Drag phenomena

Figure 6.6(a) presents the combined effects of the Reynolds number (*Re*) and slip parameter (λ) on pressure drag coefficients (C_{dp}), friction drag coefficient (C_{df}), drag ratio (C_{dp}/C_{df}) and total drag (C_d) of a single sphere in Newtonian fluids. For all values of λ, the value of pressure drag coefficient decreases with the increasing Reynolds number. **Figure 6.6(b)** presents the combined effects of Reynolds number and slip parameter on friction drag coefficient (C_{df}) of a sphere in Newtonian fluid. Here too, regardless of values of the slip parameter, the friction drag coefficient decreases with the increasing Reynolds number. **Figure 6.6(c)** presents the effect of Reynolds number and slip parameter on drag ratio of a sphere in Newtonian fluid. For all values of λ, the value of pressure drag coefficient increases with the increasing Reynolds number. **Figure 6.6(d)** shows the combined effects of the Reynolds number and slip parameter on the total drag coefficient (C_d) of unbounded sphere in Newtonian fluid. Qualitatively trends are similar to the friction drag coefficient trends (**Figure 6.6(a-b)**); For Newtonian fluids, as the value of the slip parameter decreases the drag coefficient decreases because the slipping nature of particle surface increases with decreasing slip parameter and this slippery behavior reduces the resistance for fluid to flow past slip sphere of small λ value.

From the engineering applications view point, a correlation for the C_d of a sphere in Newtonian fluids can be very useful in real life applications and thus on the basis of present numerical simulations following form of the empirical correlation is found to be suitable:

$$C_d = \frac{18}{Re^{0.9}}\left[1+0.279\lambda^{0.237}\right]+0.167\lambda^{0.31} \qquad (6.1)$$

The above equation reproduces the present numerical simulations with an average error of ±8.08% which rises to a maximum of 22.81% for extreme values of the slip parameter.

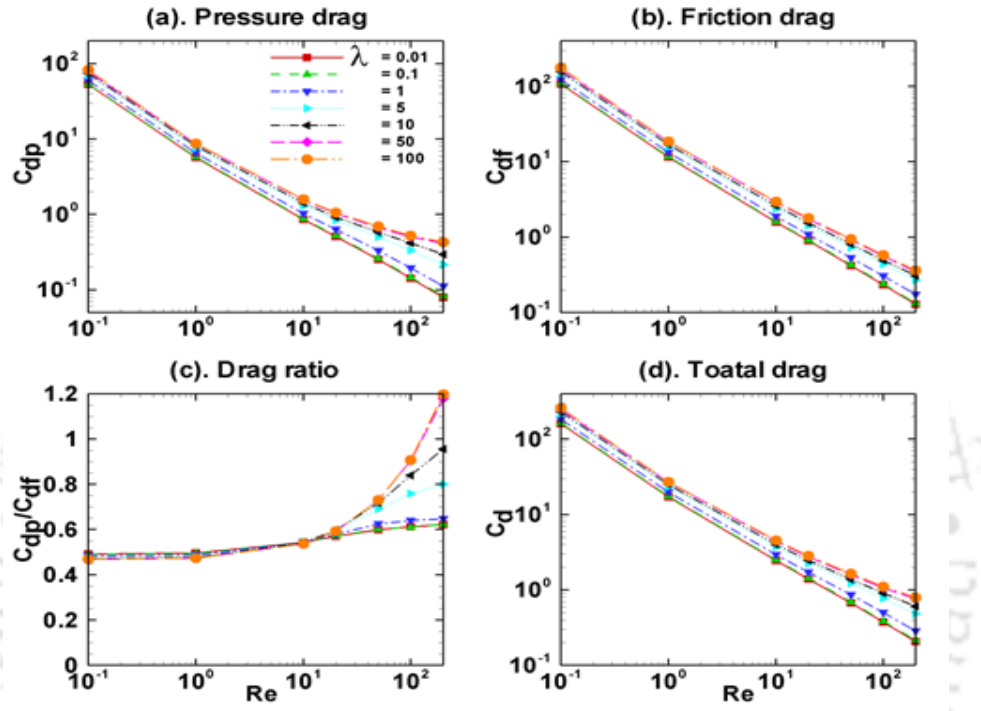

Figure 6.6 Pressure drag coefficients (C_{dp}), friction drag coefficient (C_{df}), drag ratio (C_{dp}/C_{df}) and total drag (C_d) of a single sphere in Newtonian fluids at different values of slip parameter.

6.2. Momentum Transfer Study of a Single Spherical Particle in Power-law Liquids

The values of the present pertinent dimensionless parameters consider to delineate their effects on the flow and drag behavior of a single spherical particles in power-law liquids with velocity slip at the interface are: Re = 0.1, 1, 10, 20, 50, 100, 200, n = 0.5, 0.6, 0.8, 1, 1.2, 1.4, 1.6, and λ = 0.01, 0.1, 1, 2, 5, 10, 50, 100.

6.2.1. Flow patterns

Figure 6.7 shows the streamline (upper half) and iso-vorticity (lower half) contours around a single sphere with varying dimensionless slip parameter in a shear-thinning power-law liquids of n = 0.5 at Re = 100. In this figure maximum and minimum values of stream function and iso-vorticity are shown. The difference between values of any two consecutive streamlines is 0.1 and similarly difference between values of any two consecutive iso-vorticity contours is also 0.1. It can be seen from this figure that for slip parameter $\lambda \leq 1$, there is no flow separation and the streamlines are attached to the surface of the sphere. Thus for small values of slip parameter, the flow pattern is similar to the case of fully-slip flow past a spherical bubble. As the value of the slip parameter increases to λ = 5, a recirculation wake appears at the rear end of the sphere and the flow is separated. Because of increasing slip parameter, the surface immobility increases which leads to increased vorticity which eventually separates the flow in the rear of the slip sphere. Further increase in slip parameter, the size of the recirculation wake increases; and for λ = 100, the size of the recirculation wake is close to that of no-slip flow past a sphere in a power-law fluid of n = 0.5. From the iso-vorticity contours, it can be seen that the vorticity is being carried away in the flow direction for all values of slip parameter; however, for $\lambda \geq 5$, a small void is formed in the rear end of the sphere which is because of the formation of recirculation wake. The size of this void increases with the increasing slip parameter because the amount of vorticity being generated increases with λ. **Figures 6.8** and **Figures 6.9** shows the streamline (upper half) and iso-vorticity (lower half) contours around a single slip sphere in a Newtonian (n = 1) and in a shear-thickening power-law liquids of n = 1.6 at Re = 100 for different values of the slip parameter. In these Figures as well, the minimum and maximum values of the stream function and iso-vorticity contours are shown. The difference between values of two consecutive

stream functions is 0.1 and the difference between two consecutive iso-vorticity contours is 0.1. Qualitatively similar behaviors in flow patterns are observed as in the case of n = 0.5 (**Figure 6.7**); however, the size of the recirculation wake decreases with the increasing power-law index for a given value of slip parameter.

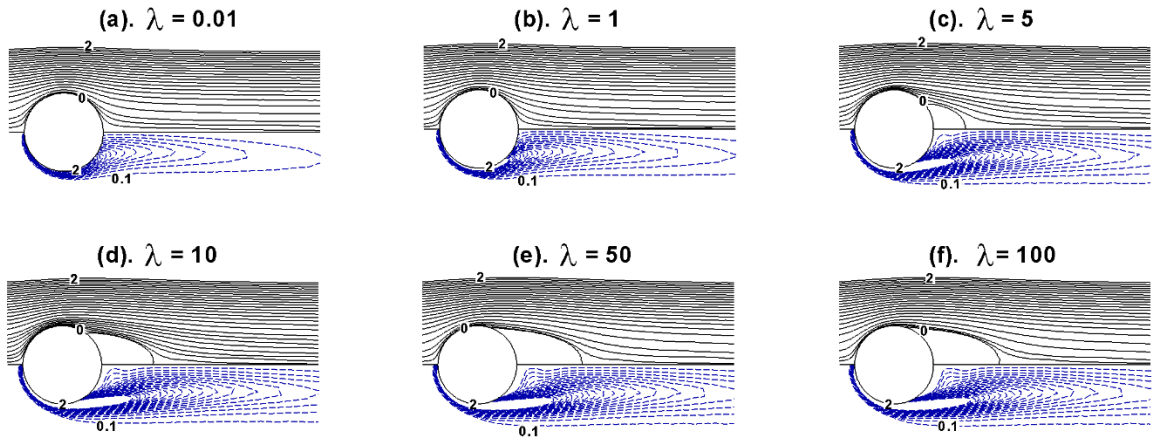

Figure 6.7 Streamlines (upper half) and vorticity contours (lower half) around a sphere in a power-law fluid of n = 0.5 at Re = 100 for different values of λ.

The effects of slip parameter (λ), power-law index (n) and Reynolds number (Re) on the length of recirculation wake (L_r) and flow separation angle (θ_s) are summarized in **Figures 6.10** and **Figures 6.11**. It can be seen from **Figures 6.10** that for all values of the power-law index, the size of the recirculation wake increases with the increasing slip parameter (i.e., towards no-slip condition) and/or with the increasing Reynolds number; however, increase in the size of recirculation wake is very small for the case of λ = 5 as Re increasing from Re = 100 to Re = 200. For a given value of slip parameter, the recirculation wake length shows mixed behavior with respect to power-law index; however, for a given value of Reynolds number, the recirculation wake length decreases with the increasing power-law index. Further the separation angles in **Figure 6.11** are measured from the rear stagnation point; and for all values of power-law indices,

this angle increases with the increase in Reynolds number and/or slip parameter except for the case of $\lambda = 5$.

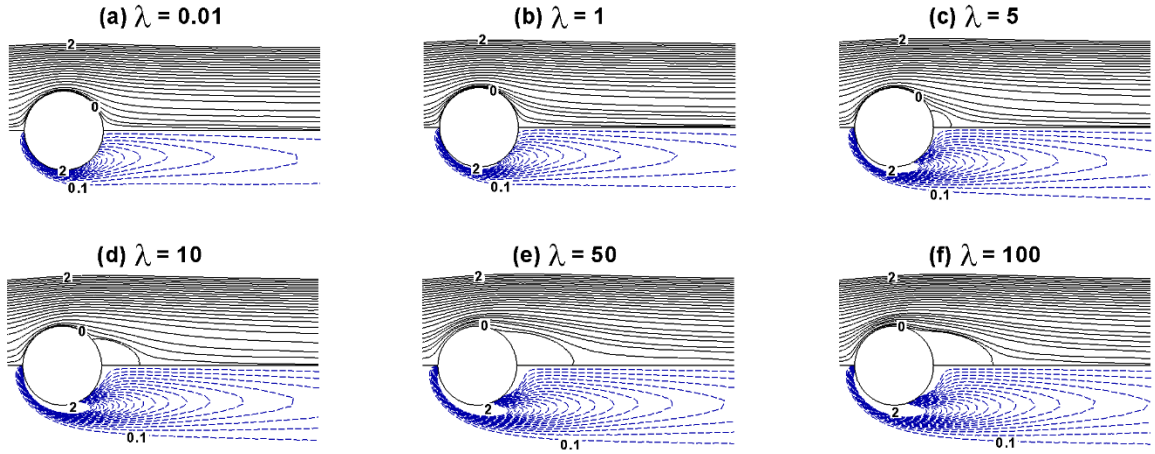

Figure 6.8 Streamlines (upper half) and vorticity contours (lower half) around a sphere in a Newtonian fluid ($n = 1$) at $Re = 100$ for different values of λ.

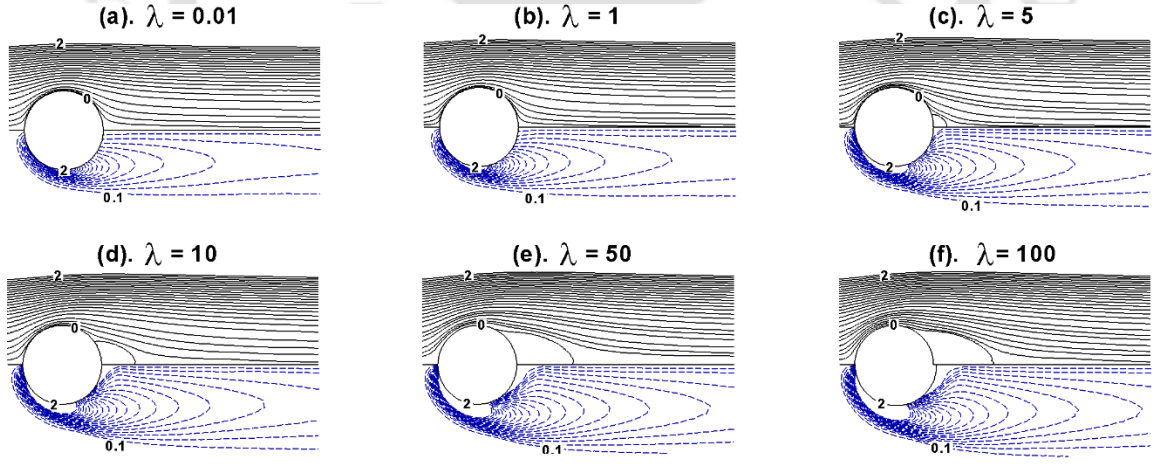

Figure 6.9 Streamlines (upper half) and vorticity contours (lower half) around a spheres in a power-law fluid of $n = 1.6$ at $Re = 100$ for different values of λ.

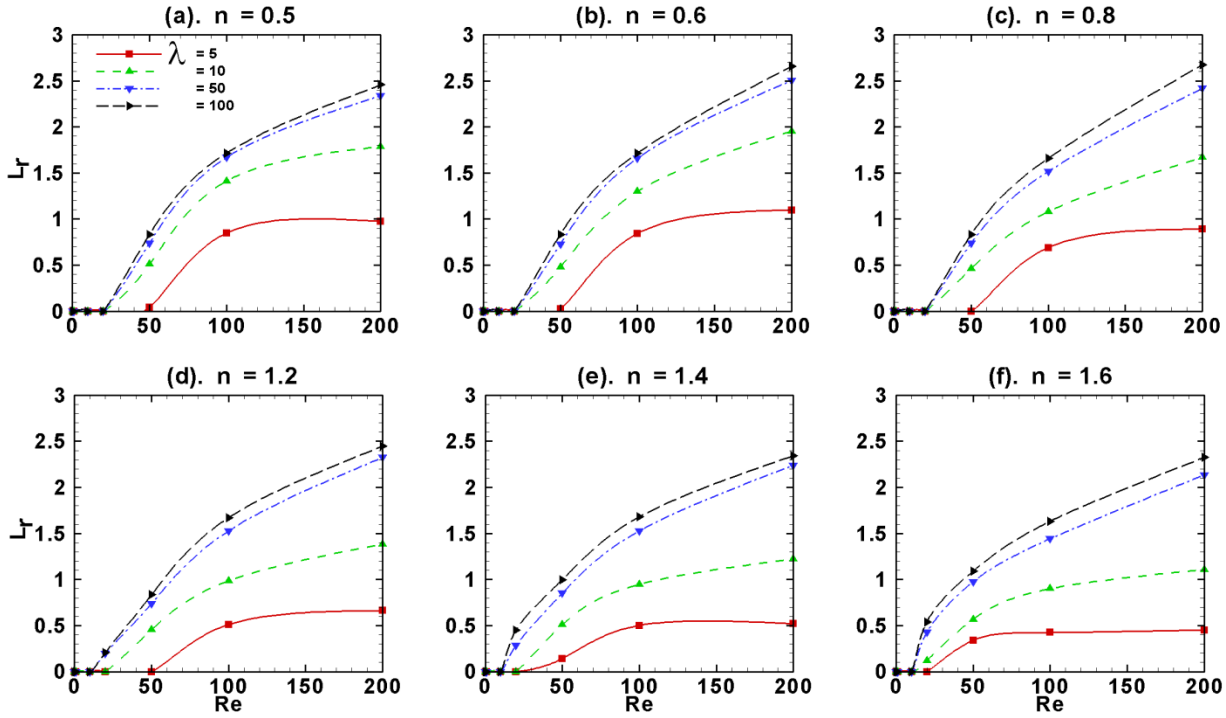

Figure 6.10 Recirculation length (L_r) versus *Re* for various combinations *n* and λ.

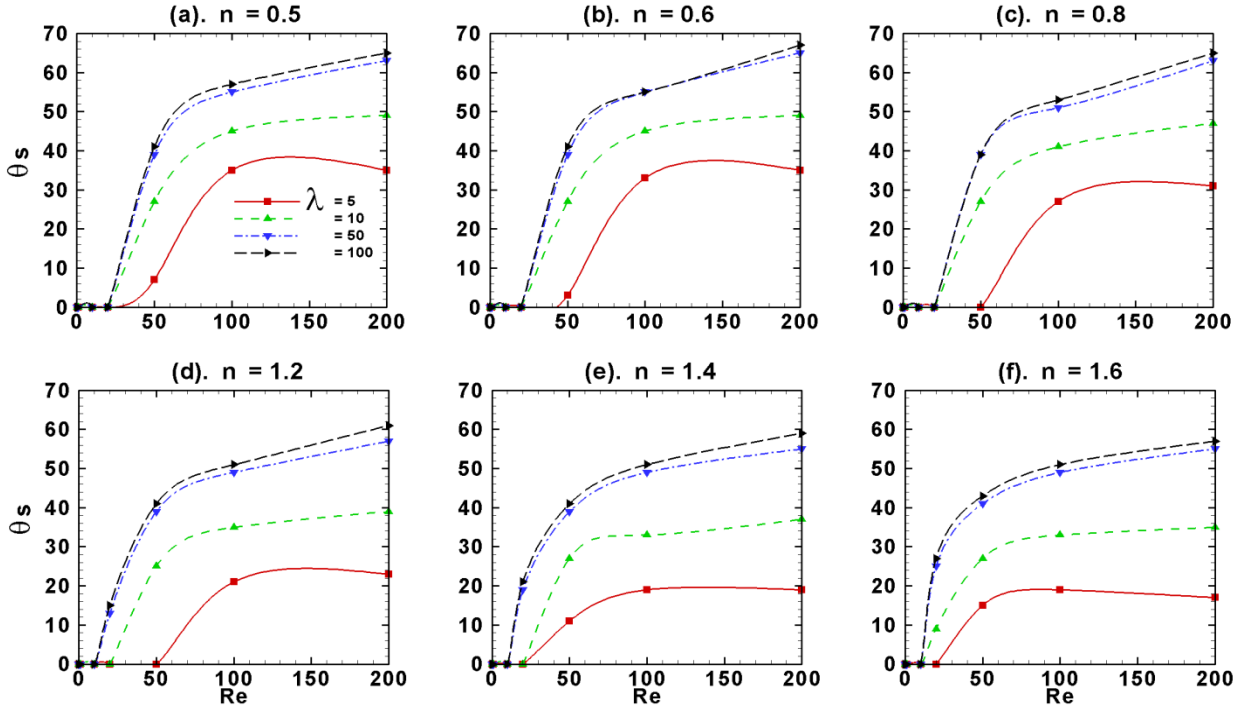

Figure 6.11 Separation angle (θ_s) versus *Re* for various combinations of *n* and λ.

6.2.2. Surface pressure distribution

Figure 6.12 presents the distribution of pressure coefficient (C_p) along the surface of a smooth sphere in power-law liquids at *Re* = 50 for different values of slip parameter. For a given value of power-law index, regardless of values of slip parameter, the pressure coefficient is maximum at the front stagnation point, as one traverse from front stagnation point it gradually decreases to a minimum value at around equator of the sphere and as one traverses to rear stagnation point it increases because of pressure recovery. The maximum value of pressure coefficient at front stagnation point decreases with decreasing slip parameter; whereas the value of pressure coefficient at rear stagnation point increases with decreasing slip parameter, and the minimum value of pressure coefficient at around equator, decreases with the decreasing slip parameter. Further the difference between pressure coefficient values at front and rear stagnation point increases with the increasing slip parameter.

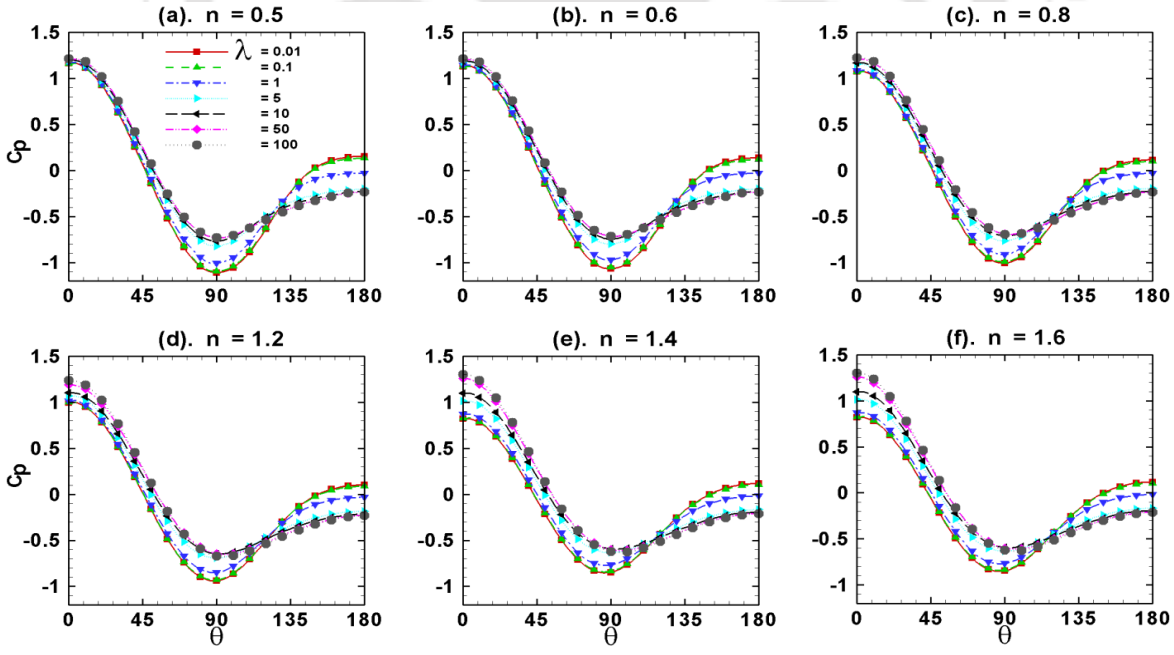

Figure 6.12 Surface pressure coefficient distribution along the surface of a sphere in power-law liquids at *Re* = 50.

6.2.3 Surface velocity distribution

Because of imposed slip velocity boundary condition along the surface of a smooth sphere, certain amount of slip velocity exists for a given value of slip parameter. Thus **Figure 6.13** shows the distribution of tangential velocity (v_θ) along the surface of the sphere in power-law liquids at Re = 20 for different slip parameters. At Re = 20, there is no flow separation for any combination of power-law index and the slip parameter. Thus, for all combinations of the slip parameter and the power-law index, the tangential velocity is zero at front stagnation point, and as one traverses along the surface of sphere, the tangential velocity gradually increases to some maximum value at around equator of the sphere and again gradually decreases to zero value at the rear stagnation point. However, the maximum value of tangential velocity at around equator is large for λ = 0.01 and because of decrease in slip (or increasing immobility) the tangential velocity decreases as the value of λ increases. Further the tangential velocity decreases with the increasing power-law index due to increasing the apparent viscosity. **Figure 6.14** shows the similar effects on tangential velocity but at Re = 200. Because of presence of recirculation wakes (for $\lambda \geq 5$), in the rear end of the slip sphere, the tangential velocity exhibits a secondary curve. The size of the secondary curve increases with the decreasing power-law index and/or with the increasing slip parameter.

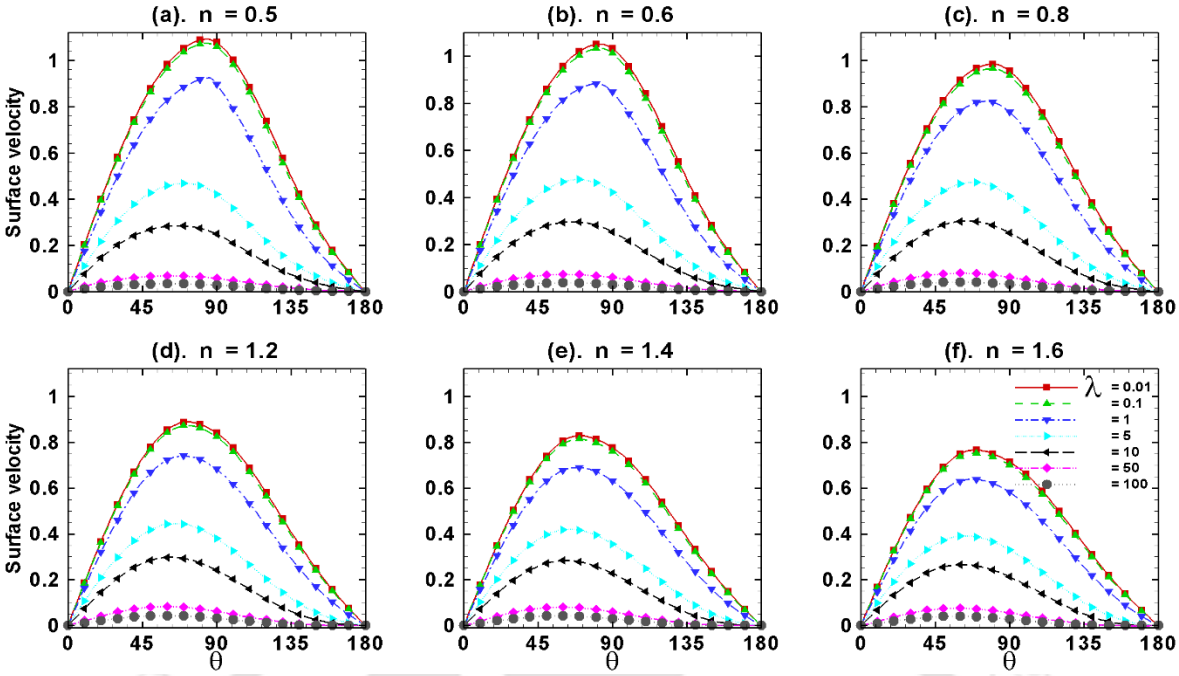

Figure 6.13 Surface velocity distribution along the surface of a sphere in power-law liquids at *Re* = 20.

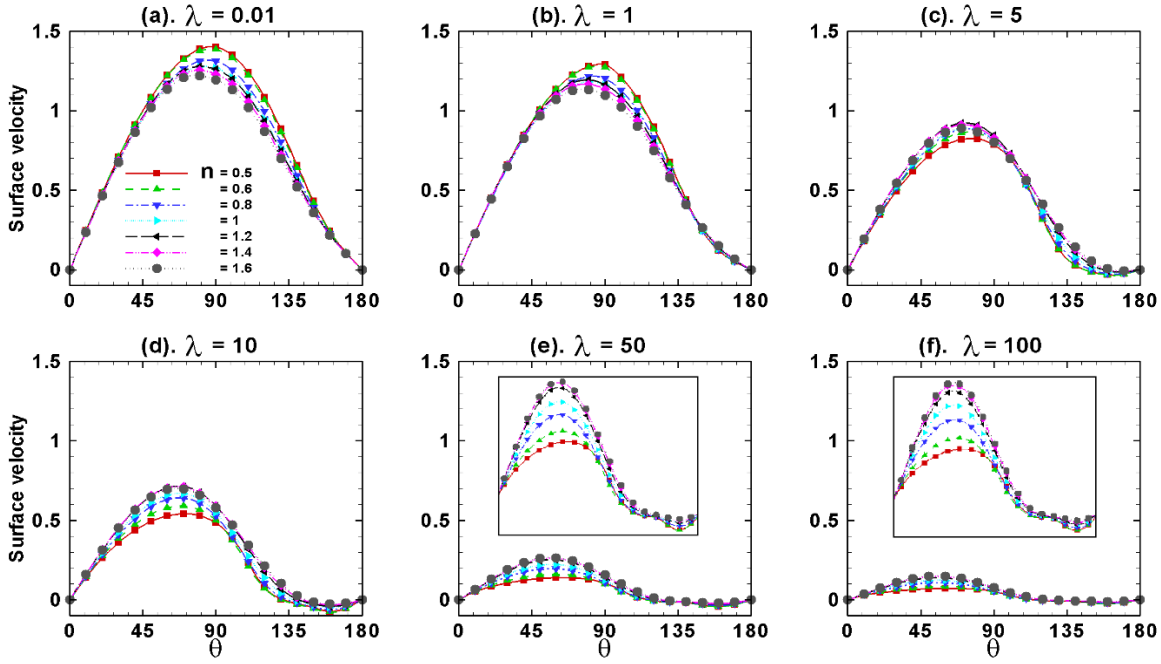

Figure 6.14 Surface velocity distribution along the surface of a sphere in power-law liquids at *Re* = 200.

6.2.4. Surface viscosity distribution

Figure 6.15 represents the viscosity distribution along the surface of a smooth sphere in power-law liquids at *Re* = 20 for different slip parameters. For shear-thinning fluids ($n < 1$), for small values of slip parameters (i.e., $\lambda \leq 1$), from front stagnation point to equator of sphere the viscosity gradually increases to attain a local maximum and again it gradually decreases as one traverses to rear stagnation point. However, for moderate to large values of slip parameter (i.e., $\lambda = 5 - 100$), from front stagnation point to equator the viscosity decreases and again it drastically increases to some maximum value at rear stagnation point. For shear-thickening fluids ($n > 1$) opposite trends are observed.

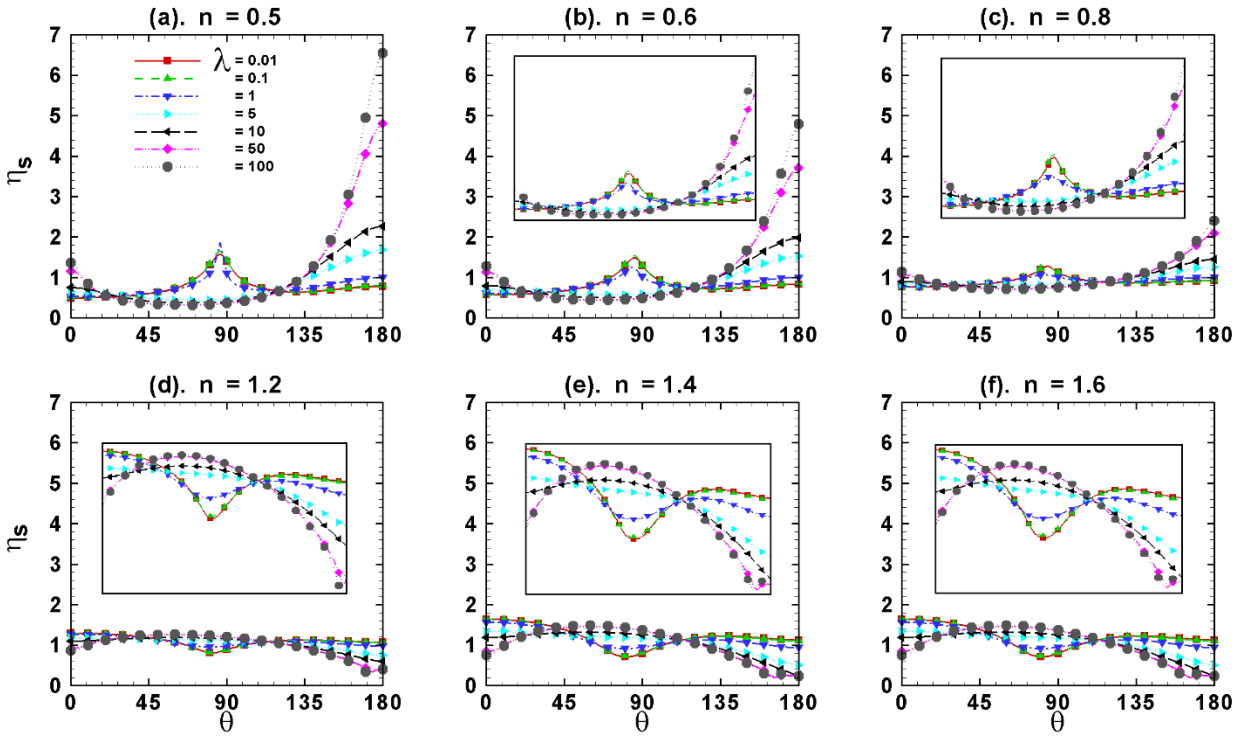

Figure 6.15 Surface viscosity distribution along the surface of a slip in power-law liquids at *Re* = 20.

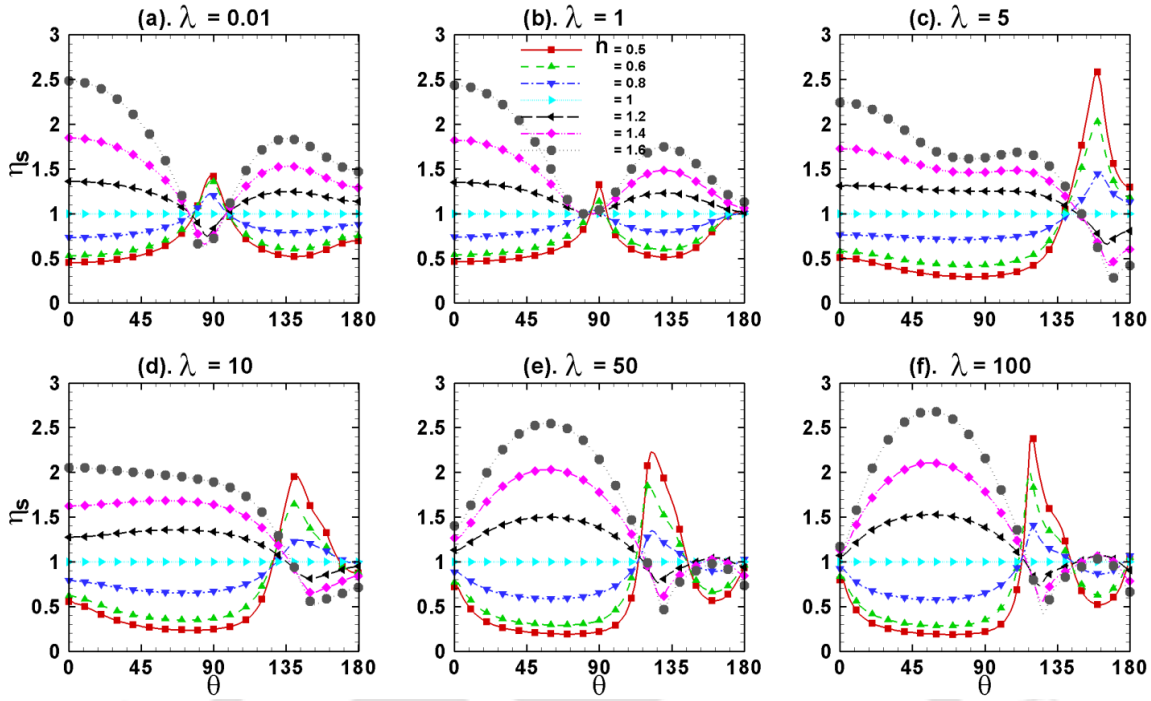

Figure 6.16 Surface viscosity distribution along the surface of a sphere in power-law liquids at *Re* = 200.

Figure 6.16 shows the effect of power-law index and slip parameter on the viscosity distribution along the surface of the sphere at *Re* = 200. For $\lambda \leq 1$ (**Figures 6.16(a-b)**), for shear-thinning fluids ($n < 1$), the trends are similar as in the case of *Re* = 20; however, for shear-thickening fluids ($n > 1$), trends are opposite compared to the cases of shear-thinning fluids. Further, for moderate to large values of slip parameters, i.e., for $\lambda = 5 – 100$, unlike in the case of *Re* = 20, both for shear-thinning ($n < 1$) and shear-thickening ($n > 1$) fluids, a secondary curve is present in the case of *Re* = 200 because of the presence of recirculation wake in the rear end of the sphere.

6.2.5. Drag phenomena

Figure 6.17 presents the combined effects of the Reynolds number (*Re*), power-law index (n) and slip parameter (λ) on pressure drag coefficients (C_{dp}) of a single smooth sphere in power-law

fluids. For all values of n and λ, the value of pressure drag coefficient decreases with the increasing Reynolds number. For $\lambda = 0.01 - 1$, for all values of the Reynolds number, as the power-law index increases the value of the pressure drag coefficient decreases. However, for slip parameter $\lambda = 5$, though for $Re < 50$, the trends are same as in the case of $\lambda \leq 1$; but for $Re \geq 50$, the effect of power-law index is almost insignificant. Further for slip parameter $\lambda \geq 10$, the C_{dp} versus Re curve exhibit a crossover Reynolds number at $Re \approx 50$, i.e., below this crossover Reynolds number the C_{dp} decreases with the increasing power-law index but a reverse trend is observed above this crossover Reynolds number.

Figure 6.18 presents the combined effects of Re, n and λ on friction drag coefficient (C_{df}) of a single smooth sphere in power-law liquids. Here too, regardless of values of the power-law index and the slip parameter, the friction drag coefficient decreases with the increasing Reynolds number. For $\lambda \geq 1$, the C_{df} versus Re curves exhibit a crossover Reynolds number which increases with the increasing slip parameter. Below this crossover Reynolds number, the value of C_{df} decreases with the increasing power-law index and reverse trend is observed for Reynolds number greater than crossover Reynolds number. **Figure 6.19** shows the combined effects of the Reynolds number, power-law index and the slip parameter on the total drag coefficient (C_d) of unbounded single smooth sphere in power-law liquids. Qualitatively trends are similar to the friction drag coefficient trends (**Figure 6.18**); however, the crossover Reynolds number does not increase with the slip parameter. For Newtonian fluids, as the value of the slip parameter decreases the drag coefficient decreases because the slipping nature of particle surface increases with decreasing slip parameter and this slippery behavior reduces the resistance for fluid to flow past slip sphere of small λ value.

Figure 6.20 shows the combined effects of slip parameter (λ), power-law index (n) and Reynolds number (Re) on normalized drag coefficient, i.e., ratio between total drag coefficient of a sphere in power-law liquidss (of different values of n) and total drag coefficient of a sphere in Newtonian fluids (n = 1). For all values of slip parameters and shear-thinning fluids (n < 1), the normalized drag coefficient decreases with the increasing Reynolds number; on the other hand, for shear-thickening fluids (n > 1) reverse trends are observed. For all values of slip parameters, the normalized drag coefficient versus Reynolds number behavior exhibits a crossover Reynolds number with respect to the power-law index of the liquids. This crossover Reynolds number is almost independent of the slip parameter.

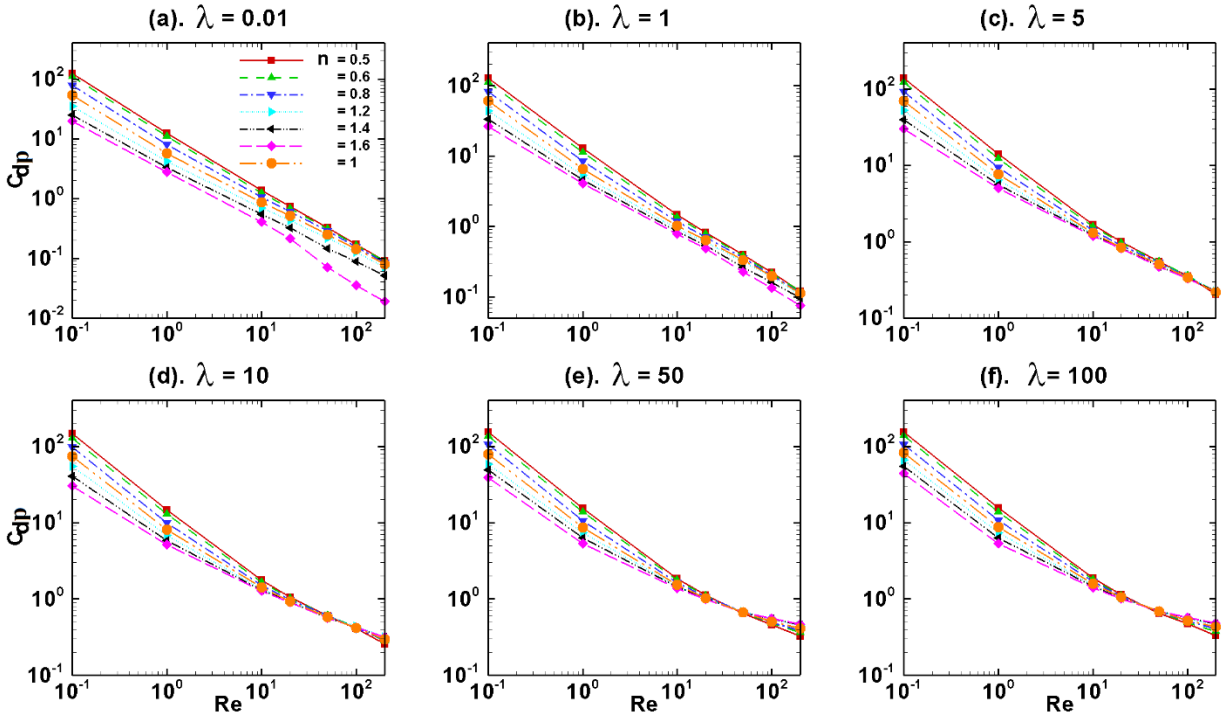

Figure 6.17 Effects of Re, n and λ on pressure drag coefficient (C_{dp}) of a single sphere.

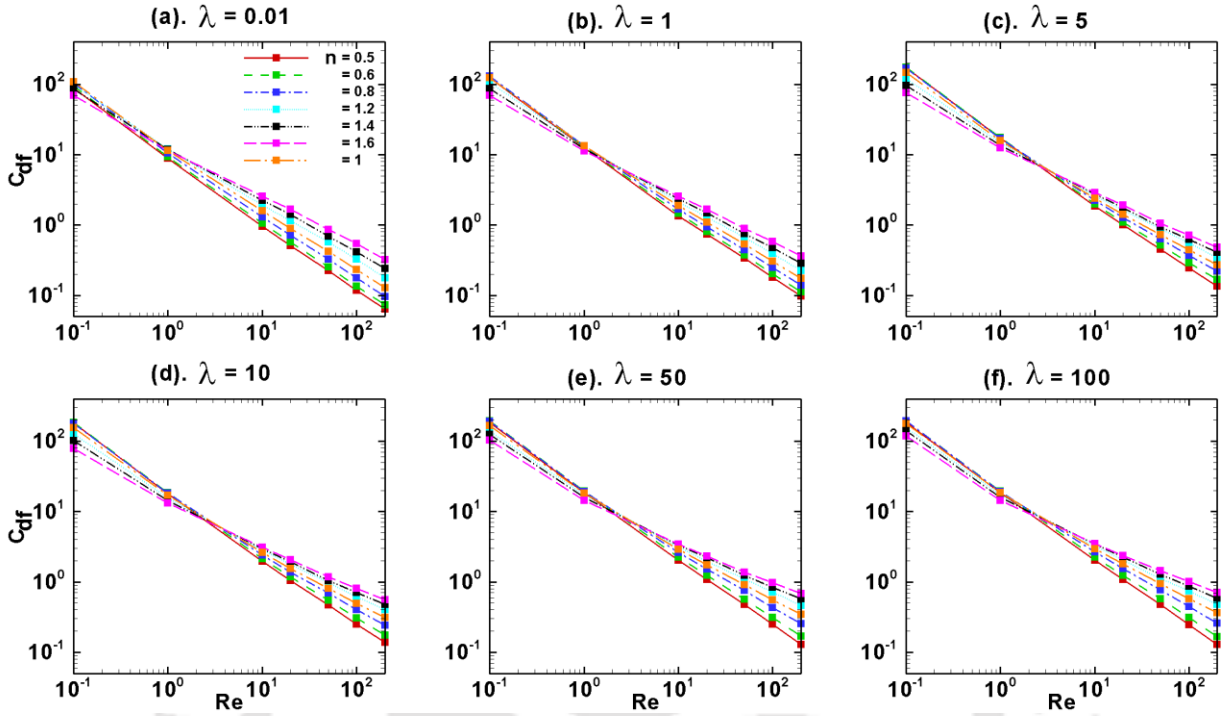

Figure 6.18 Effects of *Re*, *n* and λ on friction drag coefficient (C_{df}) of a single sphere.

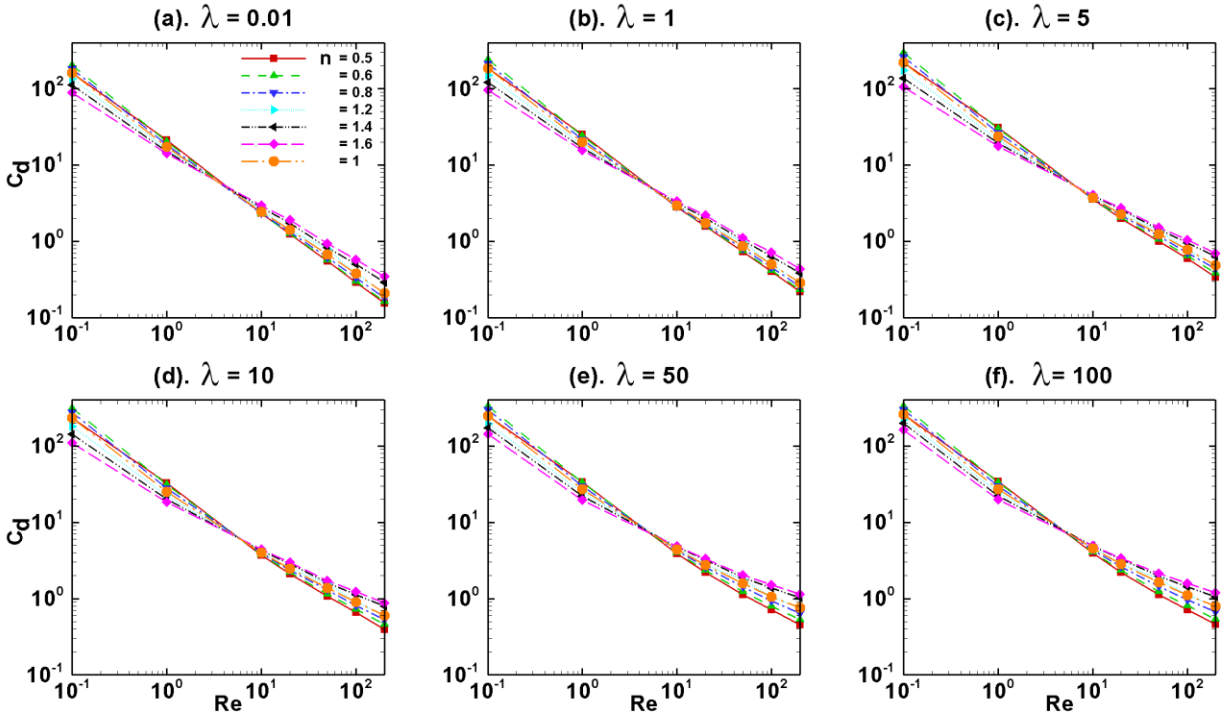

Figure 6.19 Effects of *Re*, *n* and λ on total drag coefficient (C_d) of a single sphere.

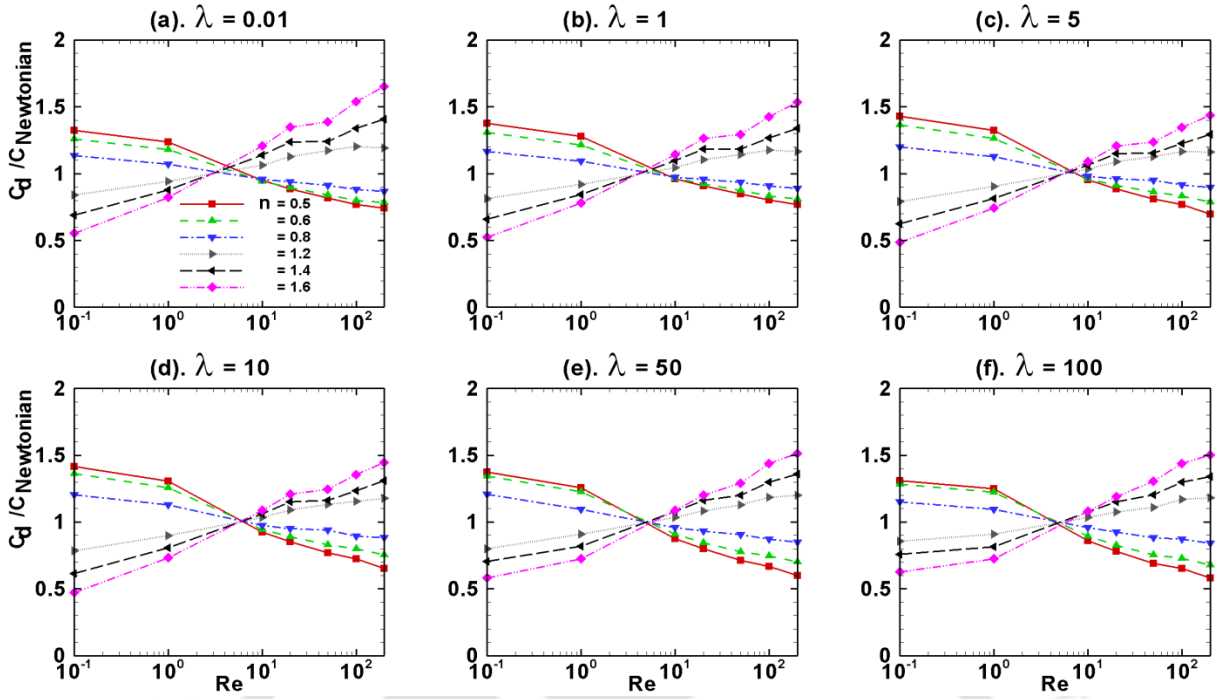

Figure 6.20 Ratio between C_d of the sphere in power-law liquids and in Newtonian liquids.

From the engineering applications view point, a correlation for the C_d of a smooth sphere in power-law liquids can be very useful in real life applications and thus on the basis of present numerical simulations (344 data points) following form of the empirical correlation is found to be suitable:

$$C_d = \frac{18.5}{Re^{(1-0.1n^{1.7})}}\left[1+\frac{0.23\lambda^{0.232}}{n}\right]+\frac{0.169\lambda^{0.31}}{n^{0.827}}-0.01\lambda^{0.1}n^{2.8} \tag{6.2}$$

The above equation reproduces the present numerical simulations with an average error of ±9.56% which rises to a maximum of 29.97% for extreme values of the power-law index and the slip parameter.

6.3. Heat Transfer Study of a Single Spherical Particle in Newtonian Fluids

The following ranges of dimensionless parameters are considered to discuss the heat transfer phenomena of a single sphere in Newtonian fluids with fluid slippage at the interface: Re = 0.1, 1, 10, 20, 50, 100, 200; Pr = 1, 10, 50, 100 and λ = 0.01, 0.1, 1, 5, 10, 50, 100.

6.3.1. Isotherm contours

Figure 6.21 presents the isotherm contours around a single sphere at Re = 1 when Pr = 1 (above the central line) and Pr = 100 (below the central line) for different values of the slip parameter. In this figure the values of the isotherm contours on the surface of sphere is 1 (i.e., the dimensionless temperature is 1 at the sphere surface) and in the free stream is zero (i.e., the dimensionless temperature at the free stream is zero). The difference between any two consecutive isotherm contours in **Figure 6.21** is 0.1. For Re = 1 and Pr = 1, because of domination of conduction mode of heat transfer compared to convection, the isotherm contours are diffused in the radial direction rather than being convected in the flow direction. Further in this case the rate of the heat transfer is very small that the dimensionless temperature of 0.2 values is very far away from the location of sphere. This trend for Re = 1 and Pr = 1 is consistent with the literature observations and is unaffected by the value of the dimensionless slip parameter. Indeed for all values of the dimensionless slip parameter, the isotherm contours are qualitatively almost similar for each value of slip parameter when Re = 1 and Pr = 1. This may be due to the negligible effect of slip velocity at such small Prandtl numbers. At these conditions the thermal boundary layer is thick and independent of the slip parameter. However, for the same Re = 1, but when the Prandtl number increases to 100 (below the central line), the significant

contribution of convective heat transfer can be seen and sufficient numbers of isotherm contours are close to the sphere surface indicating the boundary layer has become thinner with increasing Prandtl number. Further the dimensionless temperature of 0.1 value is also in the close proximity of sphere indicating the rate of heat transfer has significantly increased even at Re = 1 by the increase of Prandtl number to 100. **Figure 6.22** presents the isotherm contours around spheres for different values of the slip parameter when Pr = 1 (above the central line) and Pr = 100 (below the central line) but at Re = 20. Here too the values of isotherm contours at either extreme are depicted in the figure and the difference between any two consecutive isotherm contours is 0.1. Because of increasing the Reynolds number to 20, the contribution from convective flow is has also increased though both the diffusion and convection are not of the same order of magnitude. Because of this increasing contribution of convection flow, the isotherm contours are carried away in the flow direction for both values of the Prandtl numbers, however, for Pr = 100 more number of isotherm contours are clustered near the particle surface indicating thinning of thermal boundary layer. By comparing with Re = 1 (**Figure 6.21**), in the case of Re = 20 (**Figure 6.22**), more numbers of isotherm contours are clustering near the sphere for both values of the Prandtl number because of decreasing boundary layer thickness due to increased Reynolds number. **Figure 6.23** shows the isotherm contours in the vicinity of heated single sphere for different values of the slip parameter when Pr = 1 (above the central line) and Pr = 100 (below the central line) at Re = 100. In this figure also the limiting values of the isotherm contours are depicted and the difference between any two consecutive isotherm contours is 0.1. At Re = 100, the convection forces dominate the flow compared to the viscous forces, thus for both values of the Prandtl numbers the isotherm contours are carried in the flow direction and more numbers of isotherm contours clusters around the sphere. However, unlike in the cases of Re = 20 (**Figure**

6.22) and *Re* = 1 (**Figure 6.21**), at *Re* = 100 a recirculation wake of significant size occurs for all $\lambda > 1$; and thus because of the presence of this recirculation wake in the streamlines, the isotherm contours in the rear of the sphere are distorted and sucked towards the sphere as seen in **Figure 6.23(c)** and **Figure 6.23(d)**.

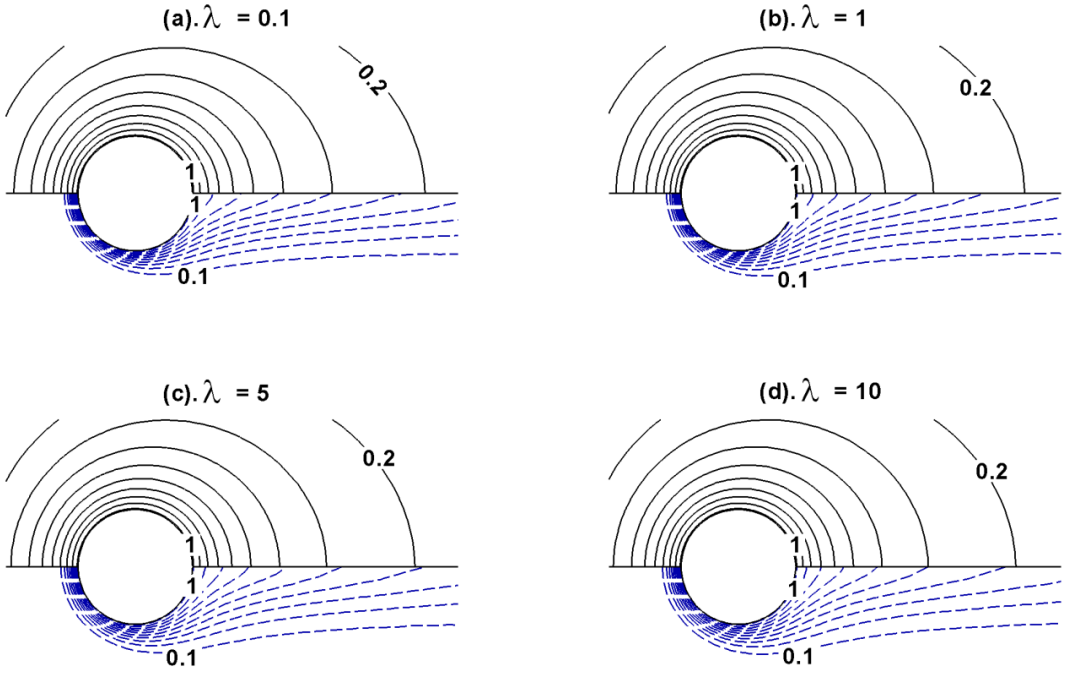

Figure 6.21 Isotherm contours around a single sphere at *Re* = 1 when *Pr* = 1 (upper half) and *Pr* = 100 (lower-half).

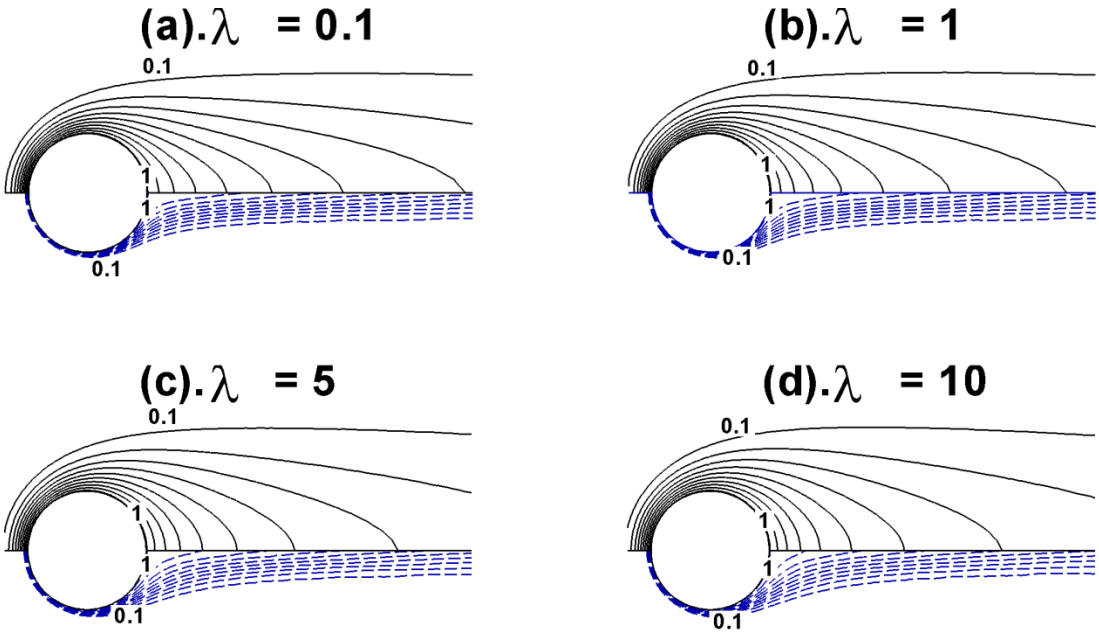

Figure 6.22 Isotherm contours around a single sphere at *Re* = 20 when *Pr* = 1 (upper half) and *Pr* = 100 (lower-half).

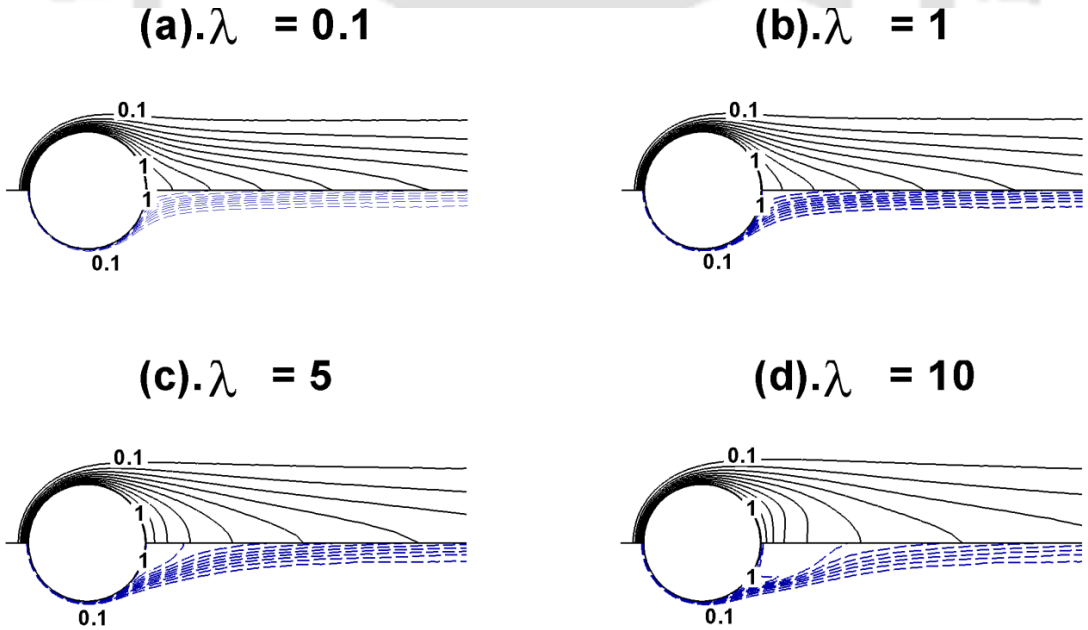

Figure 6.23 Isotherm contours around a single sphere at *Re* = 100 when *Pr* = 1 (upper half) and *Pr* = 100 (lower-half).

6.3.2. Local Nusselt number

Figure 6.24 presents the variation in values of the Nusselt number along the surface of the sphere at *Re* = 20 for different values of the Prandtl numbers as function of slip parameter. As discussed previously at *Re* = 20, for all values of the slip parameter the recirculation wake did not appear in the rear end of the sphere. Therefore, as one traverses from the front stagnation point to the rear stagnation point, the values of the local Nusselt number gradually decreases from its maximum value at the front stagnation point to some minimum value at the rear stagnation point. For *Pr* = 1 (**Figure 6.24(a)**), a crossover distribution of local Nusselt number with respect to slip parameter is observed at around $\theta \sim 130\text{-}135°$, it moves to around $\theta \sim 150°$ and $\theta \sim 165°$ as the value of Prandtl number increases to 10 (**Figure 6.24(b)**) and 50 (**Figure 6.24(c)**), respectively; however, it disappears for *Pr* = 100 (**Figure 6.24(d)**). **Figure 6.24** shows the variation of local Nusselt number for different values of the Prandtl number and slip parameter but at *Re* = 200. At *Re* = 200 the convection forces are predominant in the hydrodynamics thus significant recirculation wakes in the rear of slip spheres are observed at *Re* = 200 when $\lambda > 1$ and the size of this wake increases with the increasing slip parameter. Accordingly the variation in local Nusselt number is qualitatively similar to the case of *Re* = 20 up to the point of separation, i.e., the value of Nusselt number gradually decreases from the front stagnation point to the point of flow separation.

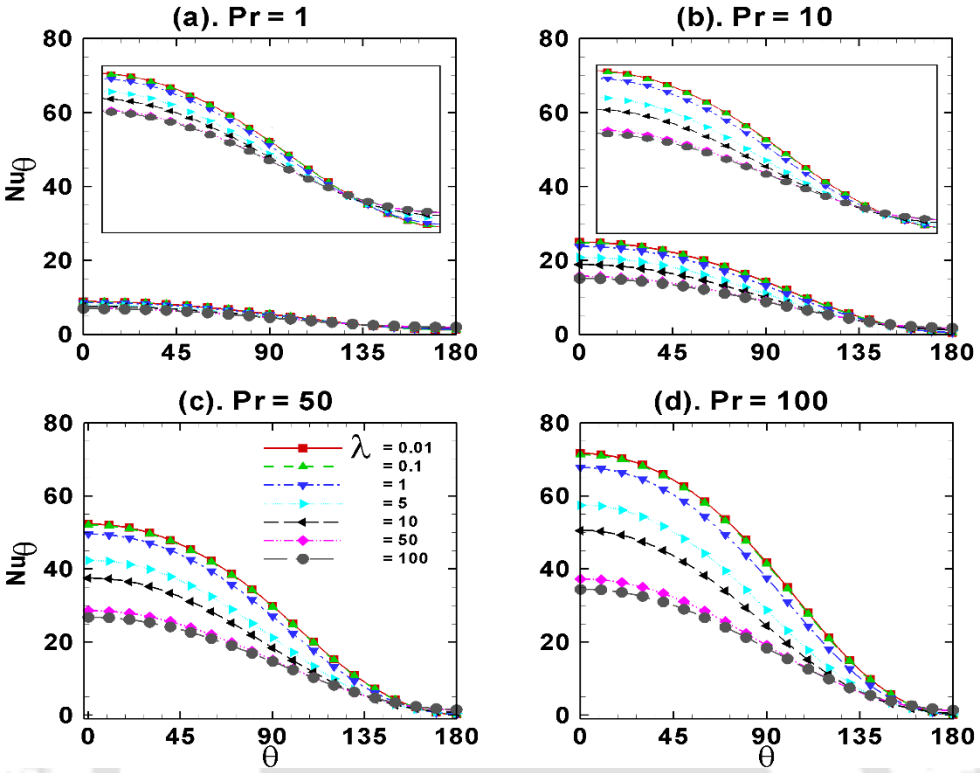

Figure 6.24 Local Nusselt number distribution along the surface of a single sphere at *Re* = 20 for different *Pr* and λ.

However, in the recirculation wake zone, the local Nusselt number increases from the point of flow separation to the rear stagnation point because of adverse pressure gradients in the wake region. Further it is observed that as the value of the slip parameter increases the value of the Nusselt number decreases at any location from the front stagnation point to the point of flow separation. However, in the remaining portion of sphere surface, i.e., from the point of flow separation to rear stagnation point a reverse trend is observed because of the adverse pressure gradients in the recirculation wake region.

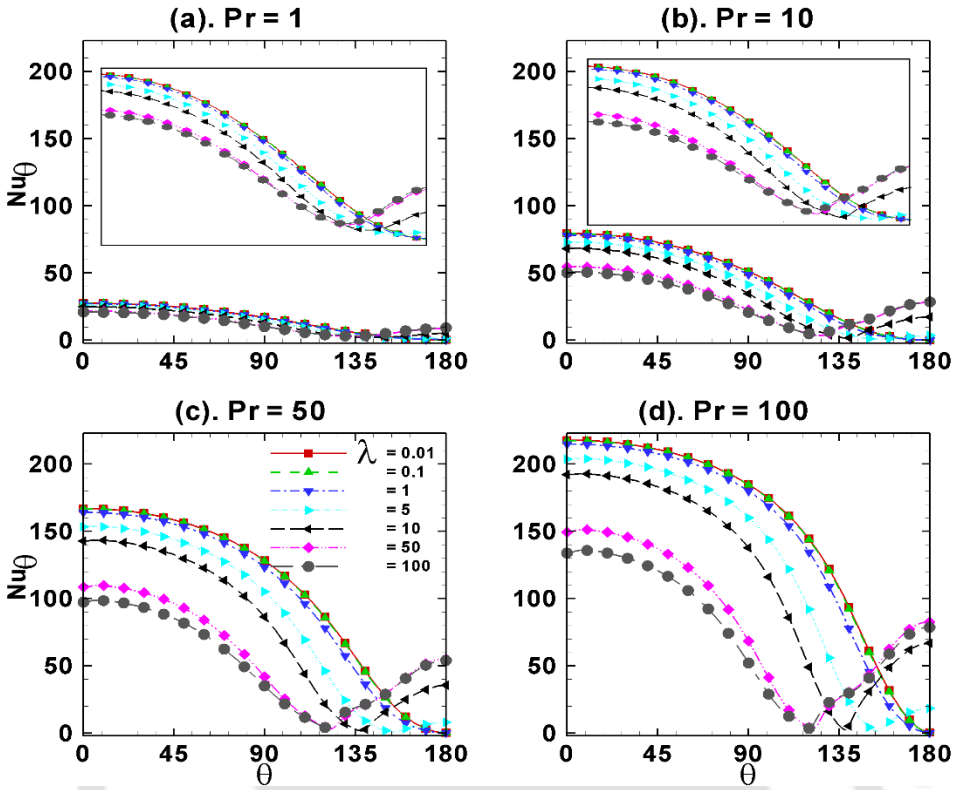

Figure 6.25 Local Nusselt number distribution along the surface of a single sphere at *Re* = 200 for different *Pr* and λ.

Figure 6.26 presents the local Nusselt number distribution along the surface of a sphere of different slip parameter at *Re* = 50 as function of Prandtl number; and qualitatively similar trends can be seen as in the case of **Figure 6.25**. However, regardless the value of the slip parameter, the local value of Nusselt number increases with the Prandtl number in both zones i.e., before and after the point of recirculation wake formation.

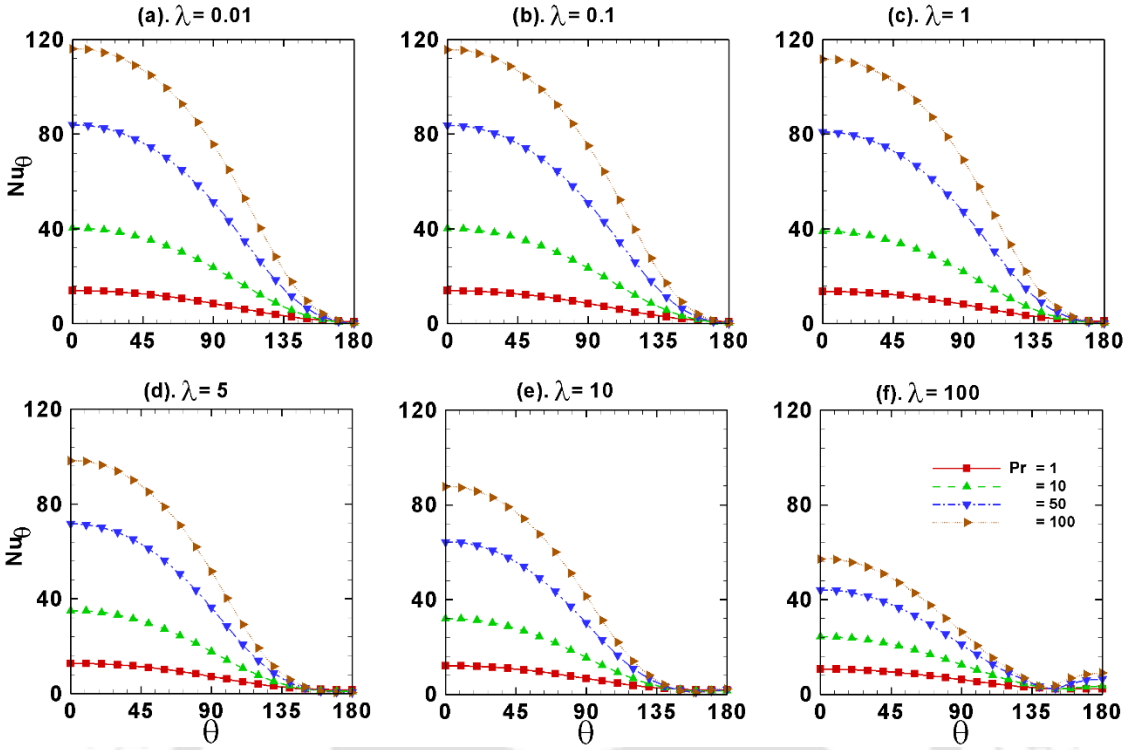

Figure 6.26 Local Nusselt number distribution along the surface of a single sphere at *Re* = 50 for different *Pr* and λ.

6.3.3. Average Nusselt number

Figure 6.27 shows the combined effects of the Reynolds number and slip parameter on the average Nusselt number versus Peclet number variations of a single sphere in Newtonian liquids. Regardless the values of the Reynolds number and the slip parameter, the value of the average Nusselt number is approximately two when Peclet number is order of 1 which indicates the rate of heat transfer is dominated by conduction under these conditions. Further regardless the values of the Reynolds number and slip parameter, the average Nusselt number increases with the increasing Peclet number because of increasing contribution from the convection. Because of the same reason, regardless the value of the slip parameter, the values of the average Nusselt number increases with the increasing Reynolds number. On the other hand, as the value of the slip parameter increases the values of average Nusselt number decreases for all value of Peclet

number > 1 because of increasing boundary layer thickness with the increasing slip parameter (i.e., from infinite slip to completely no-slip condition). In summary, the average Nusselt number increases with the increasing Reynolds/Prandtl numbers and/or with the decreasing slip parameter.

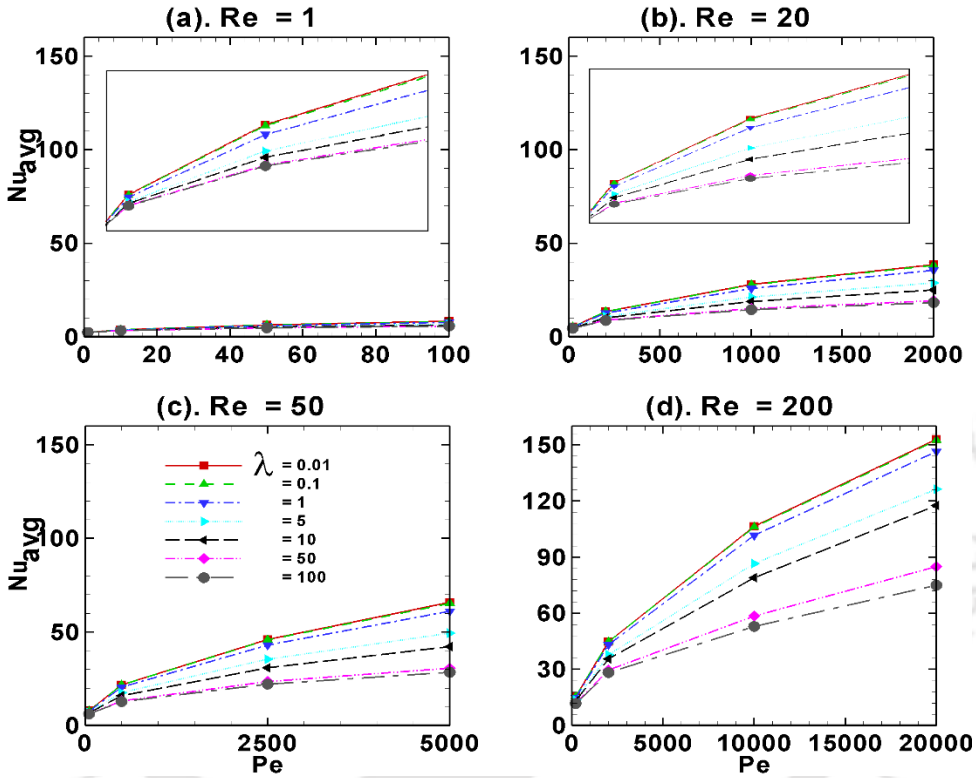

Figure 6.27 Average Nusselt numbers of a single sphere in Newtonian fluids with velocity slip at the interface.

Finally, the following simple predictive correlation for the average Nusselt number of single slip sphere in Newtonian fluids with velocity slip at the interface is developed on the basis of present numerical results.

$$Nu_{avg} = 0.869\,\mathrm{Re}^{0.505}\,\mathrm{Pr}^{0.431}\,\lambda^{-0.052} + 1.418\,\mathrm{Pr}^{0.023} \tag{6.3}$$

This correlation reproduces the present numerical results (196 data points) with an average error of ±9.82% which rises to a maximum of ±36.36% for extreme cases.

6.4. Heat Transfer Study of a Single Spherical Particle in Power-law Fluids

In this work the following range of dimensionless parameters are considered to explore the heat transfer behavior of spheres in unconfined power-law fluids with velocity slip at the interface: *Re* = 0.1, 1, 10, 20, 50, 100, 200; *Pr* = 1, 10, 50, 100; λ = 0.01, 0.1, 1, 5, 10, 50, 100; and *n* = 0.5, 0.6, 0.8, 1, 1.2, 1.4, 1.6.

6.4.1. Isotherm contours

Figure 6.28 shows the distribution of isotherm contours in the vicinity of sphere with fluid-slippage at the interface in power-law liquids of *n* = 0.5 at *Re* = 20 for *Pr* = 1 (above the central line) and *Pr* = 100 (below the central line) at different values of the dimensionless slip parameter. The minimum and maximum values of isotherm contours are depicted in the Figure and the difference between two consecutive isotherms is 0.1. For the case of $Re \leq 20$, the flow separation or recirculation wake in the rear of the sphere is not observed regardless the values of the power-law index and the slip parameter. Therefore, in **Figure 6.28** (for *Re* = 20 and all values of the Prandtl numbers), the distortion of isotherm contours are not seen for any value of the slip parameter. In the case of *Re* = 20 and *Pr* = 1 (upper half), irrespective of the values of the of slip parameters, the isotherm contours are diffused around the sphere with only little convection in the flow direction because of large contribution from the conduction mode of heat transfer and with little contribution from the convection mode of the heat transfer. On the other hand, for the case of *Re* = 20 and *Pr* = 100 (lower half), for all values of the slip parameters, the isotherm contours are clustering close to the surface of the sphere and rapidly moving in the flow direction. This is because of large contribution of the convection mode of heat transfer and small but negligible contribution from the conduction mode of heat transfer. In other words, Peclet

number is 20 and 2000 respectively in the upper and lower halves of the spheres since the Reynolds number is 20. That is by increasing the Peclet number from 20 (for Re = 20 and Pr = 1) to 2000 (for Re = 20 and Pr = 100), the momentum transfer by molecular mechanisms started dominating than the heat conduction. Furthermore, for both values of the Prandtl number, the isotherm contours slowly move towards the sphere surface with gradual increase of the slip parameter.

Figure 6.29 shows the isotherm contours around a sphere with fluid slippage at the interface in power-law liquids of n = 0.5 at Re = 100 for Pr = 1 (above the central line) and Pr = 100 (below the central line) as function of the dimensionless slip parameter. Here too minimum and maximum values of isotherm contours are depicted and the difference between any two consecutive isotherm contours is 0.1. At Re = 100 and n = 0.5, a significant size of recirculation wake is formed in the rear end of the spheres with fluid-slippage at the interface when $\lambda \geq 5$ and it increased with the slip parameter [6]. Therefore, for $\lambda = 5$ (**Figure 6.29(c)**) and $\lambda = 10$ (**Figure 6.29(d)**) at both values of the Prandtl numbers, the isotherm contours in the rear end of the sphere with slipping interface are distorted and sucked towards the sphere because of the adverse pressure gradients experienced by the sphere due to the formation of the recirculation wake. With the increasing slip parameter the magnitude of slip reduces thus the distortion of isotherm contours increases with the slip parameter. Furthermore, the degree of distortion and suction of isotherm contours towards the sphere is higher in the case of Pr = 100 because of domination of the convection. On the other hand, for $\lambda \leq 1$, the thermal boundary layer is thinner and the isotherm contours are undistorted for both values of the Prandtl number because of the fluid slip and due to absence of recirculation wake for $\lambda \leq 1$ respectively. By comparing **Figure 6.28** and **Figure 6.29**, it can be seen that the thermal boundary layer becomes thinner with the increasing

Reynolds and/or Prandtl numbers and/or with the decreasing slip parameter; and thus the rate of heat transfer increased with decreasing λ and/or increasing *Re* and/or *Pr*.

Figure 6.30 and **Figure 6.31** shows the isotherm contours in the vicinity of a single sphere with varying degree of surface slip at *Re* = 20 and *Re* = 100 respectively when *Pr* = 1 (above the central line) and *Pr* = 100 (below the central line) but in shear-thickening fluids of *n* = 1.6. The difference between any two consecutive isotherm contours is 0.1 and their minimum and maximum values are depicted in Figures. For a given combination of the slip parameter ($\lambda \geq 5$) and Reynolds number (*Re* > 20), the size of the recirculation wake in the rear of the sphere in power-law fluids decrease with the increasing power-law index, i.e., the size of recirculation wake is larger for shear-thinning fluids (*n* < 1) followed by Newtonian (*n* = 1) and shear-thickening fluids (*n* > 1). This is because of the apparent viscosity of power-law fluids which increases with the increasing power-law index for a given amount of shear-rate. Further the trends of isotherm contours of slip spheres in shear-thickening fluids (**Figure 6.30** and **Figure 6.31**) for different combinations *Re, Pr* and λ are qualitatively similar as in the case of shear-thinning fluids (**Figure 6.28** and **Figure 6.29**). However, the degree of distortion of isotherm contours in the case of shear-thickening fluids is small because of the reduced recirculation size by increasing the value of the power-law index for a given combination of the Reynolds number and the slip parameter. Furthermore the boundary layer becomes thicker as the fluid rheology changes from shear-thinning to shear-thickening nature for all possible combinations of the *Re, Pr* and λ.

In order to discuss the effect of power-law fluid rheology on the isotherm contours around sphere with velocity slip at the interface, the isotherm contours in **Figure 6.32–Figure 6.36** are plotted depicting either extreme values of the power-law index in the upper halves and

lower halves of the spheres for different combinations of the Reynolds, Prandtl and slip numbers. For instance, **Figure 6.32** depicts the isotherm contours around spheres in power-law liquids of n = 0.5 (upper half) and n = 1.6 (lower half) at Re = 10 and Pr =1 for different values of the slip parameter. Regardless the values of the slip parameters, for the case of shear-thinning fluids (n = 0.5), the isotherm contours are carried in the flow direction for a longer distance than in the case of shear-thickening fluids (n = 1.6). This is because of increasing apparent viscosity with the increasing power-law index. Similarly **Figure 6.33** shows the isotherm contours around spheres in power-law liquids of n = 0.5 (upper half) and n = 1.6 (lower half) at Re = 10 but when Pr = 100 for different values of the slip number. Qualitatively similar trends are seen as in **Figure 6.32** but the distance that isotherm contours carried in flow direction in shear-thinning fluids is slightly large compared to the case of the shear-thickening fluids. This may be ascribed to the reason that at large Prandtl numbers, the convective heat transfer is predominant compared to conduction heat transfer; and thus the rheology of fluid plays a little role. **Figure 6.33** shows the isotherm contours around spheres with slip velocity at the interface for Re = 200 and Pr = 1 in power-law liquids of n = 0.5 (upper half) and n = 1.6 (lower half) for different values of the slip parameter. At Re = 200, when $\lambda > 1$, recirculating wake appeared in the rear end of the sphere for both the cases of shear-thinning and shear-thickening fluids but for $\lambda \leq 1$, no such recirculation wakes appeared. Because of this reason, for $\lambda > 1$, isotherm contours are distorted for both the cases of shear-thinning (n = 0.5) and shear-thickening (n = 1.6) fluids. However the isotherm contours are carried forward in the flow direction for slightly large distance in the case of shear-thickening fluids (n = 1.6) than in the case of shear-thinning fluids (n = 0.5) which is a reverse case when compared to Re = 20; and the effect of fluid rheology on isotherm contours is found to be less significant for $\lambda \leq 1$. In other words, the isotherm contours are strongly sucked towards

the sphere due to which the rate of heat transfer is large in shear-thinning fluids than in shear-thickening fluids when the slip parameter is greater than unit. Similarly **Figure 6.35** shows the isotherm contours around a sphere with slip velocity at the interface in power-law liquids of n = 0.5 (upper half) and n = 1.6 (lower half) at Re = 200 but for Pr = 100; and qualitatively similar trends are seen as in **Figure 6.34** but in the case of Pr = 100 at Re = 200 a thermal void is found in the rear end and its size is significantly larger for the case of shear-thinning fluids compared to shear-thickening fluids provided the slip parameter $\lambda > 1$.

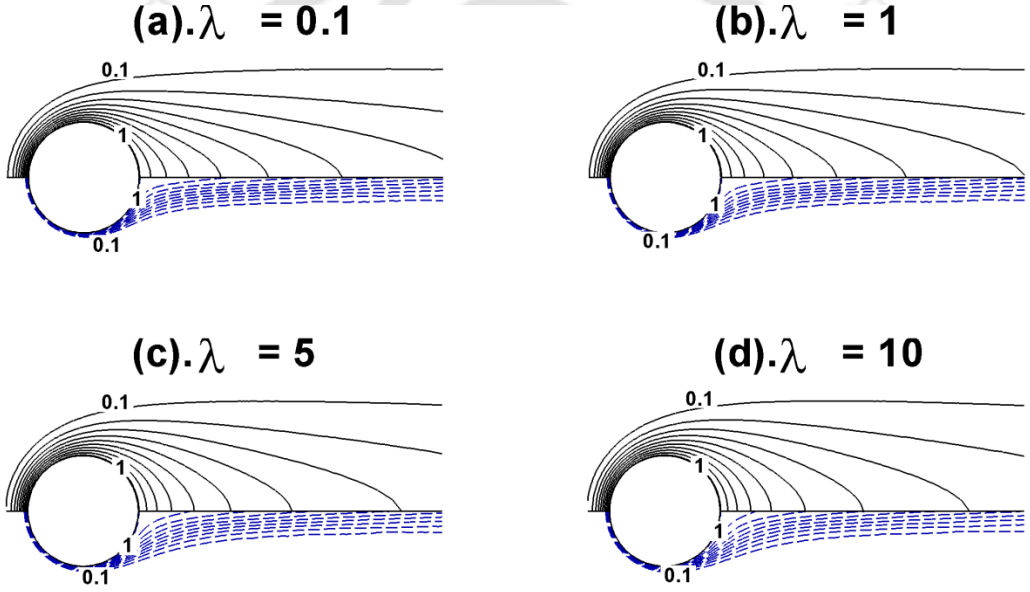

Figure 6.28 Isotherm contours around a sphere for n = 0.5 and Pr = 1 (upper half) and Pr = 100 (lower half) at Re = 20.

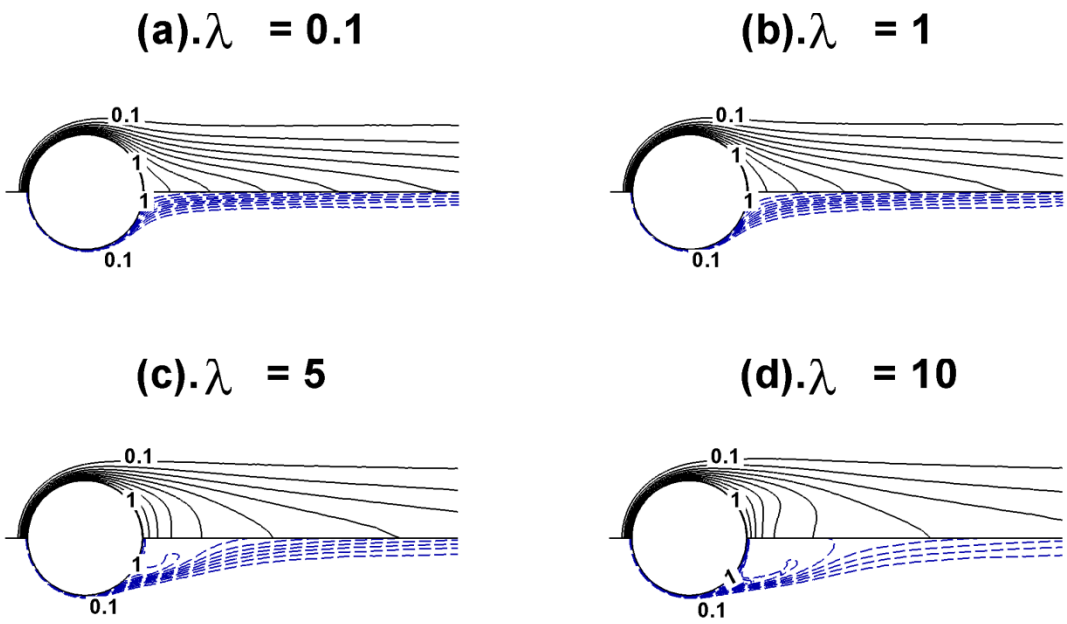

Figure 6.29 Isotherm contours around a sphere for n = 0.5 and Pr = 1 (upper half) and Pr = 100 (lower half) at Re = 100.

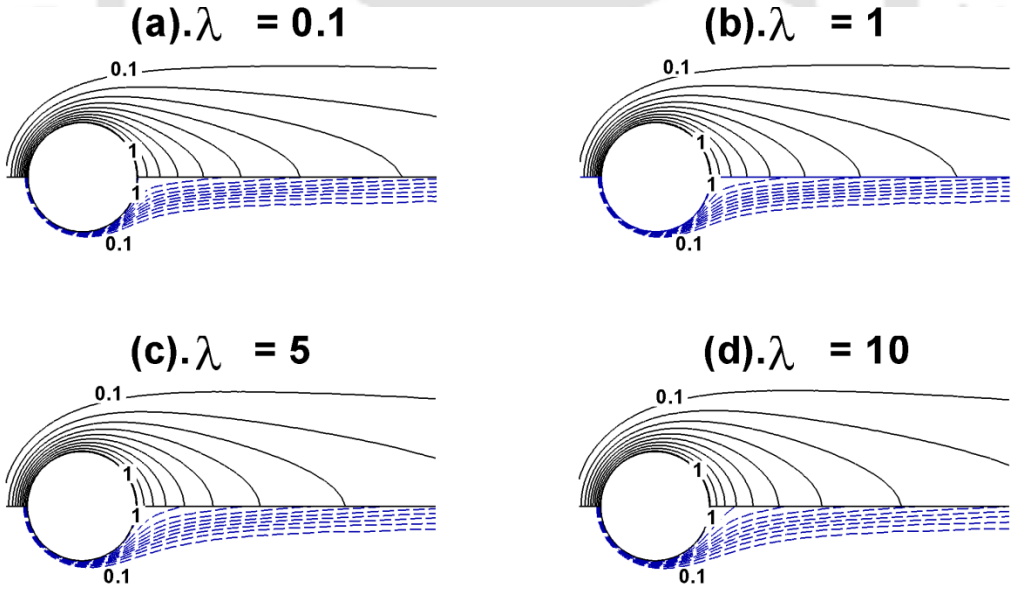

Figure 6.30 Isotherm contours around a sphere for n = 1.6 and Pr = 1 (upper half) and Pr = 100 (lower half) at Re = 20.

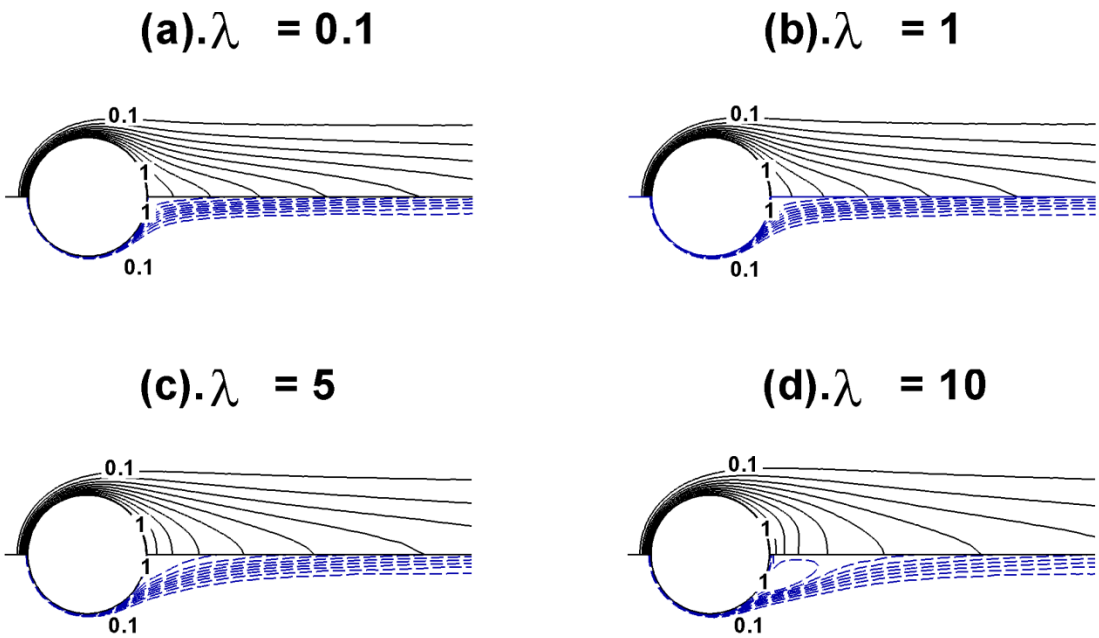

Figure 6.31 Isotherm contours around a sphere for n = 1.6 and Pr = 1 (upper half) and Pr = 100 (lower half) at Re = 100.

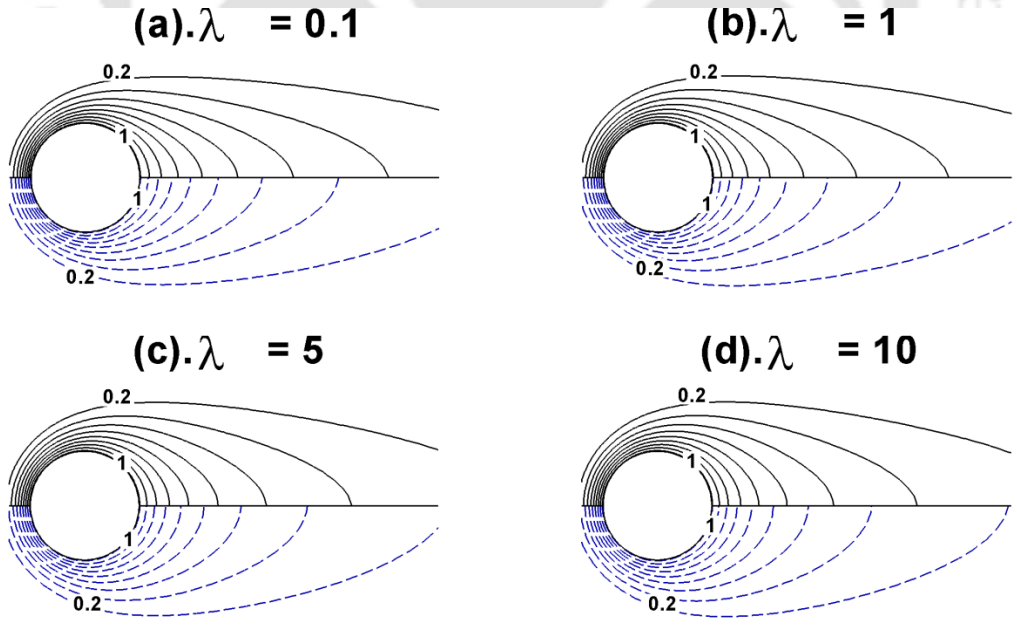

Figure 6.32 Isotherm contours around sphere with velocity slip in power-law liquids of n = 0.5 (upper half) and n = 1.6 (lower half) at Re = 10 and Pr = 1.

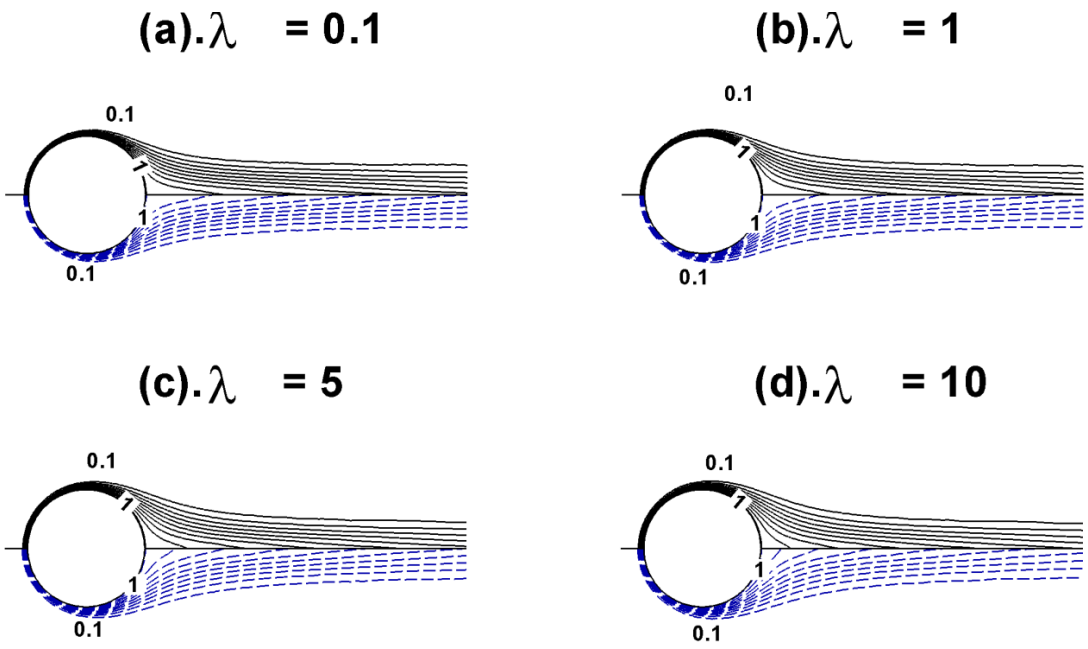

Figure 6.33 Isotherm contours around sphere with velocity slip in power-law liquids of n = 0.5 (upper half) and n = 1.6 (lower half) at Re = 10 and Pr = 100.

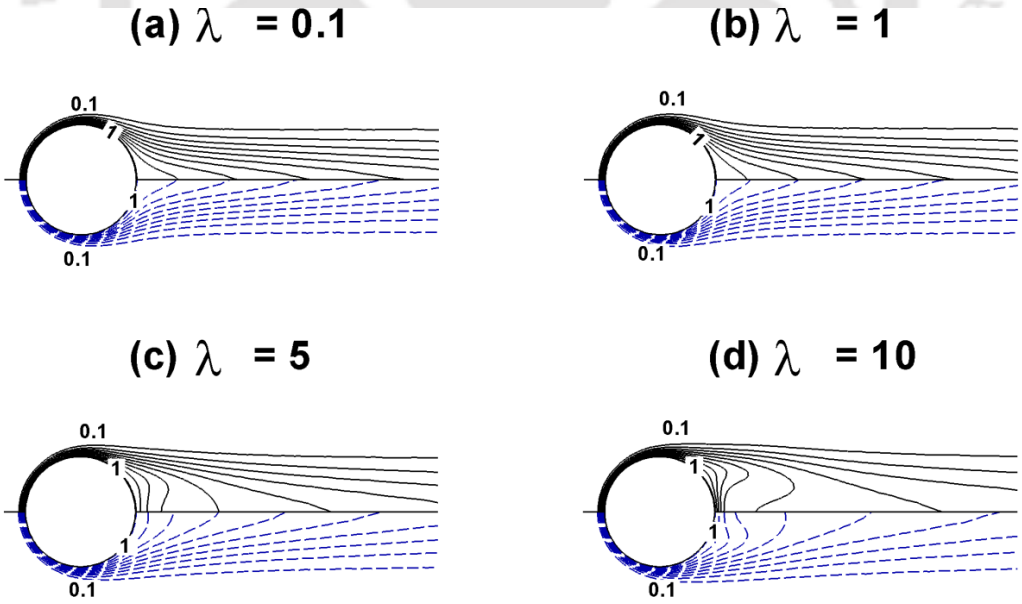

Figure 6.34 Isotherm contours around sphere with velocity slip in power-law liquids of n = 0.5 (upper half) and n = 1.6 (lower half) at Re = 200 and Pr = 1.

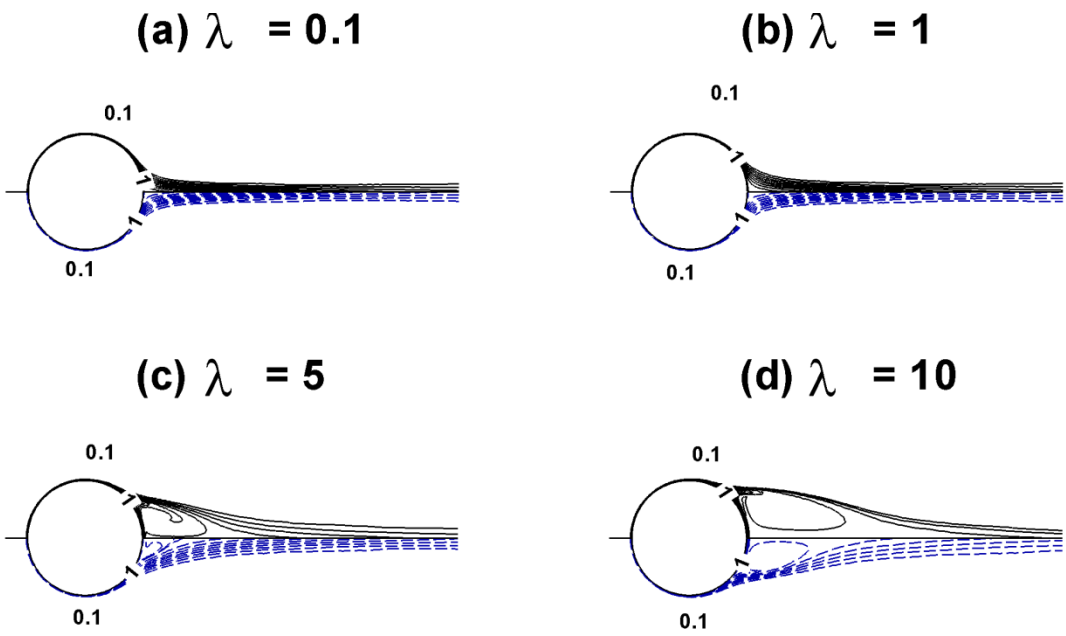

Figure 6.35 Isotherm contours around sphere with velocity slip in power-law liquids of n = 0.5 (upper half) and n = 1.6 (lower half) at Re = 200 and Pr = 100.

6.4.2. Surface Nusselt number

Figure 6.36 presents the variations in the local Nusselt numbers along the surface of the sphere with interface fluid-slippage in power-law liquids of n = 0.5 at Re = 20 for different values of the Prandtl numbers and slip parameters. The thermal boundary layer is thin at the front stagnant point and it gradually thickens as one traverse to the rear stagnation point along the surface of the sphere. Because of this reason the local Nusselt number is maximum at front stagnation point and as one traverses along the surface of spherical particle the local Nusselt number gradually decreases up to the rear stagnation point provided the recirculation wake is absent. If the recirculation wake is occurring then the local Nusselt number decreases from its maximum value at the front stagnation point to a minimum value at the point of flow separation, and then again gradually increases to a certain intermediate value at the rear stagnation point. Thus for the

Prandtl number of unit and slip parameters (**Figure 6.36(a)**), the local Nusselt number gradually decreases from its maximum value at the front stagnation point to a minimum value at the rear stagnation point because the flow separation or formation of recirculation wake is absent at *Re* = 20. For *Pr* = 10, 50, 100 (**Figure 6.36(b)** – **Figure 6.36(d)**), except for the cases of $\lambda = 50$ and $\lambda = 100$, the local Nusselt number trends are qualitatively similar as in the case of *Pr* = 1 with only difference being is increase in the value of the local Nusselt number with the increase in Prandtl number. For $\lambda = 50, 100$ when $Pr \geq 10$ (**Figures 6.36(b)** – **Figure 6.36(d)**), the surface Nusselt number increases for a short distance from the front stagnation point to a position around $\theta \sim 45^{o}$ and then again it gradually decreases up to rear stagnation point as in the case of other values of the slip parameter. Furthermore, for a fixed value of the Prandtl number, as the value of the slip parameter increases the local Nusselt number decreases because of increasing boundary layer thickness as the slippage of fluid along the surface of sphere decreases. This indicates that for a given value of the Reynolds and Prandtl number, the rate of heat transfer decreases with the increasing slip parameter regardless of the values of the power-law index.

Figure 6.37 shows the variations in the local Nusselt number of a single sphere with fluid-slippage at the interface in power-law liquids of *n* = 0.5 for different values of the Prandtl number and slip parameter but at a larger value of the Reynolds number, *Re* = 200. Regardless of the value of the Prandtl number, when $\lambda \leq 1$, the local Nusselt number variations in the case of *Re* = 200 (**Figure 6.37**) are qualitatively similar to the case of *Re* = 20 (**Figure 6.36**) because of absence of recirculation wake when $\lambda \leq 1$ even at *Re* = 200. However, for $\lambda \geq 5$, the local Nusselt number decreases up to the point of flow separation in the rear half of the sphere and then it gradually increases because of distortions seen in the isotherm contours due to the flow separation. Furthermore, by comparing **Figure 6.36** and **Figure 6.37**, it can be seen that the local

Nusselt number increased with the Reynolds number for all values of the slip parameters and the Prandtl numbers.

Figure 6.38 and **Figure 6.39** shows the effects of the slip parameter on the Nusselt number along the surface of the sphere for different values of Prandtl number in power-law liquids of n = 1.6 at Re = 20 and Re = 200, respectively. Qualitatively similar trends are seen as in the case of shear-thinning fluids of n = 0.5 (**Figures 6.36** and **Figure 6.37**), but as the power law index increased to n = 1.6, the local value of the Nusselt number decreased because of increased boundary layer thickness due to increased apparent viscosity of the shear-thickening fluids. Furthermore, unlike the case of shear-thinning fluids (**Figures 6.36** and **Figure 6.37**), the local rise in surface Nusselt number of the sphere (from front stagnation point to around $\theta \sim 45°$) is absent in the case of shear-thickening fluids (**Figures 6.38** and **Figure 6.39**) for all values of the slip parameter.

Figures 6.40 – 6.43 show the effect of the power-law fluid behavior index (n) on the variations in local (surface) Nusselt numbers of the sphere with velocity slip at the interface at Re = 50 for Pr = 1, 10, 50, 100 respectively. In the case of Re = 50 and $\lambda \leq 10$, flow recirculation wake is not found in the rear of the sphere regardless the nature of the power-law fluid considered. Therefore for all values of the power-law index, slip parameters and Prandtl numbers, the local Nusselt number gradually decreases as one traverses along the surface of the sphere from the front stagnation point to the rear stagnation point. However, for given combination of the power-law index and Prandtl number, the local values of Nusselt number along the surface of the sphere decreases with the increasing slip parameter which indicates reduction in the rate of heat transfer with increasing slip parameter. Further for a fixed combination of the slip number and the Prandtl number, as the value of the power-law index

increases, the local values of the Nusselt number along the surface of the sphere decreases indicating the rate of heat transfer is higher for shear-thinning fluids followed by Newtonian and shear-thickening fluids. Finally, for a given combination of the slip parameter and the power-law fluid behavior index, the local values of the Nusselt number along the surface of the spheres increases as the value of the Prandtl number increases indicating increased rate of heat transfer due to increased contribution from the convective heat transfer.

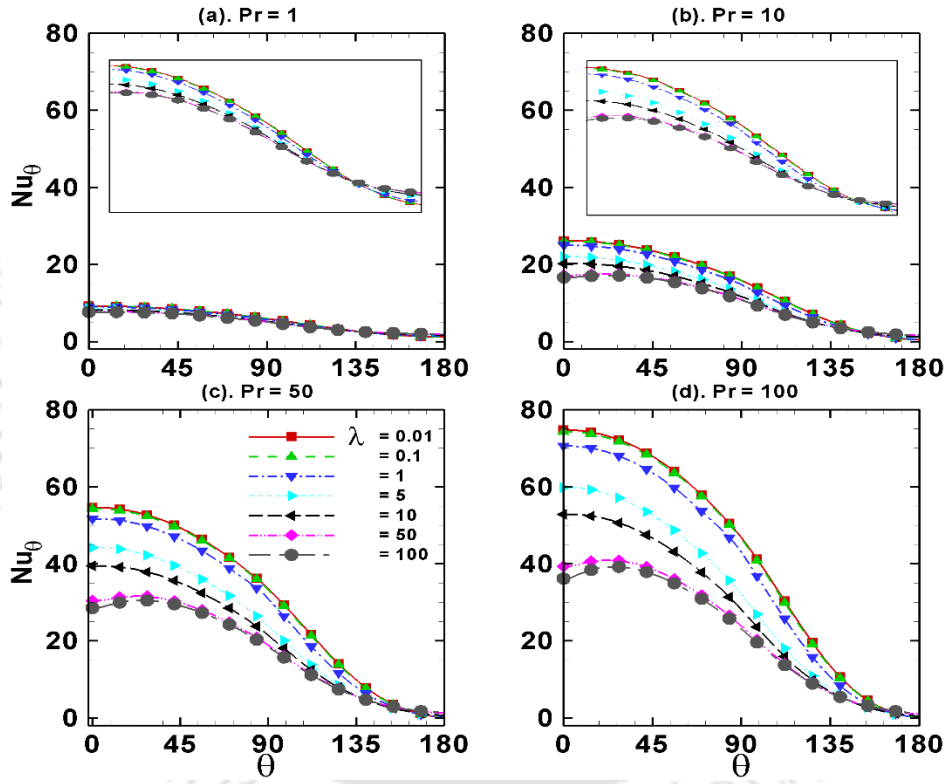

Figure 6.36 Effect of slip parameter λ on the surface *Nu* around slip sphere for n = 0.5 at different values Prandtl number *Pr* and at *Re* = 20.

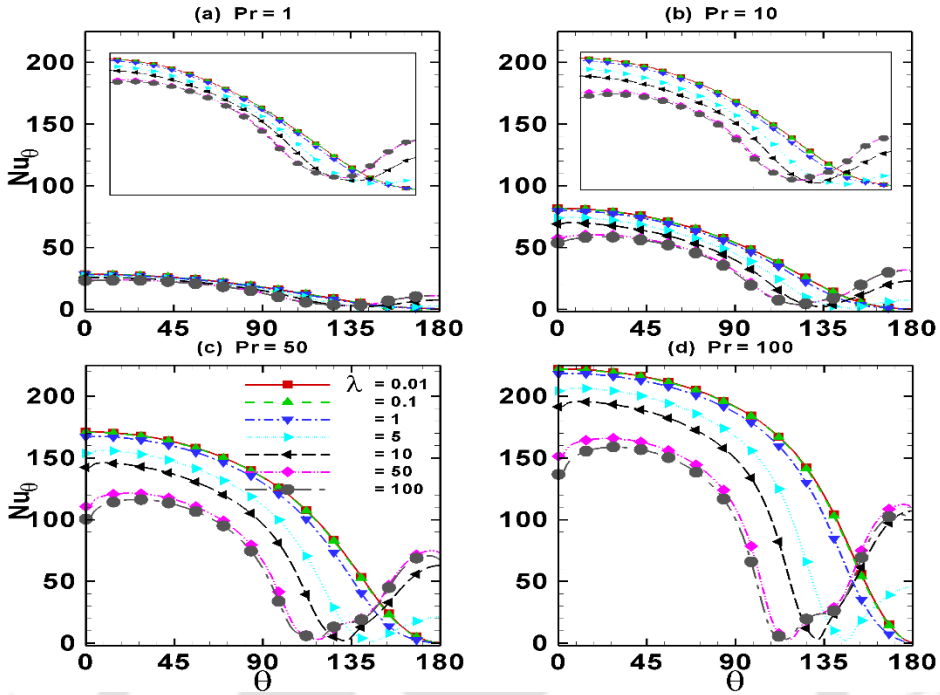

Figure 6.37 Effect of slip parameter λ on the surface *Nu* around sphere for n = 0.5 at different values Prandtl number *Pr* and at *Re* = 200.

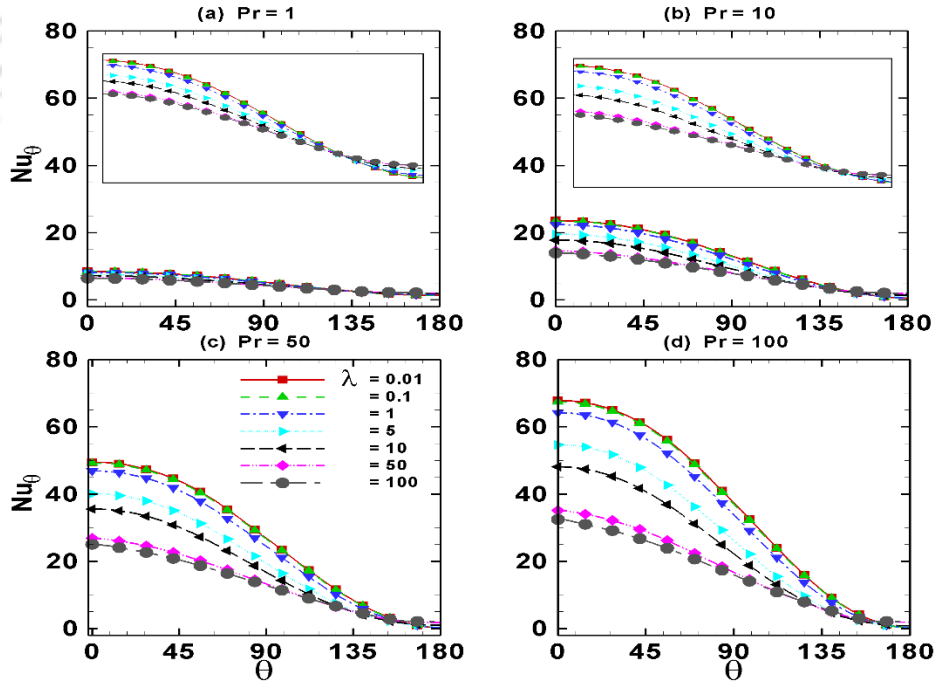

Figure 6.38 Effect of slip parameter on the surface *Nu* around sphere for n = 1.6 at different values Prandtl number and at *Re* = 20.

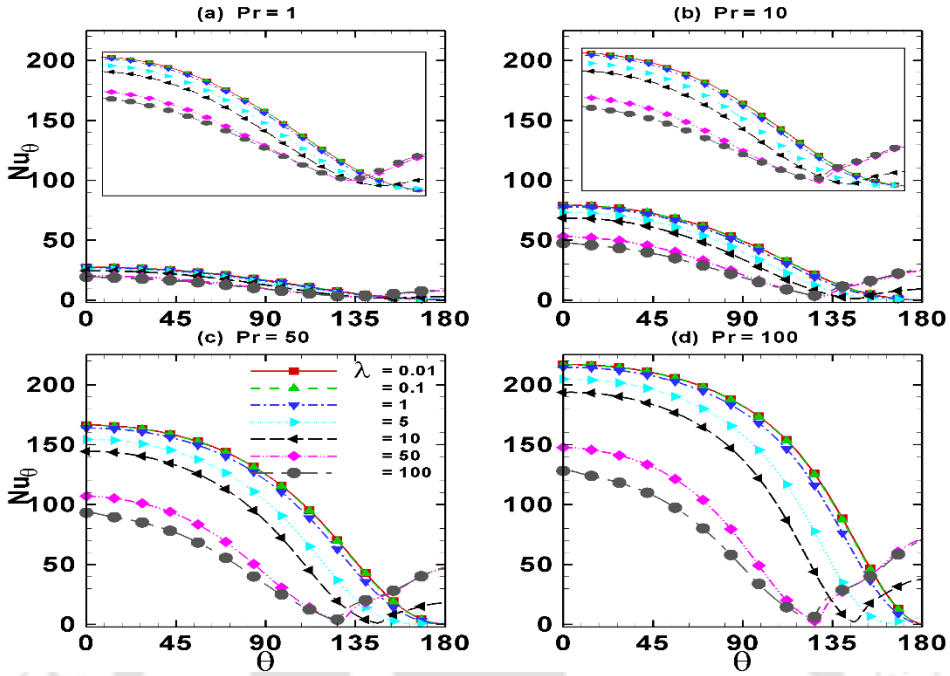

Figure 6.39 Effect of slip parameter λ on the surface *Nu* around sphere for n = 1.6 at different values Prandtl number *Pr* and at *Re* = 200.

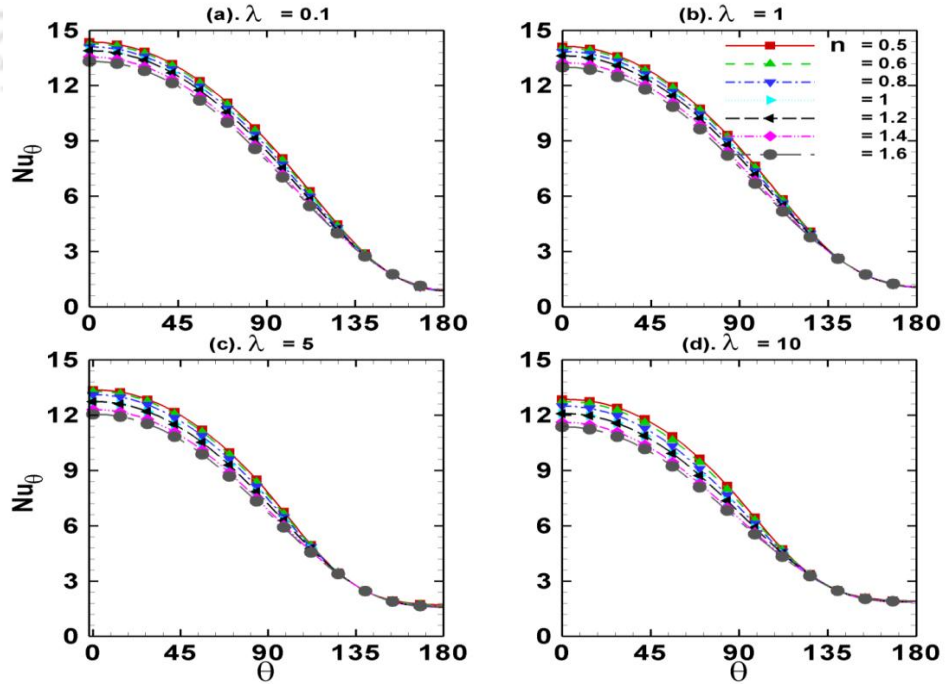

Figure 6.40 Effect of power-law index on local Nusselt number of sphere in power-law fluids with velocity slip at the interface for *Re* = 50 and *Pr* = 1.

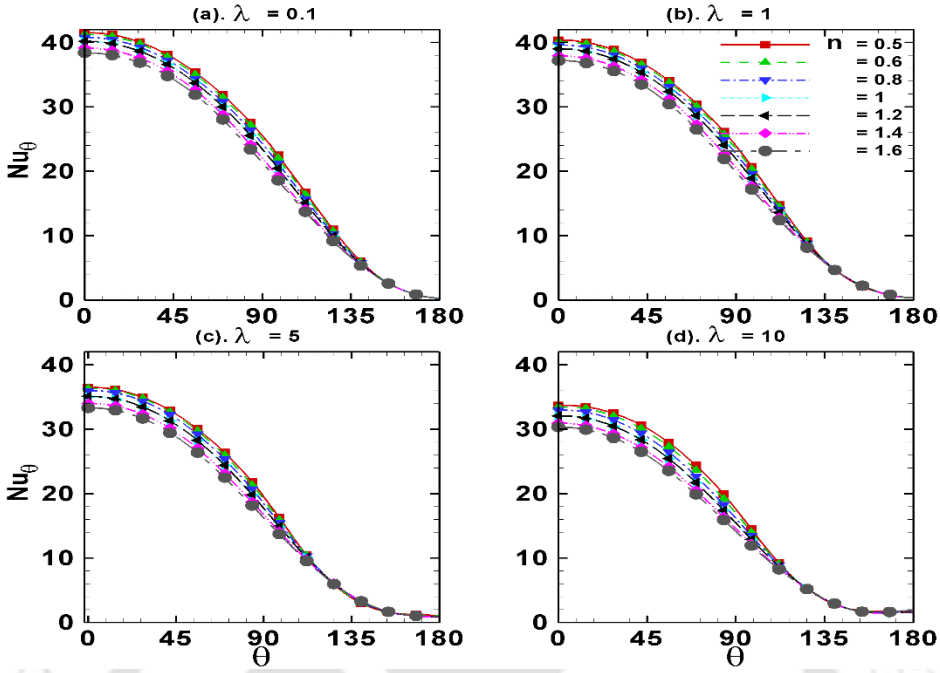

Figure 6.41 Effect of power-law index on local Nusselt number of sphere in power-law fluids with velocity slip at the interface for *Re* = 50 and *Pr* = 10.

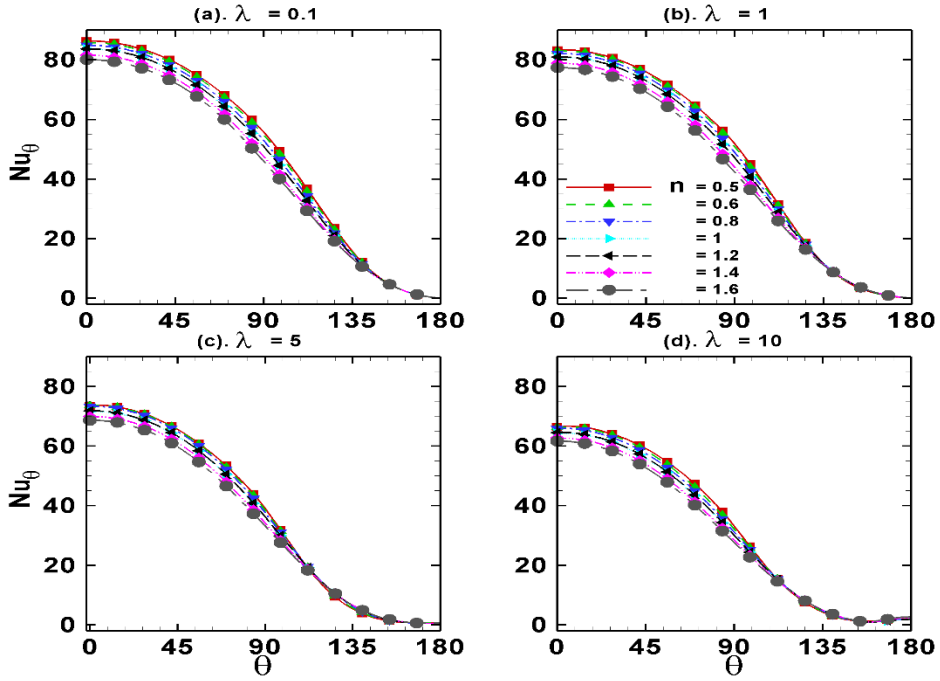

Figure 6.42 Effect of power-law index on local Nusselt number of sphere in power-law fluids with velocity slip at the interface for *Re* = 50 and *Pr* = 50.

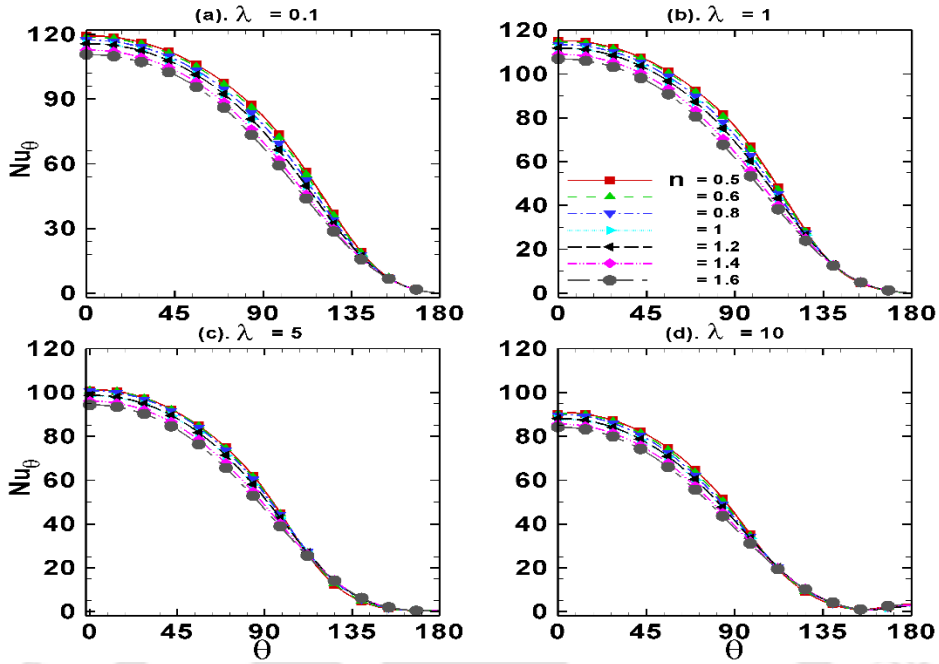

Figure 6.43 Effect of power-law index on local Nusselt number of sphere in power-law fluids with velocity slip at the interface for *Re* = 50 and *Pr* = 100.

6.4.3. Average Nusselt number

Figure 6.44 and **Figure 6.45** shows the variations in the average Nusselt numbers of the sphere with interface velocity slip in power-law liquids of *n* = 0.5 (**Figure 6.44)** and *n* = 1.6 (**Figure 6.45**) at different values of the slip parameters and Reynolds numbers. The average Nusselt number increases with the increase in the Peclet number regardless of the values of the slip parameter, power-law index and the Reynolds numbers because of increasing contribution of convection mode of heat transfer with the increasing Peclet number. Further irrespective of the values of the Reynolds number, Peclet number and the power-law index, the average Nusselt number decreases with the increase in the slip parameter. This is due to the reduction in magnitude of the fluid slip over the surface as the value of the slip parameter increases. The average Nusselt number increases with the increasing Reynolds number for all values of the

power-law index and the slip parameters. **Figure 6.46** presents the effects of the power-law index on the average Nusselt numbers of a single sphere at *Re* = 50 (where both the viscous and convection forces are of comparable order to each other) for different values of the slip parameters and the Prandtl numbers. As the power-law index decreases the thermal boundary layer becomes thinner, hence the average Nusselt number increases with decreasing power-law index for all values of the Peclet numbers, Reynolds numbers and the slip parameters. The apparent viscosity of the fluid around the surface of sphere decreases with the decreasing power-law index (*n*) resulting in steep velocity gradients which in turn enhances the heat transfer rate from a sphere to surrounding fluid. Therefore, the average Nusselt number is higher for shear-thinning fluids followed by the Newtonian and shear-thickening fluids. Finally, the rate of the heat transfer from the surface of a single sphere to the surrounding power-law liquids increased as the slip parameter decreased and/or Reynolds/Prandtl number increased and/or power-law index decreased. Though the results of average Nusselt numbers presented in **Figures 6.44**–**Figure 6.46** are self-explanatory both qualitatively and quantitatively, developing an empirical correlation on the basis of the present numerical results would be useful in new applications involving slip flow past heated spheres. Thus the following form for the empirical correlation is found to be suitable:

$$Nu_{avg} = 1 + \frac{0.566\,\mathrm{Re}^{0.586}\,\mathrm{Pr}^{0.468}}{\lambda^{0.065} n^{0.17}} + \frac{0.825\,\mathrm{Pr}^{0.051}\,\lambda^{0.039}}{n^{0.143}} \tag{6.4}$$

The above correlation reproduces the present numerical results (1176 data points) with an average error of ±7.1% which rises to a maximum of ±34.5%. This correlation is valid for the entire range of present conditions, i.e., $0.1 \le Re \le 200$, $0.5 \le n \le 1.6$, $0.01 \le \lambda \le 100$ and $1 \le Pr \le 100$. However, its fit with the present numerical values of the average Nusselt number is excellent when $Pr < 50$ for all values of the Reynolds number, slip number and the power-law

index, but it under predicts the numerical values with approximately 25% error for the cases when $Pr > 100$; $Re = 50–200$; $\lambda = 0.01–1$ and $\lambda = 50–100$ for all values of the power-law index.

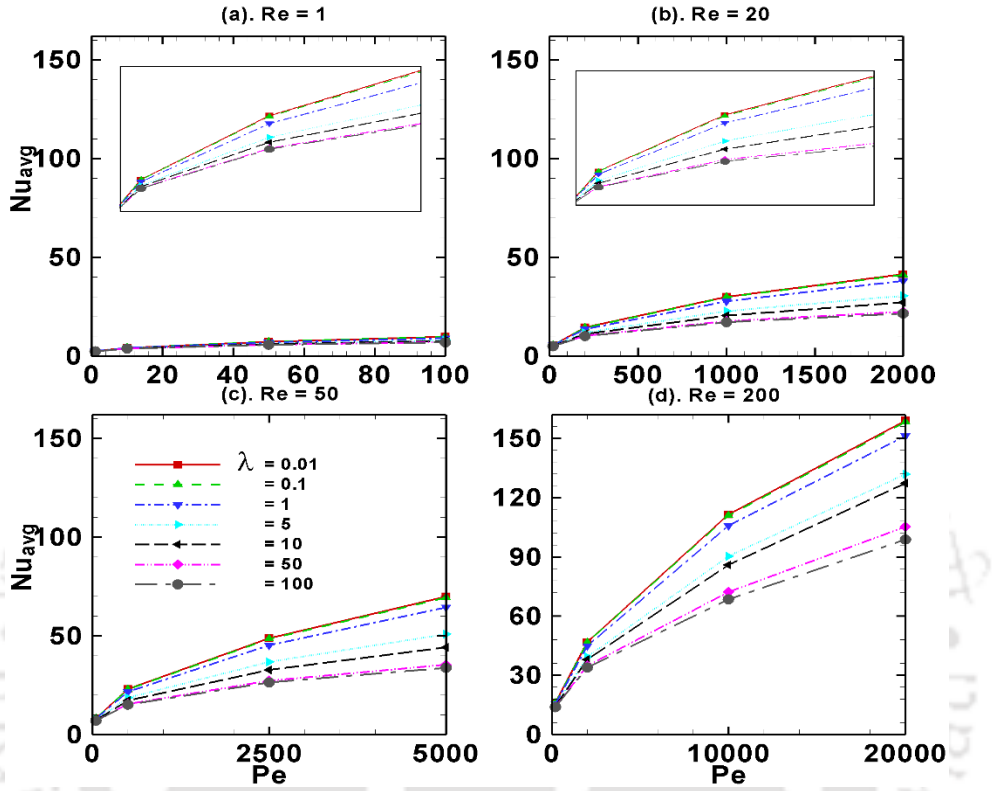

Figure 6.44 Variation of average *Nu* of sphere with velocity slip at the interface in power-law fluids of $n = 0.5$ at different values Reynolds number.

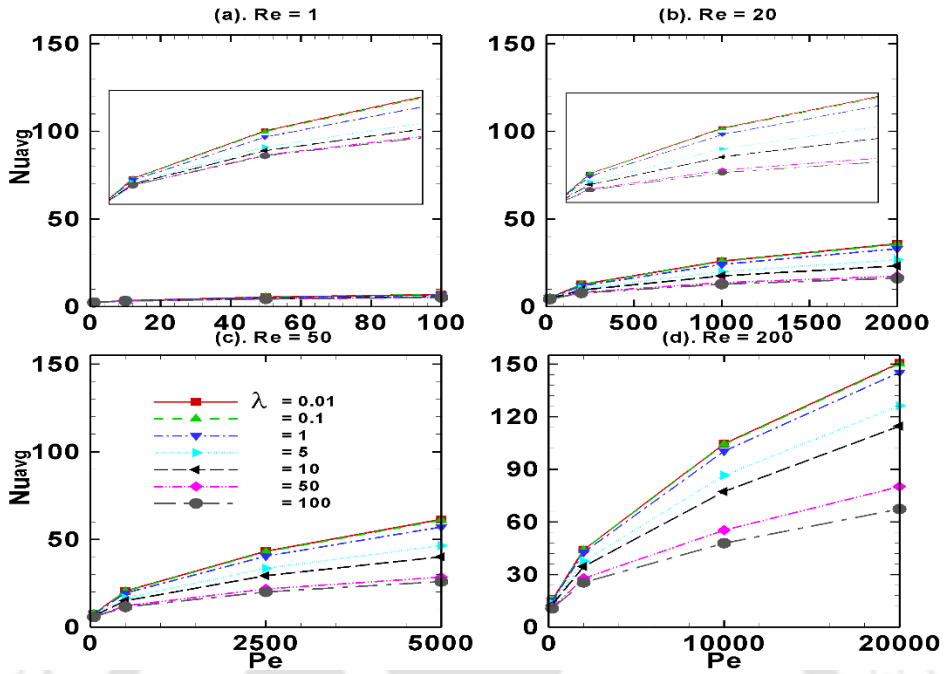

Figure 6.45 Variation of average *Nu* of sphere with velocity slip at the interface in power-law fluids of n = 1.6 at different values Reynolds number.

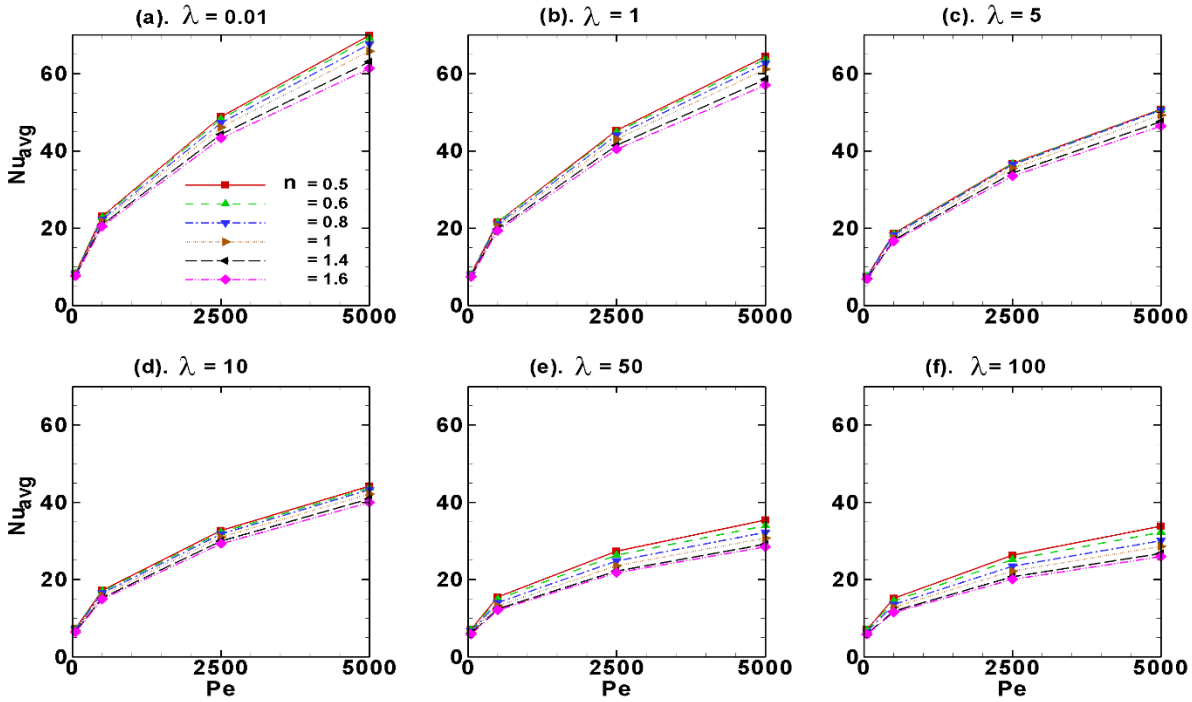

Figure 6.46 Variation of average *Nu* around a sphere for different values of slip parameter and power-law index at *Re* = 50.

6.5. Momentum Transfer Study of Assemblages of Spherical Particles in Newtonian Fluids

The values of the present pertinent dimensionless parameters consider delineating their effects on the flow and drag behavior of assemblages of spherical particles in Newtonian fluids with velocity slip at the interface are: Re = 0.1, 1, 10, 20, 50, 100, 200, Φ = 0.1, 0.2, 0.3, 0.4, 0.5 and λ = 0.01, 0.1, 1, 2, 5, 10, 50, 100.

6.5.1. Flow phenomena

Figure 6.47 represents streamlines (upper half of the circle) and vorticity (lower half of the circle) contours in a cell of assemblages of slip spheres of volume fraction 0.1 at Re = 0.1 for different values of the slip parameter. In this figure maximum and minimum values of stream function and iso-vorticity are depicted. The difference between values of any two consecutive streamlines is 0.1 and similarly difference between values of any two consecutive iso-vorticity contours is also 0.1. Regardless of the value of slip parameter, the streamlines exhibit fore and aft symmetry; and the detachment of the fluid is not observed. Similar effects of slip parameter on the vorticity contours are also observed. Thus, at such small Reynolds number, the effect of slip parameter on both streamlines and vorticity contours are seem to be small; and the steady attached flow is observed for all values of the slip parameter. **Figure 6.48** shows the effect of slip parameter on streamlines (upper half) and vorticity contours (lower half) in a cell of assemblages of spheres of volume fraction 0.1 at Re = 200. In this figure also maximum and minimum values of stream function and iso-vorticity are depicted. The difference between values of any two consecutive streamlines is 0.1 and similarly difference between values of any two consecutive iso-vorticity contours is also 0.1. For $\lambda \leq 5$ (**Figure 6.48(a-c)**), the streamline

patterns indicated that the flow is still steady and attached even at *Re* = 200; however, the vorticity contours are being carried away along the flow direction because of the domination of the convection force at *Re* = 200. However, as the slip parameter increases to λ = 10 (**Figure 6.48(d)**), a small recirculation wake is observed at the rear end of the spheres in the cell; and the size of the recirculation wake increases as the slip parameter increases further to λ = 50 (**Figure 6.48(e)**) and λ = 100 (**Figure 6.48(f)**). Because as the value of the slip parameter increases, the fluid slip at the solid surface decreases; and thus the amount of vorticity that can be created around the sphere increases with increasing slip parameter. Qualitatively similar trends observed for other combinations of the Reynolds number, slip parameter and volume fraction of spheres. Therefore, the detachment of the flow is found to be strongly influenced by both the volume fraction and the fluid slip on the surface of spheres.

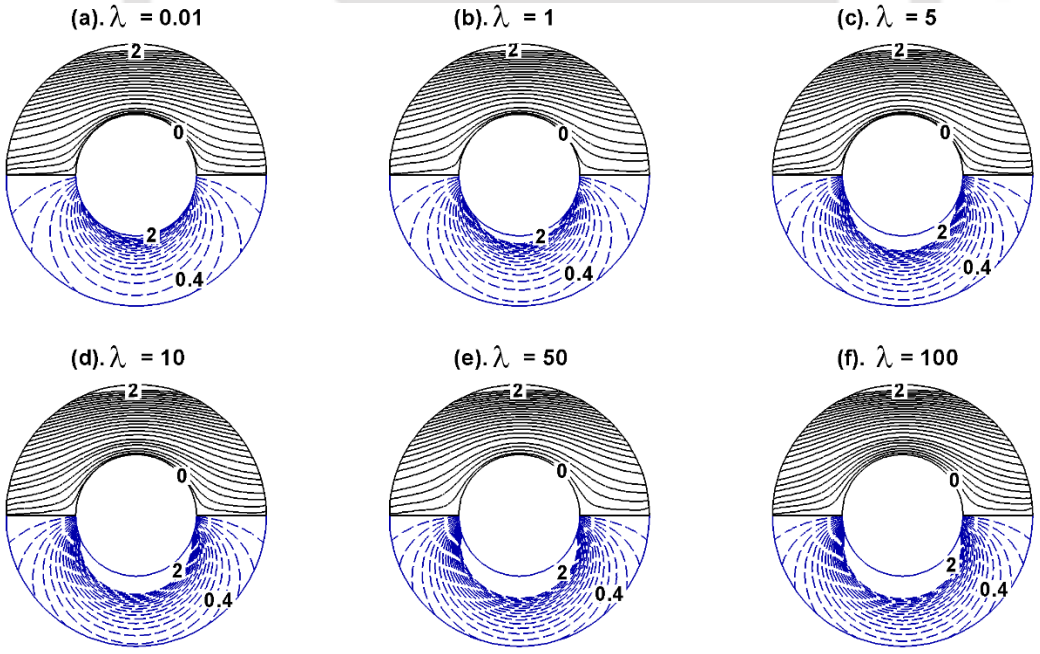

Figure 6.47 Streamlines and iso-vorticity contours in assemblages of spheres of volume fraction 0.1 at *Re* = 0.1 for different values of λ.

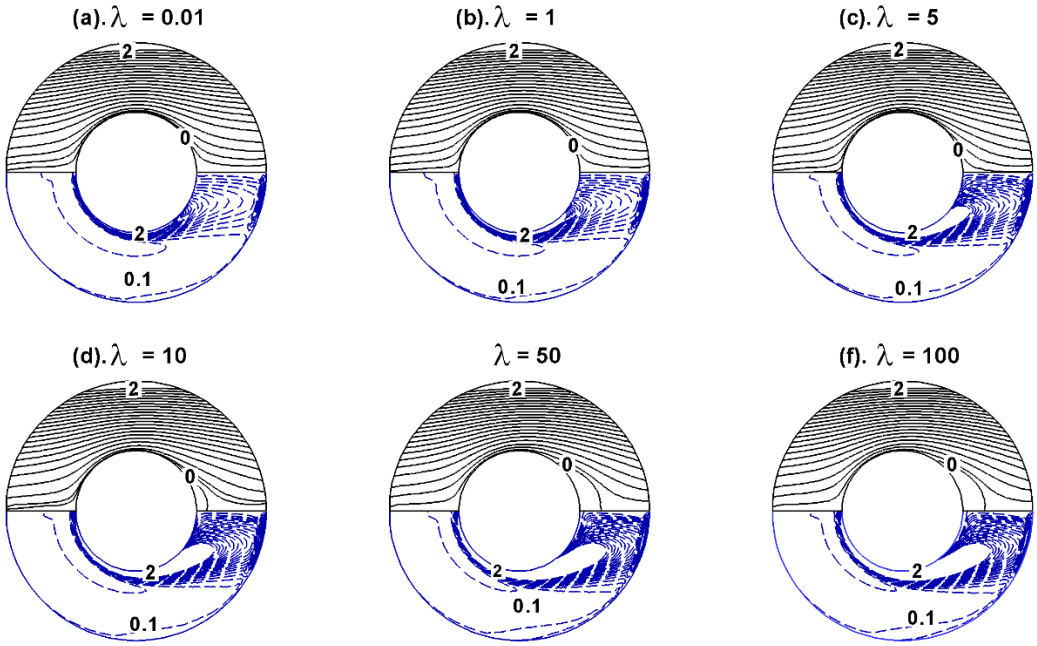

Figure 6.48 Streamlines and iso-vorticity contours in assemblages of sphere of volume fraction 0.1 at *Re* = 200 for different values of λ.

6.5.2. Surface pressure coefficients

Figure 6.49 shows the effect of slip parameter on distribution of pressure coefficient along the surface of a representative sphere in cells of volume fractions Φ = 0.1, 0.3, 0.5 at *Re* = 100. Regardless of the value of the volume fraction, at front stagnation point, the value of the pressure coefficient is minimum for λ = 0.01 and maximum for λ = 100; whereas at the rear stagnation point, the trends are opposite. For intermediate values of the slip parameter, the pressure coefficient lies within these two limiting values both at the front and the rear stagnation points. The reason for this trend can be ascribed to the degree of the fluid slip at the solid surface, i.e., the recovery of the pressure is large in the case of more slipping spheres (small λ) and it is poor in the case of spheres with small degree of slippage (large λ). For small value of λ, there is no flow separation and wake formation at the rare end of the spheres, hence less pressure drop and

large recovery of pressure at rare end of the spheres. Therefore, it can be concluded that for fixed values of the Reynolds number and the volume fraction, the assemblages of spheres with large slippage (decreasing λ) offer less pressure drop whereas the assemblages of spheres with less slippage (increasing λ) offer more pressure drop during their sedimentation in an unconfined Newtonian liquid. **Figure 6.50** shows the effect of volume fraction of spheres on the surface pressure coefficient along the surface of a representative sphere in cells at *Re* = 50 for different values of the slip parameter. For all volume of the slip parameter, the value of the pressure coefficient at the front stagnation point is maximum for Φ = 0.5 and it is minimum for Φ = 0.1; and for intermediate values of the volume fraction, the value of the pressure coefficient lies between these two limits. However, at the rear stagnation point, the value of the pressure coefficient is maximum for Φ = 0.5 and minimum for Φ = 0.1 only when $\lambda \leq 1$ (**Figure 6.50(a-b)**); but when $\lambda > 1$ (**Figure 6.50(c-f)**), opposite trends are observed. This concludes that during settling of slip spheres, larger the volume fraction higher is the pressure drop; and it is significantly affected by the slip parameter.

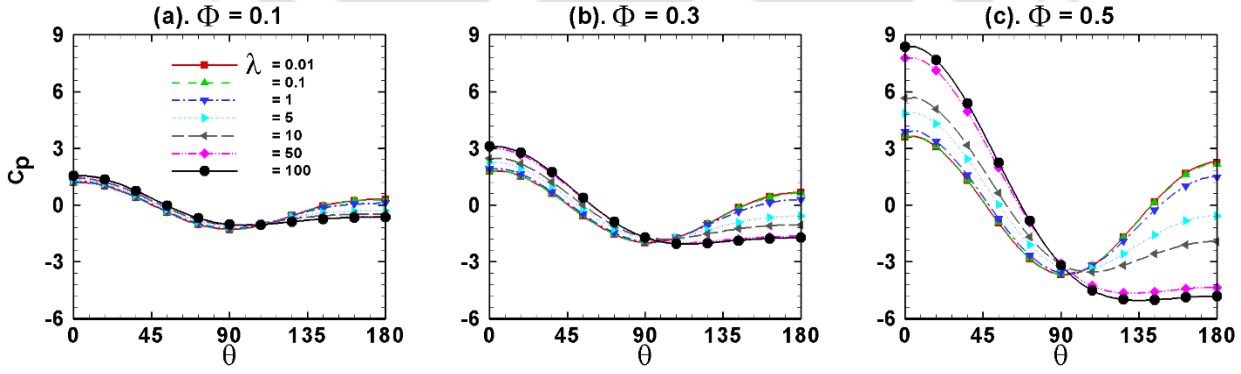

Figure 6.49 Distribution of pressure coefficient along the surface of sphere at *Re* = 100.

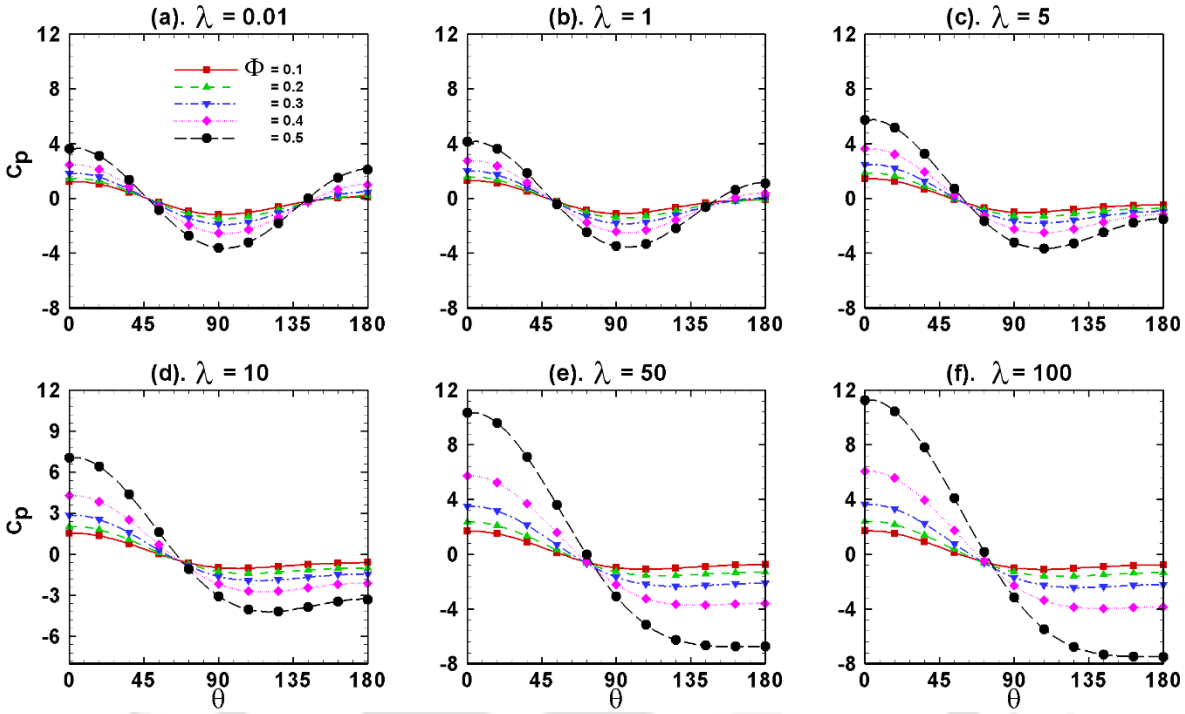

Figure 6.50 Distribution of pressure coefficient along the surface of sphere at *Re* = 50.

6.5.3. Surface vorticity distribution

Figure 6.51 shows the effect of the slip parameter on the distribution of the vorticity along the surface of a representative spheres in cells of volume fraction Φ = 0.1, 0.3, 0.5 at *Re* = 100. In general, the vorticity along the surface of spherical object increases from zero value at front stagnation point to a certain large value at around θ = 50° - 70°, then again gradually decreases until the point of flow separation (in case of flow detachment) and finally forms a secondary wake in the rear end before relaxing at rear stagnation point with zero value. This secondary wake does not exist for the case of attached flow without any recirculation wake; and here too similar trends are observed. Briefly, for all values of the volume fraction, the surface vorticity value is maximum for λ = 100 and it is minimum for λ = 0.01. For intermediate values of λ, the vorticity distribution is in the interim of the two vorticity curves for the case of λ = 0.01 and λ =

100. For all values of the volume fraction and the slip parameter, there is no secondary wake formation in the vorticity curve because of the absence of the recirculation wake at *Re* = 100.

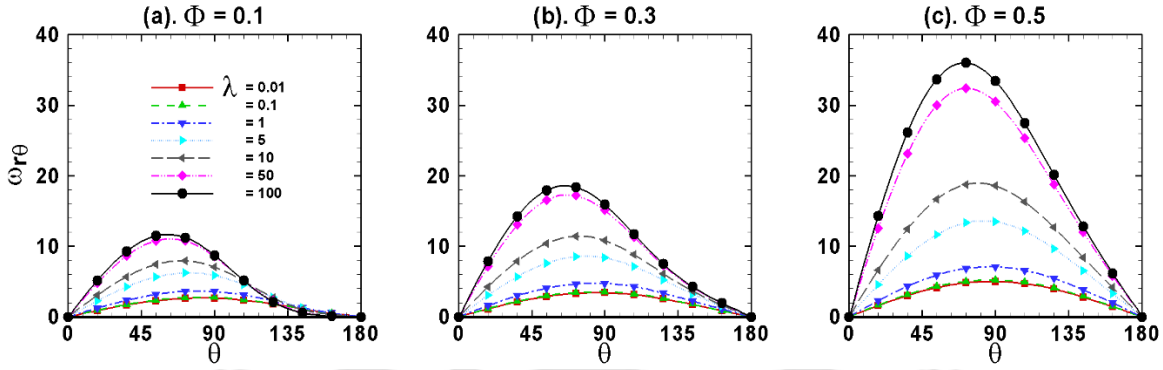

Figure 6.51 Distribution of vorticity along the surface of sphere at *Re* = 100.

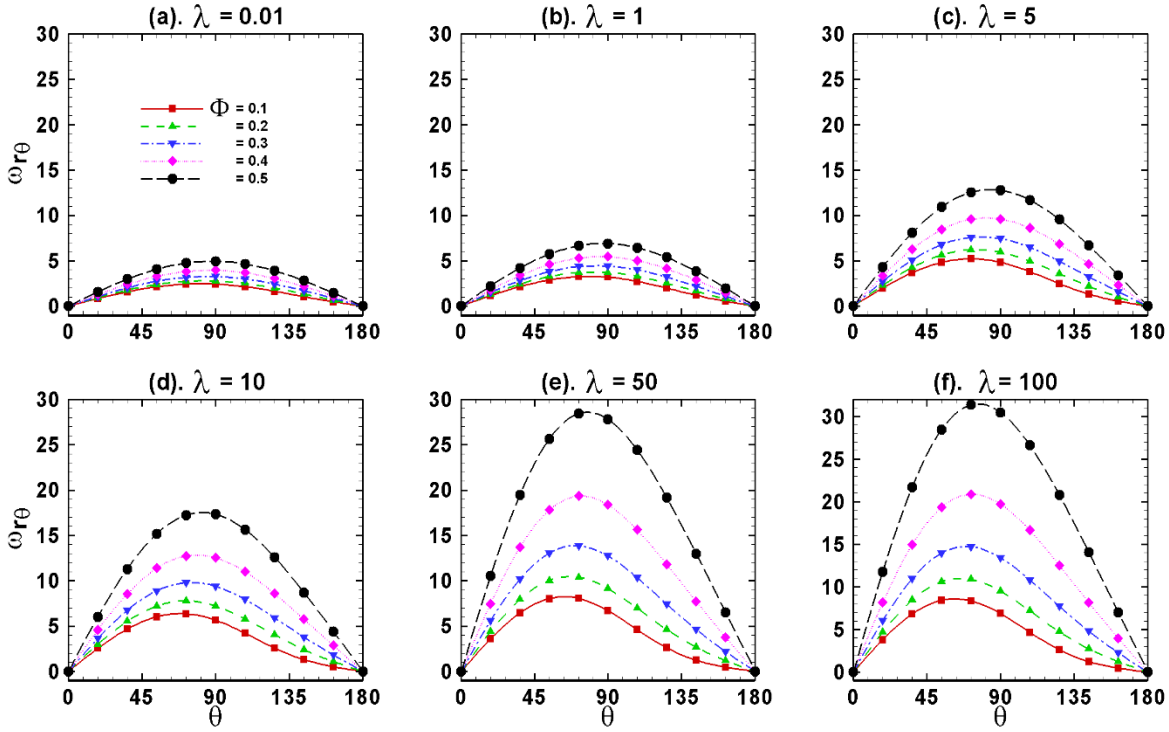

Figure 6.52 Distribution of vorticity along the surface of sphere at *Re* = 50.

Figure 6.52 shows the effect of the volume fraction of the spheres on the distribution of the vorticity along the surface of the representative sphere in cells at *Re* = 50 for different values

of the slip parameter; and qualitatively similar trends are observed as in the case of **Figure 6.51**. Here too there is no secondary wake formation in the rear end of the representative sphere because there is no flow detachment for all values of the slip parameter at Re = 50. However, regardless of values of the slip parameter, the vorticity increases with the increasing volume fraction because of increased hindrance from neighboring slip spheres.

6.5.4. Drag phenomena

Figure 6.53 represents drag coefficients of spheres of varying volume fraction for different values of the Reynolds number and slip parameter. For all values of the slip parameter and volume fraction, the characteristic drag curve is recovered, i.e., the total drag coefficient decreases with the increasing Reynolds number. For any combination of the Reynolds number, and slip parameter, as the volume fraction of spheres decreases, the total drag coefficient decreases because of decreasing hindrance from neighbor spheres. Furthermore, for fixed values of the Reynolds number and volume fraction, the drag coefficient decreases with the decreasing slip parameter because of increasing fluid slip along the surface of the sphere. Therefore, it can be concluded that the drag on assemblages of spheres in Newtonian fluids decreases (thus settles easily) with the decreasing volume fraction and/or decreasing slip parameter and/or increasing Reynolds number. However, it is often required to know the hindrance effect because of neighboring particles in such multiple particle systems. Thus, **Figure 6.54** shows the combined effects of the Reynolds number, slip parameter and the volume fraction on the ratio between the drag coefficients of assemblages of spheres (C_d) to the drag coefficient of unconfined single slip sphere (C_{d0}) in Newtonian fluids. For all values of the slip parameter and the volume fraction, the hindrance effect is severe at small Reynolds number. However, for $\lambda \leq 1$ (**Figure 6.54(a-b)**), as the value of the Reynolds number increases, the ratio C_d/C_{d0} exhibits a local minimum which

increases with the increasing volume fraction of the spheres. For λ = 5 (**Figure 6.54 (c)**), this local minimum disappears for the volume fractions less than 20%; however, for λ > 5 (**Figure 6.54 (d-f)**), there is no such local minimum for all values of the volume fraction. Thus, for small values of slip parameter ($\lambda \leq 1$), the effect of hindrance is small at intermediate Reynolds number for all volume fractions. However, for $\lambda > 5$, the hindrance effect decreases with the increasing Reynolds number and/or with the decreasing volume fraction.

Figure 6.55 shows the combined effects of the Reynolds number, slip parameter and volume fraction of spheres on the ratio between the pressure and the friction drag coefficients. For all values of the slip parameter and the volume fraction, as the value of the Reynolds number increases the C_{dp}/C_{df} ratio increases; however, the effect of the Reynolds number is insignificant up to Re = 10; but for all values of the Reynolds number, this ratio increases with the increasing volume fraction except for λ = 0.01. Furthermore, for fixed values of the Reynolds number and the volume fraction, as the value of the slip parameter increases, the ratio between the pressure and the friction drag coefficients increases. Thus, it can be concluded that for all values of the slip parameter and the volume fraction, the relative contribution from pressure and friction drag coefficients is unaffected by the increase in the Reynolds number up to Re = 10; however, for Re > 10, the relative contribution increases with the Reynolds number and the volume fraction. Finally, with the increasing slip parameter (decreasing slippage) and/or with the increasing volume fraction and/or with the increasing Reynolds number (Re > 10), the relative contributions from pressure to friction drag coefficients increases.

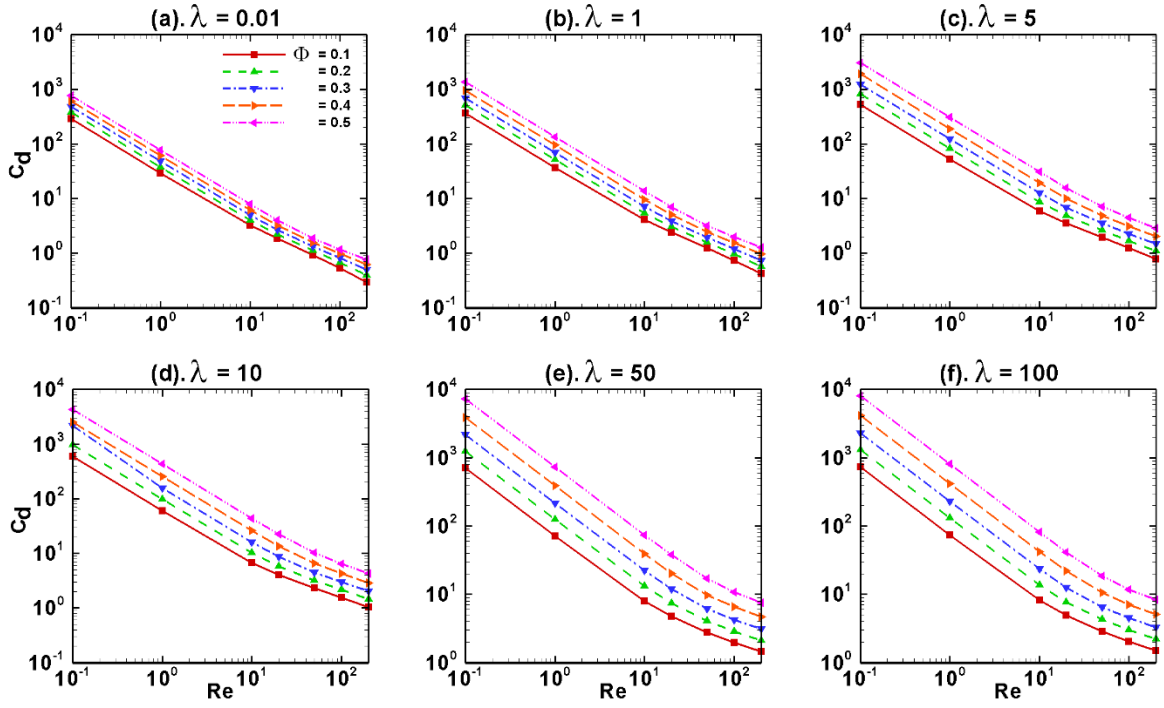

Figure 6.53 Total drag coefficients of assemblages of spheres in Newtonian fluids.

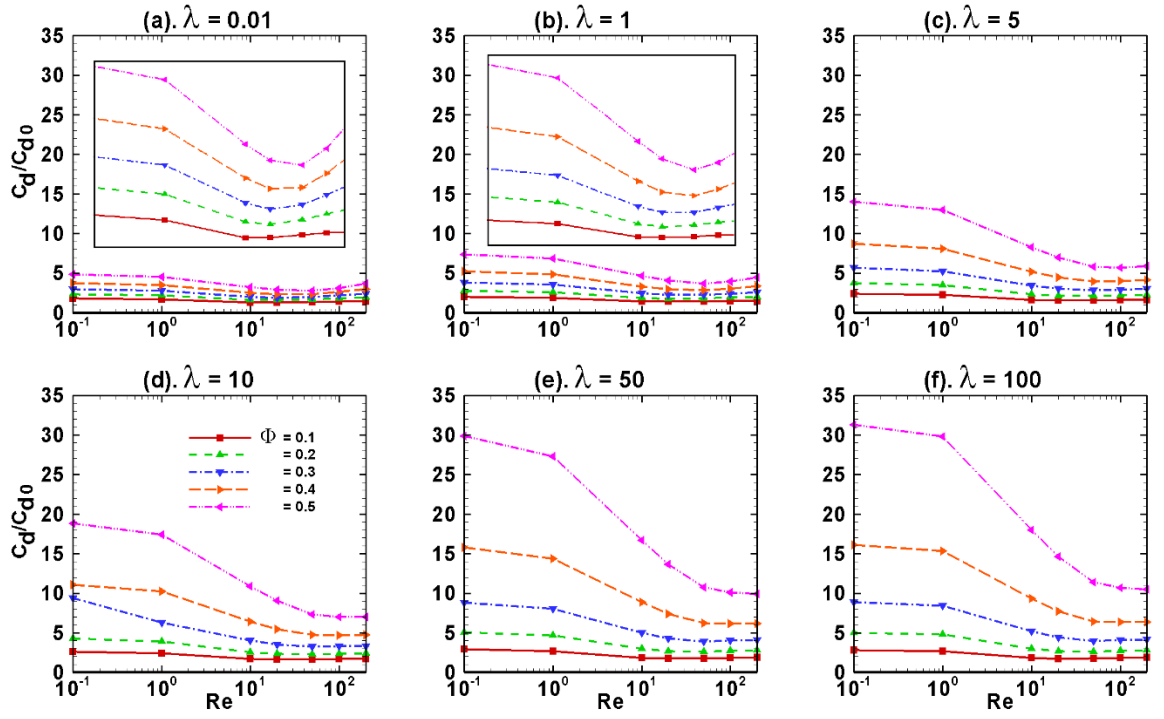

Figure 6.54 Ratio of total drag coefficients of assemblages of spheres to that of an unconfined single sphere.

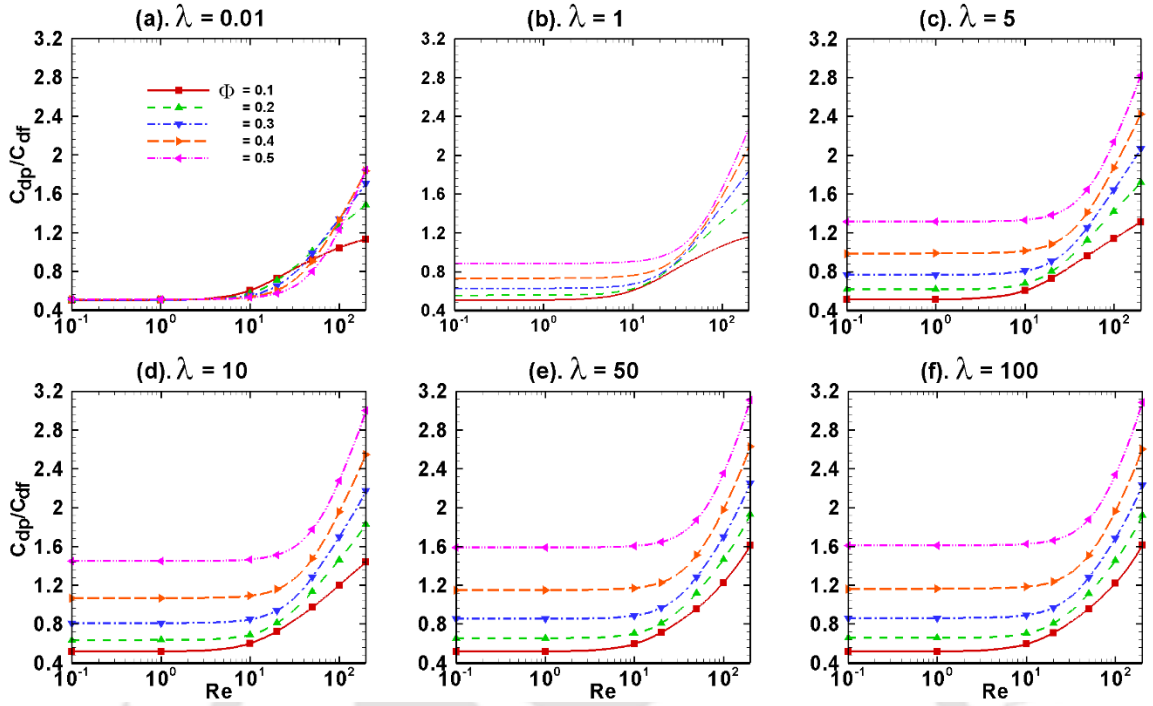

Figure 6.55 Ratio of pressure to friction drag coefficients of assemblages of spheres.

6.6. Momentum Transfer Study of Assemblages of Spherical Particle in Power-law Fluids

The values of the present pertinent dimensionless parameters consider to delineate their effects on the flow and drag behavior of assemblages of spherical particles in power-law fluids with velocity slip at the interface are: *Re* = 0.1, 1, 10, 20, 50, 100, 200, *n* = 0.6, 0.8, 1, 1.2, 1.4, 1.6, *Φ* = 0.1, 0.2, 0.3, 0.4, 0.5 and λ = 0.01, 0.1, 1, 2, 5, 10, 50, 100.

6.6.1. Flow pattern

Figure 6.56 shows the streamlines (above the central line cutting each sphere in two halves) and vorticity contours (below the central line cutting each sphere in two halves) around a target sphere in an assemblage of spheres of volume fraction 0.1 in a shear-thinning fluid of power-law index (n) = 0.6 at *Re* = 0.1 for different values of the slip number (λ). In this figure maximum

and minimum values of stream function and iso-vorticity are depicted. The difference between values of any two consecutive streamlines is 0.1 and similarly difference between values of any two consecutive iso-vorticity contours is also 0.1. Because at such small value of Reynolds number, only the viscous terms are dominant leaving behind the convective terms, the streamlines are closely following the curvature of the sphere without any flow separation regardless the values of the slip parameter. Indeed the difference in streamline patterns are indistinguishable by changing the slip parameter from one value to other indicating the effect of slip number on streamlines is negligible at such small Reynolds number. The vorticity is also diffused around the sphere in the radial direction for all values of the slip parameter; but as the value of slip parameter is gradually increasing more amount of vorticity is created around the sphere as its surface gradually turns into no-slip surface from infinite slip surface. Further for λ = 1, a small void along the surface of slip sphere is observed size of which is gradually increased with the increasing slip parameter. Similarly, in **Figure 6.57**, streamlines and vorticity contours are shown at Re = 200 when Φ = 0.1 and n = 0.6 for different values of the slip parameter. Here also the maximum and minimum values of stream function and iso-vorticity are depicted. The difference between values of any two consecutive streamlines is 0.1 and similarly difference between values of any two consecutive iso-vorticity contours is also 0.1. The difference in parameters used in **Figures 6.56** and **Figure 6.57** is the difference in the value of the Reynolds number. At large value of Reynolds numbers the convective forces are dominative compared to the viscous forces and there is possibility of flow separation depending on the degree of the velocity slip at the interface. For slip parameter $\lambda \leq 5$ (**Figure 6.57(a-c)**), the streamlines are following the curved surface of the sphere without any flow separation. But for λ = 10 (**Figure 6.57(d)**), the surface of the sphere is close to no-slip behavior and a small recirculation wake is

observed in the rear of the sphere. The size of this recirculation wake is increased as the value of the slip parameter is further increased to λ = 50 (**Figure 6.57(e)**) and λ = 100 (**Figure 6.57(f)**) because of decreased slip nature of the spheres. The vorticity is also carried away in the flow direction at *Re* = 200 for all values of the slip parameter; and gradually more vorticity is created as the value of the slip parameter is gradually increased. The size of the vorticity void is also increased gradually with the slip parameter because of decreased slippage of the fluid at fluid-solid interface. **Figures 6.58** and **Figure 6.59** shows the streamlines and vorticity contours around a sphere in assemblages of Φ = 0.1 at *Re* = 0.1 and *Re* = 200 respectively but in shear-thickening fluids of *n* = 1.6. In this figures also maximum and minimum values of stream function and iso-vorticity are depicted. The difference between values of any two consecutive streamlines is 0.1 and similarly difference between values of any two consecutive iso-vorticity contours is also 0.1. In the case of shear-thickening fluids, at *Re* = 0.1 (**Figure 6.58**), the streamlines and iso-vorticity contours are depicting qualitatively almost similar trends as in the case of shear-thinning fluids (**Figure 6.56**) for identical value of the slip parameter but with only one major difference. The difference is that each vorticity contour display a kind of small kink around the equator line vertically moving away from the sphere and its intensity decreases as the sphere gradually becomes no-slip sphere with gradual increase in the slip parameter. At *Re* = 200, the major differences in streamlines contours in shear-thinning fluids (**Figure 6.57**) and shear-thickening fluids (**Figure 6.59**) is substantial reduction in the size of the recirculation wake in the case of shear-thickening fluids, in fact, for λ = 10, no recirculation wake is found in the case of *n* = 1.6 (**Figure 6.59**) whereas it is of considerable size in the case of *n* = 0.6 (**Figure 6.57**). Similarly in the vorticity contours as well the size of vorticity void is substantially increased in the case of shear-thickening fluids. Qualitatively similar trends are observed for

other combinations of the parameters, hence are not repeated; however briefly they can be summarized as below. The size of the recirculation wake behind spheres decreased with the decreasing slip parameter (i.e., increasing fluid slippage at the interface), decreasing Reynolds number, increasing volume fraction of particles and increasing power-law index of the fluid. In other words, in the case of the shear-thinning nature of fluids, the fluid slippage effects are nominal at the interface whereas reverse is true for the case of the shear-thickening fluids for identical combinations of the Reynolds number and particles volume fraction.

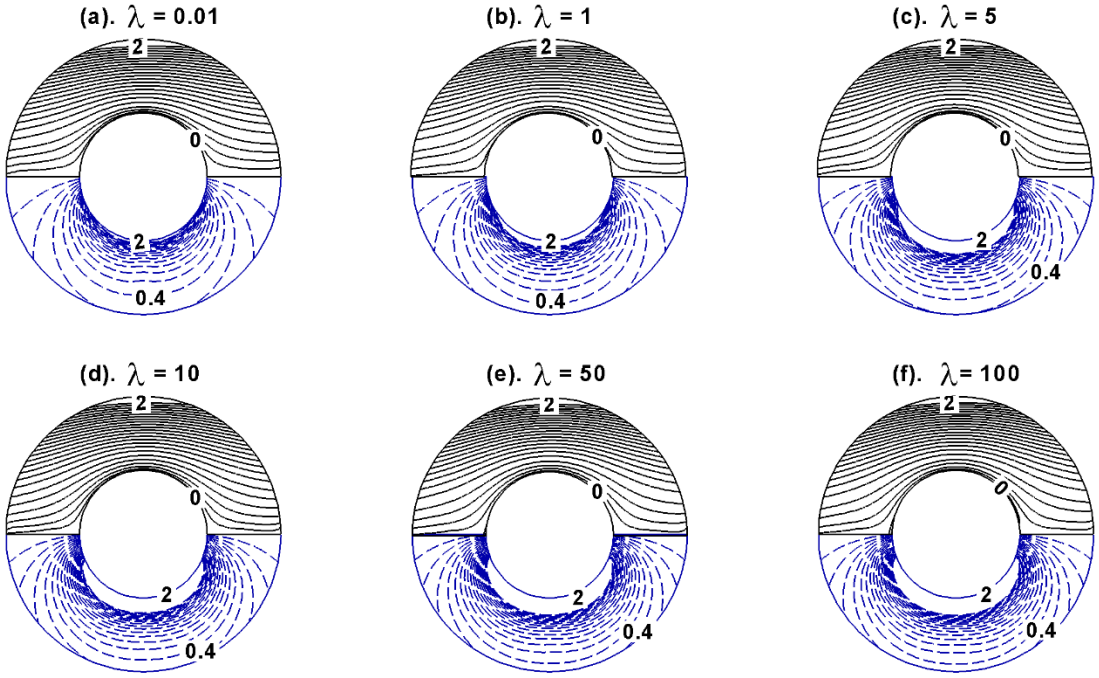

Figure 6.56 Streamlines (upper half) and vorticity (lower half) contours in assemblage of spheres of volume fraction = 0.1, n = 0.6 at Re = 0.1.

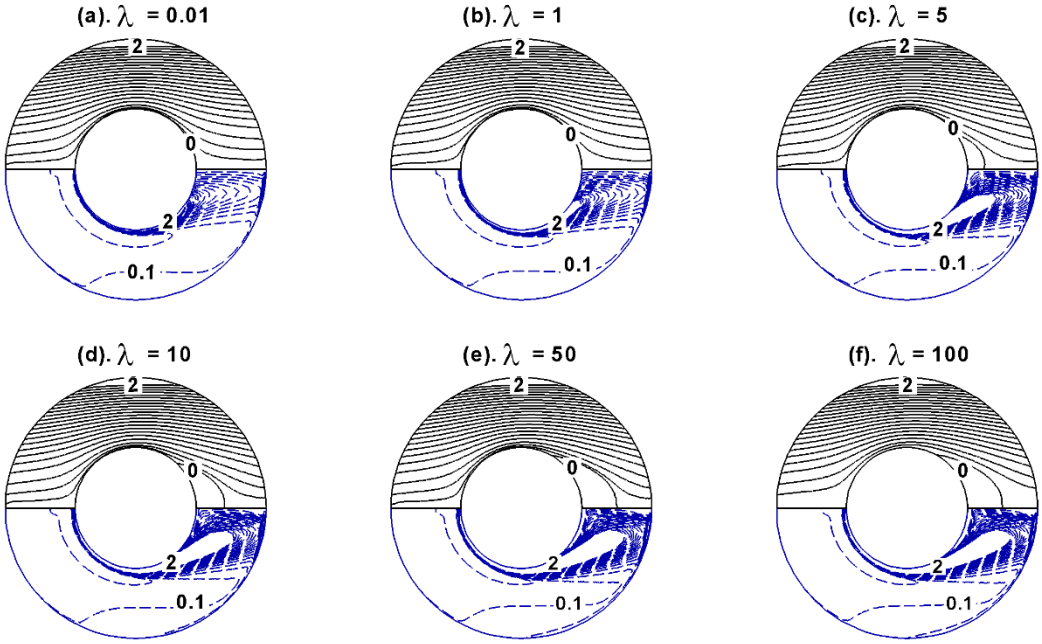

Figure 6.57 Streamlines (upper half) and vorticity (lower half) contours in assemblage of spheres of volume fraction = 0.1, n = 0.6 at Re = 200.

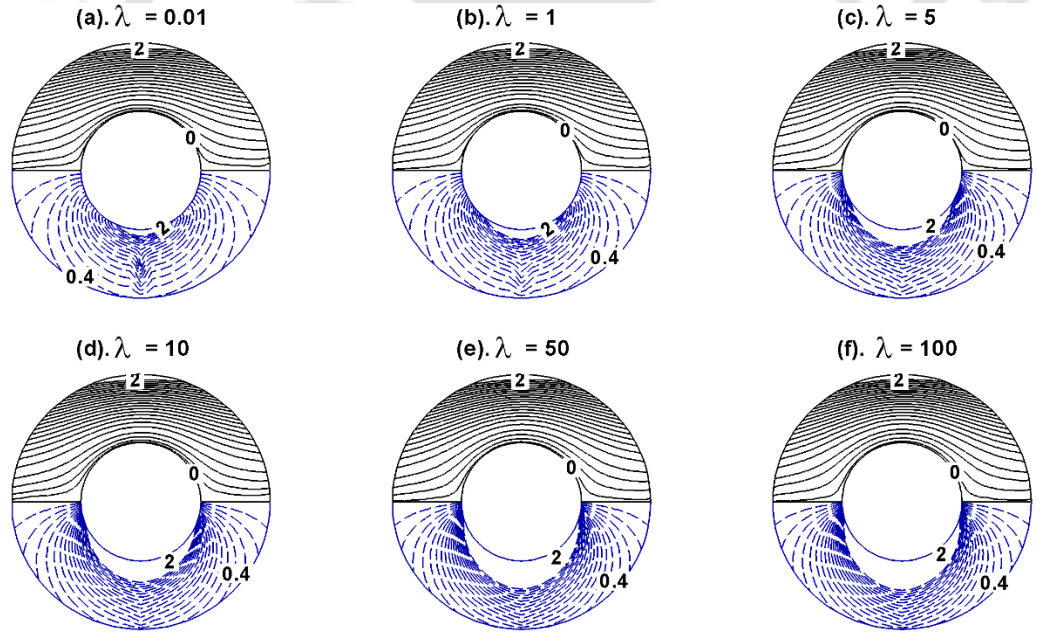

Figure 6.58 Streamlines (upper half) and vorticity (lower half) contours in assemblage of spheres of volume fraction = 0.1, n = 1.6 at Re = 0.1.

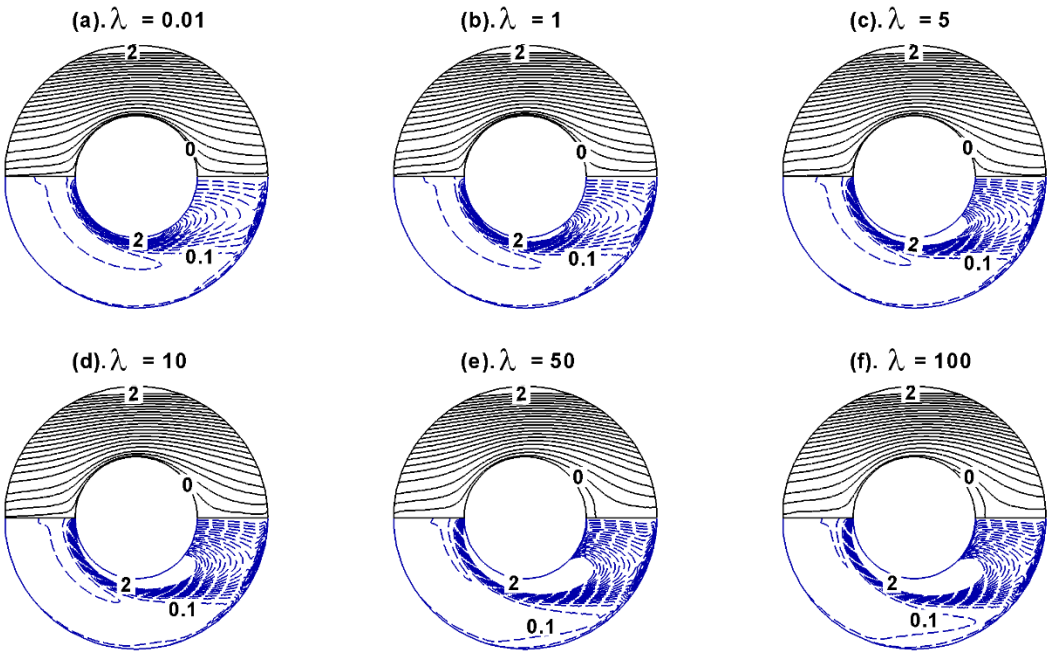

Figure 6.59 Streamlines (upper half) and vorticity (lower half) contours in assemblage of spheres of volume fraction = 0.1, n = 1.6 at Re = 200.

6.6.2. Surface pressure distribution

From the steady fully converged pressure field obtained in the complete computational domain the pressure along the surface of the spheres is extracted for various combinations of the Reynolds number, volume fraction of spheres, slip parameters and the power-law index; and are discussed here. The surface pressure coefficient is in general maximum at the point on the solid object where the first fluid particle hits the solid object, i.e., at front stagnation point, and this pressure coefficient gradually decreases to a minimum value at around the equator point and then again gradually increases indicating the pressure recovery depending the values of the pertinent parameters. **Figure 6.60** shows the distribution of surface pressure coefficient around spheres in assemblages of different volume fractions at Re = 100 in shear-thinning fluids (n = 0.6) (**Figure 6.60(a-c)**) and shear-thickening fluids (n = 1.6) (**Figure 6.60(d-f)**). In the case of

shear-thinning fluids and volume fraction 0.1 (**Figure 6.60(a)**), in the front half of the sphere the local pressure coefficient value increases with the increasing slip parameter. But in the rear half of the sphere crossover trends in local pressure coefficient values are observed for slip parameter > 5 because of flow separation occurred due decreasing slippage effect; however, for slip parameter < 5 there is no such crossover because of no recirculation wake formed for low values of the slip parameter. As the value of the volume fraction increased to 0.3 (**Figure 6.60(b)**) and 0.5 (**Figure 6.60(c)**), no such crossover trends in the rear half of the sphere are observed because of no recirculation wake formation for any value of the slip parameter even at *Re* = 100. In the case of shear-thickening fluids (**Figure 6.60(d-f)**), such crossover is not observed for any combination of the particle volume fraction and slip parameter but the pressure recovery is poor i.e., the difference between the pressure coefficient values at front and rear stagnation points is much larger than in the case of shear-thinning fluids (**Figure 6.60(a-c)**). This indicates that the pressure drag coefficient would be much larger in the case of shear-thickening fluids than in the case of shear-thinning fluids. **Figure 6.61** shows Surface pressure coefficient on the assemblage of spheres of volume fraction = 0.1 in shear thinning (*n* = 0.6) (**Figure 6.61(a-c)**) and shear thickening (**Figure 6.61(d-f)**) fluids at different values of Reynolds number. As the Reynolds number increases, there is significant recovery of pressure in the rear half of the sphere because of recirculation wake formation. Other trends are similar as that observed in **Figure 6.60(a-c)** (*n* = 0.6) and **Figure 6.60(d-f)** (*n* = 1.6).As well qualitatively similar trends are observed for other combinations of the Reynolds number, power-law index, volume fraction and slip parameter.

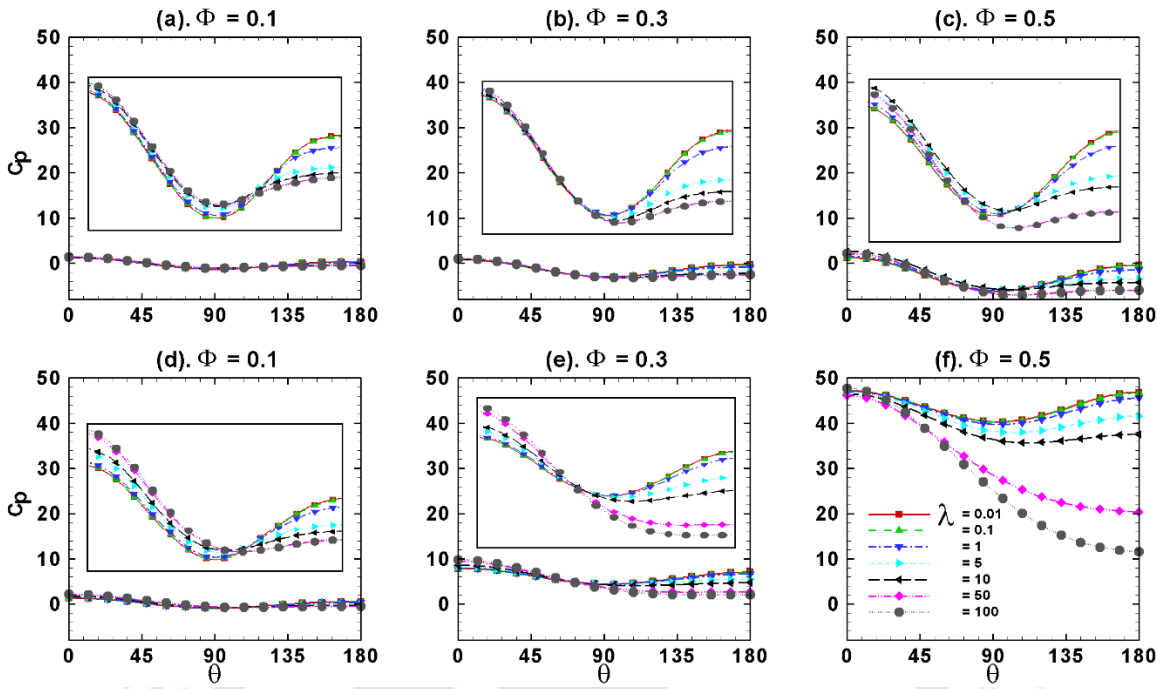

Figure 6.60 Surface pressure coefficient on the surface of particles in assemblage in shear thinning fluid (n = 0.6) (a – c) and shear thickening (n = 1.6) (d – f) at Re = 100.

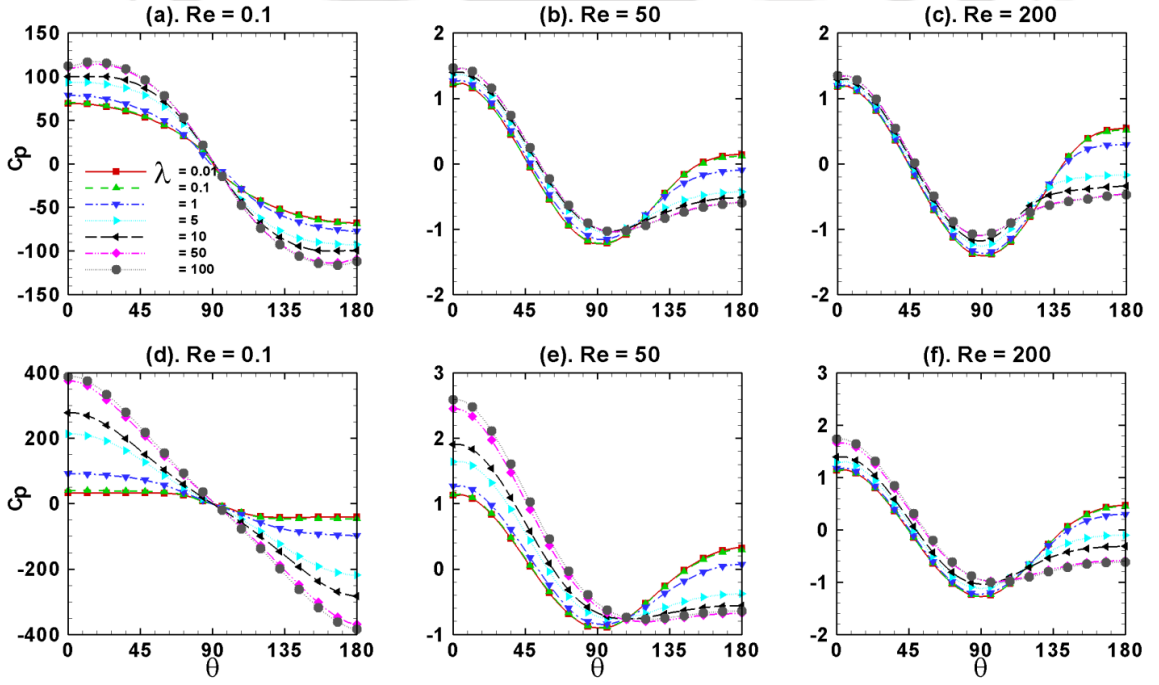

Figure 6.61 Surface pressure distribution on the spheres at different value of Reynolds number for volume fraction = 0.1, n = 0.6 (a – c) and n = 1.6 (d – f).

6.6.3. Surface vorticity distribution

The vorticity along the surface of the sphere is extracted from the vorticity contours obtained in the entire computational domain by solving equation (3.21) using the fully converged velocity profile for different combinations of the dimensionless numbers involved in this work. The vorticity is in general zero at the front stagnation point, then it increases to a maximum value at around the equator, then gradually falls to zero value at the rear stagnation point provided if there is no recirculation wake formation in the rear of the sphere. In the case of recirculation wake formation, the surface vorticity change its slope or sign at the flow separation point and forms a secondary curve between the point of flow separation and the rear stagnation point. Similar trends are seen in **Figures 6.62** presents the distribution of the surface vorticity around sphere in assemblages of different volume fractions at Re = 100 in shear-thinning fluids (n = 0.6) (**Figure 6.62(a-c)**) and shear-thickening fluids (n = 1.6) (**Figure 6.62(d-f)**). In the case of shear-thinning fluids and volume fractions of 0.1 (**Figure 6.62(a)**), secondary curves due to the presence of recirculation wakes are seen only for slip parameters > 10; however in the case of volume fractions 0.3 (**Figure 6.62(b)**) and 0.5 (**Figure 6.62(c)**), no such secondary curves are seen even for slip parameters > 10 because of no recirculation wake formation even at Re = 100 when volume fraction > 0.2. But in the case of shear-thickening fluids (**Figure 6.62(d-f)**), no matter whatever is the value of the volume fraction of present range of conditions, there is no secondary curve because of no recirculation wake formation for any value of the slip parameter. However for slip parameter < 1, around the equator the primary vorticity curve loses its smoothness because of kink seem in vorticity contours in shear-thickening fluids (**Figure 6.58** and **Figure 6.59**). Qualitatively similar trends are seem for other combinations of the pertinent dimensionless parameters. **Figure 6.63** shows surface vorticity distribution on the assemblage of spheres of

volume fraction = 0.1 in shear thinning, n = 0.6 (**Figure 6.63(a-c)**) and shear thickening, n = 1.6 (**Figure 6.63(d-f)**) fluids at different value of Reynolds numbers. Qualitatively similar trends observed as in **Figure 6.62(a-c)** (n = 0.6) and **Figure 6.62(d-f)** (n = 1.6). This figure represent the effect of Reynolds number on surface vorticity distribution, it can be seen from **Figure 6.63** vorticity increases around the spheres in assemblages with increasing Reynolds number. In summary the local value of the vorticity increases with the increasing slip parameter, with increasing particle volume fraction, with the increasing Reynolds number but with the decreasing power-law index.

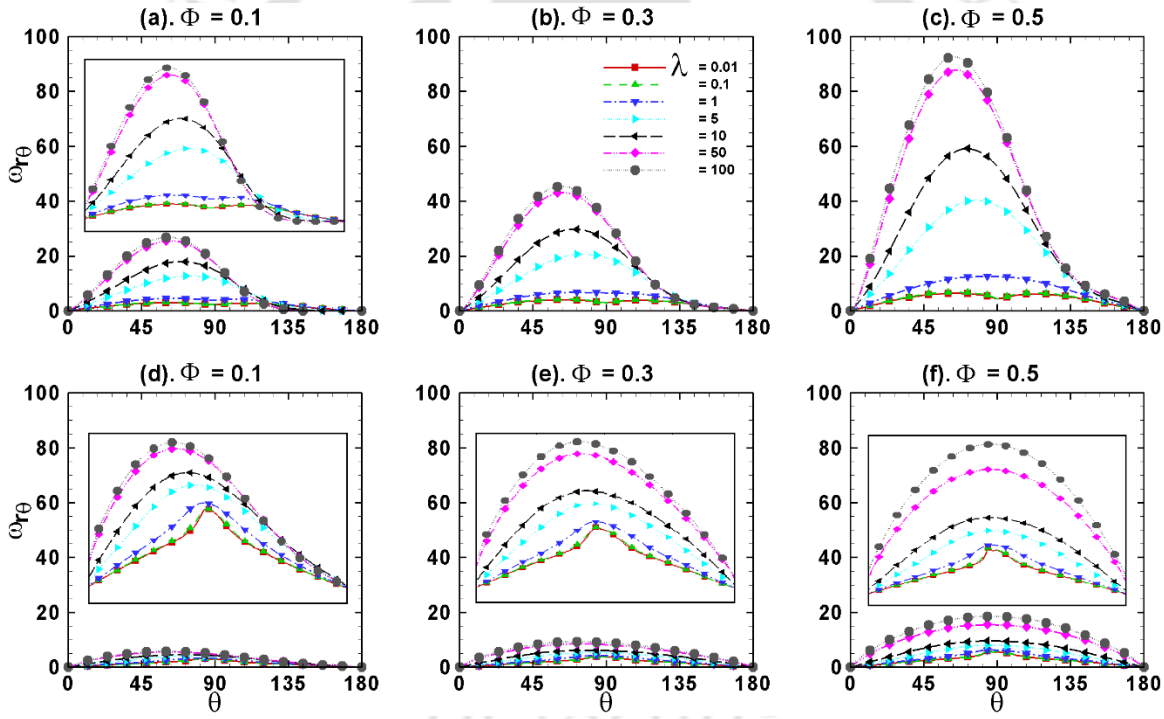

Figure 6.62 Surface vorticity distribution on the spheres in assemblage in shear thinning fluid (n = 0.6) (a – c) and shear thickening (n = 1.6) (d – f) at Re = 100.

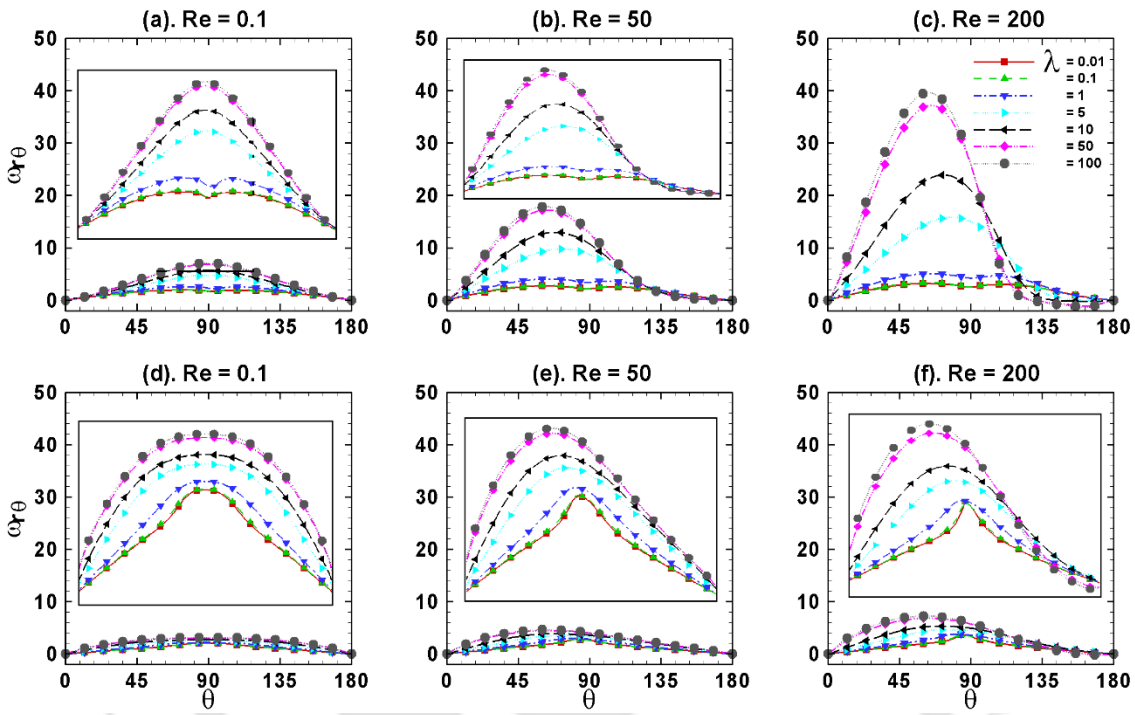

Figure 6.63 Surface vorticity distribution on the spheres at different value of Reynolds number for volume fraction = 0.1, n = 0.6 (a – c) and n = 1.6 (d – f).

6.6.4. Surface viscosity distribution

For non-Newtonian fluids the viscosity varies from point to point in the entire computational domain according to the local shear stress – shear rate combination. The viscosity in the entire domain is obtained by substituting the final steady velocity field in equation (3.7) and then its values along the surface of the spheres is extracted for different combinations of dimensionless numbers; and a few details are presented herein. **Figure 6.64** shows the distribution of viscosity of shear-thinning fluids of n = 0.6 (**Figure 6.64(a-c)**) and of shear-thickening fluids of n = 1.6 (**Figure 6.64(d-f)**) at Re = 20 for different values of the volume fraction of spheres and slip parameter. In the case of shear-thinning fluids and volume fraction of Φ = 0.1 (**Figure 6.64(a)**), for slip parameter, $\lambda \leq 1$, the local value of viscosity at the front stagnation point is minimum, then it gradually increases to a local maximum value at around equator and finally it decreases

gradually to attain a minimum local value at the rear stagnation point. But in the case of slip parameter > 1, from a maximum local value at the front stagnation point, the surface viscosity gradually decreases to a minimum value at around equator and then finally reaches a local maximum value at the rear stagnation point. The other difference is that for slip parameter < 1, the local maximum value at the equator forms a relatively sharp peak at around equator; whereas for slip parameter > 1, there is no local minimum at around the equator, i.e., the change in surface viscosity is smooth between two end points. As the particle volume fraction gradually increases, there is no much change in the case of slip parameter < 1 but for slip parameter > 1 the smooth curve slightly become flatter; however, for $\lambda = 1$, surprisingly the surface viscosity is more or less constant like of a Newtonian fluid. In the case of shear-thickening fluids, qualitatively opposite trends are seen compared to the cases of shear-thinning fluids for all values of the slip parameter except for slip parameters of 5 and 10. Qualitatively similar trends are seen for other combinations of the Reynolds number, power-law index, and volume fraction and slip parameter with only differences in local minimum or local maximum values at different locations along the surface of the spheres. **Figure 6.65** shows the effect of power-law index and slip parameter on the viscosity distribution for different value of volume fraction spheres in shear thinning ($n = 0.6$) (a – c) and shear thickening ($n = 1.6$) (d – f) fluids at $Re = 200$. For $\lambda \leq 1$, for shear-thinning fluids ($n = 0.6$) and shear-thickening fluids ($n = 1.6$) the trends are similar as in the case of for shear-thinning fluids ($n = 0.6$) (**Figure 6.64(a-c)**) and shear-thickening fluids ($n = 1.6$) **Figure 6.64(d-f)** at $Re = 20$. However, for moderate to large values of slip parameters a secondary curve is appears at the rear end of spheres of volume fraction $\Phi = 0.1$ for shear-thinning ($n = 0.6$) and shear-thickening ($n = 1.6$) fluids at $Re = 200$, because of presence of recirculation wake in the rear end of the sphere.

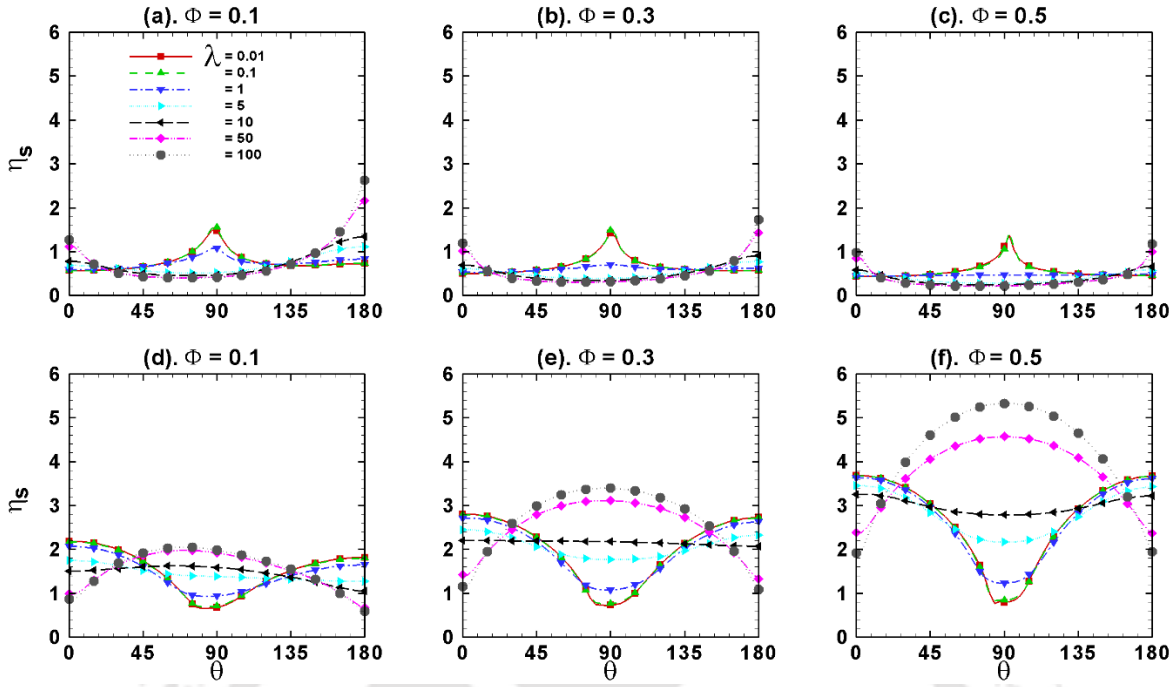

Figure 6.64 Surface viscosity distribution on the slip sphere at different value of volume fraction of dispersed phase at *Re* = 20 for n = 0.6 (a – c) and n = 1.6 (d – f).

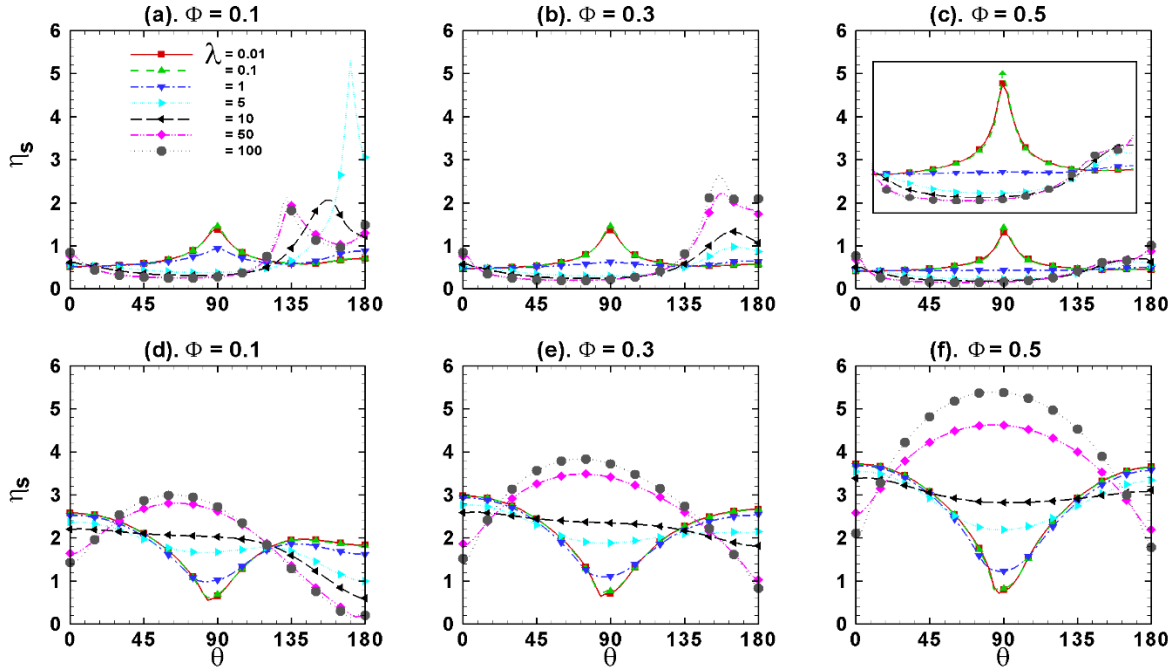

Figure 6.65 Surface viscosity distribution on the slip sphere at different value of volume fraction of dispersed phase at *Re* = 200 for *n* = 0.6 (a – c) and *n* = 1.6 (d – f).

6.6.5. Surface velocity distribution

Since along the surface of the sphere, the linear slip velocity boundary condition is used here in this study, the interface possesses some amount of tangential velocity varying with slip parameter, Reynolds number, volume fraction of spheres and the power-law index. The tangential velocity along the surface is extracted from the same velocity component obtained in the entire computational domain and is presented here as function of pertinent parameters. The surface velocity is zero at the front stagnation point and it gradually increases along the surface up to equator and then it gradually decreases to zero value at the rear stagnation point. The maximum surface velocity at around equator is large for small values of the slip parameter (i.e., large fluid slippage) and it decreases with the increasing slip parameter, i.e., with the decreasing fluid slippage at the surface. However, except the stagnation points, the local values of the surface velocity are strong functions of not only the slip parameter but also of the Reynolds number, particle volume fraction and the power-law index of the fluids. **Figure 6.66** shows the effect of slip parameter on the distribution of surface velocity at Re = 20 for different values of the slip parameter and the particle volume fraction in the assemblages in shear-thinning fluids of n = 0.6 (**Figure 6.66(a-c)**) and shear-thickening fluids of n = 1.6 (**Figure 6.66(d-f)**). Some observations from this figure include that the local value of the surface velocity decreases with the decreasing slip parameter, decreasing volume fraction and increasing power-law index. Qualitatively similar trends are observed for other values of the Reynolds number but the local value of the surface velocity increases with the increasing Reynolds number.

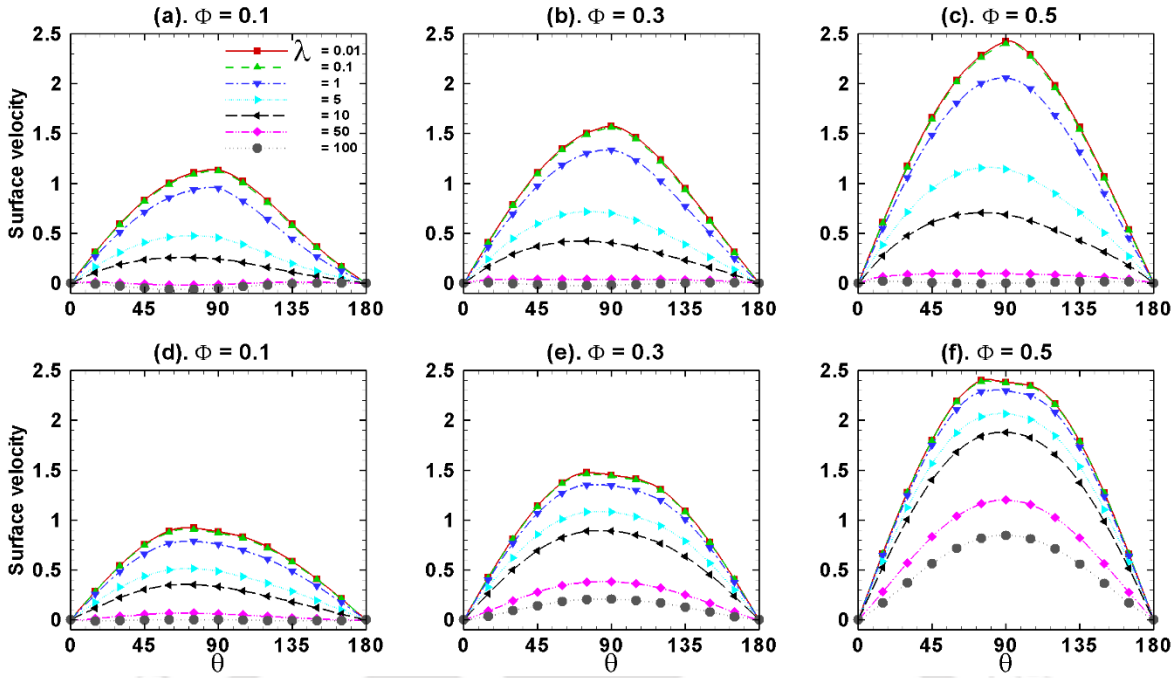

Figure 6.66 Surface velocity distribution on the surface of particles at *Re* = 20, *n* = 0.6 (a-c) and *n* = 1.6 (d-f).

6.6.6. Drag coefficient

The velocity and pressure profiles along the surface of the spheres are substituted in equations (3.17) and (3.18) to obtain the pressure and friction drag coefficients; and the summation of both values is the total drag coefficients. The individual and total drag coefficients and the ratio between both individual drag coefficients are evaluated for different combinations of the Reynolds number, slip parameter, volume fraction of spheres and the power-law index of the fluids; and are delineated here. **Figure 6.67** presents the drag coefficients of assemblages of spheres in shear-thinning fluids of *n* = 0.6 with velocity slip at the interface for different values of the slip parameter, particle volume fraction and the Reynolds numbers. Regardless the values of the slip parameter and volume fraction, the characteristic drag curve, i.e., decreasing drag coefficient with increasing Reynolds number is observed. For fixed combination of the Reynolds number and volume fraction, the drag coefficient increases with the increasing slip parameter

because of decreasing fluid slippage at the interface results in decreasing settling rate of particle. For any combination of the Reynolds number and the slip parameter, the drag coefficient is found to increase with the increasing volume fraction because of increasing hindrance from the neighboring particles.

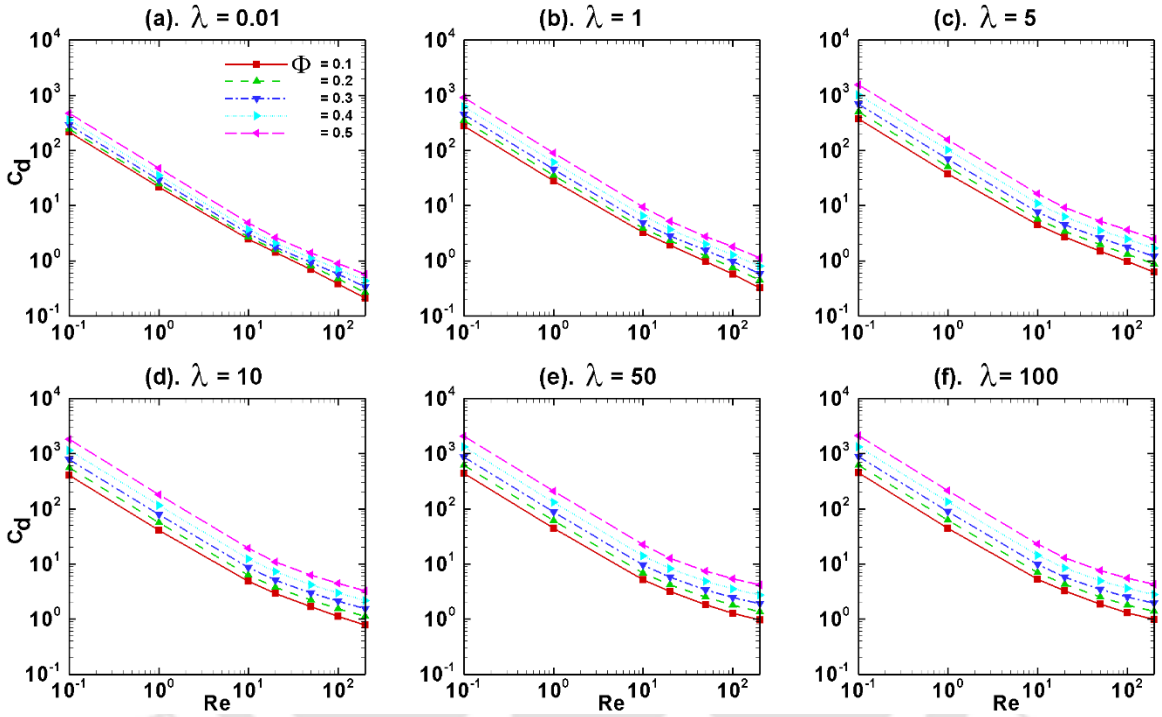

Figure 6.67 Total drag coefficients of the assemblage of particles in shear thinning fluid (n = 0.6).

Figure 6.68 shows the drag coefficients of assemblages of spheres in shear-thickening fluids of n = 1.6 with velocity slip at the interface; and qualitatively similar trends are seen as in the case of shear-thinning fluids of n = 0.6 (**Figure 6.67**); however, regardless the values of the Reynolds number, slip parameter and the volume fraction, the drag coefficient increases with the increasing power-law index because of increasing apparent viscosity of the fluid. **Figure 6.69** presents the ratio between pressure and friction drag coefficients of assemblages of spheres in shear-thinning fluids of n = 0.6 with velocity at the fluid-solid interface for different values of

the Reynolds number, slip parameter and the particle volume fraction. Regardless the values of the slip parameter and volume fraction of particles, the drag ratio is found be independent of the Reynolds number up to *Re* = 10 and thereafter it increases with Reynolds number. For all combinations of the slip parameter and the Reynolds number, the drag ratio increases with the holdup except for the case of $\lambda = 0.01$ for which mixed trends are observed with respect to holdup. Further the drag ratio increases with the increasing slip parameter irrespective of the combination of the Reynolds number and the particle volume fraction.

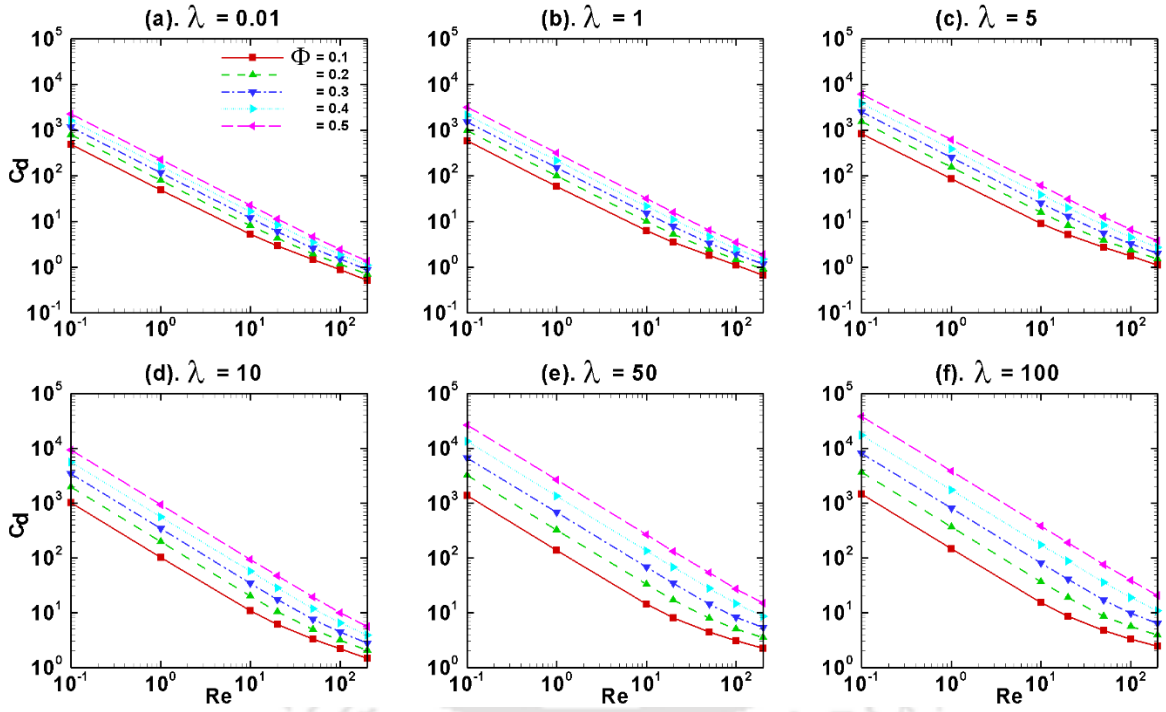

Figure 6.68 Total drag coefficients of the assemblage of particles in shear thickening fluid (*n* =1.6).

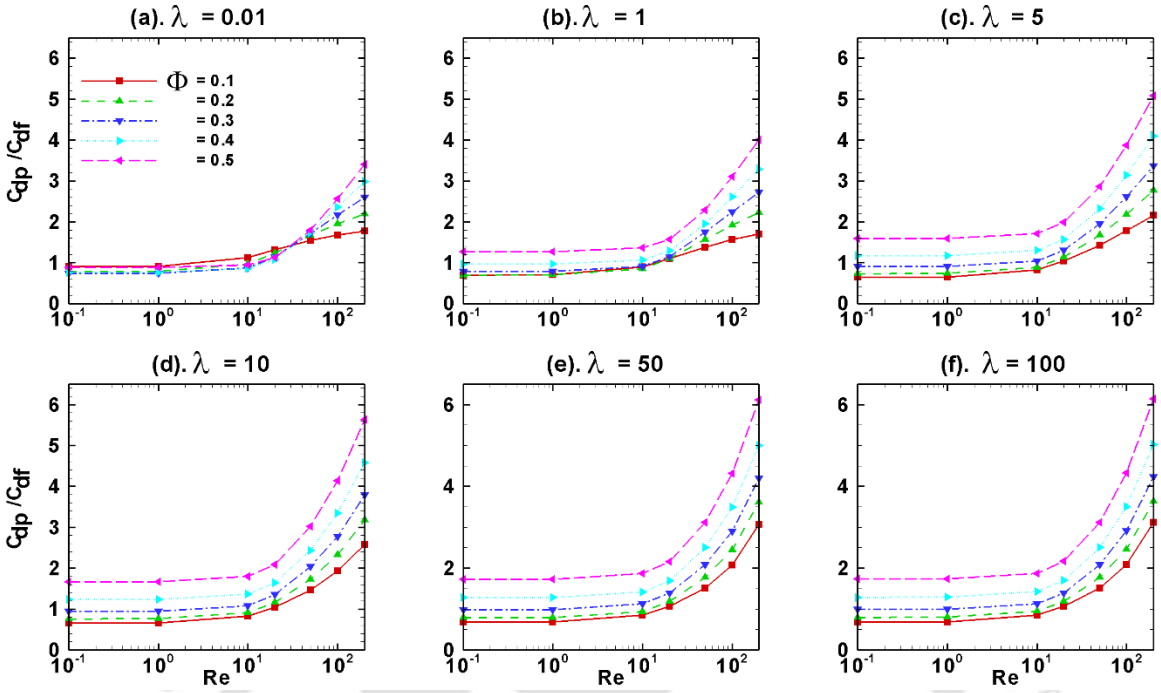

Figure 6.69 Total drag coefficients of the assemblage of particles in shear thinning fluid (*n* = 0.6).

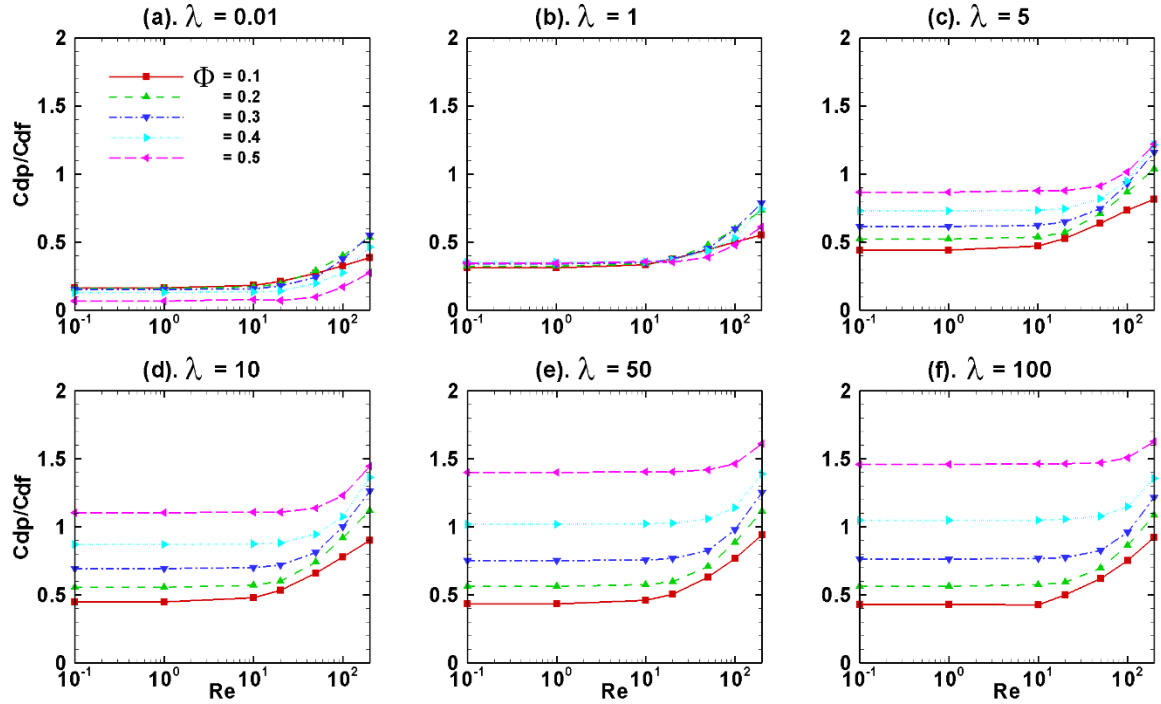

Figure 6.70 Total drag coefficients of the assemblage of particles in shear thickening fluid (*n* = 1.6).

Figure 6.70 shows the drag ratio of assemblages of spheres in shear-thickening fluids of n = 1.6 for different combinations of the Reynolds number, slip parameter and the volume fraction; and though qualitatively similar trends are seen as in the case of shear-thinning fluids but following differences are also noteworthy. For slip parameter > 1, the effect of Reynolds number on drag ratio is seems to be less in shear-thickening fluids as compared to shear-thinning fluids. The mixed trends of drag ratio with respect to the particle volume fraction is found to be significant even up to $\lambda = 1$ in the case of shear-thickening fluids.

6.7. Heat Transfer Study of Assemblages of Spherical Particles in Newtonian Fluids

In this work the following range of dimensionless parameters are considered to explore the heat transfer behavior of assemblages of spheres in Newtonian fluids with velocity slip at the interface: Re = 0.1, 1, 10, 20, 50, 100, 200; Pr = 1, 10, 50, 100; λ = 0.01, 0.1, 1, 5, 10, 50, 100; and Φ = 0.1, 0.2, 0.3, 0.4, 0.5.

6.7.1. Isotherm contours

Figure 6.71 and **Figures 6.72** shows the isotherm contours around assemblages of spherical particles of volume fraction Φ = 0.1 in Newtonian fluids for Pr = 1 (upper half) and Pr = 100 (lower half) at Re = 0.1 and Re = 100, respectively. In this figures the maximum and minimum values of isotherm contours are depicted and the difference between values of any two consecutive isotherm contours is 0.05. At the small values of Reynolds and Prandtl numbers, i.e., Re = 0.1 and Pr = 1, the isotherm contours are uniformly distributed around the spherical particles for all values of slip parameter λ. However, depending on values of Prandtl number and Reynolds number, isotherm contours may be carried in the flow direction due to convection

effects. Thus at *Pr* = 100 (lower half) and *Re* = 0.1 **(Figure 6.71),** these isotherm contours are partially carried away in the flow direction, but at *Pr* = 100 (lower half) and *Re* = 100 **(Figure 6.72)**, a large amount of isotherm contours are carried away in the flow direction and the thermal boundary layer becomes thinner. On the other hand, unlike the case of a single spherical particle, the distortion in these contours is almost negligible for both values of Reynolds numbers, because of no flow recirculation (for *Re* = 0.1) and negligible flow recirculation (for *Re* = 100) for the case of assemblages of spheres. The thickness of the thermal boundary layer has increased with an increasing slip parameter for all Reynolds numbers and thus the rate of heat transfer decreased with an increasing slip parameter λ. However, the thermal boundary layer thickness has decreased with an increasing Reynolds number to improve the rate of heat transfer.

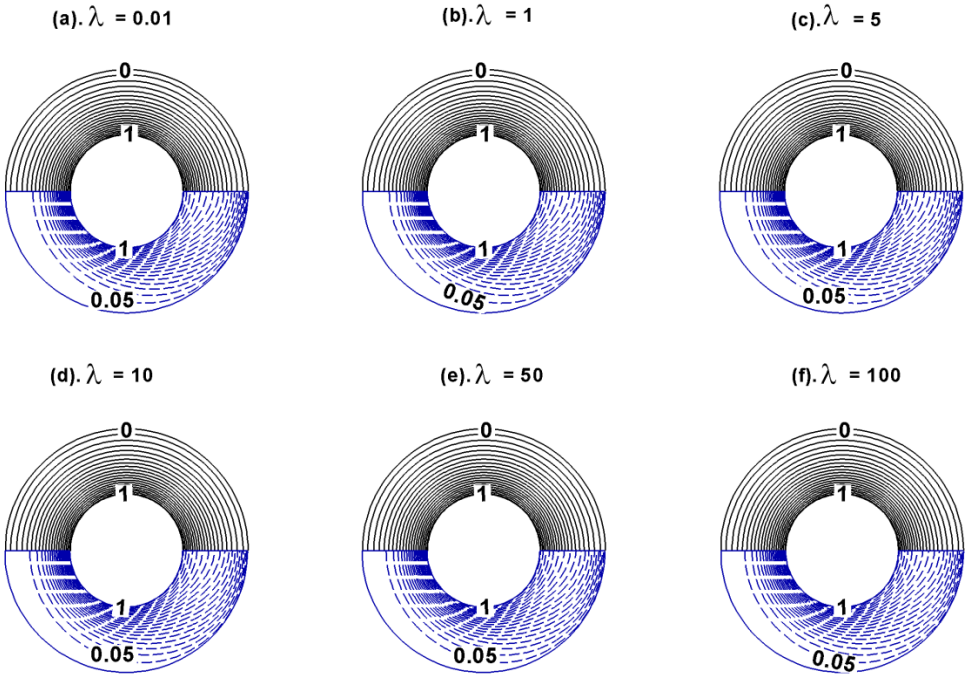

Figure 6.71 The isotherm contours for Φ = 0.1 with *Pr* = 1 (upper half) and *Pr* = 100 (lower half) at *Re* = 0.1.

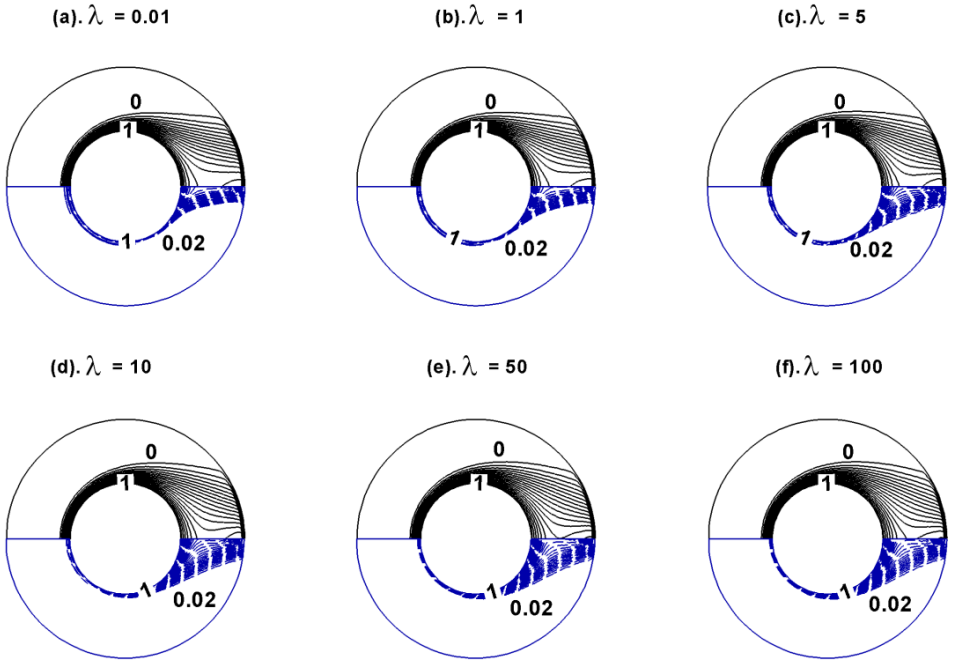

Figure 6.72 The isotherm contours for Φ = 0.1 with *Pr* = 1 (upper half) and *Pr* = 100 (lower half) at *Re* = 100.

6.7.2. Surface Nusselt number

Figure 6.73 and **Figure 6.74** shows the effect of Prandtl number *Pr* on the surface *Nu* around assemblages of spherical particles of volume fractions of dispersed phase of Φ = 0.1 and Φ = 0.5, respectively, in Newtonian fluids at *Re* = 100 for different slip parameters (λ). For a small value of Prandtl number *Pr* = 1, there is less change in the value of the Nusselt number along the surface of the particle. This is due to the fact that at such a small value of Prandtl number, the thermal boundary layer is relatively thick and the thermal diffusion is the main mode of heat transfer with little contribution from convection. As the value of the Prandtl number increased, the value of the Nusselt number increased at the front stagnant point because of thinning of the boundary layer due to the increased contribution of convective heat transfer in the front part, whereas the value of the Nusselt number at the rear end remained almost unaltered. Therefore the

expected the rate of heat transfer increases with an increasing Prandtl number; though, similar trends are observed for all values of the slip parameter.

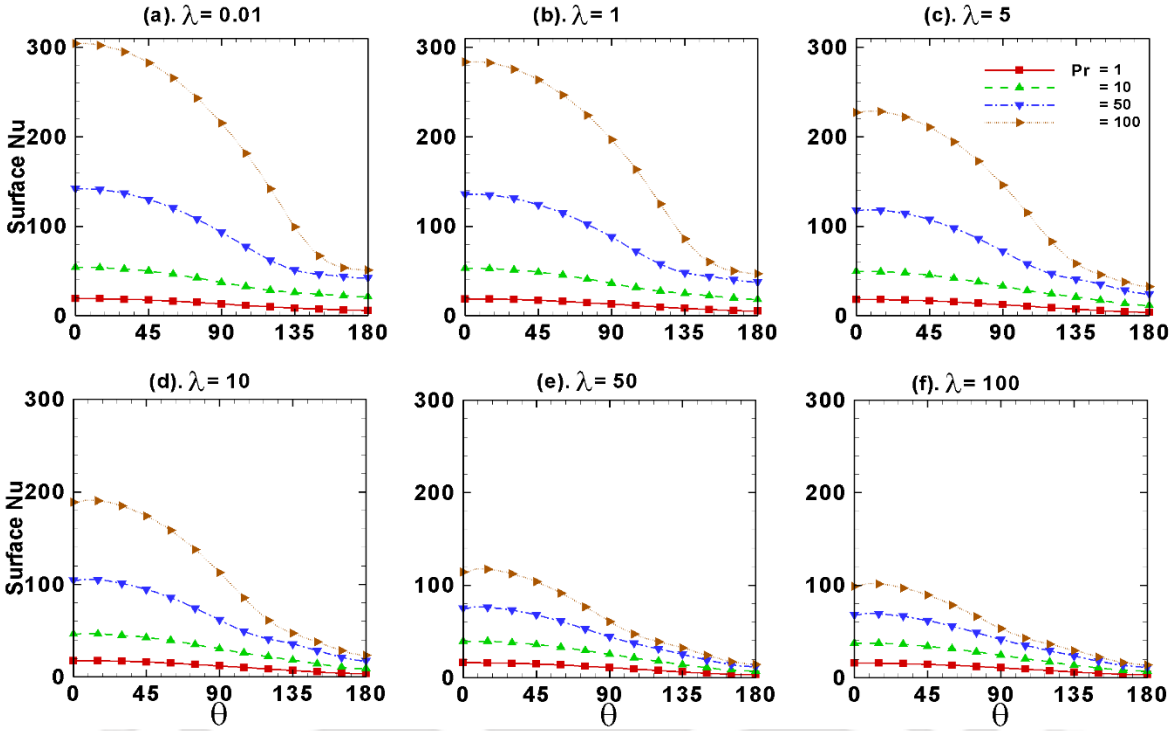

Figure 6.73 Effect of *Pr* on the surface *Nu* for Φ = 0.1 at *Re* = 100 and different slip parameters.

Figure 6.75 and **Figure 6.76** show the effect of the slip parameter λ on the surface *Nu* around the assemblages of spherical slip particles of volume fraction Φ = 0.1 in Newtonian fluids at *Re* = 0.1 and *Re* = 100, respectively, for different values of Prandtl number and slip parameter. As the value of the slip parameter increases, the value of the Nusselt number at the front stagnant point decreases whereas it is almost constant at the rear end. Therefore the overall heat transfer rate decreases as the value of slip parameter increases for all values of Φ. For all values of Prandtl number and slip parameter as one traverses from the front stagnant point to the rear end the local value of Nusselt number decreases, however for *Pr* = 1 as the value of slip parameter increases the local value of Nusselt number at the front stagnant point decreases, whereas at the rear end it

increases and thus there is a crossover of the local value on the top of the particle surface. In **Figure 6.77** and **Figure 6.78**, qualitatively similar effects are observed for other values of the volume fraction of the spheres and the Reynolds numbers.

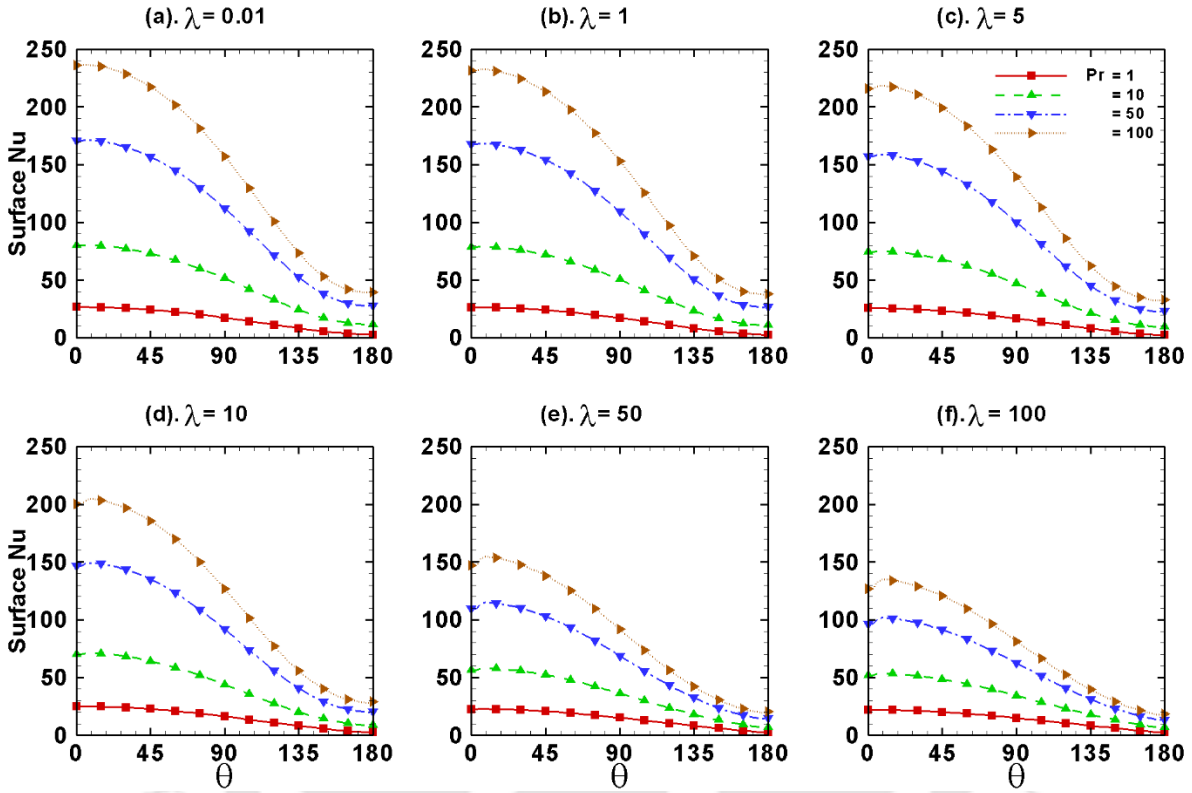

Figure 6.74 Effect of *Pr* on the surface *Nu* for Φ = 0.5 at *Re* = 100 and different slip parameters.

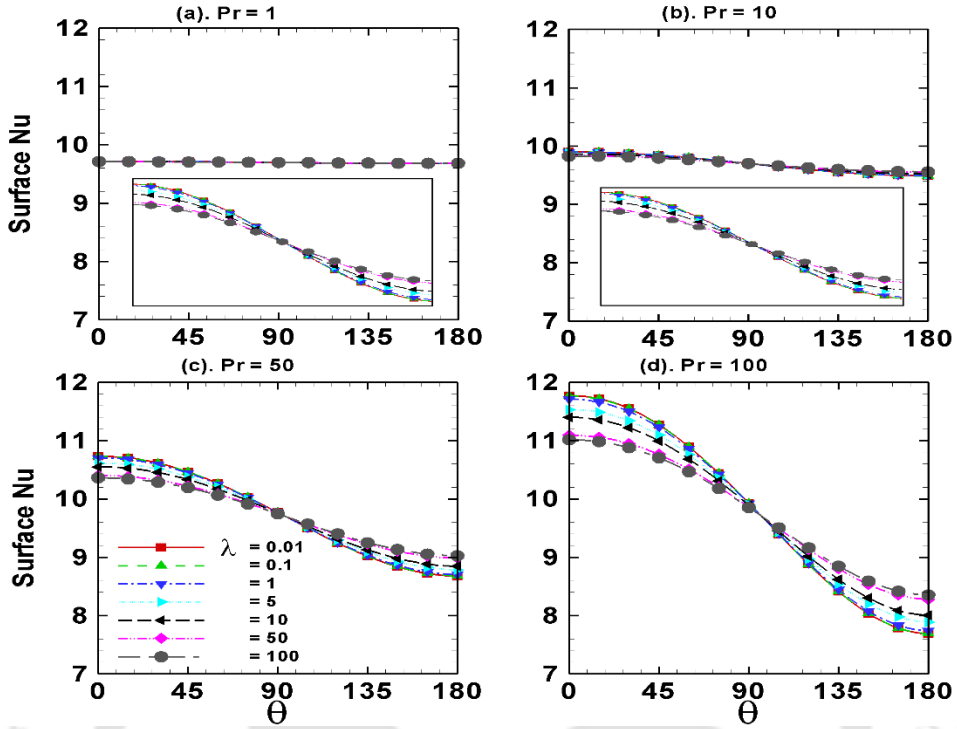

Figure 6.75 Effect of λ on surface *Nu* for $\Phi = 0.5$ at different *Pr* when *Re* = 0.1.

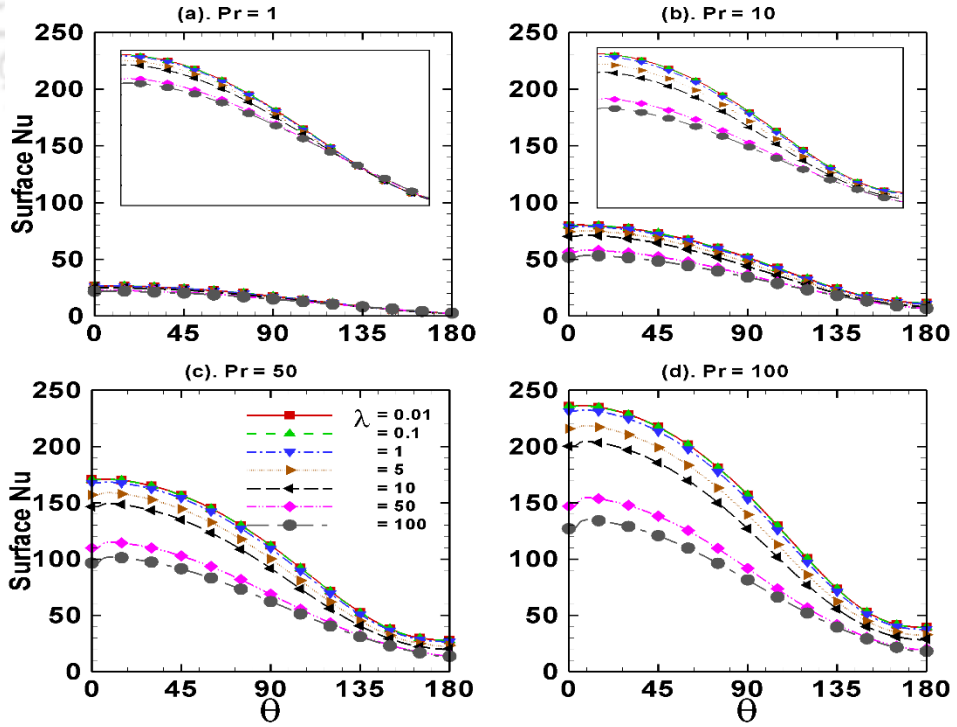

Figure 6.76 Effect of λ on surface *Nu* for $\Phi = 0.5$ at different *Pr* when *Re* = 100.

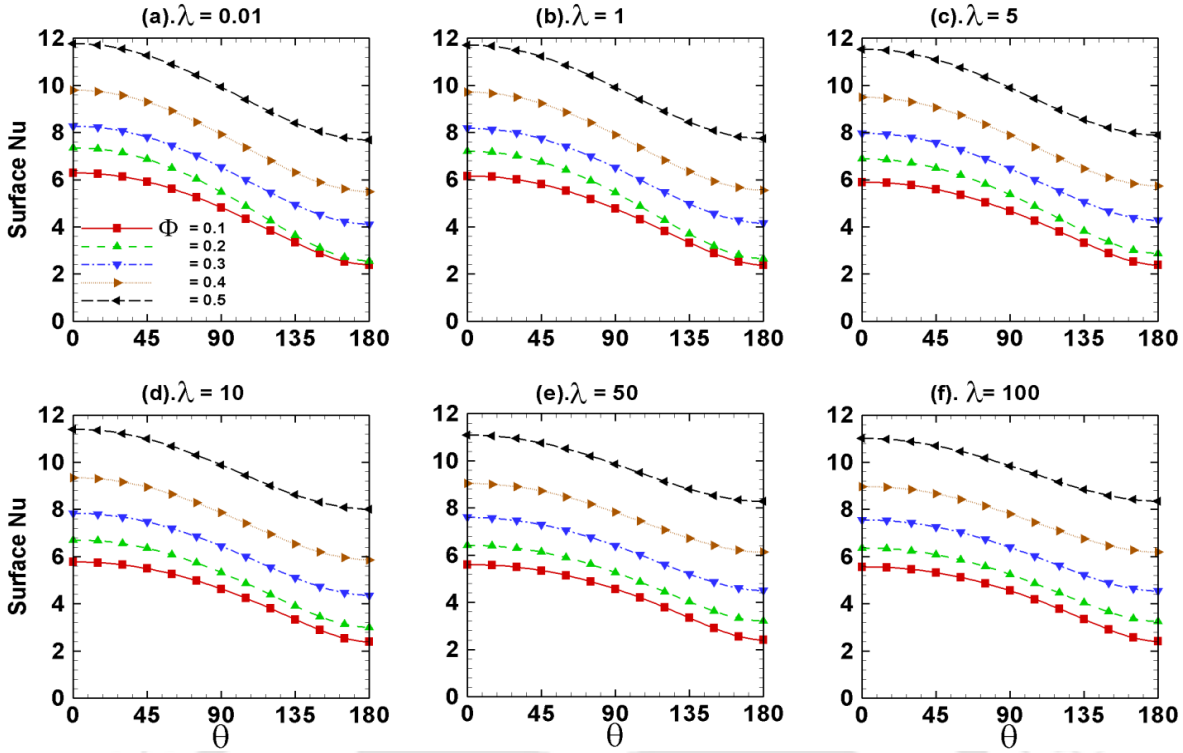

Figure 6.77 Surface Nu at *Re* = 0.1 and *Pr* = 100 for different values of *Φ*.

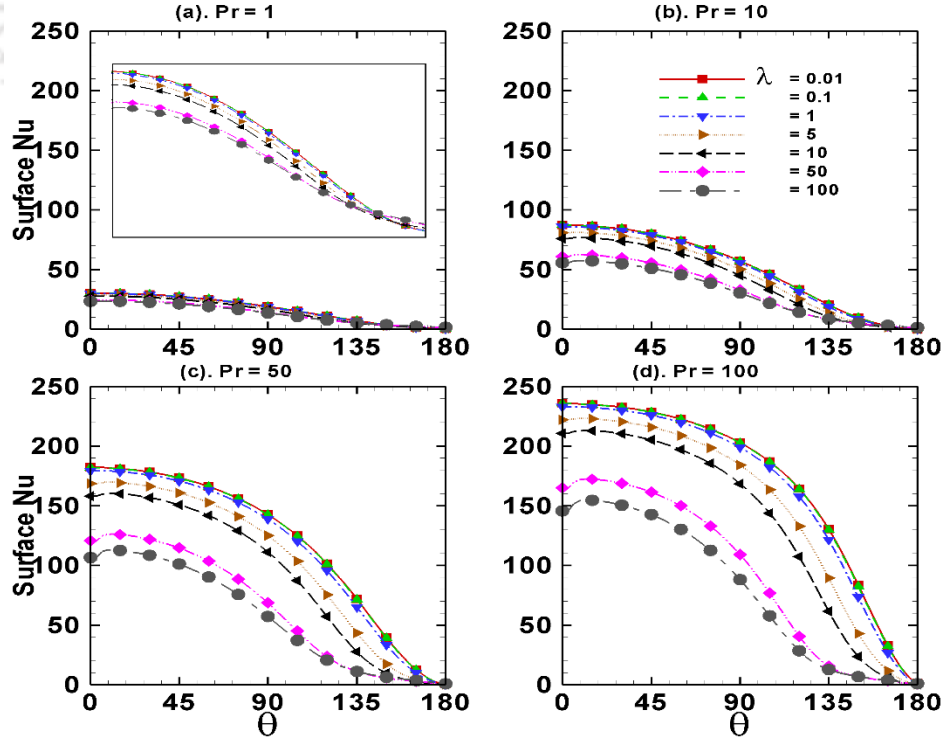

Figure 6.78 Surface Nu for *Φ* = 0.2 at *Re* = 200 for different values of Prandtl numbers.

6.7.3. Average Nusselt number

Figure 6.79 and **Figure 6.80** shows the variation of the average Nusselt numbers for Newtonian fluid flow past the assemblages of spheres of volume fraction of Φ = 0.1 and Φ = 0.5, respectively, for different Reynolds and Peclet number at various values of the slip parameter. The average Nusselt number increased with an increasing Peclet number at all Reynolds numbers, slip parameter and volume fraction of dispersed phases. However for small values of *Pe* there is a small effect of slip parameter (small λ) on the average Nusselt number. Further the average Nusselt number decreases with the increase in the slip parameter at all Reynolds numbers, Peclet numbers and volume fraction of spheres. This is due to the fact that the convection near the particle surface decreases as the particle surface approached the no-slip boundary condition for $\lambda \rightarrow \infty$ (no-slip). These characteristics can also be clearly observed in **Figure 6.81**.

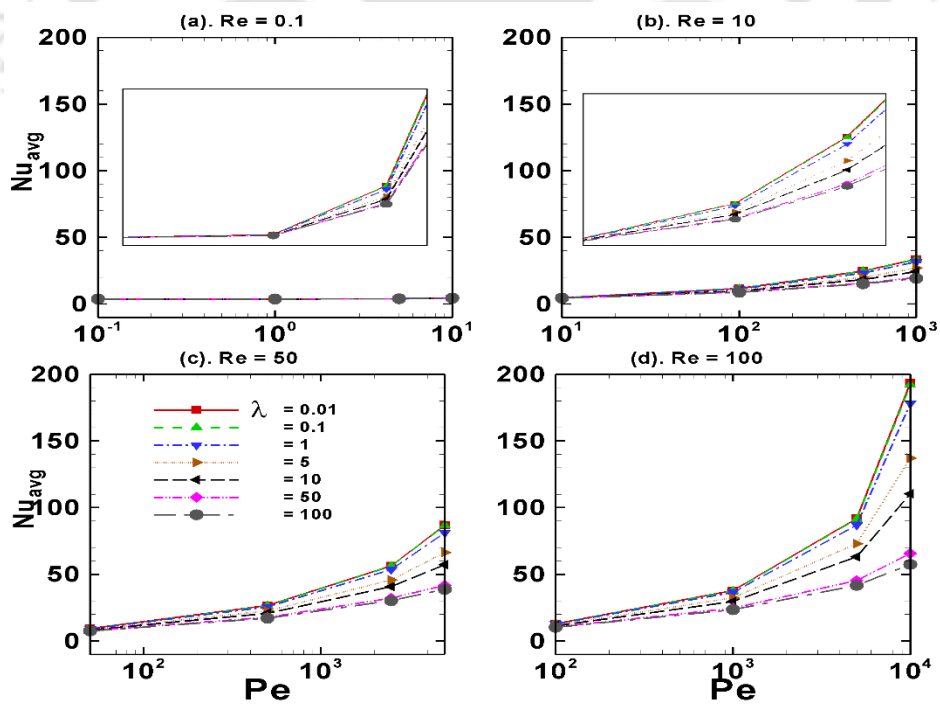

Figure 6.79 Average Nusselt numbers of assemblages of the spheres at different values of *Re* for Φ = 0.1.

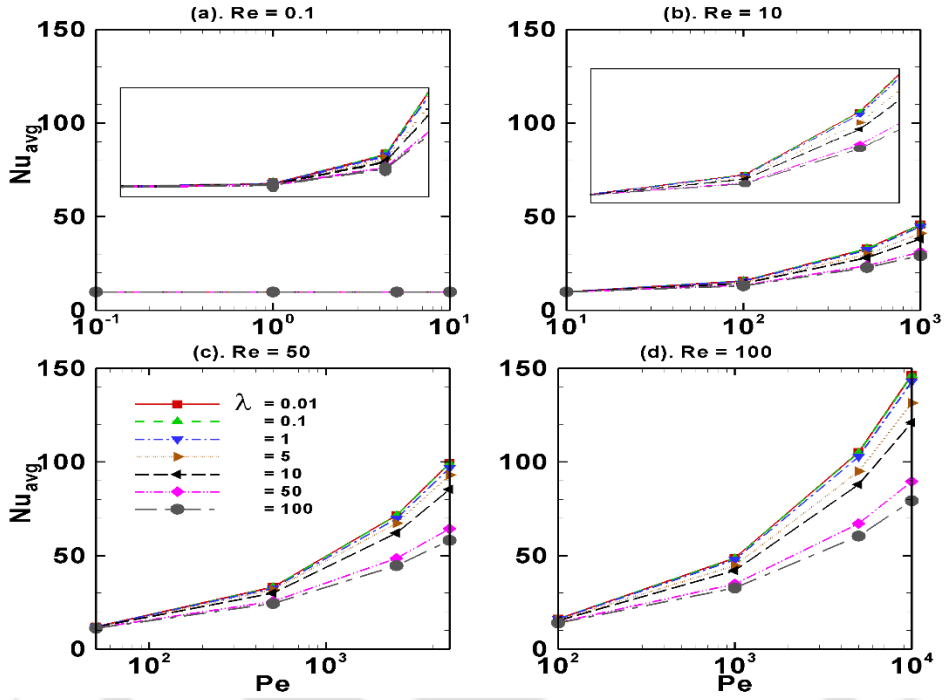

Figure 6.80 Average Nusselt numbers of assemblages of the spheres at different values of *Re* for $\Phi = 0.5$.

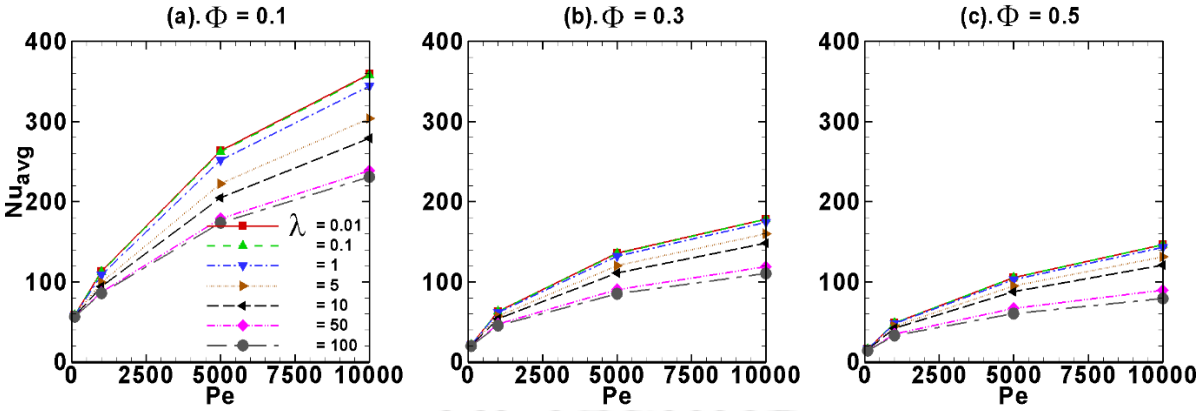

Figure 6.81 Average Nusselt numbers of assemblages of the spheres at *Re* = 100 for different values of volume fraction of smooth slip spheres.

Finally, it is useful to develop a simple predictive correlation based on the present numerical results for average Nusselt number which can be used to estimate the rate of heat

transfer from assemblages of slip spheres in new applications. The following expression was found to be satisfactory to correlate the present numerical results:

$$Nu_{avg} = 0.385 Re^{0.621} Pr^{0.562} \lambda^{-0.063} \exp(0.513\Phi) + 10.384 Pr^{0.0029} \Phi^{0.521} \quad (6.5)$$

The above equation reproduces the present numerical results with an average error of ±10.29% which rises to maximum of ±53.96 %.

6.8. Heat Transfer Study of Assemblages of Spherical Particles in Power-law Fluids

In order to delineate the effects of the Reynolds number (*Re*), the Prandtl number (*Pr*), slip parameter (λ) and the power-law index (*n*) on the isotherm contours and on the Nusselt numbers (*Nu*), the following ranges are considered: *Re*: 0.1, 1, 5, 10, 20, 50, 100, 200, *Pr*: 1, 10, 100, 1000, λ = 0.01, 0.1, 1, 5, 10, 50, 100; Φ = 0.1, 0.2, 0.3, 0.4, 0.5 and *n* = 0.6, 0.8, 1.2, 1.4, 1.6.

6.8.1. Isotherm contours

Figure 6.82 shows the isotherm contours around assemblages of spherical particles of volume fraction Φ = 0.1 in shear thinning fluid, *n* = 0.6 for *Pr* = 1 (upper half) and *Pr* = 100 (lower half) at *Re* = 0.1. In this figures the maximum and minimum values of isotherm contours are depicted and the difference between values of any two consecutive isotherm contours is 0.05. At the small value of Reynolds and Prandtl number, i.e., *Re* = 0.1 and *Pr* = 1, the isotherm contours are uniformly distributed around the spherical particles for all values of slip parameter λ. However, depending on values of Prandtl number and Reynolds number, isotherm contours may be carried in the flow direction due to convection effects. Thus at *Pr* = 100 (lower half) and *Re* = 0.1, these isotherm contours are uniformly carried away in the flow direction. **Figure 6.83** shows the isotherm contours around assemblages of spherical particles of volume fraction Φ = 0.1 in shear

thinning fluid, n = 0.6 for Pr = 1 (upper half) and Pr = 100 (lower half) at Re = 100. Here also the maximum and minimum values of isotherm contours are depicted and the difference between values of any two consecutive isotherm contours is 0.05. At Re = 100 and Pr = 1, a large amount of isotherm contours are carried away in the flow direction because of enhance the convection. As Prandtl number increases to 100, again large number of isotherm contours carried away in the direction of flow and coming closer to spheres. On the other hand, not at all like the account of a single particle, the distortion in these contours is almost negligible for both values of Reynolds numbers, because of no flow recirculation (for Re = 0.1) and negligible flow recirculation (for Re = 100) for the case of assemblages of spheres. The thickness of the thermal boundary layer has increased with an increasing slip parameter for all Reynolds numbers and thus the rate of heat transfer decreased with an increasing slip parameter λ. However, the thermal boundary layer thickness has decreased with an increasing Reynolds number and the rate of heat transfer enhance. **Figure 6.84** and **Figure 6.85** shows the isotherm contours around assemblages of spherical particles of volume fraction Φ = 0.1 in shear thickening fluid, n = 1.6 for Pr = 1 (upper half) and Pr = 100 (lower half) at Re = 0.1 and Re = 100 respectively. In this figures the maximum and minimum values of isotherm contours are depicted and the difference between values of any two consecutive isotherm contours is 0.05. Similar trends have been observed for shear thickening fluid as in the case of shear thinning fluids (**Figure 6.82** (Re = 0.1) and **Figure 6.83** (Re = 100)). Except, for fixed values of the Reynolds numbers, Prandtl numbers and slip parameter, the thermal boundary layer becomes thicker for shear thickening fluid as compared to that of shear thinning fluid. Hence, the rate of heat transfer is dominant in shear-thinning fluids followed by the Newtonian and shear-thickening fluids. In other words, the rate of heat transfer from the slip sphere to the surrounding power-law fluid decreases with the increasing power-law

index (n). Furthermore, at fixed slip parameter values and Reynolds number, the degree of distortion of isotherms increases with the decreasing power-law index. Further, the thermal boundary layer become thicker with the increasing slip parameter and decreasing Prandtl number for fixed values of the Reynolds numbers and power-law index, hence the heat transfer rate decreases with the increasing slip parameter and decreasing Prandtl number.

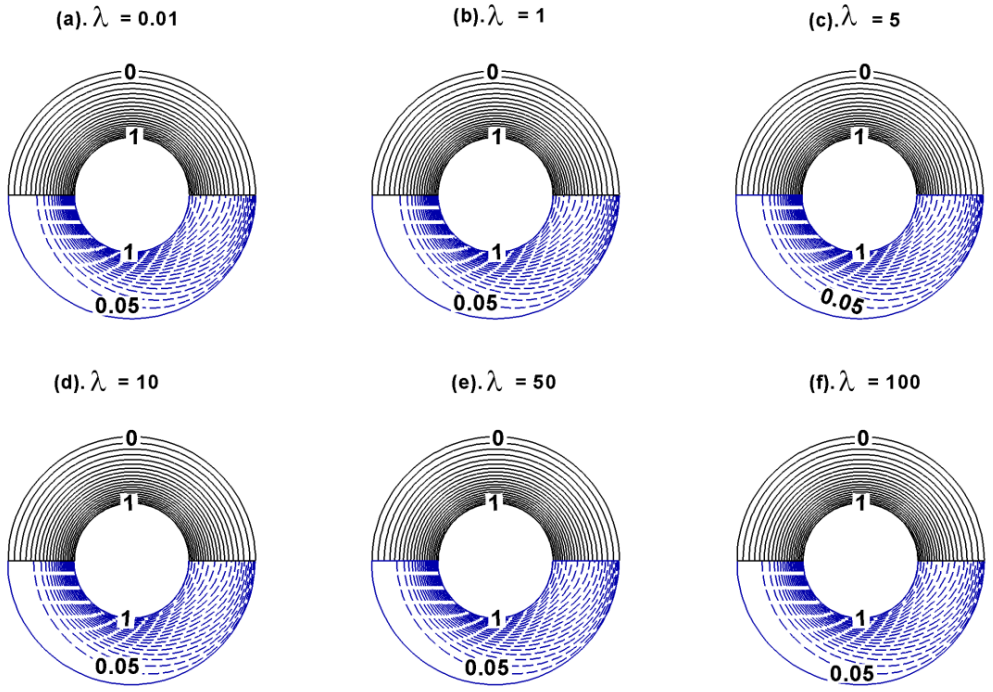

Figure 6.82 Isotherm contours around assemblages of spheres (Φ = 0.1) in power-law fluid (n = 0.6) for Pr = 1 (upper half) and Pr = 100 (lower half) at Re = 0.1.

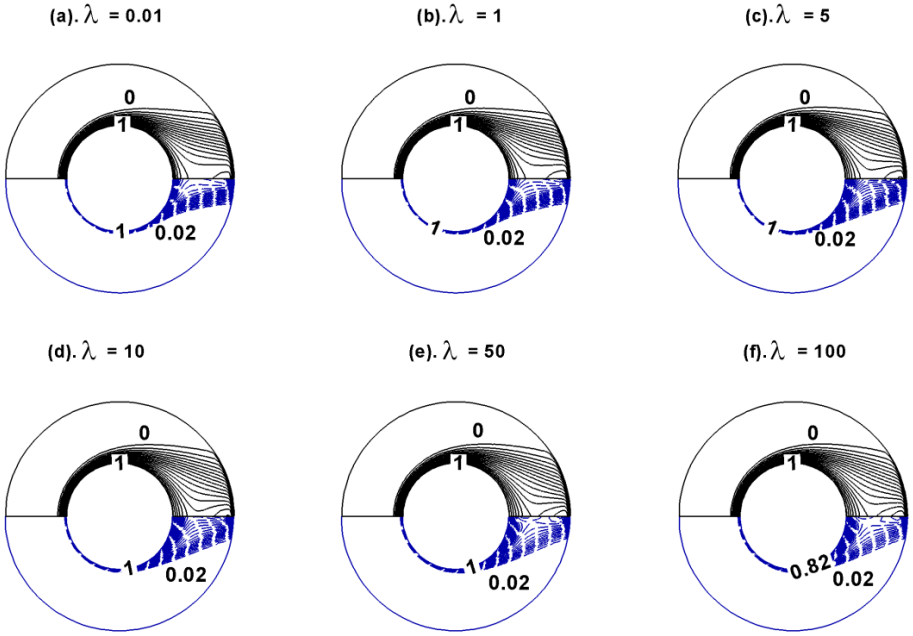

Figure 6.83 Isotherm contours around assemblages of spheres (Φ = 0.1) in power-law fluid (n = 0.6) for Pr = 1 (upper half) and Pr = 100 (lower half) at Re = 100.

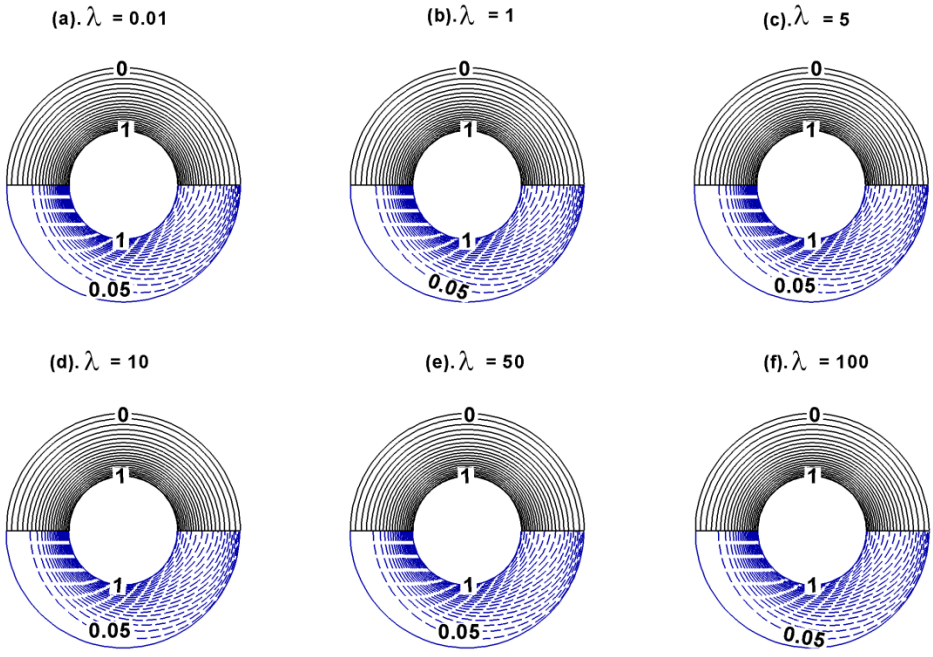

Figure 6.84 Isotherm contours around assemblages of spheres (Φ = 0.1) in power-law fluid (n = 1.6) for Pr = 1 (upper half) and Pr = 100 (lower half) at Re = 0.1.

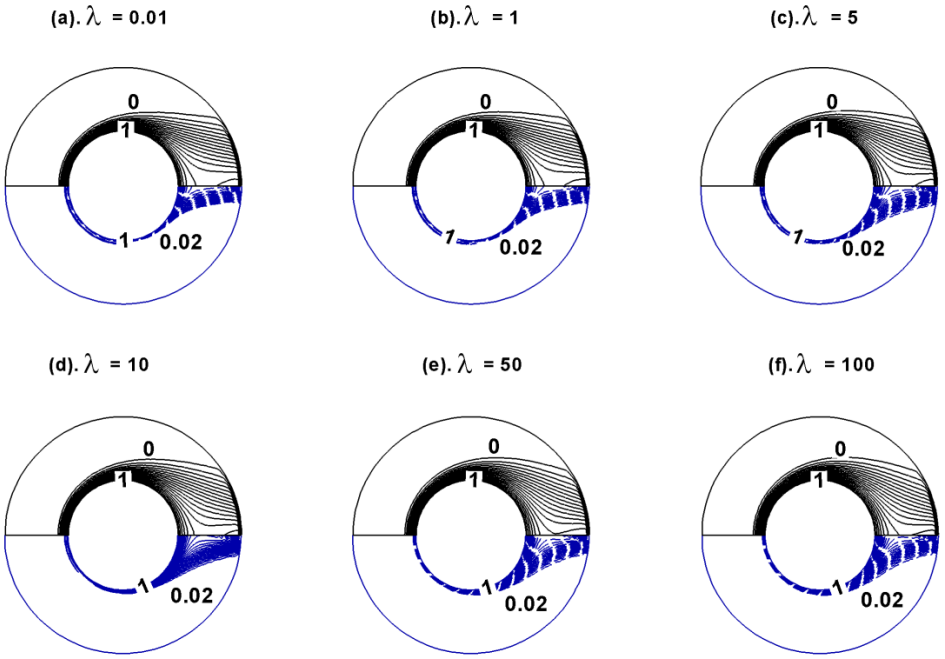

Figure 6.85 Isotherm contours around assemblages of spheres (Φ = 0.1) in power-law fluid (n = 1.6) for *Pr* = 1 (upper half) and *Pr* = 100 (lower half) at *Re* = 0.1 (a-d) and *Re* = 100 (e-h).

6.8.2. Surface Nusselt number

Figure 6.86 shows the variation of surface Nusselt number around assemblage of spheres (Φ = 0.5) in shear thinning fluid (*n* = 0.6) at *Re* = 0.1. At small value of Reynolds number *Re* = 0.1 and Prandtl number *Pr* = 1, there is much less transmutation in the Nusselt number value along the surface of the spheres. This is due to the fact that at low value of Prandtl number, the thermal boundary layer is comparatively thick and mode of heat transfer is through thermal diffusion with minute impact of convection. The thermal boundary layer is thin at the front stagnant point and it gradually thickens as one traverse to the rear stagnation point along the surface of the sphere. Because of this reason the surface Nusselt number is maximum at front stagnation point and as one traverses along the surface of spherical particle the surface Nusselt number gradually decreases up to the rear stagnation point provided the recirculation wake is absent. Similar trends

observed here also because there is no flow separation at the rear end of spheres. As the value of Prandtl number from 1 to 100 surface Nusselt number increases at the front point due to the more convection than diffusion whereas at rear end it remain almost intact. Therefore, the heat transfer rate increases with increasing Prandtl number. Similar trend are observed for all values of Prandtl number. As the value of slip parameter increases the surface Nusselt number at the front stagnant point gradually decreases whereas reverse trends observed at the rear end of spheres. **Figure 6.87** shows the variation of surface Nusselt number around assemblage of spheres (Φ = 0.5) in shear thinning fluid (n = 0.6) at Re = 100. Here, similar trends observed as in case of Re = 0.1 (**Figure 6.86**) with respect to Prandtl number but at Re = 100 as the value of slip parameter increases the surface Nusselt number decreases at the front stagnant point as well as at the rear end of spheres.

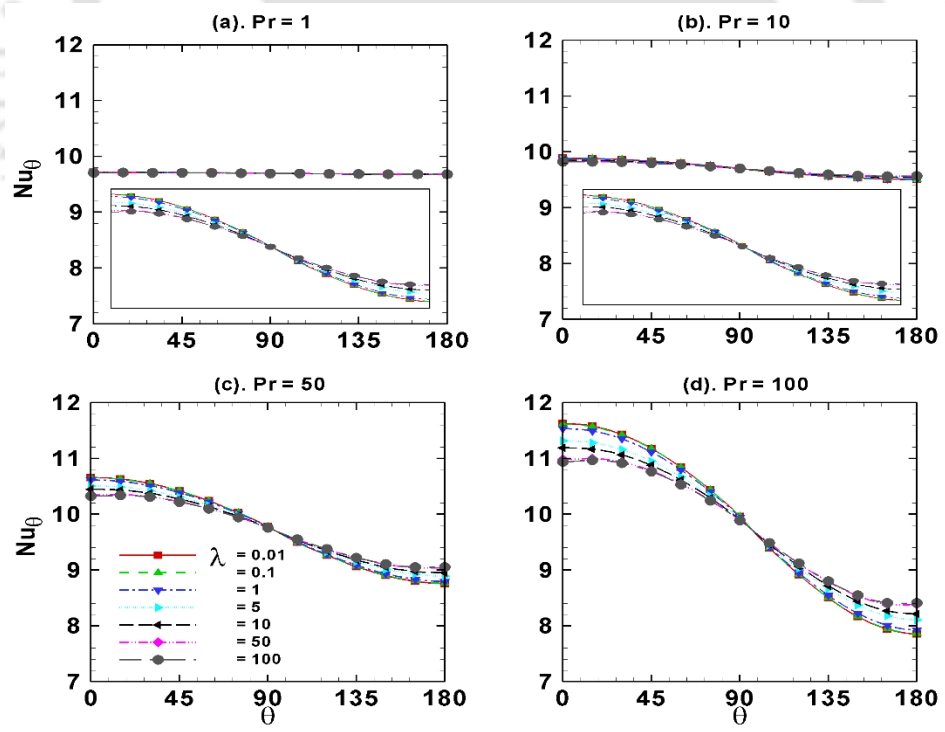

Figure 6.86 Surface Nusselt number around assemblage of spheres (Φ = 0.5) in power-law fluid (n = 0.6) at Re = 0.1.

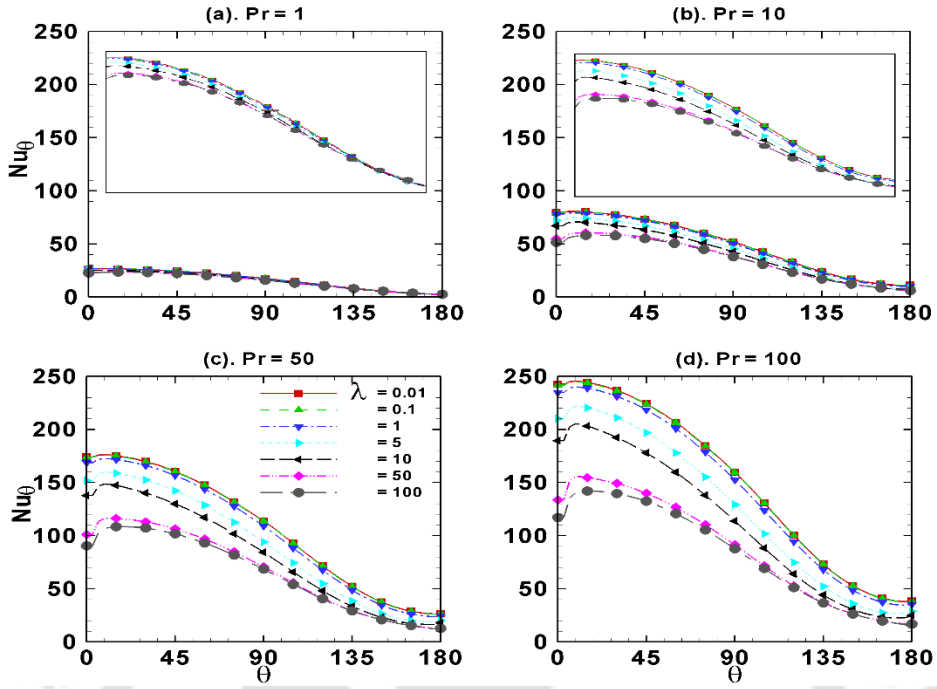

Figure 6.87 Surface Nusselt number around assemblage of spheres (Φ = 0.5) in power-law fluid (n = 0.6) at Re = 100.

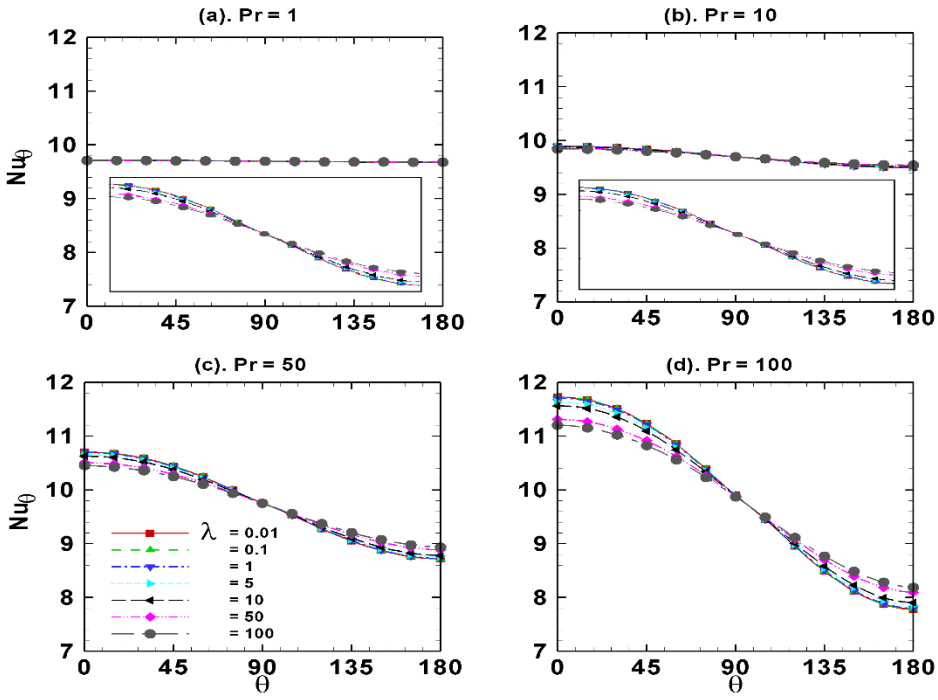

Figure 6.88 Surface Nusselt number around assemblage of spheres (Φ = 0.5) in power-law fluid (n = 1.6) at Re = 0.1.

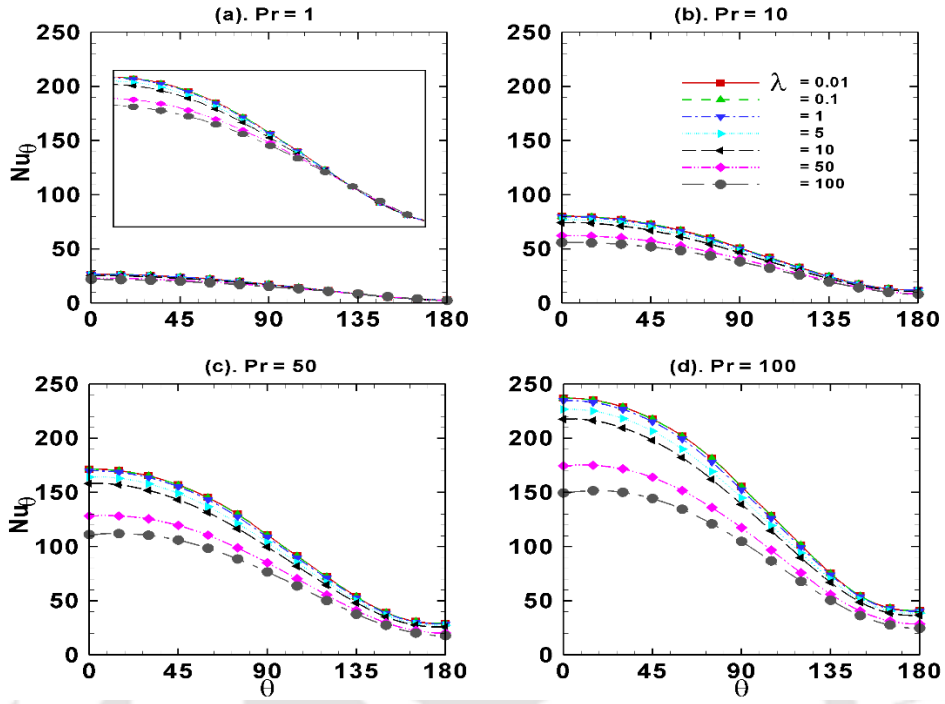

Figure 6.89 Surface Nusselt number around assemblage of spheres (Φ = 0.5) in power-law fluid (n = 1.6) at Re = 100.

Figure 6.88 and **Figure 6.89** represents the variation of surface Nusselt around assemblages of spheres of volume fraction, Φ = 0.5 in shear thickening fluids (n = 1.6) for different values of Prandtl number Pr and slip parameter λ at Re = 0.1 and Re = 100 respectively. Qualitatively similar trends are seen as in the case of shear-thinning fluids of n = 0.5 (**Figure 6.86** and **Figure 6.87**), but as the power law index increased to n = 1.6, the local value of the Nusselt number decreased because of increased boundary layer thickness due to increased apparent viscosity of the shear-thickening fluids. Further for a fixed combination of the slip number, Prandtl number and volume fraction of spheres, as the value of the power-law index increases, the surface values of the Nusselt number along the surface of the sphere decreases indicating the rate of heat transfer is higher for shear-thinning fluids followed by Newtonian and shear-thickening fluids. Finally, for a given combination of the slip number, power-law fluid behavior index and volume

fraction of spheres, the values of the Nusselt number along the surface of the spheres increases as the value of the Prandtl number increased indicating increased rate of heat transfer due to increased contribution from the convective heat transfer.

6.8.3. Average Nusselt Number

Figure 6.90 shows the variation of the average Nusselt numbers of volume fraction of spheres, Φ = 0.1 in shear thinning fluid (n = 0.6) at different Reynolds numbers and slip parameters. The average Nusselt number increases with the increase in the Peclet number regardless the values of the slip parameter and Reynolds numbers because of increasing contribution of convection mode of heat transfer with the increasing Peclet number. Though for small values of Peclet number there is insignificant effect on the average Nusselt number for small value of Reynolds number (Re = 0.1). Further irrespective of the values of the Reynolds number and Peclet number the average Nusselt number decreases with the increase in the slip parameter. This is due to the reduction in magnitude of the fluid slip over the surface as the value of the slip parameter increases. The average Nusselt number increases with the increasing Reynolds number at values of the Peclet number and the slip parameters. Finally the average Nusselt number increases with increasing Peclet number and Reynolds numbers while average Nusselt number decreases with increasing slip parameter at given values of volume fraction of sphere and power-law index. Whereas **Figure 6.91** presents the variation of the average Nusselt numbers of volume fraction of spheres, Φ = 0.5 in shear thinning fluid (n = 0.6) at different Reynolds numbers and slip parameters. Qualitatively, similar effect of slip parameter, Reynolds number and Peclet number on average Nusselt number observed as in case of Φ = 0.1, except magnitude of average Nusselt number for Φ = 0.5 is greater than that of Φ = 0.1 at given values of Peclet number, Reynolds number, slip parameter and power-law index. Thus, the average Nusselt number increases with

increasing volume fraction of spheres regardless the values of Peclet number, Reynolds numbers and slip parameter. **Figure 6.92** and **Figure 6.93** represents the variation of the average Nusselt numbers of volume fraction of spheres, Φ = 0.1 (**Figure 6.92**) and Φ = 0.5 (**Figure 6.93**) in shear thickening fluid (n = 1.6) at different Reynolds numbers and slip parameters. Here, also similar trends of average Nusselt number observed along with Peclet number, Reynolds number and slip parameter as in case of volume fraction of spheres, Φ = 0.1 (**Figure 6.90**) and Φ = 0.5 (**Figure 6.91**) in shear thinning fluid (n = 0.6), except the magnitude of average Nusselt number is less for shear thickening fluid (n = 1.6) compared to shear thinning fluid (n = 0.6) due to thickening of fluids. Thus, the average Nusselt number decreases with the increasing power-law index at all values of the Peclet number, Reynolds number and the slip parameters. **Figure 6.94** presents the effects of the power-law index on the average Nusselt numbers of volume fraction of spheres Φ = 0.1 at Re = 20. As the power-law index decreases the thermal boundary layer becomes thinner, hence the average Nusselt number increases with decreasing power-law index for all values of the Peclet numbers, Reynolds numbers and the slip parameters. The apparent viscosity of the fluid around the surface of spheres decreases with the decreasing power-law index (n) resulting in steep velocity gradients which in turn enhances the heat transfer rate from a slip sphere to surrounding fluid. Therefore, the average Nusselt number is higher for shear-thinning fluids followed by the Newtonian and shear-thickening fluids. Finally, the rate of the heat transfer from the assemblage of spheres to the surrounding power-law fluids increases as decreasing the slip parameter and/or increasing Reynolds/Prandtl number and/or decreasing power-law index and/or increasing volume fraction of spheres.

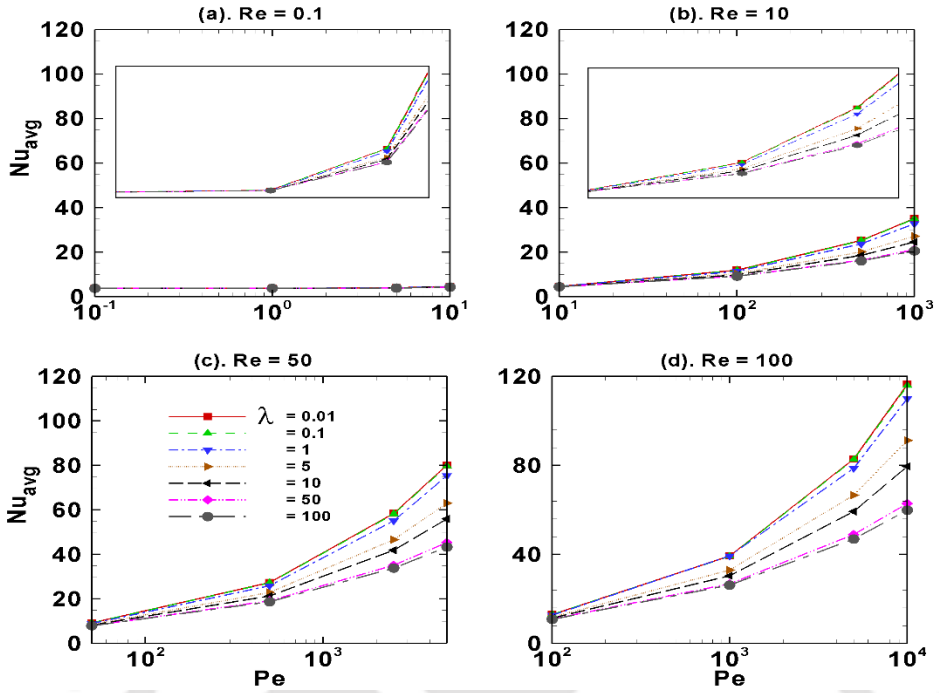

Figure 6.90 Average Nusselt numbers of volume fractions of spheres Φ = 0.1 in power-law fluid (n = 0.6) with velocity slip at the interface.

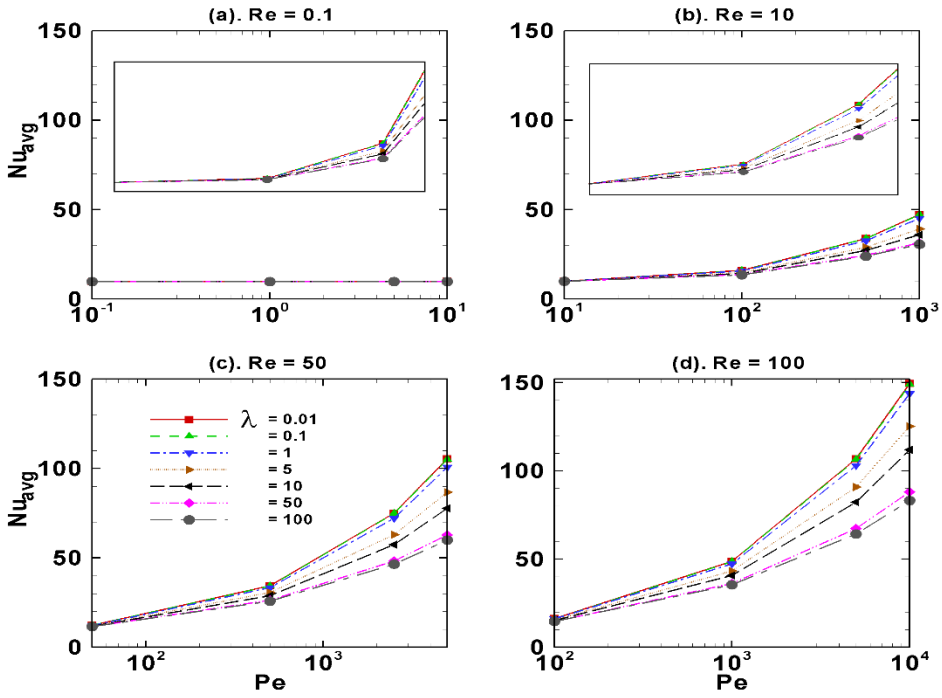

Figure 6.91 Average Nusselt numbers of volume fractions of spheres Φ = 0.5 in power-law fluid (n = 0.6) with velocity slip at the interface.

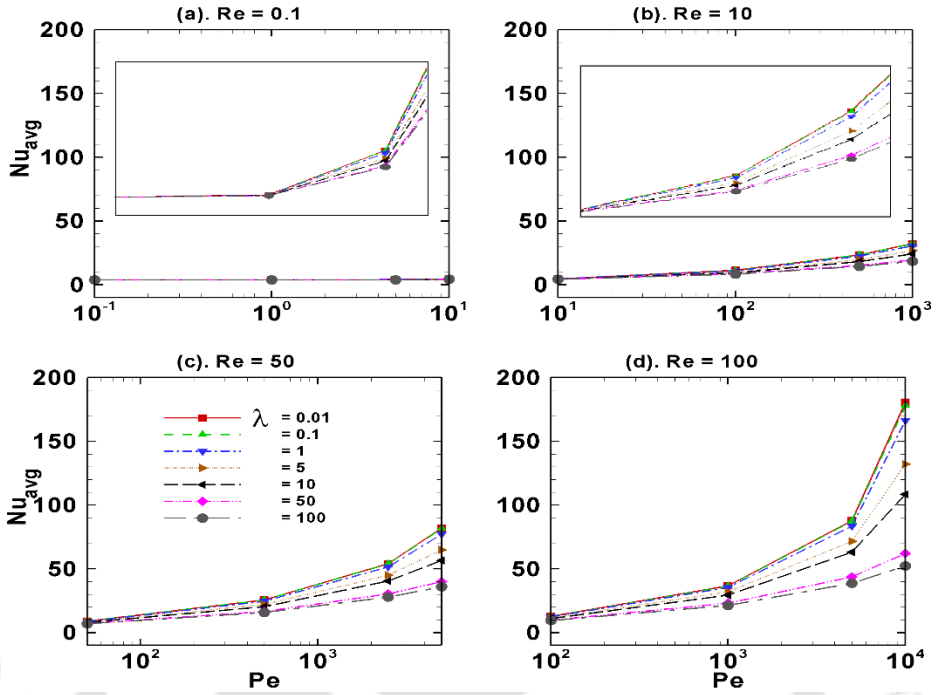

Figure 6.92 Average Nusselt numbers of volume fraction of spheres Φ = 0.1 in power-law fluid (n = 1.6) with velocity slip at the interface.

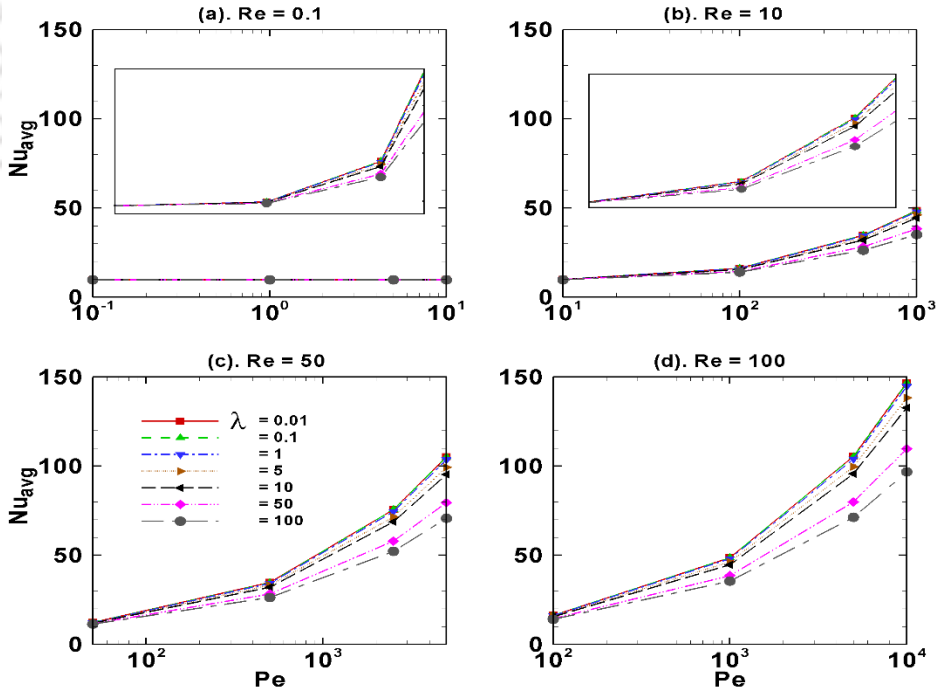

Figure 6.93 Average Nusselt numbers of volume fraction of spheres Φ = 0.5 in power-law fluid (n = 1.6) with velocity slip at the interface.

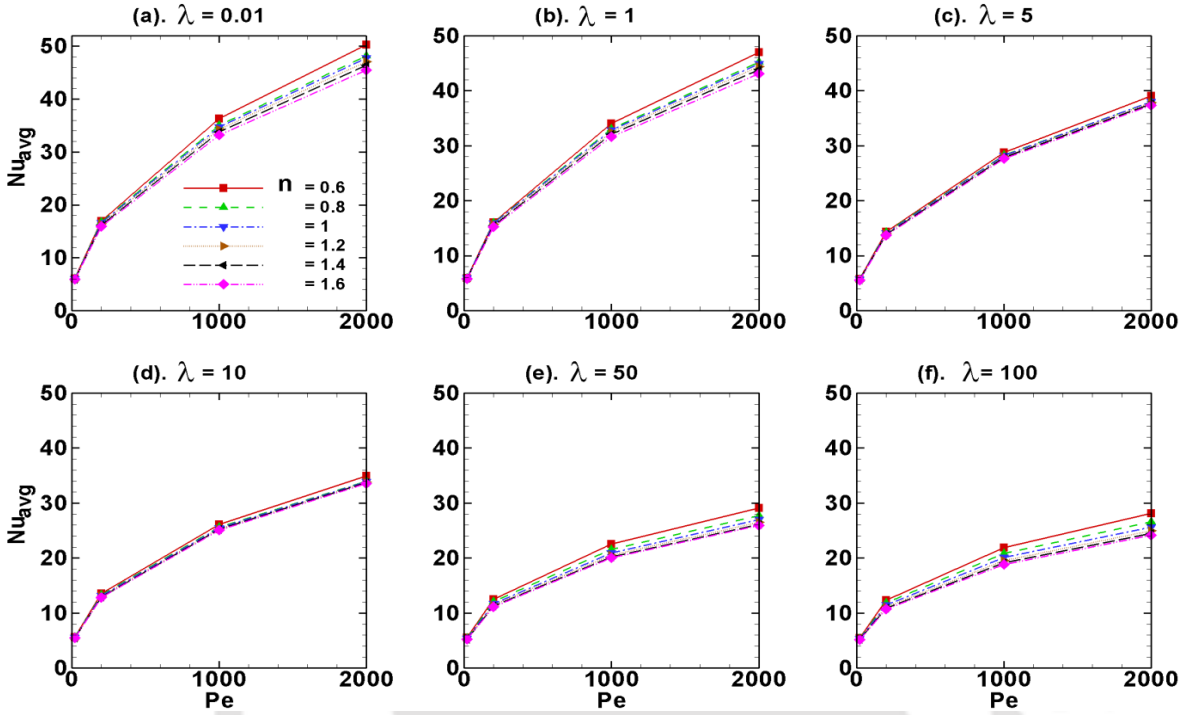

Figure 6.94 Average Nusselt numbers of assemblages of spheres of Φ = 0.1 at Re = 20 for different values of power-law index.

Finally, a simple predictive correlation has been developed based on the present numerical results of average Nusselt numbers which can be used to evaluate the rate of heat transfer from assemblages of spheres to power-law fluids in new applications. The following expression is found to be adequate to reproduce the present numerical results (Data points: 5880):

$$Nu_{avg} = 0.4195 Re^{0.617} Pr^{0.569} \lambda^{-0.0562} \exp\left(0.447\Phi/1.401n\right) + 11.033\Phi^{0.5645} \qquad (6.6)$$

The above expression reproduces the present numerical results with an average error of ±9.99% and maximum error of ±59.85 %.

CONCLUSIONS AND FUTURE SCOPE

7.1. Conclusions

7.1.1. Momentum transfer of single slip spheres in Newtonian and power-law fluids

The flow and drag behavior of unconfined single solid spheres in Newtonian and power-law fluids with velocity slip at the interface have been studied. The flow patterns indicate that for all values of the power-law index, there is no flow separation for $\lambda \leq 1$ and/or $Re \leq 20$. However, for all values of the power-law index, in the case of $\lambda \geq 5$ and/or $Re > 20$, a recirculation wake in the rear of the sphere appears and its size increases with the increase in the slip parameter and Reynolds number. For all values of power-law indices, the flow separation angle increases with the increase in Reynolds number and slip parameter except for the case of $\lambda = 5$. Regardless of values of the power-law index and the Reynolds number, the difference between C_p values at front and rear stagnation point increases with increase in the slip parameter. Regardless of values of the power-law index, the surface tangential velocity decreases with the increase in the slip parameter and because of presence of recirculation wake (for $Re > 20$ and $\lambda \geq 5$) in the rear end of the sphere the tangential velocity exhibits a secondary curve. The size of this secondary curve increases with decrease in the power-law index and/or with the increase in the slip parameter. The normalized drag coefficient exhibits a crossover Reynolds number with respect to the power-law index; and it is almost independent of the slip parameter. Finally, a simple predictive correlation for the total drag coefficient of a single sphere in power-law fluids with slip velocity at the interface is proposed.

7.1.2. Heat transfer from single slip sphere to Newtonian liquids

The isotherm contours and the local and average Nusselt numbers of a single sphere in Newtonian fluids with fluid-slippage at the interface are numerically obtained. The convection of isotherm contours increases with the increasing Reynolds/Prandtl numbers whereas they decrease with the slip parameter. At Re = 20, the local Nusselt number distribution has displayed a crossover with respect to slip parameter when Pr = 1 at $\theta \sim 130\text{-}135°$ which gradually moves toward the rear stagnation point as Prandtl number increases and finally disappears at Pr = 100. At $Re > 20$ and $\lambda > 1$, it is observed that as λ increases the value of Nusselt number decreases at any location between the front stagnation point and the point of flow separation. However, in the remaining portion of sphere surface, i.e., between the point of flow separation and rear stagnation point a reverse trend is observed. For $Re > 20$ and $\lambda > 1$, irrespective of the values of the slip parameter, the local value of the Nusselt number increases with the Prandtl number in both zones i.e., before and after the point of flow separation. The average Nusselt number decreases with the slip parameter regardless the values of the Reynolds and Prandtl numbers. Finally a simple predictive correlation for the average Nusselt numbers of a single sphere in Newtonian fluids with slip velocity at the interface is proposed.

7.1.3. Heat transfer from single slip sphere to power-law liquids

The heat transfer phenomena between a single spherical particle with fluid-slippage due to apparent slip at the interface and power-law fluids are analyzed in terms of the isotherm contours and local and average Nusselt numbers for the wide ranges of the pertinent dimensionless parameters. For slip parameter $\lambda \leq 1$, regardless the values of Reynolds and Prandtl numbers, as one move along the surface of the sphere from the front stagnation point to the rear end, the value of surface Nusselt number gradually decreases. For $\lambda \geq 5$ and $Re > 20$, rise in the values of

local Nusselt numbers in the rear end of the sphere observed because of the formation of the recirculation wakes. As the value of the slip parameter increases the magnitude of slip over surface of spherical particle reduces, hence the rate of heat transfer decreases at all the values of the Reynolds and Prandtl numbers and the power-law fluid behavior index. However, at the small value of the Peclet number, the effect of the slip parameter on the surface and average Nusselt numbers is insignificant. As the value of the Peclet number increases, the average value of the Nusselt number increases at all the values of *Re*, *n* and λ due to enhancing the convection. However, for small values of Peclet numbers, the average Nusselt number is almost constant regardless the values of the slip parameter. As the value of the power-law index decreases, the thickness of the thermal boundary layer decreases thus enhancement in the rate of heat transfer is observed with decreasing power-law index. Finally on the basis of present numerical results a simple predictive correlation for the average Nusselt numbers of spheres with velocity slip at the interface in power-law liquids was developed.

7.1.4. Momentum transfer of assemblages of slip spheres in Newtonian fluids

The hydrodynamics of assemblages of the spheres has been numerically investigated using a finite difference method based simplified marker and cell algorithm implemented on staggered grid in spherical coordinate system. The detachment of flow can be delayed by decreasing the value of the slip parameter and/or by increasing the value of the volume fraction of the spheres. For fixed values of Reynolds number and volume fraction, the assemblages of spheres with large slippage (small λ) offer less pressure drop whereas the assemblages of spheres with less slippage (large λ) offer more pressure drop during their sedimentation in an unconfined Newtonian fluid. The total drag coefficients of assemblages of the spheres in Newtonian fluids decreases (thus settle easily) with the decreasing volume fraction and/or decreasing slip parameter and/or

increasing Reynolds number. For $\lambda \leq 1$, the effect of hindrance is small at intermediate Reynolds number for all volume fractions; however, for $\lambda > 5$, the hindrance effect decreases with the increasing Reynolds number and/or with the decreasing volume fraction.

7.1.5. Momentum transfer of assemblages of slip spheres in power-law fluids

The effects of the Reynolds number, volume fraction of spheres, slip parameter and power-law index on the flow and drag behavior of assemblages of spheres in power-law liquids with velocity slip at the fluid-particle interface have been numerically investigated over wide range of dimensionless parameters. The size of the recirculation wake behind spheres decreases with the decreasing slip parameter (i.e., increasing fluid slippage at the interface), decreasing Reynolds number, increasing volume fraction of particles and increasing power-law index of the fluid. The local value of the vorticity increases with the increasing slip parameter, with increasing particle volume fraction, with increasing Reynolds number but with the decreasing power-law index. In the case of shear-thickening fluids, the pressure recovery is poor i.e., the difference between the pressure coefficient values at front and rear stagnation points is much larger than in the case of shear-thinning fluids. The local value of the surface velocity decreases with the decreasing slip parameter, decreasing volume fraction of particles, decreasing Reynolds number and increasing power-law index. The total drag coefficients of the spheres in assemblages in power-law fluids decreases with the increasing Reynolds number, decreasing slip parameter, decreasing volume fraction and decreasing power-law index. The ratio between pressure and friction drag coefficients increases with increasing slip parameter, increasing volume fraction, increasing Reynolds number and decreasing power-law index. However, the effect of Reynolds number on drag ratio is small up to $Re = 10$ in case of shear-thinning fluids but for shear-thickening fluids it

is almost independent up to Re = 50 – 100 depending on the value of the slip parameter. Further for slip parameter $\lambda < 1$, the volume fraction shows mixed trends on the drag ratio.

7.1.6. Heat transfer from assemblages of slip spheres to Newtonian fluids

The heat transfer characteristics of assemblages of smooth spheres in Newtonian fluids are obtained over wide ranges of dimensionless parameters, namely, Re, Pr, λ and Φ. Irrespective of the values of Re, λ, Pr and Φ, as one traverses from the front stagnation point along the surface to the rear end, the value of Nusselt number at the surface of the particle decreases. As the value of the slip parameter increases, the rate of heat transfer decreases for all values of Re, Pr and Φ. However, for small values of Pe, the effect of λ on the local and average Nusselt number is very weak and the heat transfer coefficient is almost constant. As the value of the volume fraction of the spheres increases, the heat transfer coefficient also increases for all values of the Reynolds and Prandtl numbers and slip parameter. As the value of the Peclet number increases, the average value of the Nusselt number also increases for all values of Re, λ and Φ. However, for small values of Peclet numbers, the average value of the Nusselt number is almost constant for all values of the λ for a fixed value of Φ. As the value of the Prandtl number increases, the thermal boundary layer decreases thereby enhancing the rate of heat transfer. Finally based on the present numerical results a simple predictive correlation has been developed which reproduces the present numerical results with an average error of ±10.29%.

7.1.7. Heat transfer from assemblages of slip spheres to power-law liquids

The values of the convective heat transfer coefficients for assemblages of spheres in power-law fluid have been obtained for wide ranges of the dimensionless parameters, namely, Re, Pr, n, λ and Φ. Irrespective of the values of Re, λ, n, Pr and Φ, as one traverses from the front stagnation

point along the surface to the rear end, the value of Nusselt number at the surface of particle decreases. As the value of the slip parameter increases, the rate of heat transfer decreases for all values of *Re*, *Pr*, *n* and Φ. However, for small values of *Pe*, the effect of λ on the local and average Nusselt number is very weak and the heat transfer coefficient is almost constant. For low Prandtl numbers $Pr \approx 1$, the heat transfer is mainly due to the thermal diffusion. As the value of the volume fraction Φ increases, the heat transfer coefficient also increases for values of the Reynolds number $Re \leq 50$, all value of the Prandtl number and the slip parameter. As the value of the Peclet number increases, the average value of Nusselt number also increases for all values of *Re*, λ, *n* and Φ. However, for small values of Peclet numbers, the average values of Nusselt number are almost unchanged for all values of the λ for a fixed value of Φ. As the values of Prandtl number increases, the thermal boundary layer decreases thereby enhancing the rate of heat transfer, whereas as values of power-law index increases thermal boundary layer increases.

7.2. Scope for Future Work

- Using the similar linear velocity slip boundary condition one can study the momentum and heat transfer phenomena for different geometries like cylinder, spheroid, etc. in power law fluids.
- Several slip models are available like power-law, Maxwell's, and second-order slip models; using these models, one can analyze effect of slip on the momentum and heat transfer characteristics.
- The heat transfer problems can be analyzed using temperature jump boundary condition along with velocity slip.

References

1. Batchelor, G. K., *An Introduction to Fluid Dynamics*, Cambridge University Press, (1967).
2. Day, M. A., The no-slip condition of fluid dynamics, *Erkenntnis*, **33**, 285–296 (1990).
3. Tanner, R. I., *Engineering Reology*, Oxford University Press, 2nd edition, (2000).
4. Pozrikidis, C., *Fluid Dynamics: Theory, Computation, and Numerical Simulation*, Kluwer Academic Publishers, (2001).
5. Bernoulli, D., *Hydrodynamica*, Opus Academicum (1738).
6. Coulomb, C. A., *Memoires de l'Institut National des Sciences et des Arts: Sciences Mathematiqueset Physiques*, Vol. 3 (1801).
7. Stokes, G. G., On the theories of the internal friction of fluids in motion, and of the equilibrium and motion of elastic solid, *Trans. Cambridge Philos. Soc*., **8**, 287–304 (1845).
8. Stokes, C. G., *Mathematical and Physical Papers*, Vol. I., Cambridge University Press, Cambridge, (1880), Stokes, C. G., *Mathematical and Physical Papers*, Vol. III., Cambridge University Press, Cambridge (1901).
9. Masey, B. S., *Mechanics of Fluids*, Chapman and Hall, London, (1989).
10. Goldstein, S., *Mechanics of Fluids*, Clarendon press, Oxford, (1938).
11. Goldstein, S. *Mechanics of Fluids*, Clarendon Press, Oxford, Vol. II, 677–680 (1938).
12. Vinogradova, O. I., Slippage of water over hydrophobic surfaces, *Int. J. Miner. Process.*, **56**, 31–60 (1999).
13. Debye, P., and Cleland, R. L., Flow of liquid hydrocarbons in porous vycor, *J. Appl. Phys.*, **30**, 843–849 (1959).

14. Ruckenstein, E., and Rajora, P., On the no-slip boundary condition of hydrodynamics, *J. Colloid Interface Sci*., **96**, 488–493 (1983).
15. Churaev, N. V., Sobolev, V. D., and Somov, A. N., Slippage of liquids over lyophobic solid surfaces, *J. Colloid Interface Sci*., **97**, 574–581 (1984).
16. Galt J., and Maxwell, B., Velocity profiles for polyethylene melts, *Mod. Plast*., 115–189 (1964).
17. Kalika, D., and Denn, M. M., Wall slip and extrudate distortion in linear low density polyethylene, *J. Rheol*., **31**, 815–834 (1987).
18. Lim, F. J., and Schowalter, W. R., Wall slip of narrow molecular weight distribution polybutadienes, *J. Rheol*., **33**, 1359–1382 (1989).
19. Hatzikiriakos S. G., and Dealy, J. M., Wall slip of molten high density polyethylene, I. Sliding plate rheometer studies, *J. Rheol*., **35**, 497–523 (1991).
20. Hatzikiriakos, S. G., and Dealy, J. M., wall slip of molten high density polyethylenes, II. Capillary rheometer studies, *J. Rheol*., **36**, 703–741 (1992).
21. Brochard-Wyart, F., and Gennes de, P. G., Shear dependent slippage at a polymer/solid interface, *Langmuir*, **8**, 3033–3037 (1992).
22. Migler, K. B., Hervet, H., and Leger, L., Slip transition of a polymer melt under shear stress, *Phys. Rev. Lett*., **70**, 287–290 (1993).
23. Leger, L., Hervet, H., Charitat, T., and Koustos, V., The stick-slip transition in highly entangled poly(styrene-butadiene) melts, *Adv. Colloid Interface Sci*., **94**, 39–52 (2001).

24. Kraynik, A. M., and Schowalter, W. R., Slip at the wall and extrudate roughness with aqueous solutions of polyvinyl alcohol and sodium borate, *J. Rheol*., **25**, 95–114 (1981).

25. Cohen, Y., and Metzner, A. B., Adsorption effects in the flow of polymer solutions through capillaries, *Macromolecules*, **15**, 1425–1429 (1982).

26. Cohen, Y., and Metzner, A. B., Apparent slip flow of polymer solutions, *J. Rheol*., **29**, 67–102 (1985).

27. Cohen Y., and Metzner, A. B., An analysis of apparent slip flow of polymer solutions, *Macromolecules*, **25**, 28–35 (1986).

28. Yaras, P., Kalyon, D. M. and Yilmazer, U., Flow instability in capillary flow of concentrated suspension, *Rheol. Acta*, **33**, 48–59 (1994).

29. Soltani, F., and Yilmazer, U., Slip velocity and slip layer thickness in flow of concentrated suspensions, *J. Appl. Polym. Sci*., **70**, 515–552 (1998).

30. Kalyon, D. M., Apparent slip and viscoplasticity of concentrated suspensions, *J. Rheol*., **49**, 621–643 (2005).

31. Derakhshandeh, B., Hatzikiriakos, S. G., and Bennington, C. P. J., Rheology of pulp suspensions using ultrasonic doppler velocimetry, *Rheol. Acta*, **49**, 1127–1140 (2010).

32. Derakhshandeh, B., Hatzikiriakos, S. G., and Bennington, C. P. J., Apparent yield stress of pulp fibre suspensions, *J. Rheol*., **54**, 1137–1154 (2010).

33. Ballesta, P., Petekidis, G., Poon, I. L., and Besselin, W. C. K., Wall slip and flow of concentrated hard-sphere colloidal suspensions, *J. Rheol*., **56**, 1005–1012 (2012).

34. Pal, R., Slippage during the flow of emulsions in rheometers, *Colloids Surf.*, **162**, 55–66 (2000).

35. Buscall, R., Wall slip in dispersion rheometry, *J. Rheol.*, **54**, 1177–1185 (2010).

36. Larsen, R. J., Kim, J. W., Zukoski, C. F., and Weitz, D. A., Fluctuations in flow produced by competition between apparent wall slip and dilatancy, *Rheol. Acta*, **53**, 333–347 (2014).

37. Jiang, T. Q., Young, A. C., and Metzner, A. B., The rheological characterization of HPG gels: Measurement of slip velocities in capillary tubes, *Rheol. Acta*, **25**, 397–414 (1986).

38. Walls, H. J., Caines, S. B., Sanchez, A. M., and Khan, S. A., Yield stress and wall slip phenomena in colloidal silica gels, *J. Rheol.*, **47**, 847–870 (2003).

39. Meeker, S. P., Bonnecaze, R. T., and Cloitre, M., Slip and flow in soft particle pastes, Phys. Rev. Lett., **92**, 198302 (2004).

40. Meeker, S. P., Bonnecaze R. T., and Cloitre, M., Slip and flow in pastes of soft particles: Direct observation and rheology, *J. Rheol.*, **48**, 1295–1318 (2004).

41. Aktas, S., Kalyon, D. M., Marin-Santibanez, B. M., and Gonzalez, J. P., Shear viscosity and wall slip behavior of a viscoplastic hydrogel, *J. Rheol.*, **58**, 513–537 (2014).

42. Ballesta, P., Besseling, R., Isa, L., Petekidis, G., and Poon, W. C. K., Slip and flow of hard-sphere colloidal glasses, *Phys. Rev. Lett.*, **101**, 258301–4 (2008).

43. Ballesta, P., Petekidis, G., Isa, L., Poon W. C. K., and Besseling, R., Wall slip and flow of concentrated hard-sphere colloidal suspensions, *J. Rheol.*, **56**, 1005–1039 (2012).

44. Halliday P. J., and Smith, A. C., Estimation of the wall slip velocity in the capillary flow of potato granule pastes, *J. Rheol*., **39**, 139–149 (1995).

45. Aichholzer, W. and Fritz, H. G., Rheological characterization of thermoplastic starch materials, *Starches*, **50**, 77–83 (1998).

46. Enzendorfer, C., Harris, R. A., Valko, P., Economides, M. J., Fokker P. A., and Davies, D. D., Pipe viscometry of foam, *J. Rheol*., **39**, 345–358 (1995).

47. Denkov, N. D., Subramanian, V., Gurovich, D., and Lips, A., Wall slip and viscous dissipation in sheared foams: Effect of surface mobility, *Colloids Surf*., A, **263**, 129–145 (2005).

48. Bertola, V., A note on the effects of liquid viscoelasticity and wall slip on foam drainage, *J. Phys. Condens. Matter*, **19**, 246105 (2007).

49. Robert, L., Demay, Y., and Vergnes, B., Stick-slip flow of high density polyethylene in a transparent slit die investigated by laser doppler velocimetry, *Rheol. Acta*, **43**, 89–98 (2004).

50. Kalika, D., and Denn, M. M., Wall Slip and Extrudate Distortion in Linear Low Density Polyethylene, *J. Rheol*., 31, 815-834 (1987).

51. Rosenbaum, E. E., Randa, S. K., Hatzikiriakos, S. G., Stewart, C. W., Henry, D. L., and Buckmaster, M., Boron nitride as a processing aid for the extrusion of polyolefins and fluoropolymers, *Polym. Eng. Sci*., **40**, 179–190 (2000).

52. Vinogradov, G. V., Malkin, A. Y., Yanovskii, Y. G., Borisenkova, E. K., and Yarlykov, B. V., Viscoelastic properties and flow of narrow distribution polybutadienes and polyisoprenes, *J. Polym. Sci., Polym. Phys. Ed*., **10**, 1061–1084 (1972).

53. Mhetar, V. R., and Archer, L. A., Slip in entangled polymer melts, 1. General feature, *Macromolecules*, **31**, 8607–8616 (1998).

54. Mhetar, V. R., and Archer, L. A., Slip in entangled polymer melts, 2. Effect of surface treatment, *Macromolecules*, **31**, 8617–8622 (1998).

55. Birinci, E., and Kalyon, D. M., Development of extrudate distortions in poly(dimethyl siloxane) and its suspensions with rigid particles. *J. Rheol*., **50**, 313–352 (2006).

56. Henson, D. J., and Mackay, M. E., Effect of gap on the viscosity of monodisperse polystyrene melts – slip effects, *J. Rheol*., **39**, 359–369 (1995).

57. Mackay M. E., and Henson, D. J., The effect of molecular mass and temperature on the slip of polystyrene melts at low stress levels, *J. Rheol*., **42**, 1505–1517 (1998).

58. Kanoh, Y., Shibata, T., Nishimura, T., Usui, H., and Saeki, T., Wall slip of molten polymers in various conduits – Influence of solid surface conditions, *Nihon Reologi Gakkaishi*, **25**, 37–41 (1997).

59. Koran, F., and Dealy, J. M., Wall slip of polyisobutylene: Interfacial and pressure effects, *J. Rheol*., **43**, 1291–1307 (1999).

60. Paskin, E. D., Motion of polymer liquids under unstable conditions and in channel terminals, *Rheol. Acta*, **17**, 663–675 (1978).

61. Hervet, H., and Leger, L., Flow with slip at the wall: from simple to complex fluids, *C. R. Phys*., **4**, 241–249 (2003).

62. Kazatchkov, I. B., Hatzikiriakos, S. G., and Stewart, C. W., Extrudate distortion in the capillary/slit extrusion of a molten polypropylene, *Polym. Eng. Sci*., **35**, 1864–1871 (1995).

63. Kamerkar, P. A., and Edwards, B. J., An experimental study of slip flow in capillaries and semi-hyperbolically converging dies, *Polym. Eng. Sci*., **47**, 159–167 (2007).

64. Rides, M., Allen, C., Fleming, D., Haworth, B., and Kelly, A., Inter comparison of slip flow velocity measurements of filled polymers by capillary extrusion rheometry, *Polym. Test*., **27**, 308–320 (2008).

65. Mennig, G., Visual observations of slip in flow of polymer melts, *J. Macromol. Sci., Part B: Phys*., **B14**, 231–254 (1977).

66. Knappe, W., and Krumbock, E., Slip flow of non-plasticized PVC compounds, *Rheol. Acta*, **25**, 296–307 (1986).

67. Fras, I., Cassagnau, P., and Michel, A., Lubrication and slip flow during extrusion of plasticized PVC compounds in the presence of lead stabilizer, *Polymer*, **40**, 1261–1269 (1999).

68. Vinogradov, G. V., and Ivanova, L. I., Viscous properties of polymer melts and elastomers exemplified by ethylene-propylene copolymer, *Rheol. Acta*, **6**, 209–222 (1967).

69. Ozkan, S., Gillece, T., Senak, L., and Moore, D. J., Characterization of yield stress and slip behaviour of skin/hair care gels using steady flow and LAOS measurements and their correlation with sensorial attributes, *Int. J. Cosmet. Sci*., **34**, 193–201 (2012).

70. Plucinski, J., Gupta, R. K., and Chakrabarti, S., Wall slip of mayonnaises in viscometers, *Rheol. Acta*, **37**, 256–269 (1998).

71. Ariawan, A. B. Ebnesajjad, S., and Hatzikiriakos, S. G., Paste extrusion of polytetrafluoroethylene (PTFE) fine powder resins, *Can. Chem. Eng. J.*, **80**, 1153–1165 (2002).

72. Patil, P. D., Feng, J. J., and Hatzikiriakos, S. G., Constitutive modeling and flow simulation of polytetrafluoroethylene (PTFE) paste extrusion, *J. Non-Newtonian Fluid Mech*., **139**, 44–53 (2006).

73. Sofou, S., Muliawan, E. B., Hatzikiriakos, S. G. and Mitsoulis, E., Rheological characterization and constitutive modeling of bread dough, *Rheol. Acta*, **47**, 369–381 (2008).

74. Martin, P. J., Odic, K. N., and Russell, A. B., Rheology of commercial and model ice creams, *Appl. Rheol*., **18**, 12913–12921 (2008).

75. Pit, R., Hervet, H., and Leger, L., Friction and slip of a simple liquid at a solid surface, *Tribol. Lett*., **7**, 147–152 (1999).

76. Boehnke, U. C., Remmler, T., Motschmann, H., Wurlitzer, S., Hauwede, J., and Fischer, Th. M., Partial air wetting on solvophobic surfaces in polar liquids, *J. Colloid Interface Sci*., **211**, 243–254 (1999).

77. Pit, R., Hervet, H., and Leger, L., Direct experimental evidence of slip in hexadecane: Solid interface, *Phys. Rev. Lett*. **85**, 980–983 (2000).

78. Zhu, Y., and Granick, S., Rate-dependent slip of Newtonian liquids at smooth surfaces, *Phys. Rev. Lett*., **87**, 096105 (2001).

79. Baudry, J., Charlaix, E., Tonck, A., and Mazuyer, D., Experimental evidence for a large slip effect at a non-wetting fluid-solid interface, *Langmuir*, **17**, 5232–5236 (2001).

80. Zhu, Y., and Granick, S., Limits of the hydrodynamic no-slip boundary condition, *Phys. Rev. Lett*., **88**, 106102 (2002).

81. Tretheway, D. C., and Meinhart, C. D., Apparent fluid slip at hydrophobic microchannel walls, *Phys. Fluids*, **14**, L9–12 (2002).

82. Craig, V. S. J., Neto, C., and Williams, D. R. M. Shear-dependent boundary slip in an aqueous Newtonian liquid, *Phys. Phys. Rev. Lett*., 87, 054504 (2001).

83. Bonaccurso, E., Kappl, M., and Butt, H., Hydrodynamic force measurements: boundary slip of water on hydrophilic surfaces and electrokinetic effects, *J. Phys. Rev. Lett*., **88**, 076103 (2002).

84. Watanabe, K., Yanuar, and Udagawa, H., Drag reduction of a Newtonian fluid in a circular pipe with a highly water-repellent wall, *J. Fluid. Mech*., **381**, 225–238 (1999).

85. Zhu, Y., and Granick, S. No-slip boundary condition switches to partial slip when fluid contains surfactant, *Lang.*, **18**, 10058–10063 (2002).

86. Thompson, P. A., and Robbins, M. O., Shear-flow near solids-epitaxial order and flow boundary conditions, *Phys. Rev. A*, **41**, 6830–6837 (1990).

87. Barrat, J. L., and Bocquet, L., Large slip effect at a non-wetting fluid-solid interface, *Phys. Rev. Lett*., **82**, 4671 (1999).

88. Pit, R., Hervet, H., and Leger, L., Direct experimental evidence of slip in hexadecane: Solid interfaces, *Phys. Rev. Lett*., **85**, 980–983, (2000).

89. Campbell, S. E., Luengo, G., Srdanov, V. I., Wudl, F., and Israelachvili, J. N., Very low viscosity at the solid–liquid interface induced by adsorbed C^{60} monolayers, *Nature* (London), **382**, 520–522 (1996)

90. Watanabe, K., Yanuar, and Udagawa, H., Drag reduction of Newtonian fluid in a circular pipe with a highly water-repellent wall, *J. Fluid. Mech*., **381**, 225–238 (1999).

91. Pit, R., Hervet, H., and Leger, L., Direct Experimental Evidence of Slip in Hexadecane: Solid Interfaces, *Phys. Rev. Lett*., **85**, 980–990 (2000).

92. Bonaccurso, E., Kappl, M., and Butt, H. J., Hydrodynamic force measurements: boundary slip of water on hydrophilic surfaces and electrokinetic effects, *Phys. Rev. Lett*., **88**, 076103 (2002).

93. Bonaccurso, E., Butt, H. S., and Craig, V. S. J., Surface roughness and hydrodynamic boundary slip of a Newtonian fluid in a completely wetting system, *Phys. Rev. Lett*., 90, 144501 (2003).

94. Choi, C. H., Johan, K., Westin, A., and Breuer, K. S., Apparent slip flows in hydrophilic and hydrophobic microchannels, *Phys. Fluids*, **15**, 2897–2902 (2003).

95. Craig, V. S. J., Neto, C., and Williams, D. R. M., shear dependent boundary slip in an aqueous Newtonian liquid, *Phys. Rev. Lett*., **87**, 054504 (2001).

96. Henry, C. L., Neto, C., Evans, D. R., Biggs, S., Craig, V. S. J., The effect of surfactant adsorption on liquid boundary slippage, *Physica*, **A339**, 60–65 (2004).

97. Neto, C., Craig, V. S. J., Williams, D. R. M., Evidence of shear-dependent boundary slip in Newtonian liquids, *Eur. Phys. J*., **E12**, S71–S74 (2003).

98. Zhu, Y., and Granick, S., Rate-dependent slip of Newtonian liquid at smooth surfaces, *Phys. Rev. Lett*., **87**, 096105 (2001).

99. Zhu, Y., and Granick, S., Apparent slip of Newtonian fluids past adsorbed polymer layers, *Macromolecules*, **35**, 4658–4663 (2002).

100. Zhu, Y., and Granick, S., Limits of the hydrodynamic no-slip boundary condition, *Phys. Rev. Lett*., **88**, 106102 (2002).

101. Zhu, Y., and Granick, S., No-slip boundary condition switches to partial slip when fluid contains surfactant, *Langmuir*, **18**, 10058–10063 (2002).

102. Churaev, N. V., Sobolev, V. D., and Somov, A. N., Slippage of liquids over lyophobic solid surfaces, *J. Colloid Int. Sci*., **97**, 574–581 (1984).

103. Kunert, C., and Harting, J., roughness induced boundary slip in microchannel flows, *Phys. Rev. Lett*., **99**, 176001 (2007).

104. Ybert, C., Barentin, C., Cottin-Bizonne, C., Joseph, P., and Bocquet, L., Achieving large slip with superhydrophobic surfaces: Scaling laws for generic geometries Physics, *Phys. Fluids*, **19**, 123601 (2007).

105. Cottin-Bizonne, C., Barrat, J. L., Bocquet, L., and Charlaix, E., Low-friction flow of liquid at nanopatterned interfaces, *Nature Mater*., **2**, 237–240 (2003).

106. Sbragaglia, M., Benzi, R., Biferale, L., Succi, S., and Toschi, F., Surface roughness-hydrophobicity coupling in microchannel and nanochannel flows, *Phys. Rev. Lett*., **97**, 204503 (2006).

107. Gennes, P. G., On fluid/wall slippage, *Langmuir*, **18**, 3413–3414 (2002).

108. Steinberger, A., Cottin-Bizonne, C., Kleimann, P., and Charlaix, E., High friction on a bubble mattress, *Nature Mater*., **6**, 665–668 (2007).

109. Lauga, E., and Brenner, M. P., Dynamic mechanisms for shear-dependent apparent slip on hydrophobic surfaces, *Phys. Rev., E*, **70**, 026311 (2004).

110. Harting, J., Kunert, C., and Herrmann, H. J., Lattice Boltzmann simulations of apparent slip in hydrophobic microchannels, *Europhys. Lett*., **75**, 328–334 (2006).

111. Schnell, E., Slippage of water over nonwettable surfaces, *J. Appl. Phys*., **27**, 1149–1152 (1956)

112. Kiseleva, O. A., Sobolev, V. D., Chuarev, N. V., Slippage of the aqueous solutions of cetyltrimethylammonium bromide during flow in thin quartz capillaries, *Colloid J*., **61**, 263–264 (1999).

113. C. L. M. H. Navier, Sur les lois du mouvement des fluids, *Mem. Acad. Roy. Sci. Inst. Fr*., **6**, 389–440 (1827).

114. Churaev, N. V., Ralston, J., Sergeeva, I. P., and Sobolev, V. D., Electrokinetic properties of methylated quartz capillaries, *Adv. Colloid Int. Sci*., **96**, 265–278 (2002)

115. Lumma, D., Best, A., Gansen, A., Feuillebois, F., Radler, J. O., and Vinogradova, O. I., Flow profile near a wall measured by double-focus fluorescence cross-correlation, *Phys. Rev. E*, **67**, 056313 (2003)

116. Maciel, A., Salas, V. Soltero, J.F.A., Guzman, J., and Manero, O., On the wall slip of polymer blends, *J. Poly. Sci. Part B*, **40**, 303–316 (2002).

117. Rosenbaum, E. E., and Hatzikiriakos, S.G. Wall slip in the capillary flow of molten polymers subject to viscous heating, AIChE J., **43**, 598608 (1997).

118. Blyler, L. L., and Hart, A. C., Capillary flow instability of ethylene polymer melts, *Poly. Eng. Sci*., **10**, 193–203 (1970).

119. Sun, M., and Ebner, C., Molecular dynamics study of flow at a fluid-wall interface, *Phys. Rev. Lett*., **69**, 3491–3494 (1992).

120. Morris, D. L., Hannon, L., and Garcia, A. L., Slip length in a dilute gas, *Phys. Rev. A*, **46**, 5279–5281 (1992).

121. Arya, G., Chang, H. C., and Maginn, E. J. Molecular simulations of knudsen wall slip: effect of wall morphology, Mol Simulat., **29**, 697–709 (2003).

122. Lichter, S., Martini, A., Snurr, R. Q., and Wang, Q., Liquid slip in nanoscale channels as a rate process, *Phys. Rev. Lett*., **98**, 226001 (2007).

123. Cieplak, M., Koplik, J., and Banavar, J. R., Boundary conditions at a fluid-solid interface, *Phys. Rev. Lett*., **86**, 803–806 (2001).

124. Voronov, R. S., Papavassiliou, D. V., and Lee, L. L., Slip length and contact angle over hydrophobic surfaces, *Chem. Phys. Lett*., **441**, 273–276 (2007).

125. Jabbarzadeh, A., Atkinson, J. D., and Tanner, R. I., Wall slip in the molecular dynamics simulation of thin films of hexadecane, *J. Chem. Phys*., **110**, 2612–2620 (1999).

126. Gupta, S. A., Cochran, H.D., and Cummings, P. T., Shear behavior of squalane and tetracosane under extreme confinement, I. Model, simulation method, and interfacial Slip, *J. Chem. Phys*., **107**, 10316–10326 (1997).

127. Zhang, J., and Kwok, D. Y., Apparent slip over a solid-liquid interface with a no-slip boundary condition, *Phys. Rev. E*, **70**, 056701, (2004).

128. Hatzikiriakos, S. G., Stewart, C. W., Dealy, J. M., Effect of surface-coating on wall slip of LLDPE, *Int. Polym. Process*., **8**, 30–35 (1993).

129. Hatzikiriakos, S. G., Hong, P., Ho, W., and Stewart, C.W., The effect of teflon tm coatings in polyethylene capillary extrusion, *J. Appl. Pol Sci*., **55**, 595–603 (1995).

130. Ansari, M., Inn, Y. W., Sukhadia, A. M., DesLauriers, P. J., and Hatzikiriakos, S. G., Wall slip of HDPEs: Molecular weight and molecular weight distribution effects, *J. Rheol*., **57**, 927–950 (2013).

131. Inn, Y. W., Melt fracture and wall slip of metallocene-catalyzed bimodal polyethylenes in capillary flow, *J. Rheol*., **57**, 393–398, (2013).

132. Sabzevari, S. M., Cohen, I., and Wood-Adams, P. M., Wall slip of bidisperse linear polymer melts, *Macromolecules*, **47**, 3154–3160 (2014).

133. Sabzevari, S. M., Cohen, I., and Wood-Adams, P. M., Wall slip of tridisperse polymer melts and the effect of unentangled versus weakly entangled chains, *Macromolecules*, **48**, 8033–8040 (2014).

134. Pearson, J. R. A., and Petrie, C. J. S., *In polymer systems: deformation and flow*, Ed. Wetton, R. E., and Whorlow, R. H., Macmillan, London, **163** (1968).

135. Chernyak, Y. B., and Leonov, A. I., On the theory of the adhesive friction of elastomers, *Wear*, **108**, 105–138 (1986).

136. Yarin, A. L., and Graham, M. D., A model for slip at polymer/solid interfaces, *J. Rheol*., **42**, 1491–1504 (1998).

137. Tang, H. S., and Kalyon, D. M., Unsteady circular tube flow of compressible polymeric liquids subject to pressure-dependent wall slip, *J. Rheol*., **52**, 507–525 (2008).

138. Kazatchkov, I. B., and Hatzikiriakos, S. G., Relaxation effects of slip in shear flow of linear molten polymers, *Rheol. Acta*, **49**, 267–274 (2010).

139. Ebrahimi, M., Ansari, M., and Hatzikiriakos, S. G., Wall slip of polydisperse linear polymers using double reptation, *J. Rheol*., **59**, 885–901 (2015).

140. (a) Drda P. A., and Wang, S. Q., Stick-slip transition at polymer melt/solid interfaces, *Phys. Rev. Lett*., **75**, 2698–2701 (1995) (b) Leger, L., Hervet, H., Massey,

G., and Durliat, E., Wall slip in polymer melts, *J. Phys., Condens. Matter*, **9**, 7719–7739 (1997).

141. Barnes, H. A., A review of the slip (wall depletion) of polymer solutions, emulsions and particle suspensions in viscometer: It's cause, character and cure, j. non-Newt fluid mech., **56**, 221–251 (1995).

142. Kalyon, D. M., Gevgilili, H., Kowalczyk, J. E., Prickett, S. E., and Murphy, C. M., Use of adjustable-gap on-line and off-line slit rheometers for the characterization of the wall slip and shear viscosity behavior of energetic formulations, *J. Energ. Mater*., **24**, 175–193 (2006).

143. Coussot, P., *Rheometry of Pastes, Suspensions and Granular Materials*, Wiley, New Jersey, (2005).

144. Seth, J. R., Cloitre, M., and Bonnecaze, R. T., Influence of short-range forces on wall-slip in microgel pastes, *J. Rheol*., **52**, 1241–1270 (2008).

145. Koplik, J., Banavar, J. R., and Willemsen, J. F., Molecular-dynamics of fluid-flow at solid-surfaces, *Phys. Fluid A-Fluid Dyn*., **1**, 781–794 (1989).

146. Thompson, P. A., and Troian, S. M., A general boundary condition for liquid flow at solid surfaces, *Nature*, **389**, 360–362 (1997).

147. Bocquet, L., and Barrat, J. L., Hydrodynamic boundary-conditions and correlation-functions of confined fluids, *Phys. Rev. Lett*., **70**, 2726–2729 (1993).

148. Jabbarzadeh, A., Atkinson, J. D., and Tanner, R. I., Effect of the wall roughness on slip and rheological properties of hexadecane in molecular dynamics simulation of couette shear flow between two sinusoidal walls, *Phys. Rev. E*, **61**, 690–699 (2000).

149. Galea, T. M., and Attard, P., Molecular dynamics study of the effect of atomic roughness on the slip length at the fluid-solid boundary during shear flow, *Lang*., **20**, 3477–3482 (2004).

150. Lichter, S., Roxin, A., and Mandre, S., Mechanisms for liquid slip at solid surfaces, *Phys. Rev. Lett*., **93**, 086001 (2004).

151. Krim, J., FMMLS-1: Friction at macroscopic and microscopic length scales, *Am. J. Phys*. **70**, 890–897 (2002)

152. Gao, J., Leuedtke, W. D., and Landman, U., Layering transitions and dynamics of confined liquid films, *Phys. Rev. Lett*., **79**, 705–709 (1997)

153. Silliman, W. J., and Scriven, L. E., Separating flow near a static contact line: Slip at a wall and shape of a free surface, *J. Comput. Phys*., **34**, 287–313 (1980)

154. Raviv, U., Giasson, S., Frey, J., and Klein, J., Viscosity of ultra-thin water films confined between hydrophobic and hydrophilic Surfaces, *J. Phys.: Condens. Matter*, **14**, 9275–9283 (2002)

155. Israelachvili, J. N., Measurement of viscosity of liquids in very thin films, *J. Colloid Interface Sci*. **110**, 263–71 (1986).

156. Prandtl, L., *Motion of Fluids with very Little Viscosity, National Advisory Committe for Aeronautics*, Technical memorandum No. 452 (1927)

157. Bushnell, D. M., and Moore, K. J., Drag reduction in nature, *Annu. Rev. Fluid Mech*., **23**, 65–79 (1991)

158. Schmatko, T., Hervet, H., and Leger, L., Friction and slip at simple fluid-solid interfaces: the roles of the molecular shape and the solid–liquid interaction, *Phys. Rev. Lett*., **94**, 244501 (2005)

159. Bazant, M. Z., and Vinogradova, O. I., Tensorial hydrodynamic slip, *J. Fluid Mech*., **613**, 125–134 (2008).

160. Kamrin K., Bazant, M. Z., and Stone, H. A., Effective slip boundary condition for arbitrary periodic surface: the surface mobility tensor, *J. Fluid Mech*. **658**, 409–412 (2010)

161. Feuillebois, F., Bazant, M. Z., and Vinogradova, O. I., Effective slip over superhydrophobic surfaces in thin channels, *Phys. Rev. Lett*., **102**, 026001 (2009)

162. Helmholtz H., and von Piotrowski G., *Über Reibung tropfbarer Flüssigkeiten*, In: *Wissenschaftliche Abhandlungen*, Helmholtz, H., ed., Sitzungsberichte, Wien (1860).

163. Kundt A., and von Warburg E.: Über Reibung und Wärmeleitung verdünnter Gase, *Ann. Phys*., **156**, 177–211 (1876).

164. Weidemann, G., Über die Bewegung von Flüssigkeiten im Kriese der geschlossen galvanischen Säule, *Ann. Phys*., **163,** 321–352 (1852).

165. Whetham, W.C.D., On the alleged slipping at the boundary of a liquid in motion, *Phil. Trans. Royal Soc. London*, **48**, 225–230 (1890).

166. Maxwell, J. C., On stresses in rarefied gases arising from inequalities of temperature, *Phil. Trans. Royal Soc. London*, **170**, 231–256 (1879).

167. Karniadakis, G. E., Beskok, A., and Aluru, N., *Microflows and Nanoflows: Fundamentals and Simulation*, Springer (2005).

168. Beskok, A., and Karniadakis, G. E., A model for flows in channels, pipes and ducts at micro and nanoscales, *Nanoscale Microscale Thermophys., Eng*., **3**, 43–77 (1999).

169. To Q. D., Bercegeay C., Lauriat G., Leonard C., and Bonnet G., A slip model for micro/nano gas flows induced by body forces, *Microfluid Nanofluid*, **8**, 417–422 (2010).

170. Loyalka, S. K., Approximate method in kinetic theory, *Phys. Fluid*., **14**, 2291–2294 (1971).

171. Loyalka, S. K., Petrellis, N., and Stvorick, S. T., Some numerical results for the BGK model: Thermal creep and viscous slip problems with arbitrary accommodation of the surface, *Phys. Fluid*., **18**, 1094-1099 (1975).

172. Maurer, J., Tabeling, P., Joseph, P., and Willaime, H., Second-order slip laws in microchannels for helium and nitrogen, *Phys. Fluid*, **15**, 2613–2621 (2003).

173. Myong, R. S., Gaseous slip models based on the Langmuir adsorption isotherm, Phys. Fluid, **16**, 104–117 (2004).

174. Fichman, M., and Hetsroni, G., Viscosity and slip velocity in gas flow in microchannels, *Phys. Fluid*, **17**, 123102 (2005).

175. Lilley, C. R., and Sader, J. E., Velocity profile in the Knudsen layer according to the Boltzmann equation, *Proc. R. Soc*., **A464**, 2015–2035 (2008).

176. Xue, H., and Fan, Q., A High order modification on the analytic solution of microchannel gaseous flows, In: Proceeding of ASME fluids engineering division summer meeting, Boston, USA, FEDSM 2000–11313 (2000).

177. Bahukudumbi, P., Park, J. H., Beskok, A., A unified engineering model for steady and quasi-steady shear-driven gas microflows, *Microscale Thermophys Eng*., **7**, 291–315 (2003).

178. Karniadakis, G. E., and Beskok, A., *Micro Flows: Fundamentals and Simulation*, Springer, New York (2002).

179. Jie, D., Diao, X., Cheong, K. B., and Yong, L. K., Navier–Stokes simulations of gas flow in micro devices, *J. Micromech Microeng*., **10**, 372–379 (2000).

180. Lockerby, D. A., Reese, J. M., Emerson. D. R., and Barber, R. W., Velocity boundary condition at solid walls in rarefied gas calculations, *Phys. Rev. E*, **70**, 017303 (2004)

181. Ng, E. K., and Liu, N., A multicoefficient slip-corrected Reynolds equation for micro-thin film gas lubrication, *Int. J. Rotat. Mach*., **2**, 105–111 (2005).

182. Lauga, E., and Stone, H. A., Effective slip in pressure-driven stokes flow, *J. Fluid Mech*., **489**, 55–77 (2003).

183. Wu, L., Slip model for rarefied gas flows at arbitrary Knudsen number, *Appl. Phys. Lett*., **93**, 253103 (2008).

184. Voronov, R. S., Papavassiliou, D. V., and Lee, L. L. Review of fluid slip over superhydrophobic surfaces and its dependence on the contact angle, *Ind. Eng. Chem. Res*., **47**, 2455–2477 (2008).

185. Richards, S., No-slip boundary condition, *J. Fluid Mech*., **59**, 707–719 (1973).

186. Ponomarev, I. V. and Meyerovich, A. E., Surface roughness and effective stick-slip motion, *Phys. Rev. E*, **67**, 026302 (2003).

187. Jansons, K. M., Determination of the macroscopic (partial) slip boundary condition for a viscous-flow over a randomly rough-surface with a perfect slip microscopic boundary-condition, *Phys. Fluids*, **31**, 15–17 (1988).

188. Sarkar, K., and Prosperetti, A., Effective boundary conditions for stokes flow over a rough surface, *J. Fluid Mech*., **316**, 223–240 (1996).

189. Priezjev, N. V., Darhuber, A. A., and Troian, S. M., Slip behavior in liquid films on surfaces of patterned wettability: comparison between continuum and molecular dynamics simulations, *Phys. Rev. E*, **71** (2005).

190. Hocking, L. M., Moving fluid interface on a rough surface, *J. Fluid Mech*., **76**, 801–817 (1976).

191. Watanabe, K., Yanuar & Udagawa, H. Drag reduction of Newtonian fluid in a circular pipe with a highly water-repellent wall, *J. Fluid Mech*., **381**, 225–238 (1999).

192. Cottin-Bizonne, C., Barentin, C., Charlaix, E., Bocquet, L., and Barrat, J. L., Dynamics of simple liquids at heterogeneous surfaces: molecular-dynamics simulations and hydrodynamic description, *Eur. Phys. J. E*, **15**, 427–438 (2004).

193. Walther, J. H., Werder, T., Jaffe, R. L., and Koumoutsakos, P., Hydrodynamic properties of carbon nanotubes, *Phys. Rev. E*, **69**, 062201 (2004).

194. Martini, A., Hsu, H. Y., Patankar, N.A., and Lichter, S., Slip at high shear rates, *Phys. Rev. Lett*., **100**, 206001 (2008).

195. Priezjev, N., Shear rate threshold for the boundary slip in dense polymer films, *Phys. Rev. E*, **80**, 031608 (2009).

196. Ulmanella, U., and Ho C. M., *Molecular Effects on Boundary Condition in Micro/Nanoliquid Flows*, Huntington Quadrangle, Suite N101, Melville, NY 11747-4502, United States, American Institute of Physics, (2008).

197. Kulkarni, A. A., and Joshi, J. B., Bubble formation and bubble rise velocity in gas-liquid systems: a review, *Ind. Eng. Chem. Res*., **44**, 5873–5931 (2005).

198. Granick, S., Zhu, Y. X., and Lee, H., Slippery questions about complex fluids flowing past solids. *Nature Mat*., **2**, 221–227 (2003).

199. Tretheway, D. C., and Meinhart. C. D., Effects of absolute pressure on fluid slip in a hydrophobic microchannel, ASME 2003 International Mechanical Engineering Congress and Exposition (IMECE2003), November 15-21, Washington DC, USA, pages 561–564, (2003).

200. Black, W. B., and Graham, M. D., Wall-slip and polymer-melt flow instability, *Phys. Rev. Lett*., **77**, 956–959 (1996).

201. Guo, F., Wong, P. L., Geng, M., and Kaneta, M., occurrence of wall slip in elastohydrodynamic lubrication contacts, *Tribology Lett*, **34**, 103–111 (2009).

202. Holland, F. A., and Bragg, R., *Fluid Flow for Chemical Engineers*, Edward Arnold, 2nd edition (1995).

203. Tretheway, D. C., and Meinhart, C. D., A generating mechanism for apparent fluid slip in hydrophobic microchannels, *Phys. Fluid*, **16**, 1509–1515 (2004)

204. Lauga, E., and Stone, H. A., Effective slip in pressure-driven stokes flow, *J. Fluid Mech*., **489**, 55–77 (2003).

205. Choi, C. H., and Kim, C. J., Large slip of aqueous liquid flow over a nanoengineered superhydrophobic surface, *Phys. Rev. Lett*., **96**, 066001 (2006).

206. Reed, L. D., and Morrison, F. A., Particle interactions in viscous flow at small values of Knudsen number, *J. Aerosol Sci*., **5**, 175–189 (1974).

207. Padmavathi, B. S., Amaranath, T., and Nigam, S. D., Stokes flow past a sphere with mixed slip-stick boundary conditions, *Fluid Dyn. Res*., **11**, 229–234 (1993).

208. Sherief, H. H., Faltas, M. S., and Saad, E. I., Slip at the surface of a sphere translating perpendicular to a plane wall in micropolar fluid, *ZAMP*, **59**, 293–312 (2008).

209. Sherief, H. H. Faltas, M. S. and Ashmawy, Galerkin representations and fundamental solutions for an axisymmetric microstretch fluid flow, *J. Fluid Mech*., **619**, 277–293 (2009).

210. Basset, B., *A Treatise on Hydrodynamics*, Cambridge University Press, Cambridge, (1888).

211. Keh, H. J., and Chen, S. H., The motion of a slip spherical particle in an arbitrary Stokes flow, *Eur. J. Mech. B/Fluids*, **15**, 791−807 (1996).

212. Hatzikiriakos, S. G., Wall Slip of Molten Polymers, *Progr. Polym. Sci*., **37**, 624–643 (2012).

213. Luk, S., Mutharasan, R., and Apelian, D., Experimental observation of wall slip: tube and packed bed flow, *Ind. Eng. Chem. Res*., **26**, 1609–1616 (1987).

214. Faltas, M. S., and Saad, E. I., Stokes flow past an assemblage of slip eccentric spherical particle-in-cell models, *Math. Meth. Appl. Sci*., **34**, 1594–1605 (2011).

215. Happel, J., Viscous flow in multiparticle systems: slow motion of fluids relative to beds of spherical particles, *AIChE J*., **4**, 197–201 (1958).

216. Kuwabara, S., The forces experienced by randomly distributed parallel cylinders or spheres in a viscous flow at small Reynolds numbers, *J. Phys. Soc. Japan*., **14**, 527–532 (1959).

217. Atefi, G. H., Niazmand, H., Meigounpoory, M. R., Numerical analysis of 3-D flow past a stationary sphere with slip condition at low and moderate Reynolds numbers, *J. Dis. Sci. Technol*., **28**, 591–602 (2007).

218. Smoluchowski, M., Ueber warmeleitung in verdunnten gasen, *Annalen der Physik und Chemie*, **64**, 101–130, (1898).

219. Zade, A. Q., Renksizbulut, M. and Friedman, J., Boundary conditions for multi-component slip-flows based on the kinetic theory of gases, In: Proceedings of the sixth international ASME conference on Nanochannels, Microchannels and Minichannels, ICNMM 2008, June 23–25, 2008, Darmstadt, Germany.

220. Gokcen, T. and MacCormack, R. W., Nonequilibrium effects for hypersonic transitional flows using continuum approach, AIAA Paper 1987-1115, 1987, presented at the 27th Aerospace Sciences Meeting, Reno, NV, Jan. 1989.

221. Mohajer, B., Aliakbar, V., Shams M., and Moshfegh, A., Heat transfer analysis of a microspherical particle in the slip flow regime by considering variable properties, *Heat Transfer Eng*., **36**, 596–610 (2015).

222. Taylor, T. D., Heat transfer from single spheres in a low Reynolds number slip flow, *Phys. Fluids*, **6**, 7–12 (1963).

223. Strom, H., and Sasic, S., Heat transfer effects on particle motion under rarefied conditions, *Int. J. Heat Fluid Fl*ow., **43**, 277–284 (2013).

224. Vasudeviah, M., and Balamurugan, K., Heat transfer in a slip-flow past a sphere, *Fluid Dyn. Res*., **22**, 281–296 (1998).

225. Vajjha, S. R., and Das, D. K., A review and analysis on influence of temperature and concentration of nanofluids on thermophysical properties, heat transfer and pumping power, *Int. J. Heat Mass Trans*., **55**, 4063–4078 (2012).

226. Martin, M. J., and Boyd, I. D., Momentum and heat transfer in a laminar boundary layer with slip flow, *J. Thermophys. Heat Trans*., **20**, 1–6 (2006).

227. Bao, F. B., and Lin, J. Z., Burnett simulation of gas flow and heat transfer in micro Poiseuille flow, *Int. J. Heat Mass Transfer*., **51**, 4139–4144 (2008).

228. Dongari, N., and Agrawal, A., Analytical solution of gaseous slip flow in long microchannels, *Int. J. Heat Mass Transfer*, **50**, 3411–3421 (2007).

229. Rached, J., and Daher, N., Numerical prediction of slip flow and heat transfer in micro-channels, In: Proceedings of the 6th annual engineering students conference, American University of Beirut, Beirut, Lebanon, 109–114 (2007).

230. Kakac, S., Vasiliev, L. L., Bayazitoglu, Y., and Yener, Y., *Microscale Heat Transfer-Fundamentals and Applications*, Springer, Neatherlands (2005).

231. Minkowycz, W. J., Sparrow, E. M., and Abraham, J. P., *Nanoparticle Heat Transfer and Fluid Flow*, CRC Press (2013).

232. Clift, R., Grace, J.R., Weber, M.E., *Bubbles, Drops and Particles*, Academic press, New York (1978).

233. Michaelides, E.E., *Particles, Bubbles and Drops: Their Motion, Heat and Mass Transfer*, World Scientific, Singapore (2006).

234. Chhabra, R.P., *Bubles, drops and particles in Non-Newtonian fluids*, 2nd edition, CRC Press, Boca Raton, FL (2006).

235. Neto, C., Evans, D. R., Bonaccurso, E., Butt, H. J., and Craig, V. S. J., Boundary slip in Newtonian liquids: a review of experimental studies, *Rep. Prog. Phys*., **68**, 2859–2897 (2005).

236. Sochi, T., Slip at fluid-solid interface, *Polym. Rev*., **51**, 309–340 (2011).

237. Lauga, E., Brenner, M. P., Stone, H. A., The no-slip boundary condition: a review, Chapter 19 in: *Handbook of Experimental Fluid Dynamics*, C. Tropea, A. Yarin, J. F. Foss (Eds.), Springer, (2007).

238. S. Colin, Gas microflows in the slip flow regime: A critical review on convective heat transfer, *J. Heat Trans*., **134**, 020908 (1–13) (2012).

239. Kandlikar, S. G., Colin, S., Peles, Y., Garimella, S., Pease, R. F., Brandner J.J., and Tuckerman, D. B., Heat transfer in microchannel – 2012, Status and research needs, *J. Heat Trans*., **135**, 091001 (1–18) (2013).

240. Allen, H. S., The motion of a sphere in a viscous fluid, *Lord Raylegh, Phil. Mag*., **50**, 306–323 (1900).

241. Takata, S., Sone, Y., and Aoki, K., Numerical analysis of a uniform flow of a rarefied gas past a sphere on the basis of the Boltzmann equation for hard-sphere molecules, *Phys. Fluids A* 5, **726**, 716–737 (1993).

242. Keh, H. J. and Shiau, S. C., Effects of inertia on the slow motion of aerosol particles, *Chem. Eng. Sci*., **55**, 4415–4421 (2000).

243. Barber, R. W., and Emerson, D. R., Analytical solution of low Reynolds number slip flow past a sphere, CP663, Rarefied Gas Dynamics: 23rd International Symposium, (2000).

244. Keh, H. J., and Huang C. H., Slow motion of axisymmetric slip particles along their axes of revolution, *Int. J. Engg. Sci*., **42**, 1621–1644 (2004)

245. Wen, S. B., and Lai, C. L., Theoretical analysis of flow passing single sphere moving in a micro-tube. *Proc. R. Soc. Lond. A.*, **459**, 495–526 (2003).

246. Meigounpoory, M. R., Atefi, G. H., Niazmand, H., and Mirbozorgi, A., Numerical investigation of slip effect on the three dimensional flow past an impenetrable rotating spherical nano particle, *J. Dis. Sci. Technol*., **28**, 591–602 (2007).

247. Swan, J. W., and Khair, A. S., On the hydrodynamics of slip-stick spheres, *J. Fluid Mech*., **606**, 115–132 (2008).

248. Willmott, G., Dynamics of a sphere with inhomogeneous slip boundary conditions is stoke flow, *Phys. Rev. E* **77**, 055302(R), (2008).

249. Luo, H., and Pozrikidis, C., Effect of surface slip on Stokes flow past a spherical particle in infinite fluid and near a plane wall, *J. Eng. Math*., **62**, 1–21 (2008).

250. Moshfegh, A., Shams, M., Ahmadi, G., and Ebrahim, R., A novel slip correction factor for spherical aerosol particles, *Eng. Technol*., **46**, 108–114 (2008).

251. Moshfegh, A., Shams, M., Ahmadi, G., and Ebrahim, R., A new expression for spherical aerosol drag inslip flow regime, *J. Aerosol Sci*., **41**, 384–400 (2010).

252. Feng, Z. G., A correlation of the drag force coefficient on a sphere with interface slip at low and intermediate Reynolds numbers, *J. Disp. Sci. Tech*., **31**, 968–974 (2010).

253. Datta, S., and Singhal, S., Slip flow past a sphere with a source at its centre, *Int. J. Appl. Math and Mech*., **7**, 36–51 (2011).

254. Ashmawy, E., Slip at the surface of a general axi-symmetric body rotating in a viscous fluid, *Arch. Mech*., **63**, 341–361 (2011).

255. Ashmawy, E., Unsteady rotational motion of a slip spherical particle in a viscous fluid, *ISRM Math. Phys*., 1–8 (2012).

256. Ashmawy, E., Unsteady Stokes flow of a couple stress fluid around a rotating sphere with slip, *Eur. Phys. J. Plus*, **131:175**, 1–8 (2016).

257. Ashmawy, E., Drag on a slip spherical particle moving in a couple stress fluid, *Alexandria Engg. J*., **55**, 1159–1164 (2016).

258. Chang, Y. C., Keh, H. J., Translation and rotation of slightly deformed colloidal spheres experiencing slip, *J. Colloid Interface Sci*., **330**, 201–210 (2009).

259. Chang, Y. C., Keh, H. J., Creeping-flow rotation of a slip spheroid about its axis of revolution, *Theor. Comput. Fluid Dyn*., **26**, 173–183 (2012).

260. Niazmand, H., and Anbarsooz, M., Slip flow over micron-sized spherical particles at intermediate Reynolds numbers, *J. Mech. Sci. Tech*., **26**, 2741−274 (2012).

261. Varet, D. G., Hillairet, M., and Wang, C., The influence of boundary conditions on the contact problem in a 3D Navier−Stokes flow, *J. Math. Pures Appl*., **103**, 1–38 (2015).

262. Lee, T. C., and Keh, H. J., Slow motion of a spherical particle in a spherical cavity with slip surfaces, *Int. J. Eng. Sci*., **69**, 1−15 (2013).

263. Hocking, L. M., The effect of slip on the motion of a sphere close to a wall and of two adjacent spheres, *J. Eng. Math*., **7**, 207–221 (1973).

264. Datta, S., and Deo, S., Stokes flow with slip and Kuwabara boundary conditions, *Proc. Indian Acad. Sci. (Math. Sci.)*, **112**, 463–475 (2002).

265. Faltas, M. S. and Saad, E. I. Stokes flow between eccentric rotating spheres with slip regime, *Z. Angew. Math. Phys*. **63**, 905–919 (2012).

266. Ghosh, S., van den Ende, D., Mugele, F., Duits, M. H. G., Apparent wall-slip of colloidal hard-sphere suspensions in microchannel flow, *Colloids and Surfaces A: Physicochem. Eng. Aspects*, **491**, 50–56 (2016).

267. Sahu, K. C., Sameen, A., Govindarajan, R., The relative roles of divergence and velocity slip in the stability of plane channel flow, *Eur. Phys. J. Appl. Phys*. **44**, 101–107 (2008).

268. Ghosh, S., Usha, R., Sahu, K. C., Linear stability analysis of miscible two-fluid flow in a channel with velocity slip at the walls, *Phys. Fluid*, **26**, 014107 (2014).

269. Ghosh, S., Usha, R., Sahu, K. C., Double-diffusive two-fluid flow in a slippery channel: A linear stability analysis, *Phys. Fluid*, **26**, 127101 (2014).

270. Ghosh, S., Usha, R., Sahu, K. C., Absolute and convective instabilities in double-diffusive two-fluid flow in a slippery channel, *Chem. Engg, Sci*., **134**, 1–11 (2015)

271. Subramanian, N. B., and Kannan, C. S., Slip velocity characteristics in the riser of circulating fluidised bed, *Chem. Eng. Technol*., **20**, 491−494 (1997).

272. Palani, N., Ramalingam, V., Ramadoss, G., and Seeniraj, R.V., Study of slip velocity and application of drift-flux model to slip velocity in a liquid-solid circulating fluidized bed, Adv. Powder Technol., **22**, 77−85 (2011).

273. Tenneti, S., Garg, R., Subramaniam, S., Drag law for monodisperse gas–solid systems using particle–resolved direct numerical simulation of flow past fixed assemblies of spheres. Int. J. Multiphase Flow, **37**, 1072–1092 (2011).

274. Mehrabadi, M., Tenneti, S., Garg, R., and Subramaniam, S., Pseudo-turbulent gas-phase velocity fluctuations in homogeneous gas-solid flow: fixed particle assemblies and freely evolving suspensions, J. Fluid Mech., **770**, 210−246 (2015).

275. Moosail, A., and Atefi, G., Analytical solution to slow flow of a Cosserat fluid past a sphere using slip boundary condition, In: Proceedings of the 3rd IASME/WSEAS Int. Conf. on Fluid Dynamics & Aerodynamics, Corfu, Greece, August 20−22, 2005 (68−73).

276. Sherif, H. H., Faltas, M. S., and Saad E. I., Slip at the surface of a sphere translating perpendicular to a plane wall in micropolar fluid, Z. angew. Math. Phys. **59**, 293–312 (2008).

277. Kalyon, D. M., and Malik, M., Axial laminar flow of viscoplastic fluids in a concentric annulus subject to wall slip, Rheol. Acta, **51**, 805–820 (2012).

278. Ansari, M., and Hatzikiriakos, S. G., Slip effects in HDPE flows, J. Non-Newt. Fluid Mech., **167–168**, 18–29 (2012).

279. Ferras, L. L., Nobrega, J. M., and Pinho, F. T., Analytical solutions for Newtonian and inelastic non-Newtonian flows with wall slip, J. Non-Newt. Fluid Mech., 175–**176**, 76–88 (2012).

280. Ferras, L. L., Afonso, A. M., Alves, M. A., Nobrega, J. M., and Pinho, F. T., Annular flow of viscoelastic fluids: Analytical and numerical solutions, J. Non-Newt. Fluid Mech., **212**, 80–91 (2014).

281. Mallik, B. B., Nanda, S., Das, B., Saha, D., Das, D. S., and Paul, K., A non-Newtonian fluid model for blood flow using power-law through an atherosclerotic arterial segment having slip velocity, IJPCBS, **3**, 752−760 (2013)

282. Housiadas, K. D., Viscoelastic Poiseuille flows with total normal stress dependent, nonlinear Navier slip at the wall, Phys. Fluid, **25**, 043105 (2013).

283. Khan, N., and Mahmood, T., The influence of slip condition on the thin film flow of a third order fluid, Int. J. Nonlinear Sci., **13**, 105–116 (2012).

284. Allende, M., and Kalyon, D. M., Assessment of particle-migration effects in pressure-driven viscometric flows, J. Rheol., **44**, 79−90 (2000).

285. Green, H., Further development of the plastomer and its practical application to research and routine problems, In: Proceedings Am. Soc. Testing Materials, II, 20 (1920).

286. Bingham, E. C., Fluidity and Plasticity, New York, McGraw-Hill, (1922).

287. Yilmazer, U., and Kalyon, D. M., Slip effects in capillary and parallel disk torsional flows of highly filled suspensions, J. Rheol., **33**, 1197−1212 (1989).

288. Soltani, F. and Yilmazer, U., Slip velocity and slip layer thickness in flow of concentrated suspensions, J. Appl. Polym. Sci. **70**, 515–522 (1998).

289. Hu, H., and Larson, R.G., Measurement of wall-slip-layer rheology in shear-thickening wormy micelle solutions, J. Rheol., **46**, 1001–1021 (2002).

290. Ellahi, R., Effects of the slip boundary condition on non-Newtonian flows in a channel, Commun Nonlinear Sci Numer Simulat., **14**, 1377–1384 (2009).

291. Sunarso, A., Yamamoto, T., and Mori, N., Numerical analysis of wall slip effects on flow of Newtonian and non-Newtonian fluids in macro and micro contraction channels, ASME J. Fluid Eng., **129**, 23−30 (2007).

292. Taylor, T. D., Heat transfer from single spheres in a low Reynolds number slip flow, Phys. Fluids, **6**, 7–12 (1963).

293. Mikami, H., Endo, Y., and Takashima, Y., Heat transfer from a sphere to rarefied gas mixtures, Int. J. Heat Mass Trans., **9**, 1435−1448 (1966).

294. Kavanau, L. L., and Drake, R. M., Heat Transfer from Spheres to a Rarefied Gas in Subsonic Flow, California Univ. Berkeley, (1953).

295. Anbarsooz, M., and Niazmand, H., Heat transfer characteristics of slip flow over solid spheres, In: Proceedings of the Institution of Mechanical Engineers, Part C: J. Mech. Eng. Sci., October (2015).

296. Hashizame, K., and Kimura, Y., Heat transfer characteristics in liquid-solid circulating fluidized bed, Japan Society of Mechanical Proceedings (B series) Vol. 73 No. 732 (2007–8) On paper No.07–0086

297. Harms, T.M., Kazmierczak, M.J., and Gerner, F.M., Developing convective heat transfer in deep rectangular microchannels, *Int. J. Heat Fluid Flow*, **20**, 149–157 (1999).

298. Qu, W., Mala, M., and Li, D., Heat transfer for water flow in trapezoidal silicon microchannels, *Int. J. Heat Mass Trans*, **43**, 3925–3936 (2000).

299. Sparrow, E.M., and Lin, S.H., Laminar heat transfer in tubes under slip- flow conditions, *J. Heat Trans*, **84**, 363–369 (1962)

300. Ameel, T.A., Barron, R.F., Wang, X., and Warrington, R.O., Laminar forced convection in a circular tube with constant heat flux and slip flow, *Microscale Thermophys. Eng*., **4**, 303–320 (1997).

301. Tunc, G., and Bayazitoglu, Y., Heat transfer for gaseous flow in microtubes with viscous heating. In: Proceeding of the ASME Heat Transfer Div., HTD 366-2, 299–306 (2000).

302. Tunc, G., and Bayazitoglu, Y., Heat transfer in microtubes with viscous dissipation, *Int. J. Heat Mass Trans*, **44**, 2395–2403 (2001).

303. Ozturk, A., MHD slip flow between parallel plates heated with a constant heat flux, *J. Therm. Sci. Tech*., **33**, 11−20 (2013).

304. Sircar, D., Flow and heat transfer in a micro-channel gas-liquid couette flow, *Int. J. Heat Mass Trans*, **54**, 2913–2920 (2011)

305. Niazmand, H., Renksizbulut, M., and Jaghargh, A. A., Slip-flow and heat transfer in rectangular microchannels in the presence of thermal creep, *J. Therm. Sci*., **3**, 33−41 (2010).

306. El-Nahhas, A., Analytic approximations for the flows and heat transfer in microchannels between two parallel plates, *Math Prob. Eng*., 1−14 (2012)

307. Yazdi1, M. H., Abdullah, S., Hashim, I., Nopiah, Z. M., Zaharim, A., and Sopian, K., Convective Heat transfer of Slip liquid flow Past Horizontal Surface within the Porous media at Constant Heat Flux Boundary Conditions, *Recent Adv. Appl. Math*, 1−7 (2010).

308. Ambethkar, V., and Srivastava, M. K., Numerical study of an unsteady 2-D incompressible viscous flow with heat transfer at moderate Reynolds number with slip boundary conditions, *Int. J. Appl. Math*, **25**, 883−908 (2012).

309. Rana, A. S., Mohammadzadeh, A., and Struchtrup, H., A numerical study of the heat transfer through a rarefied gas confined in a microcavity, *Continuum Mech. Thermodyn*., **27**, 433–446 (2015)

310. Boutebba, S., and Kaabar, W., Conductive heat transfer through a rarefied gas confined between two coaxial cylinders, International Conference on Chemical, Civil and Environmental Engineering (CCEE-2015), Istanbul (Turkey) June 5-6 (2015).

311. Bird, B. R., Stewart, W. E., and Lightfoot, E. N., Transport Phenomena, John-Wiley, New York.

312. Harlow, F. H., and Welch, J. E., Numerical calculation of time-dependent viscous incompressible flow of fluid with free surfaces, *Phys. Fluids*, **8**, 2182−2188 (1965).

313. B. P. Leonard, A stable and accurate convective modeling procedure based on quadratic upstream interpolation, *Comp. Methods Appl. Mech. Engr*., **19**, 59–98 (1979).

314. Dhole, S. D., Chhabra, R. P., and Eswaran, V., Flow of power-law fluids past a sphere at intermediate Reynolds numbers, *Ind. Eng. Chem. Res*., **45**, 4773–4781 (2006).

315. Song, D., Gupta R. K., and Chhabra, R. P., Drag on a sphere in Poiseuille flow of shear-thinning power-law fluids, *Ind. Eng. Chem. Res*., **50**, 13105–13115 (2011).

316. Tripathi, A., Chhabra R. P., and Sundararajan, T., Power law fluid flow over spheroidal particles, *Ind. Eng. Chem. Res*., **33**, 403-410 (1994).

317. LeClair, B. P., Hamielec, A. E., and Pruppacher, H. R., A numerical study of the drag on a sphere at intermediate Reynolds numbers, *J. Atmos. Sci*., **27**, 308–315 (1970).

318. Brabston, D. C., and Keller, H. B., Viscous flows past spherical gas bubbles, *J. Fluid Mech*., **69**, 179–189 (1975).

319. Ryskin, G., and Leal, L. G., Numerical solution of free-boundary problems in fluid mechanics, Part2. Buoyancy-driven motion of gas bubble through a quiescent liquid, *J. Fluid Mech*., **148**, 1–36 (1984).

320. Feng, Z.G., and Michaelides, E. E., Drag coefficients of viscous spheres at intermediate and high Reynolds numbers. *Trans. ASME, J. Fluids Eng*., **123**, 841–849 (2001).

321. Dhole, S. D., Chhabra, R. P., and Eswaran, V., Drag of a spherical bubble rising in power-law fluids at intermediate Reynolds numbers, *Ind. Eng. Chem. Res*., **46**, 939–946 (2007).

322. Murthy, J. V. R. and Kumar, M. P., Effect of slip parameter on the flow of viscous fluid past an impervious sphere, *Int. J. App. Sci. Eng*., **12**, 203–223 (2014).

323. Feng, Z. G. and Michaelides, E. E., Heat and mass transfer coefficients of viscous spheres, *Int. J. Heat Mass Trans*., **44**, 4445-4454 (2001).

324. Dhole, S. D., Chhabra, R. P., and Eswaran, V., Mass transfer from a spherical bubble rising in power-law fluids at intermediate Reynolds numbers, *Int. Commun. Heat Mass Trans*, **34**, 971–978 (2007).

325. Song, D., Gupta, R. K., and Chhabra, R. P., Heat transfer to a sphere in tube flow of power-law liquids, *Int. J. Heat Mass Trans*, **55**, 2110–2121 (2012).

326. Gal-Or, B. and Waslo, S., Hydrodynamics of an ensemble of drops and bubbles in the presence or absence of surfactants, *Chem. Eng. Sci*., **23**, 1431–1446 (1968).

327. Gummalam, S. and Chhabra, R. P., Rising velocity of a swarm of spherical bubbles in a power-law non-Newtonian liquid, *Can J Chem Eng*., **65**, 1004–1008 (1987).

328. Chhabra R. P. Rising Velocity of a Swarm of Spherical Bubbles in Power Law Fluids at High Reynolds Numbers, *Can J Chem Eng*, **76**, 137–140 (1998).

329. Kishore, N., Chhabra, R. P., and Eswaran, V., Bubble swarms in power-law liquids at moderate Reynolds numbers: Drag and mass transfer, *Chem. Eng. Res. Des.*, **86**, 39-53 (2008)

330. Kishore N., Dhole S. D., Chhabra R. P., and Essswaran V., Momentum and heat transfer phenomena for power-law liquids in assemblages of solid spheres of moderate to large void fractions, *Num. Heat Trans., part A,* **56**, 970–986 (2009).

331. Dhole, S. D., Chhabra R. P., and Eswaran V., Power law fluid flow through beds of spheres at intermediate Reynolds numbers pressure in fixed and distended beds, *Chem. Eng. Res. Des*., **82(A5)**, 642–652 (2004).

332. Pfeffer, R., and Happel, J., An analytical study of heat and mass transfer in multiparticle systems at low Reynolds numbers, *AIChE J*., **10**, 605–611 (1964).

RESEARCH OUTPUT

Published in International Refereed Journals

1. N. Kishore and R.R. Ramteke, "Slip in flows of power-law liquids past smooth spherical particles", Acta Mech., 226, 2555-2571 (2015).

2. R. R. Ramteke and N. Kishore, "Heat transfer phenomena of assemblages of smooth slip spheres in Newtonian fluids", Heat Transfer – Asian Research, DOI: 10.1002/htj.21204 (2015).

3. R. R. Ramteke and N. Kishore, "Heat transfer from slip spheres to a shear-thickening fluid: effects of slip velocity and particle volume fraction", Procedia Eng., 127, 354-361 (2015).

4. N. Kishore and R. R. Ramteke, "Forced convective heat transfer from spheres to Newtonian fluids in steady axisymmetric flow regime with velocity slip at fluid-solid interface", Int. J Thermal Sci., 105, 206-217 (2016).

5. N. Kishore and R. R. Ramteke, "Slip in flow through assemblages of spherical particles at low to moderate Reynolds numbers", Chem. Eng. Technol., 39, 1087-1098 (2016).

6. R. R. Ramteke and N. Kishore, "Computational fluid dynamic study on forced convective heat transfer phenomena of spheres in power-law liquids with velocity slip at the interface", *Heat Transfer Engineering*, 1-18, (2017).

7. R. R. Ramteke and N. Kishore, "Effects of uniform heat flux and velocity slip conditions at interface on forced convection heat transfer of spheres in Newtonian fluids", *ASME J Heat Transfer*, 139, 104501, (2017).

8. R. R. Ramteke and N. Kishore, "Effect of Velocity Slip on Settling of Assemblages of Spherical Particles in Power-law Liquids at Low to Moderate Reynolds Numbers", *Acta Mech.*, 228, 1871-1889, (2017).

9. R. R. Ramteke and N. Kishore, "Effect of slip velocity on heat transfer phenomena of multiple smooth slip spheres in power-law liquids", under review (2017).

Book Chapter

10. R. R. Ramteke and N. Kishore, "*Slip Flow of a Shear-Thinning Power-law Fluid Past an Assemblage of Spherical Particles*", Chapter – 2 in book "Fluid Mechanics and Fluid Power – Contemporary Research" Lecture Notes in Mechanical Engineering edited by A.K. Saha et al., Springer India, 2016. DOI: 10.1007/978-81-322-2743_2 (ISBN: 978-81-322-2741-0). (Book Chapter)

National/International Conference Proceedings

11. RR Ramteke and N. Kishore, "The comparison of CWT and UHF boundary Conditions for spheres in the shear-thinning fluids", IHMTC Conference 2017 (Abstract Accepted).

12. R. R. Ramteke and N. Kishore, "Momentum transfer study of shear-thickening fluid flow over slip sphere", *Proceedings of 68th Annual Session of Indian Institute of Chemical Engineers* (CHEMCON – 2015), IIT Guwahati, India, 27-30 December (2015).

13. R. R. Ramteke and N. Kishore, "Effect of slip on forced convection heat transfer from assemblages of smooth slip spheres to shear-thinning liquids", *Proceedings of 23rd National*

Heat and Mass Transfer Conference and 1st International ISHMT-ASTFE Heat and Mass Transfer Conference, ISRO, Trivendram, Kerala, India, 17 – 20 December (2015).

14. R. R. Ramteke and N. Kishore, "Heat transfer from slip spheres to a shear-thickening fluid: effects of slip velocity and particle volume fraction", *Proceedings of the International Conference on Computational Heat and Mass Transfer (ICCHMT),* NIT Warangal, India, 30 November – 2 December (2015).

15. R. R. Ramteke and N. Kishore, "*Slip Flow of a Shear-Thinning Power-law Fluid Past an Assemblage of Spherical Particles*", *Proceedings of 5th International and 41st National Conference on Fluid Mechanics and Fluid Power*, FMFP-2014, Paper # A-152, Kanpur, India, December (2014).